Short-term Variation in Measurements of Atmospheric Ice-Nucleating Particle Concentrations

Zur Erlangung des akademischen Grades eines
DOKTORS DER NATURWISSENSCHAFTEN (Dr. rer. nat.)
von der KIT-Fakultät für Physik des
Karlsruher Instituts für Technologie (KIT)

genehmigte

DISSERTATION

von

M.Sc. Franziska Vogel

Tag der mündlichen Prüfung:	10.06.2022
Referent:	Prof. Dr. Thomas Leisner
Korreferent:	Prof. Dr. Benjamin J. Murray

Abstract

Primary ice formation in clouds is initiated by a minor subset of the total atmospheric aerosol population called ice-nucleating particles (INPs), that originate from various source regions around the globe. Tropospheric clouds containing ice crystals are a key player for facilitating life on Earth by providing fresh water originating from liquid and solid precipitation and by balancing the radiation budget with their optical properties. The number concentration of atmospheric INPs and the related number of ice crystals is highly variable and strongly depends on the aerosol type and properties. Due to changes in the ambient conditions or physical or chemical processes in the atmosphere on a time scale of minutes to a few hours, the INP concentration may vary on a similar time scale. Especially the potential short-term variation is still not well investigated and underrepresented in models, but may be addressed with automated INP measurements with a high time resolution at well controlled conditions. A major subject of the here presented thesis is to quantify the short-term variation of atmospheric INP concentrations and search for possible causes for this variation by correlating the INP measurements with other variables like the aerosol number and surface area concentration and meteorological variables.

The atmospheric INP measurements were performed with the newly developed cloud expansion chamber PINE (Portable Ice Nucleation Experiment), which is a mobile INP instrument optimized for automated and continuous INP measurements with a time resolution of about 6 min. In this work, PINE was operated at temperatures in the mixed-phase cloud regime between $-15\,^{\circ}\mathrm{C}$ and $-30\,^{\circ}\mathrm{C}$. For an extension of the covered temperature range of the INP measurements to temperatures up to about $-5\,^{\circ}\mathrm{C}$, INSEKT (Ice Nucleation Spectrometer of the Karlsruhe Institute of Technology) analysis were performed. INSEKT is a well established method and was also used to validate the PINE measurements, but has the drawback of a poor time resolution of several hours or days.

Because PINE is a newly developed instrument, intercomparison and validation experiments with other INP instruments were performed at the AIDA (Aerosol Interaction and Dynamics in the Atmosphere) cloud simulation chamber. Intercomparsion experiments with 12 different INP instruments were carried out using 5 aerosol samples with different freezing properties in the mixed-phase cloud regime. Ambient INP concentrations are highly variable, so the study in this work included for the first time an intercomparison for a wide range of INP concentrations using the same aerosol sample. Independent of the probed INP concentration, the offset between different instruments was up to 4 orders of magnitude, similar to instrument offsets reported in Hiranuma et al. (2015) and DeMott et al. (2018). The reasons for these offsets remain unclear, but may be related to different ice formation modes or pathways the different instruments are sensitive for.

Ambient INP measurements at three rural locations and one mountain site were conducted continuously over a time period between 8 weeks and 5 months. Three of the campaigns included INP monitoring with PINE with a time resolution of about 6 min, and for all campaigns INSEKT INP measurements were performed with a time resolution between 4 h and 3 days. Generally, the INP concentration at all sampling sites varied between about $0.1\,L^{-1}$ and $300\,L^{-1}$ at a temperature of about $-23\,°C$. The observed variation in the INP concentration measured with PINE in two rural environments showed enhanced positive correlations with the ambient air temperature, global radiation and planetary boundary layer height, and negative correlations with the humidity in time periods of a diurnal variation. In time periods without a diurnal variation of the INP concentration, no clear correlation with the analyzed variables was found. From this, one may conclude that the short-term variation of the INP concentration is caused by local effects, like farming activities or biological particles, which were not quantified by the measured parameters. Based on the measurements in the rural locations, a new parameterization was developed for calculating the INP concentration in models. The improved parameterization represents up to 30 % more data points within a factor of 10 from the 1:1 line than previous parameterizations applied on the data set. Some existing parameterizations relate the predicted INP concentration to the number concentration of particles with a diameter larger than 0.5 µm. Also the INAS (Ice Nucleation Active Site) density approach implies that larger aerosol particles are more likely to induce ice formation. However, the impact of the size of an aerosol particle on its ice-nucleation activity is not yet well investigated. Laboratory experiments from this work with size-selected dust aerosol depicted that in some cases the freezing probability per particle surface area is independent of the size while in other cases smaller aerosol particles showed a higher freezing activity per surface area. This variable agreement was found to be potentially related to heat sensitive particles like organics or microbes, which may be more frequent at smaller particle sizes. Moreover, when conducting size-selective INP measurements in a rural environment it was observed that within a time period of about 36 h the freezing ability of the ambient aerosol changed from a size independent freezing to a higher freezing ability of larger aerosol particles. This change in the freezing ability was connected to a change in the air mass origin, which may have caused a change in the size-dependent aerosol composition. Therefore, future size-selective INP measurements at a high time resolution should be combined with size-resolved aerosol composition analysis at a similar time resolution.

Inspired by the reliable and precise operation of PINE, the new stationary and small cloud expansion chamber AIDAm (AIDAmini) was developed. AIDAm is located in the cold room of the AIDA facility and samples aerosol from the AIDA chamber for e.g. measuring steady changes in the ice nucleation properties of aerosol particles which may undergo chemical aging or other modifications during long-term aerosol simulation experiments. The validation of AIDAm showed a good agreement of AIDAm, AIDA and INSEKT measurements for selected operation conditions. It was also proofed that AIDAm is able to distinguish between homogeneous freezing of aqueous aerosol particles at temperatures lower than $-35\,°C$ and the heterogeneous ice formation in the presence of INPs at the same temperature. With this

new instrument, the temporal evolution of the ice nucleation ability of different aerosol samples during an hour-long coating procedure at conditions of the upper troposphere was investigated. Thereby, a 20 nm thick coating layer of sulfuric acid or secondary organic aerosol was established over 5 h, which fully suppressed or clearly shifted the ice activity of the pristine aerosol, respectively.

This thesis shows the high value of automated and continuous INP measurements with a high time resolution both in the laboratory and the field and quantifies changing ice nucleation properties of aerosol particles, which may be connected to variations of environmental or meteorological processes occurring on a range of time scales from minutes to days.

Contents

1. Introduction

Since the formation of the Earth's atmosphere, aerosol particles are emitted from different sources distributed around the globe and by that impact life on Earth. Once the aerosols are released from the emission sources, they are transported into all levels in the troposphere (e.g. Jaenicke, 1982), to altitudes between up to 8 km at the pole regions and 18 km at the equator. Due to changing environmental conditions and atmospheric transport patterns, the aerosol sources and by that also their strength of emission constantly changed and so the total atmospheric aerosol population has always been originated from a highly variable pool, as indicated by the analysis of different aerosol tracers in ice cores (e.g. Eichler et al., 2009; Rubino et al., 2016; Amino et al., 2021). Independent of the emitted amount, each of the various aerosol types contributes to a certain amount to the formation of liquid cloud droplets and ice crystals in warm, mixed-phase and pure ice clouds. Hereby, warm clouds consist of only liquid cloud droplets, mixed-phase clouds of liquid cloud droplets and ice crystals and pure ice clouds of only ice crystals. This also defines the temperature range and supersaturation conditions at which they occur in the atmosphere, such that they exist at temperatures of higher than 0 °C and water saturated conditions, between 0 °C and −35 °C and water and ice saturated conditions and lower than −35 °C and ice saturated conditions, respectively (e.g. Pruppacher and Klett, 2010). Atmospheric aerosol particle fractions of almost 1 contribute to the cloud droplet formation, but only a minor amount out of the entity of aerosol particles is able to trigger ice crystal formation (e.g. Seinfeld and Pandis, 2016). Those inducing the formation of a liquid cloud droplet are called Cloud Condensation Nuclei (CCN) and aerosols triggering ice formation are called Ice-Nucleating Particles (INPs) (e.g. Pruppacher and Klett, 2010).

Clouds in the atmosphere consist of liquid cloud droplets and/or ice crystals, depending on the temperature and supersaturation conditions they form and related to that, their altitude and geographic region of occurrence. During the life cycle of a cloud, aerosol particles get activated as droplets and/or ice crystals, which then grow in size by condensation, deposition, collision and riming processes until they reach a size where they precipitate as indicated in figure 1.1 (Lohmann et al., 2016). By precipitation in liquid or solid form, clouds maintain the natural balance of the water cycle on Earth and are the most important source for fresh water supply (e.g. Chahine, 1992). Clouds are not only vital in the global water cycle, but they also play a key role for the radiation budget on the Earth's surface with their cooling and warming effects (e.g. Boucher et al., 2013). Which of these two effects prevails, strongly depends on the cloud properties, namely the amount and size of water droplets and ice crystals, related to that the region and surface albedo over which they are formed and the temperature and supersaturation conditions in the atmosphere. Generally speaking, warm clouds have a prevailing cooling effect and incoming longwave

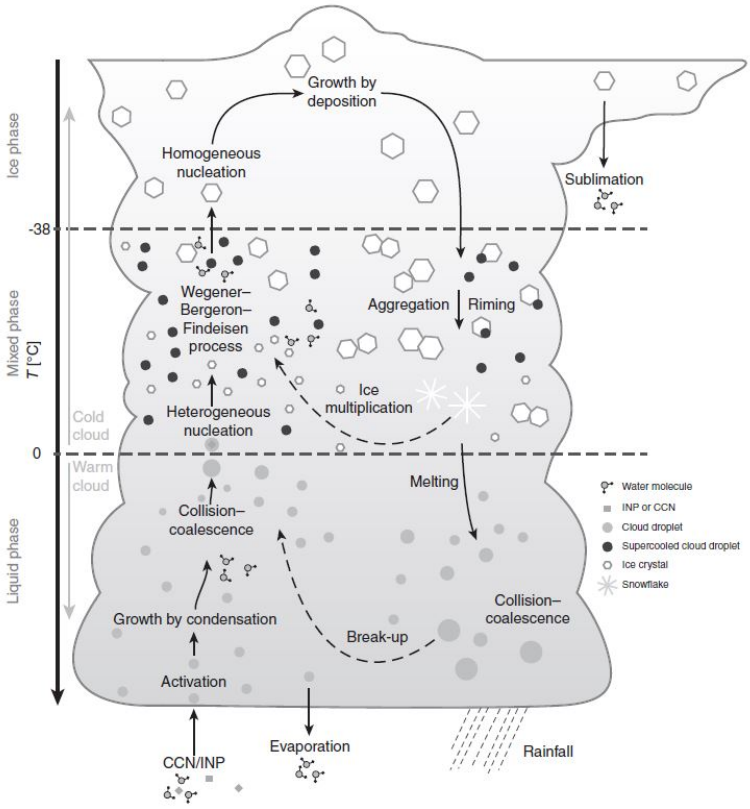

Figure 1.1.: Microphysical processes occurring in a convective cloud with a cloud base temperature higher than 0 °C and a cloud top temperature lower than −38 °C, so that warm-, mixed- and ice-phase processes take place. The small arrows show typical trajectories of a cloud particle. Figure and adapted caption taken from Lohmann et al. (2016).

radiation is reflected back to space, because they are less transparent for the incoming radiation. On the other hand, pure ice clouds contribute more to the warming of the atmosphere, by trapping the longwave radiation emitted from the Earth's surface. Consequently, less longwave radiation is reflected back to space, but also shortwave radiation is not reflected efficiently. For mixed-phase clouds, in which liquid cloud droplets and ice crystals coexist, the contribution to a cooling or warming effect can vary depending on the ratio of particles in the liquid and ice phase (e.g. Lohmann et al., 2016; Vergara-Temprado et al., 2018). In the presence of INPs, ice crystals form, which grow to sizes where they precipitate subsequently. By precipitation in liquid and solid form, the cloud becomes thinner or dissipates over time (e.g. Solomon et al., 2018). This effect is yet still highly uncertain in models, because the formation and concentration of ice crystals in clouds is still underrepresented. Mixed-phase clouds forming in the presence of high INP concentrations contain high amounts of ice crystals and the warming effect dominates. Over regions with weaker INP emission sources, aerosol particles are mostly CCNs and the cloud consists of more cloud droplets, such that these clouds have a greater cooling effect. The cooling and warming effect of clouds are both important to balance the radiation budget in the atmosphere and by that keep the average ambient temperature on a global scale constant (e.g. Storelvmo et al., 2015; Murray et al., 2021). However,

enhanced anthropogenic aerosol emissions during the last decades lead to a significant change in the aerosol population and by that the radiative properties (Lund et al., 2019). This human made modification of the aerosol population enforces the natural greenhouse effect in the atmosphere and by that the average ambient temperature will increase by 1.5 °C to 5 °C until the end of the 21st century (IPCC, 2021). An increase in the ambient air temperature may lead to changes in the cooling and warming effect of clouds, where the transition from a warming to a cooling effect is called a negative cloud phase feedback and accordingly, the transition from a cooling to a warming effect a positive cloud phase feedback. With a warming of the atmosphere, the 0 °C isotherm is shifted upwards to higher altitudes and as a consequence, mixed-phase clouds contain more liquid cloud droplets than they did initially. Due to the higher amount of liquid cloud droplets, these clouds are capable of reflecting more longwave radiation back to space, leading to a cooling effect of the cloud. Depending on whether the initial amount of ice crystals in the cloud was high or low, the amount of cloud droplets is increased by a high or low amount and by that the cloud has a strong of weak negative cloud phase feedback as shown in figure 1.2 (a) and (b). A positive cloud phase feedback, presented in figure 1.2 (c) is induced by increased emissions of INPs due to e.g. thawing of permafrost regions, where aerosol emissions were strongly reduced by the snow cover and frozen ground. The enhanced release of INPs increases the amount of ice crystals in clouds, making the clouds less opaque for longwave radiation, such that they keep the thermal radiation in the atmosphere (Murray et al., 2021). Overall, the positive cloud phase feedback is expected to prevail with an ongoing climate change (Zelinka et al., 2017). Nevertheless, there are still many uncertainties in how far aerosol emissions from different source regions change and how their change influences the INP concentration in the atmosphere and so the ice crystals number concentration and reflective properties of clouds (Storelvmo, 2017). Because INPs are rare among the whole atmospheric aerosol population and challenging to measure (DeMott et al., 2011), it is of importance to perform long-term measurements at various locations to monitor changes as well as potential driving factors for the measured variation in the INP concentration on both a short and a long time scale.

The quantification of the variation on a long and short time scale of the abundant INP concentration at different thermodynamic conditions is the effort of a whole community, where each institute has their own instrumentation. Because the instruments have different working principles and setups it is of importance to carefully characterize and intercompare them with each other under controlled conditions in the laboratory before merging the data of field INP measurements, where variable aerosol populations are present. Previous studies already intercompared multiple INP instruments with each other at mixed-phase cloud conditions and observed a variable agreement between 2 and 4 orders of magnitude for different aerosol samples (e.g. Hiranuma et al., 2015; Wex et al., 2015; DeMott et al., 2018). Thus it is still a pending topic to further point out and quantify unsolved questions, that could help to limit the observed offset between the different instruments and techniques. Especially the recent developments of new INP instruments and the efforts of atmospheric monitoring networks, which aim on integrating automated

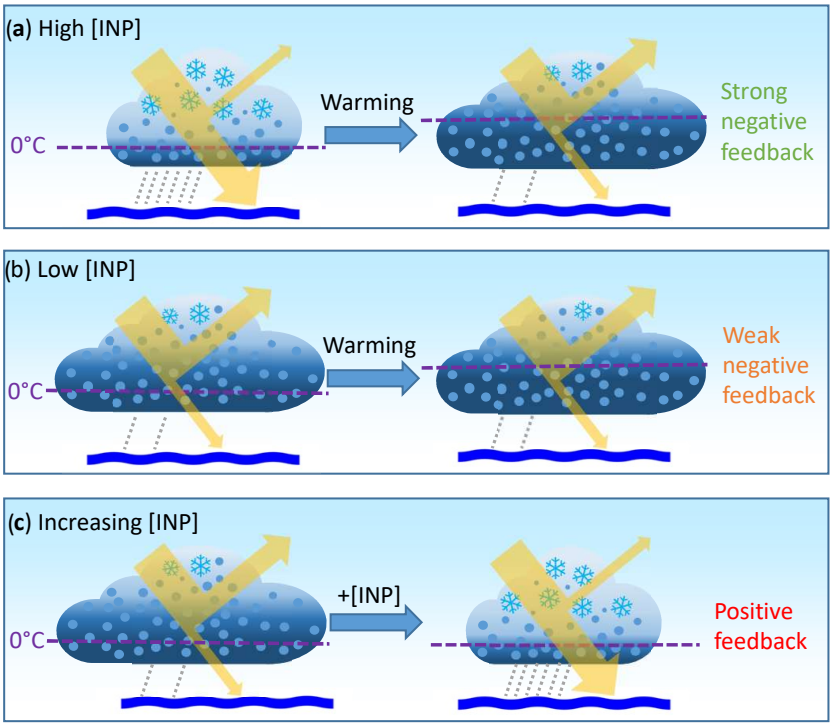

Figure 1.2.: Different cases of the cloud phase feedback in a changing atmosphere. Panel (a) considers an upward shift of the 0 °C isotherm in the atmosphere and high initial INP concentrations, leading to more cloud droplets and thus a strong negative cloud phase feedback. The case in panel (b) is similar to panel (a), but assumes low instead of high initial INP concentrations, resulting in a weak negative cloud phase feedback. In panel (c), the isotherm is kept at a constant level, and the INP concentration is increased. Due to the higher INP concentration, more ice crystals form in the cloud, which leads to a positive cloud phase feedback. Figure taken from Murray et al. (2021).

INP measurements next to the other observed variables such as aerosol number, size and composition, set more focus on intercomparison studies again.

Some of the already existing INP instruments were used in the past to investigate the long-term variation in the INP concentration at different locations and aerosol source regions. Influential factors for a variation in the INP concentration can be, on a longer time scale, seasonal changes with lower INP concentrations in winter, due to a less pronounced biological activity from plants, and higher INP concentrations in summertime, the period of the year with the highest activity of nature. Other changes on a long time scale can be caused by desertification, where desert and dry areas expand due to a lack of water. While in Cabo Verde no seasonal variation in the INP concentration was observed within a 4 year record (Welti et al., 2018), changes in the INP concentration of up to 2 orders of magnitude were observed on the Jungfraujoch and in the boreal forest in Finland (Conen et al., 2015; Schneider et al., 2021b; Brunner et al., 2021). Most of the current long-term INP measurements were done by sampling the aerosol particles on filters, which are later analyzed in the laboratory and by that have a limited time resolution of 1 day or longer. The investigation of the short-term variation in the measured INP concentration requires instruments that are capable of providing INP data with a higher time resolution of maximum 1 h. Only the last few years brought up three instrument developments for automated INP measurements directly at the sampling site

with the highest available time resolution between about 6 min and 20 min (Bi et al., 2019; Brunner and Kanji, 2020; Möhler et al., 2021) and low maintenance. This allows for long-term monitoring also at remote locations to investigate the short-term variation of the INP concentration, which yet still poorly understood. Changes in meteorological variables such as temperature, humidity, pressure and wind or changes in the aerosol size distribution are potential indicators for changing air masses and meteorological conditions, transporting potentially different aerosol populations to the measurement site or releasing aerosol particles due to an increasing turbulence. To address this question, more field INP measurements with a high time resolution over long time periods are needed in the future.

Primary ice formation in clouds is an important process for precipitation formation and the radiative budget, but microphysical processes in mixed-phase clouds are not yet well understood. Because they happen on a small spatial scale, most of the models cannot project it due to their limitation in resolution. In order to include INP measurements in models, parameterizations were developed to predict the INP concentration for various ambient environments or based on laboratory measurements on specific aerosol types (DeMott et al., 2010; Niemand et al., 2012; Tobo et al., 2013; DeMott et al., 2015; Steinke et al., 2016; Ullrich et al., 2017; Schneider et al., 2021b). Nevertheless, they still require more validation especially for broader temperatures ranges and with long-term measurements with a high time resolution to also include the measured short-term variation in the INP concentration. Many of these parameterizations suggest to relate the prediction of INPs on the concentration of aerosol particles larger than 0.5 µm in diameter and consider a time dependent freezing of the aerosol particles (detailed description in section 2.2). Another approach describes the freezing of the aerosol from a time-independent point of view, where ice active sites on the aerosol surface trigger the ice formation at a certain temperature. This gives the ice activity of an aerosol as a value normalized to the surface area concentration (Niemand et al., 2012; Ullrich et al., 2017) (detailed description in section 2.3). n_s implies that larger aerosol particles are more likely to induce ice formation. However, it is not yet well investigated in how far the size of an aerosol particle influences the ice nucleation ability. Only a few studies investigated the size dependent freezing of various aerosol types in laboratory and field measurements, but a clear picture, especially on potential factors that influence the size dependent freezing, is not yet given and more measurements are needed.

The abundance of INPs and the amount of ice formed in clouds is not only related to changing emissions of aerosol particles and the natural variation. During the residence time of INPs in the atmosphere, they can change their ice nucleation ability due to physical or chemical modification processes. Once an aerosol particle gets emitted, it can be transported over long distances and can remain in the atmosphere for several days (e.g. Betzer et al., 1988; Weinzierl et al., 2017). In this time, the aerosol particles can not only contribute to cloud droplet and ice crystal formation, but they can also interact with each other. One of the possible pathways is, that gases condense on the aerosol surface and builds up a coating layer (e.g. Seinfeld and Pandis, 2016). Most of the solid atmospheric aerosol particles have an aspherical shape and their surface can contain sites that trigger the ice formation. When gases condense on the surface of solid, aspherical aerosol particles, they change the surface and by that give them different properties. The coating

material may also block the sites on the aerosol surface that trigger the ice formation, which changes the ice nucleation ability of the aerosol (e.g. Sullivan et al., 2007, 2010). Aerosol coating procedures can occur in all levels in the atmosphere, but a significant change in the freezing ability of the aerosol and cloud formation processes is only observed for cirrus cloud conditions (e.g. Knopf and Koop, 2006; Möhler et al., 2008a; Cziczo et al., 2009). For experiments under mixed-phase cloud conditions the coating on the aerosol surface was not observed to change the ice nucleation ability (e.g. Kanji et al., 2019). At these temperatures, the liquid phase is present, which suspends the coating material on the aerosol and brings up the ice active sites on the surface again. The general effect of the freezing suppression of aerosol particles that were coated was investigated in the past. However, due to the experimental setup, coatings were often applied at non atmospheric conditions, and the measurements were only done at selected coating stages. To cover the full evolution of the freezing suppression of coated aerosol particles at atmospherically relevant conditions, laboratory instruments for automated long-term INP measurements are still needed.

The structure of this thesis is given as follows:

Chapter 2 - Theoretical Background This chapter provides more detailed information on the theoretical background of atmospheric aerosol particles and their emission sources, the formation process of cloud droplets and ice crystals in the atmosphere, the description of the ice activity of an aerosol normalized to the aerosol surface and briefly introduces the different existing techniques for INP measurements.

Chapter 3 - Experimental Methods This chapter gives a detailed description of the instruments, that were used for the laboratory and field INP measurements in this thesis, including the generation of aerosol particles in the laboratory and the characterization of aerosol particles, cloud droplets and ice crystals. The chapter is concluded with a list of the aerosol samples that were used for the laboratory ice nucleation studies.

Chapter 4 - Laboratory Intercomparison of INP Instruments This chapter shows the results of a laboratory intercomparison study of 12 different INP instruments for their measured INAS density at mixed-phase cloud conditions. The intercomparison included newly developed instruments and already existing INP instruments. Measurements were performed not only with pure aerosol systems and high INP concentrations, but also with atmospheric mixtures of CCN and low INP concentrations.

Chapter 5 - Atmospheric INP Observations and Short-term Variation This chapter discusses the short-term variation of the measured INP concentration during three different field campaigns conducted in rural environments and at a mountain site. For two of the field campaigns, which provided INP data with a high time resolution of about 6 min, it was investigated if the short-term variation in the measured INP concentration correlates with one or more of the meteorological variables or the aerosol number and size. To contribute to the improved representation of INPs in models, a new parameterization was developed to predict the INP concentration for rural environments and over a wide temperature range.

Chapter 6 - Size-Selective INP Measurements This chapter presents results on the size dependent ice-nucleation ability of aerosol particles measured both, in the laboratory and in the field. The measurements

were done by sampling the aerosol particles on filters, and for the first time with an INP instrument conducting measurements with a time resolution of about 6 min. It also gives indications to possible factors that could influence the size dependent freezing of aerosol particles.

Chapter 7 - Development and Application of the New Cloud Expansion Chamber AIDAm This chapter presents the setup of a new small cloud expansion chamber for automated long-term INP measurements with a high time resolution, which was built and validated in this work as an addition to the larger cloud expansion chamber AIDA (Aerosol Interaction and Dynamics in the Atmosphere). Because it is always at the same thermodynamic conditions as AIDA, it is ideal to monitor changes in the ice nucleation ability of the aerosol inside AIDA due to physical or chemical processes. Therefore, first measurements were done on investigating the time dependent change in the freezing behavior of different aerosol particles at cirrus cloud conditions, while they were slowly coated over hours with two different types of gaseous material.

Chapter 8 - Conclusions and Outlook This chapter summarizes the findings and results of this thesis and gives an outlook for potential future experiments.

2. Theoretical Background

Cloud formation occurs in all height levels in the troposphere, and is initiated by aerosol particles that trigger the formation of liquid cloud droplets and ice crystals. The presence of liquid cloud droplets and ice crystals classifies clouds into warm clouds, mixed-phase clouds and ice clouds. Warm clouds only consist of water droplets, whereas mixed-phase clouds contain both water droplets and ice crystals and ice clouds, most often cirrus clouds, only ice crystals. The amount and type of emitted aerosol particles defines the amount of formed cloud droplets and ice crystals at given thermodynamic conditions. While cloud droplet formation happens by condensation of water vapor on aerosol particles in the atmosphere, ice formation can occur via different pathways (e.g. Pruppacher and Klett, 2010).
This chapter gives more detailed insights into the emission sources of aerosol particles and their related number, surface and mass concentration, as well as the freezing processes initiated by aerosol particles. The final two sections describe a method that formulates the ice activity of an aerosol as a normalized value and provide an overview of the state-of-the-art instrumentation to measure INPs.

2.1. Atmospheric Aerosol Particles

Per definition, aerosol particles are solid or liquid particles suspended in a carrier gas, which is air in terms of the Earth and its atmosphere (e.g. Hinds, 2012). Atmospheric aerosol particles are emitted from numerous sources distributed around the globe. The type and amount of aerosol changes when moving from tropical regions polewards and over land and sea (e.g. Stier et al., 2005). Generally, atmospheric aerosol particles are classified as primary or secondary aerosols and as natural or anthropogenic. Primary aerosols consider all those that are directly emitted into the atmosphere. They can have natural sources such as deserts and dry areas that emit dust particles (e.g. Tegen and Schepanski, 2009), oceans and open water that release sea salt aerosol (e.g. Schulz et al., 2004) or biological sources that contribute particles like pollen, spores and bacteria (e.g. Després et al., 2012) to the aerosol population. Otherwise, primary aerosol particles are of anthropogenic origin, where soot and combustion particles are released from land, water and air traffic and industrial processes or debris from road traffic (e.g. Lighty et al., 2000). In contrast to the directly emitted primary aerosol, secondary aerosol particles originate from a gas-to-particle conversion of emitted precursor gases. Natural secondary aerosol particles are those that form from organic precursor gases such as different terpenes from forest areas or marine precursor gases like iodine, DMS (Dimethyl sulfide) or MSA (methanesulfonic acid) (e.g. Hallquist et al., 2009). A very frequently abundant secondary aerosol is sulfuric acid, which can be of both natural and anthropogenic

origin. When it is formed from sulfur dioxide from e.g. volcanic eruptions it is considered as a natural aerosol and when speaking about the anthropogenic origin, sulfur dioxide is emitted from industrial burning and combustion processes (e.g. Sipilä et al., 2010).

The different aerosol sources have variable strengths and the emitted aerosol particles have highly variable concentrations on a global scale. Stier et al. (2005) described the annual mean emission of some aerosol species and showed that the main oceanic aerosol source is sea salt with emitted amounts of up to $50\,\mathrm{g\,m^{-2}\,y^{-1}}$. Over land, the strongest sources are desert regions, that contribute about $200\,\mathrm{g\,m^{-2}\,y^{-1}}$ dust aerosol particles to the total aerosol population. Aerosols like black carbon and particulate organic matter are mainly emitted over land areas with a strength that is about 1 order of magnitude less than dust in terms of mass. The main anthropogenic contribution in terms of mass to the total aerosol population is sulfur and its emission clearly points out larger cities and ship tracks on the ocean with enhanced annual emissions of up to $20\,\mathrm{g\,m^{-2}\,y^{-1}}$.

Depending on the type of the aerosol and the phase state, atmospheric aerosol particles can have a radius in the size range between a few nanometer and several micrometer as presented in figure 2.1. The size distribution of the aerosol is shown in a multi-modal representation (Whitby, 1978) with the Nucleation

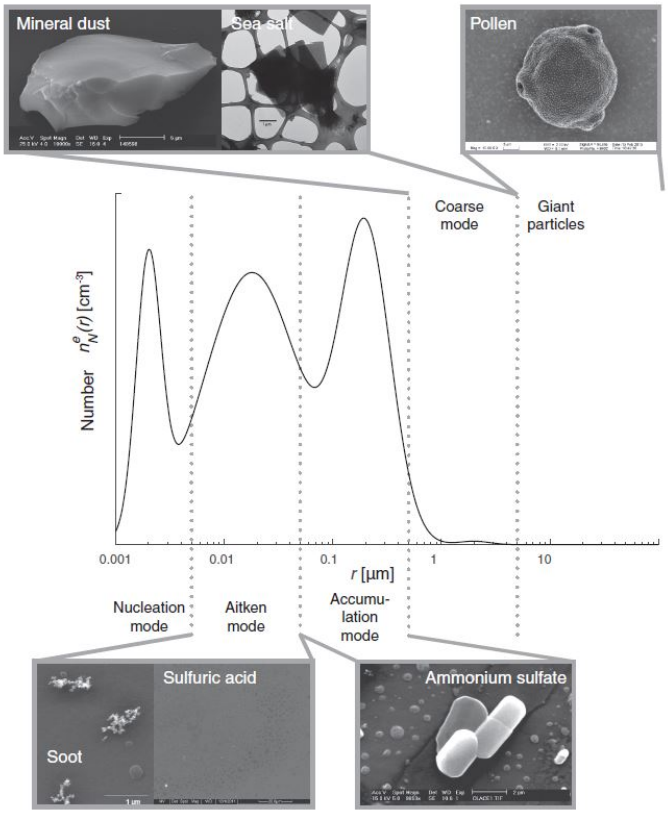

Figure 2.1.: Classification of atmospheric aerosol particles into 5 different modes. The Nucleation Mode contains aerosol particles with the smallest radius (< 5 nm) followed by the Aitken Mode (5 nm to 50 nm), the Accumulation Mode (50 nm to 500 nm), the Coarse Mode (500 nm to 5 µm) and Giant particles (> 5 µm). The graph indicates the number of particles in each of the modes. Figure taken from Lohmann et al. (2016).

mode is the mode containing the smallest aerosol particles with a particle radius smaller than 5 nm. The Nucleation mode encounters gaseous precursors that freshly nucleated to aerosol particles and grow further in size subsequently. The following two modes are the Aitken mode and the Accumulation mode, which are characterized by particles with a radius between about 5 nm and 50 nm and 50 nm and 500 nm, respectively. In the atmosphere, these are mainly soot and sulfuric acid for the Aitken mode and ammonium sulfate for the Accumulation mode. The largest aerosol particles are mineral dust and sea salt, which have a mean radius between 500 nm and 5 µm and are thus accounted to the Coarse mode, or pollen which can be even larger than 5 µm and are thus called giant particles (e.g. Lohmann et al., 2016; Seinfeld and Pandis, 2016).

The quantification of aerosol particles is done based on their attributes, where three of the main characteristics are the aerosol number, surface and mass. To generate an aerosol number, surface and mass distribution, the aerosol particles are distributed into size bins. The number concentration dn_p of aerosol particles in the size bin dd is derived with equation 2.1.

$$f_\mathrm{n}(d) = \frac{dn_\mathrm{p}}{dd} \tag{2.1}$$

For atmospheric aerosol particles, the number is the highest for the smallest size modes, namely the Nucleation mode, the Aitken mode and the Accumulation mode. Because larger aerosol particles settle down much faster than smaller particles and emission processes are different, they are much less present in the aerosol population and their number can be some orders of magnitude lower than for small particles. The second important attribute of an aerosol particle is the surface area distribution, which is given as

$$f_\mathrm{s}(d) = \pi d^2 f_\mathrm{n}(d) \ . \tag{2.2}$$

Because the individual diameter of the aerosol particles d contributes to the surface squared, larger aerosol particles have a higher relative contribution to the total aerosol surface area than smaller aerosol particles, even though they can be much less in number.

The enhanced contribution of large aerosol particles compared to small aerosol particles increases further, when accounting for the mass of the aerosol (equation 2.3), considering the particle diameter cubed and the particle density ρ.

$$f_\mathrm{m}(d) = \rho \frac{\pi}{6} d^3 f_\mathrm{n}(d) \tag{2.3}$$

Once the particles are emitted into the atmosphere, they can be transported over long distances, which strongly depends on strength of the aerosol emission source and the particle size (e.g. Jaenicke, 1982; Abdalmogith and Harrison, 2005; Knippertz and Todd, 2012; Weinzierl et al., 2017). The smaller a particle, the slower it settles out and so remains longer in the atmosphere. The longer a particle remains in the atmosphere, the more likely it becomes that it interacts with other aerosol particles or gases. Thereby,

aerosol particles can coagulated or precursor gases can condense on the surface of solid aerosol particles, coat them over the time and thus change their physical and chemical properties.

2.2. Cloud Droplet and Ice Crystal Formation in the Atmosphere

Aerosol particles that are emitted into the atmosphere can form cloud droplets at temperatures higher than the homogeneous freezing temperature of pure water at about $-35\,^{\circ}\mathrm{C}$ (e.g. Benz et al., 2005) and above a relative humidity with respect to water of 100 %. When aerosol particles induce the formation of liquid cloud droplets they are called Cloud Condensation Nuclei (CCN) (e.g. Pruppacher and Klett, 2010). In the formation process of a liquid cloud, water vapor condenses on the aerosol particle and by that induces a phase change from the initial gas phase to the liquid phase. One requirement for this to happen is, that the environment is supersaturated with respect to the new phase (Köhler, 1936). In the atmosphere, an air parcel containing a certain amount of water vapor rises up, while its temperature decreases following the dry adiabatic lapse rate. Upon this cooling process, the relative humidity with respect to water in the air parcel increases. Aerosol particles such as salts take up water from the air and deliquesce in a wide range between 40 % and 84 % at a temperature of 25 °C and for different types of salt (Seinfeld and Pandis, 2016). Once the air parcel reaches water supersaturated conditions, water vapor condenses on the CCN to form liquid cloud droplets. Other than that, supersaturated conditions in the atmosphere can occur upon mixing of air masses having different temperatures and relative humidities. In the presence of CCN, the nucleation process starts at already low supersaturations with respect to water and therefore typical atmospheric values are only slightly above 100 % (e.g. Pruppacher and Klett, 2010; McFiggans et al., 2006; Schmale et al., 2018). Liquid cloud droplets can also form via homogeneous nucleation, the formation of the liquid phase in absence of CCNs, which is not of atmospheric relevance since it requires a very high relative humidity with respect to water of up to 120 %.

From the entity of atmospheric aerosol particles, 1 to 100 out of 1×10^6 are able to trigger ice formation in both the mixed-phase and cirrus cloud regime and are called ice-nucleating particles (INPs) (e.g. Seinfeld and Pandis, 2016). Mixed-phase clouds form at temperatures between 0 °C and $-35\,^{\circ}\mathrm{C}$, which is the temperature regime in which liquid cloud droplets and ice crystals coexist. Pure ice clouds (cirrus clouds) exist at temperatures below the homogeneous freezing of water at about $-35\,^{\circ}\mathrm{C}$.

Primary ice formation in clouds, can be generally distinguished between homogeneous and heterogeneous ice nucleation.

In the absence of aerosol particles that trigger the ice formation, pure water and solution droplets freeze at temperatures lower than $-35\,^{\circ}\mathrm{C}$, known as homogeneous ice nucleation (Koop et al., 2000). At high enough supersaturations, water molecules cluster to small ice germs by collision processes. A phase change is always assigned to a change in energy, which, in the case of nucleation, is described by the change in the Gibbs free energy ΔG. The formulation of ΔG contains two terms: a volume term connected

to the energy gain due to the growth of the cluster in the new stable phase and a surface term describing the required energy for the formation of the surface in the new phase (equation 2.4) (e.g. Salby, 2012).

$$\Delta G = -N_{\text{ice}} kT \ln(S_{\text{ice}}) + 4\pi r^2 \sigma \tag{2.4}$$

The volume term is dependent on the number of molecules in the ice germ N_{ice}, the Boltzmann constant k, the temperature T and the saturation ratio with respect to ice S_{ice}, and is proportional to -N_{ice}. The surface term is described by the surface area of the ice germ ($4\pi r^2$) and the surface tension σ, and is proportional to $N_{\text{ice}}^{2/3}$.

As soon as S_{ice} exceeds 1, the nucleation process sets in and the first ice germs form, but the ice cluster is not yet stable, as the surface term is more important than the volume term and the droplet thermodynamically prefers to remain in the initial phase. In order to form a stable ice crystal and overcome the energy barrier for the phase transition, the ice germ needs to reach a critical size. At this critical size, the energy gain from the volume term is higher than the surface term. When maintaining the supersaturation conditions with respect to ice, the ice germ will then grow further in size.

The homogeneous freezing of water and solution droplets only occurs at temperatures lower than $-35\,^{\circ}\text{C}$ and high supersaturations with respect to ice of > 1.42. To overcome the energy barrier for ice formation at already higher temperatures and lower supersaturations, INPs are required to heterogeneously induce the freezing process. One approach to describe heterogeneous ice nucleation is similar to the homogeneous nucleation and considers the freezing to be a time dependent process. The second approach describing heterogeneous ice nucleation is a deterministic, time independent approach which is explained in more detail in section 2.3.

The heterogeneous ice nucleation is considered to occur via four different freezing pathways, namely immersion freezing, condensation freezing, contact freezing and deposition nucleation, as described by e.g. Yau and Rogers (1996), Hoose and Möhler (2012) and Vali et al. (2015). The first three pathways are relevant for mixed-phase cloud conditions. In the immersion freezing process, the INPs are immersed into a liquid cloud droplet at temperatures higher than the temperature at which freezing is induced. When cooling the droplet, the INP triggers the freezing of the droplet and determines its freezing temperature. Contrary to that, condensation freezing occurs when water vapor condenses on the INP surface and forms a liquid phase droplet which then freezes during the condensation process. Studies by e.g. Burkert-Kohn et al. (2017) question the differentiation of the two freezing mechanisms and suggest further experiments to proof this. The third freezing mechanism involving the supercooled liquid phase is contact freezing, where a supercooled cloud droplet comes into contact with an INP, which immediately triggers the transformation from the liquid to the solid phase. However, this freezing process and its atmospheric relevance is yet poorly understood (e.g. Ladino Moreno et al., 2013; Nagare et al., 2016). Because all these three pathways require the presence of the liquid phase, they can only occur at water supersaturated conditions. The deposition nucleation is described as the ice formation from the vapor phase at water

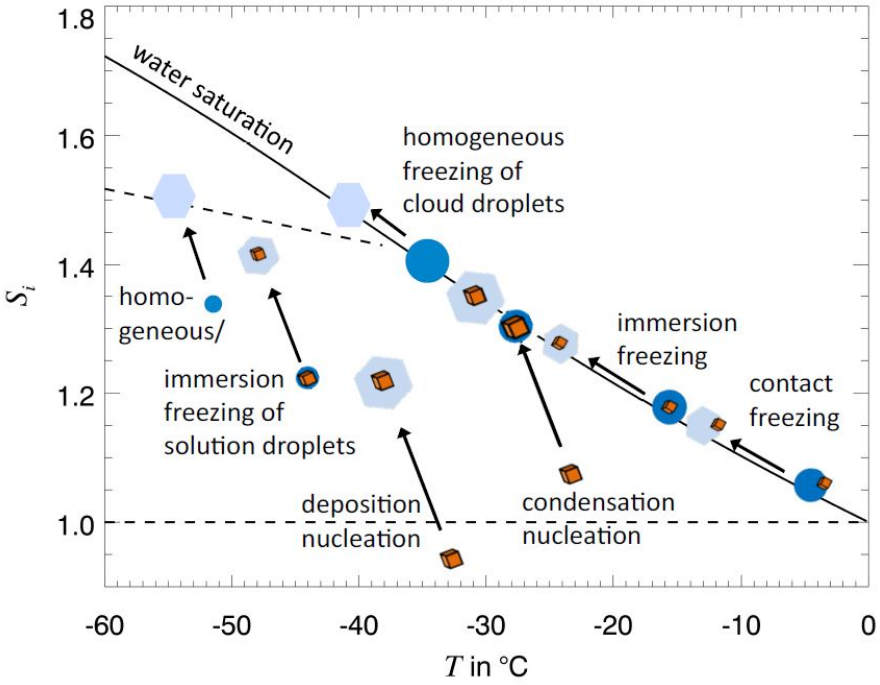

Figure 2.2.: Schematic of the different pathways of heterogeneous ice nucleation and their temperature T and supersaturation with respect to ice S_i they occur. Figure taken from Hoose and Möhler (2012).

subsaturated conditions, where water vapor freezes on the INP. This heterogeneous freezing pathway plays a key role at cirrus cloud conditions (e.g. Cziczo et al., 2013), but it can also happen in the mixed-phase cloud regime below water saturation and above ice saturation. Another freezing mechanism which may be important at cirrus cloud temperatures is the pore condensation and freezing (PCF) (e.g. Marcolli, 2014; Wagner et al., 2016; Marcolli, 2020). In this process, water vapor condenses in the pores of aerosol particles at atmospheric subsaturated conditions and the subsequent freezing occurs at already low ice supersaturation. To date it is still under discussion which of these freezing processes is more relevant at cirrus cloud conditions (David et al., 2019b).

Aerosol particles of different origin and properties act as INPs by inducing ice formation via one of the discussed pathways. But not all INPs are ice active to the same extend and in the same temperature range. Aerosol particles of biological origin are efficient INPs in the mixed-phase cloud regime and induce ice formation at already high temperatures of about $-5\,°C$. Because of their high ice activity, they mainly contribute to the INP population down to temperatures of about $-20\,°C$ and for the lower end of the given temperature range atmospheric INP concentrations of up to $100\,L^{-1}$ can be reached (e.g. Huffman et al., 2013; Tobo et al., 2013; Creamean et al., 2019; Huang et al., 2021). During airborne measurements, 33 % of the probed aerosol particles triggering ice formation at cirrus cloud conditions were found to be of biological origin (Pratt et al., 2009). Another highly ice active aerosol is dust, which starts to act as an INP at temperatures of about $-15\,°C$. Dust is not only a good INP in the mixed-phase cloud regime, but also plays a key role for the formation of cirrus clouds on a global scale at temperatures

down to −80 °C (e.g. Chou et al., 2011; DeMott et al., 2015; Ullrich et al., 2017; Boose et al., 2019; Froyd et al., 2022). At mixed-phase cloud conditions, where the ice activity of an aerosol particle is only dependent on the freezing temperature, dust reaches INP concentrations of up to $1000\,\mathrm{L}^{-1}$ close to the source regions. In the cirrus cloud regime, at temperatures below −35 °C, the freezing of aerosol particles is more dependent on the supersaturation with respect to ice and dust particles trigger ice formation throughout the whole cirrus cloud regime at already low ice saturations of between 1.1 and 1.2. Also soil dust particles, carrying to some extend organic and biological content on their surface, were found to show as high INP concentrations as dust at the same temperature and supersaturation conditions (e.g. O'Sullivan et al., 2014; Steinke et al., 2016; Paramonov et al., 2018). In comparison to dust, marine aerosol particles are less efficient INPs throughout the whole atmospheric temperature regime, but are still of importance because they have a high abundance, especially in remote oceanic regions in the absence of dust aerosol (e.g. DeMott et al., 2016; Vergara-Temprado et al., 2017, 2018; Wagner et al., 2018; Wilbourn et al., 2020). An aerosol type that is known to freeze via PCF is coal fly ash from industrial combustion processes and studies by e.g. Umo et al. (2019) showed that the ice active fraction, giving the ratio of ice crystals to aerosol particles, increased from about 0.2 % to between 10 % and 60 % after undergoing the PCF. An aerosol species that only has a minor contribution to the ice formation in the mixed-phase cloud regime is black carbon (Kanji et al., 2020; Schill et al., 2020), but at cirrus cloud conditions it was observed to form ice heterogeneously (e.g. DeMott et al., 1999; Mahrt et al., 2018). Other aerosol types such as secondary organic aerosol were also found to contribute to the ice formation at cirrus cloud conditions, but not in the mixed-phase cloud regime (e.g. Ignatius et al., 2016; Wolf et al., 2020).

2.3. Deterministic Approach to Describe the Ice Nucleation Activity of an Aerosol

Section 2.2 introduced the description of the heterogeneous ice formation in the atmosphere based on the classical nucleation theory. Another approach, which also gives a measure for the ice nucleation activity of an aerosol population, is the INAS (Ice Nucleation Active Site) density (n_s) approach (Niemand et al., 2012; Ullrich et al., 2017). It assumes no direct time dependency for the freezing process, rather than ice active sites that are equally distributed on the aerosol surface and induce freezing at a certain temperature. Having a polydisperse aerosol population, with aerosol particles of different diameters and assuming that the increase in the ice number concentration n_ice is proportional to the decrease in the number of aerosol particles available for ice formation n_ae, n_s can be described as follows:

$$\ln\left(1-\frac{n_\mathrm{ice,m}}{n_\mathrm{ae,m}}\right) = -S_\mathrm{ae,m} n_\mathrm{s} \quad . \tag{2.5}$$

The index m indicates the different size bins the aerosols are assigned to. $S_\mathrm{ae,m}$ gives the aerosol surface area of a particle in the size bin. The ratio of the ice number concentration to the aerosol number concentration is defined as the ice active fraction of an aerosol, which is most often much smaller than 1 and simplifies equation 2.5 to

$$\frac{n_{\mathrm{ice,m}}}{n_{\mathrm{ae,m}}} = S_{\mathrm{ae,m}} n_{\mathrm{s}} \quad . \tag{2.6}$$

Considering an equal ice activity throughout the whole aerosol size distribution and thus a constant n_{s}, equation 2.6 can be reformulated as

$$n_{\mathrm{s}} = \frac{\sum n_{\mathrm{ice,m}}}{\sum s_{\mathrm{ae,m}}} \quad . \tag{2.7}$$

$s_{\mathrm{ae,m}}$ is the aerosol surface area concentration of the single size bins derived from the aerosol number concentration of the aerosol multiplied by the according surface area. For mixed-phase cloud conditions, n_{s} is only dependent on the freezing temperature, but in the cirrus cloud regime an additional dependency on the saturation with respect ice needs to be considered.
The calculation of n_{s} as described by Niemand et al. (2012), was done in a cumulative way, such that a similar ice activity of all particles of the whole size range was assumed. Ullrich et al. (2017) proposed to consider the largest aerosol particles to freeze first, such that with a bin wise increase in the nucleation time, the aerosol size distribution needs to be reduced by the largest aerosol particles. n_{s} can therefore be calculated for each time bin t by

$$n_{\mathrm{s}} = \frac{n_{\mathrm{ice,t}}}{s_{\mathrm{ae,t}}} \quad . \tag{2.8}$$

In order to validate the n_{s} approach, INP measurements with size selected aerosol are needed, and the results of such measurements are discussed in chapter 6.

2.4. State of the Art of Instruments to Measure Ice-Nucleating Particles

To measure the INP concentration in both laboratory and field ice-nucleation experiments, three common techniques are used nowadays which are cloud expansion chambers (e.g. Möhler et al., 2006, 2021), continuous flow diffusion chambers (CFDCs) (e.g. Rogers, 1988) and droplet freezing experiments (e.g. Hill et al., 2014). Cloud expansion chambers and CFDCs are considered online methods, because the analyze the sampled aerosol population regarding their ice-nucleating ability in real-time. Compared that, droplet freezing experiments are so-called offline techniques, because the aerosol is sampled on a filter or an other carrier material and analyzed at a later point in the laboratory. A general overview of all the three techniques is given here, and the instruments used for the INP measurements in this work are described in detail in chapter 3.

Cloud Expansion Chambers Cloud expansion chambers are used since a couple of decades to study atmospheric cloud formation processes (e.g. Chang et al., 2016). The working principle of expansion chambers is based on simulating the adiabatic cooling of an air parcel in the atmosphere. From a thermodynamic point of view, an adiabatic expansion is seen as a process where a particle in an air parcel

does not exchange heat with its surrounding. Therefore, a decrease in temperature is required, which, in the atmosphere, is also related to a reduction in pressure and an increase in the volume (e.g. Seinfeld and Pandis, 2016). Given these conditions, an adiabatic process in the atmosphere can be described with the constant ratio

$$p_2 V_2^{\gamma} = p_1 V_1^{\gamma} = const. \quad . \tag{2.9}$$

γ is given as $\gamma = c_p/(c_p - R)$ with c_p as the specific heat capacity of dry air at constant pressure and R as the specific gas constant for air. Because in atmospheric processes, the temperature is more relevant than the volume, equation 2.9 can be written as

$$T_2 p_2^{(\frac{1-\gamma}{\gamma})} = T_1 p_1^{(\frac{1-\gamma}{\gamma})} = const. \quad . \tag{2.10}$$

The ideal temperature profile during a cloud expansion experiment in a cloud chamber would be the adiabatic profile. But because most of the state-of-the-art cloud expansion chambers keep the walls at a constant temperature while cooling the gas inside the chamber, a heat exchange between the wall and the gas is given at any time. Thus, the deviation between the real temperature profile and the adiabatic temperature profile increases throughout an ongoing expansion experiment.

At temperatures below 0 °C, cloud expansion chambers are used for investigating the ice-nucleating properties of different aerosol systems. During a cloud expansion experiment, the liquid cloud droplets and ice crystals are directly analyzed regarding their number concentration and other relevant properties and therefore such instruments give immediate information about the ice activity of the probed aerosol population.

Major parts of this thesis are based on cloud expansion chamber experiments in the laboratory and the field. Therefore, a detailed description of two already existing cloud chambers is given in section 3.1 and 3.2 and the setup and validation of a newly built cloud expansion chamber is discussed in chapter 7.

Continuous Flow Diffusion Chambers Continuous Flow Diffusion Chambers (CFDCs) are another online method to measure INPs in the laboratory and the field. The working principle and general setup was first described by Rogers (1988) and the design was further improved and developed with different geometries afterwards.

The general setup of a CFDC consists of two plates facing each other, which can be parallel plates in a vertical or horizontal orientation or two cylinders stacked into each other. Prior to an ice nucleation experiment, both plates are covered with a thin ice layer and then brought to different temperatures below 0 °C. This creates a linear temperature gradient between them. Two other important parameters are the saturation with respect to ice S_{ice} and water S_{water}, given as the ratio of the water vapor partial pressure e and the saturation pressure with respect to ice $e_{sat,ice}$ and water $e_{sat,water}$, respectively:

$$S_{\text{ice}} = \frac{e}{e_{\text{sat,ice}}} \quad , \quad S_{\text{water}} = \frac{e}{e_{\text{sat,water}}} \quad . \tag{2.11}$$

$e_{\text{sat,ice}}$ and $e_{\text{sat,water}}$ can be derived from the temperature dependent parameterizations formulated by Murphy and Koop (2005):

$$e_{\text{sat,ice}}(T) = \exp(9.550426 - 5723.265/T + 3.52068 \cdot \log(T) - 0.00728332 \cdot T) \tag{2.12}$$

$$\begin{aligned} e_{\text{sat,water}}(T) = \exp(&54.842763 - 6763.22/T - 4.21 \cdot \log(T) + 0.000367 \cdot T + \tanh(0.0415 \\ &\cdot (T - 218.8)) \cdot (53.878 - 1331.21/T - 9.44523 \cdot \log(T) + 0.014025 \cdot T)) \quad . \end{aligned} \tag{2.13}$$

Due to the temperature dependency of S_{ice} and S_{water} and the temperature gradient across the walls, a gradient in S_{ice} and S_{water} is established. When sampling aerosol particles to probe them with the CFDC regarding their ice nucleation activity, they are transported between the plates, where they are exposed to certain supersaturated conditions. When increasing the temperature gradient across the walls, the ice and water saturation ratio increases accordingly. A CFDC can be operated in two modes, one which keeps the wall temperatures and therefore the supersaturation at a constant value to allow for continuous ice-nucleation measurements. In the other operation mode, so-called saturation scans are performed, where the scan is started at subsaturated conditions and within a time of between 10 min and 30 min the water and ice saturation is slowly increased to supersaturated conditions, while keeping the temperature constant. This mode allows to study the precise onset of the ice formation and the ice number concentration at well controlled temperature and saturation conditions (e.g. Rogers, 1988; Lacher et al., 2017; Brunner and Kanji, 2020).

Generally, CFDCs provide INP data with a precise measurement of the saturation at which the ice formed, but one drawback of them is the limitation of the continuous operation. With ongoing time of an ice nucleation experiment, the icing on the wall creates more background ice crystals or depletes. After a sampling time of several hours, the ice layer on the wall needs to be renewed, which takes about 1 h to 2 h in which the INP data acquisition is paused. Moreover, most of the CFDCs require a lot of man power for continuous operation. This limits their use most often to intensive measurements periods.

CFDC measurements were part of the laboratory intercomparison studies presented in chapter 4, where the Horizontal Ice Nucleation Chamber (HINC), the Ice Nucleation Instrument of the Karlsruhe Institute of Technology (INKA) (Rogers, 1988; Schiebel, 2017) and the mobile version of INKA (mINKA) were operated. HINC has two parallel plates in horizontal orientation and INKA and mINKA are made of two cylinders stacked into each other.

Droplet Freezing Experiments In comparison to cloud expansion chambers and CFDCs, freezing experiments are offline methods where the aerosol is not directly analyzed regarding its ice nucleation

ability. For these methods, the aerosol particles are sampled on filters and then analyzed in the laboratory. The first step of the filter analysis procedure is washing-off of the aerosol particles with nanopure water. For the analysis, either small droplet volumes of 1 µL are placed on a plate or larger droplet volumes of 50 µL are pipetted into the wells of PCR plates. In both cases, the droplets are slowly cooled down with a defined temperature ramp and the temperature dependent freezing of the droplets is detected. The resulting data provide a continuous freezing spectrum of the aerosol particles. This analysis method is limited to immersion freezing, because the aerosol particles are suspended in water (Hill et al., 2014).
Another method to analyze the filters is to expose them to an environment which is supersaturated with respect to ice and/or water. This supersaturation is established by flushing particle free air through an ice bed, which is then lead to the environment in which the filter is placed. By decreasing the temperature of the ice supersaturated environment stepwise, the aerosol particles freeze at their activation temperature (Langer and Rodgers, 1975). The advantage of this method is, that it is not limited to immersion freezing, but can also quantify the ice nucleation ability of the aerosol in the deposition nucleation mode, where the liquid phase of water is avoided.
Most of the online measurements in this thesis are combined with INP measurements using the filter sampling and analysis technique INSEKT (Ice Nucleation Spectrometer of the Karlsruhe Institute of Technology) (Hill et al., 2014; Schneider et al., 2021b), which is described in more detail in section 3.3. During the laboratory intercomparison studies in chapter 4, different institutes contributed with their own filter sampling techniques, where INDA (Ice Nucleation Droplet Array) (design mostly as presented in Conen et al. (2012) and operation principle as in Hill et al. (2014)) and DRINCZ (DRoplet Ice Nuclei Counter Zurich) (David et al., 2019a) are based on the same analysis technique as INSEKT which analyzes droplet volumes of 50 µL pipetted in PCR plates. The μl-NIPI (Nucleation by Immersed Particles Instrument) and LINA (Leipzig Ice Nucleation Array) (design as presented in Budke and Koop (2015)) are similar to each other, such that droplet volumes of 1 µL is placed on a plate. The DFPC (Dynamic Processing Filter Chamber) is based on the second analysis method, where the filter is exposed to an ice supersaturated environment (Langer and Rodgers, 1975). More details on the single instruments are provided in table 4.1.

3. Experimental Methods

The INP experiments in this work are based on measurements with two different cloud expansion chambers and a filter sampling and subsequent analysis technique. This chapter gives an overview of the cloud expansion chamber AIDA (Aerosol Interaction and Dynamics in the Atmosphere), including its comprehensive instrumentation for aerosol generation and characterization, and cloud droplet and ice crystal measurements and a typical AIDA experiment at mixed-phase cloud conditions. The experimental methods are completed by in introduction to the mobile cloud expansion chamber PINE, the droplet freezing experiment INSEKT and the aerosol samples used for the laboratory ice nucleation experiments.

3.1. The Cloud Expansion Chamber AIDA

3.1.1. General Instrumentation

The cloud expansion chamber AIDA at the Karlsruhe Institute of Technology was built between 1995 and 1997 as an atmospheric simulation chamber for aerosol studies. Only later its operation was extended for investigations on aerosol-cloud-interactions and for studies on the ice-nucleation ability of different aerosol types.

AIDA (figure 3.1 and 3.2), described in detail by e.g. Möhler et al. (2003), Möhler et al. (2006) or Wagner et al. (2006), consists of a cylindrical vessel with two dished ends and is fully made out of aluminum. With a height and diameter of about 7 m and 4 m, respectively, it has a total volume of about 84 m^3. The cloud chamber is placed inside a thermal housing, in which a heat exchanger regulates the temperature of air ventilated inside the thermal housing in a wide range from 60 °C to −90 °C, by using either a refrigerating system or evaporation of liquid nitrogen. The temperature is measured on several levels on the wall of the chamber. A chain of thermocouples records the gas temperature inside the AIDA cloud chamber. The pressure in AIDA can be controlled to values between about 1000 mbar to below 1 mbar. A mixing fan, placed in the bottom of the chamber ensures that the whole air volume is well-mixed and by that the temperature and aerosol inside the chamber is distributed homogeneously.

The total water concentration inside the AIDA chamber is measured with a dew point mirror (373LX, MBW calibration) and the gas phase water concentration without and in the presence of clouds is measured with the tunable diode laser spectrometer (Sp-)APicT ((Single Path) AIDA PCI in-cloud Tunable Diode Laser) (Fahey et al., 2014). For the humidity measurements with the tunable diode laser system, a laser beam is sent across the chamber. Its intensity is dampened by the water molecules inside the chamber and the transmitted light is detected. Depending on the intensity of the transmitted light, it can directly

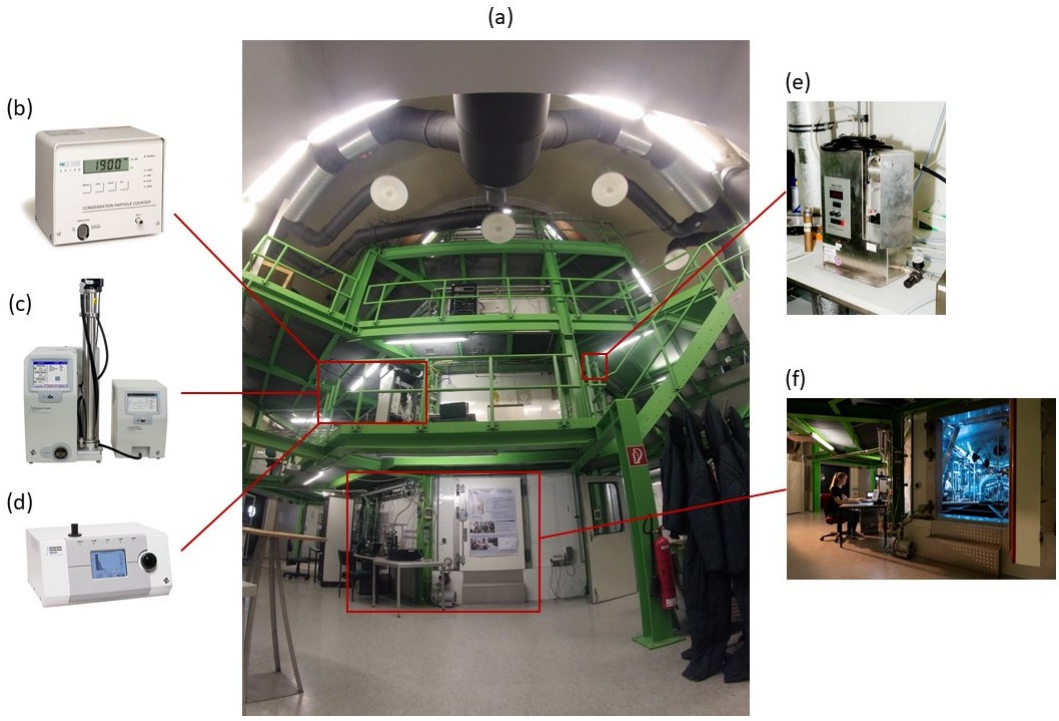

Figure 3.1.: Photo (a) in the center shows the outside of the AIDA chamber facility. The smaller photos on the side show the CPC (b) (https://tsi.com/auslaufmodelle/kondensationspartikelzahler-3010/, last seen April 14, 2022), the SMPS (c) (https://tsi.com/produkte/partikelgrossenmessgerate/scanning-mobility-particle-sizer-spektrometer/, last seen April 14, 2022), the APS (d) (https://tsi.com/produkte/partikelgrossenmessgerate/partikelgrossenmessgerate-fur-supermikron-partikel/, last seen April 14, 2022), the RBG (e) and a view into the thermal housing of AIDA (f).

be assigned to the partial pressure of the water vapor inside AIDA. With the help of the temperature dependent saturation pressure, the relative humidity with respect to ice and water is then calculated for the present humidity conditions. For the SpAPicT, the laser beam is sent through the AIDA chamber once before detection and for the APicT the beam is sent multiple times through the chamber until the signal is detected. Sending the beam through the chamber multiple times increases the sensitivity of the measurement and is mainly used for low temperature experiments in the cirrus cloud regime, where the water vapor concentrations are lower compared to mixed-phase cloud conditions.

3.1.2. Aerosol Generation

Aerosol particles such as mineral dust, salts or aqueous solution droplets are injected into AIDA with different devices, depending on the particles' phase state.

Solid dust aerosol particles are generated from a bulk sample including particles in the submicron and supermicron diameter range. To already reduce the particle population of the bulk sample by supermicron particles, the sample is sieved for particles in a diameter range between 0 µm and 75 µm. The dispersion of the particles is done using a rotating brush generator (RBG 1000, Palas GmbH, figure 3.1(d)). In the

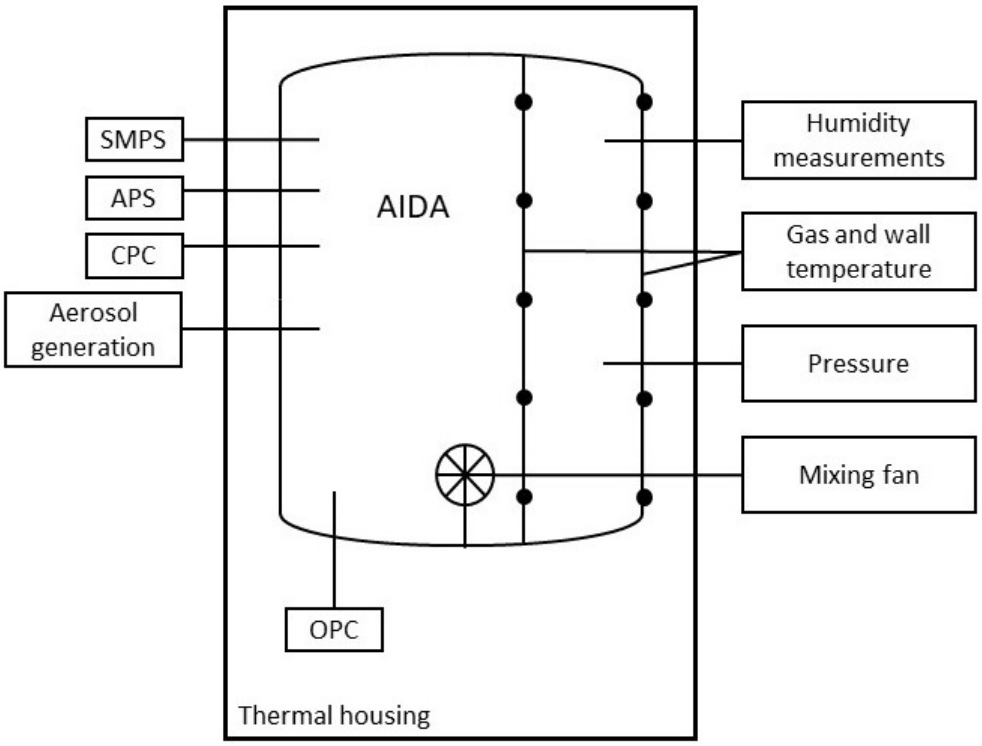

Figure 3.2.: Setup of the AIDA cloud expansion chamber, including the main instrumentation needed for the ice nucleation measurements in this work.

rotating brush generator, the bulk material containing the aerosol particles under investigation is filled into a piston, which is then placed in the instrument. The piston is slowly moved upwards in the instrument, where a rotating brush takes up the aerosol and guides the particles into an air flow. Typically, the air flow is passed trough a cyclone impactor and a dispersion nozzle to remove particles with a diameter larger than about 5 µm, which are not of major relevance for cloud formation processes in the atmosphere. The resulting aerosol in the respective size range is then transferred into the AIDA chamber.

Materials such as ammonium sulfate are also probed in the solid phase, but are most of the time not generated from a bulk sample. Instead, an ammonium sulfate solution is created consisting of between 0.1 wt% and 1 wt% ammonium sulfate and ultra pure water. This solution is then dispersed by an ultrasonic nebulizer (GA 2400, SinapTec) and the formed droplets are passed through a drying column. The resulting solid ammonium sulfate particles are then transferred into the AIDA chamber.

In the experiments presented here, not only solid aerosol particles were probed, but also aqueous solution droplets of sulfuric acid were used, which require a different injection method. Sulfuric acid droplets are injected into the AIDA chamber with a home built sulfuric acid generator. It consists of a small volume filled with concentrated sulfuric acid, which is heated to above 100 °C to vaporize it. A flow of synthetic air passed through the heated reservoir transports the sulfuric acid vapor through a tubing system, in which it cools down to room temperature. Due to the cooling, nucleation and thus a phase change from gaseous to liquid occurs and sulfuric acid droplets form, which are then passed into the AIDA chamber.

3.1.3. Aerosol Characterization

The aerosol that is injected into AIDA is characterized regarding its number concentration and size distribution. While the number concentration is measured using a single instrument, the size distribution is obtained from the combined measurement of two different instruments that make use of different aerosol properties. The following section introduces the three instruments and their measurement techniques.

Condensation Particle Counter The number concentration of aerosol particles in AIDA including particles with a diameter of 10 nm and larger is measured with a Condensation Particle Counter (CPC, 3010, TSI Inc., figure 3.1(a)). Most of the aerosol particles are too small to be detected with optical instruments, and therefore their optical size needs to be increased for optical detection. Inside the CPC, the aerosol is first passed through a saturator region, which is saturated with butanol vapor. The butanol vapor together with the aerosol particles is then transferred into a colder environment in the CPC, the condenser, in which the butanol condenses on the aerosol particles and by that increases their optical size. To actually count the particles, they cross a laser beam and the scattered light is detected (Kulkarni, 2011; Welker, 2012). The CPC operated at AIDA provides the aerosol number concentration with a time resolution of 1 s and is able to count maximum particle concentrations of $10\,000\,\mathrm{cm}^{-3}$ (TSI, 2002).

Scanning Mobility Particle Sizer The Scanning Mobility Particle Sizer (SMPS; at AIDA: DMA, 3071; CPC, 3772, both TSI Inc., figure 3.1(b)) measures the aerosol size distribution in the size range between 10 nm and 800 nm based on the particles' electrical mobility (TSI, 2021); data sheet of the latest model, but with the same size range as the model used at AIDA. When the aerosol particles enter the instrument, they are charged to a known equilibrium charge distribution. Afterwards, they pass a differential mobility analyzer in which they are classified regarding their electrical mobility and counted after the exit with a CPC (Flagan, 1999). By a continuous change of the electrical field strength, the aerosol particles are size selected into specific size bins, which provides a full size distribution of the aerosol in the respective size range (Kulkarni, 2011; Welker, 2012).
Based on the measurement technique, the SMPS gives the mobility diameter (d_{me}) of an aerosol particle. The mobility diameter considers spherical particles and is converted to the volume equivalent diameter (d_{ve}) of aspherical particles of the same volume. Aspherical particles have a higher friction in the air depending on their morphology, which is described with the dynamic shape factor χ. By that the conversion is given as

$$d_{\mathrm{ve}} = \frac{d_{\mathrm{me}}}{\chi} \quad . \tag{3.1}$$

Aerodynamic Particle Sizer The Aerodynamic Particle Sizer (APS 3021, TSI Inc., figure 3.1(c)) measures the aerosol size distribution in the particle diameter range between 0.5 µm and 20 µm, based on the aerodynamic diameter (TSI, 2013); data sheet of the latest model, but with the same size range as the

model used at AIDA. Particles entering the APS are passed through a nozzle in the inlet, which accelerates the gas flow. Due to the different inertia of the particles, they have a different velocity after having passed the nozzle. Particle detection and classification is done by detecting the scattered light of two light beams the particles have to cross inside the APS. Depending on the time between the two scattering signals, the aerosol particle is assigned to a size bin given as the aerodynamic diameter (Wilson and Liu, 1980). The aerodynamic diameter is the diameter of a spherical particle that has the same settling velocity as the measured aspherical particle. Conversion from the aerodynamic diameter (d_{ae}) to the volume equivalent diameter (d_{ve}) is done by using

$$d_{ve} = \sqrt{\frac{\chi}{\rho}} \cdot d_{ae} \quad , \tag{3.2}$$

where ρ is the average density of the aerosol particles.
After the conversion of the SMPS and APS data to a volume equivalent diameter, both measurements are combined to obtain the full size distribution of the aerosol in AIDA. Both instruments require a certain time to properly measure the aerosol size distribution and therefore the time for one measurement is set to 6 min and 4 min for the SMPS and APS, respectively.

3.1.4. Optical Detection of Aerosol Particles, Cloud Droplets and Ice Crystals

[1] The number concentration and size distribution of the aerosol particles, cloud droplets and ice crystals in AIDA can be measured with an optical particle counter (OPC). At the AIDA cloud chamber facility, two welas (Weißlichtaerosolspektrometer) systems are used, which consist of a detector unit (welas 2300 and welas 2500, Palas GmbH) and a control unit (welas 2000, Palas GmbH).
The welas sensor uses a white light source and detects the light scattered by individual particles in a range of scattering angles around 90° (sideward scattering). Particles crossing the detection volume scatter the light in a size and shape dependent way, such that aspherical particles, like ice crystals, show a higher intensity of the scattered light than spherical particles with the same volume. By that, ice crystals can be distinguished from liquid cloud droplets because of their larger optical size (Järvinen et al., 2014).
The air flow under investigation from the AIDA chamber crosses the cuvette inside the welas sensor, but only 10.5 % of the total air volume is analyzed in the optical detection volume. This detected fraction needs to be considered when calculating droplet and ice number concentrations of an AIDA experiment.

3.1.5. Typical AIDA Experiment at Mixed-phase Cloud Conditions

Before the start of a cloud experiment, AIDA is preconditioned and the wall and gas temperature are set to a temperature value in the mixed-phase cloud regime between 0 °C and −35 °C and to ice saturated

[1] A slightly modified version of this section is part of a manuscript which is close to initial submission to the Journal *Review of Scientific Instruments*: Franziska Vogel, Lairssa Lacher, Jens Nadolny, Harald Saathoff, Ottmar Möhler, Thomas Leisner (2022): Development and first application of a new cloud simulation experiment for lab-based aerosol-cloud studies

conditions. Ice saturated conditions are established and maintained by injecting water vapor into the AIDA chamber, which then forms a thin ice layer on the walls. At temperatures below 0 °C, the gas is subsaturated with respect to water when it is already saturated with respect to ice (figure 2.2), and the difference between both saturation rations increases with decreasing temperature. At mixed-phase cloud

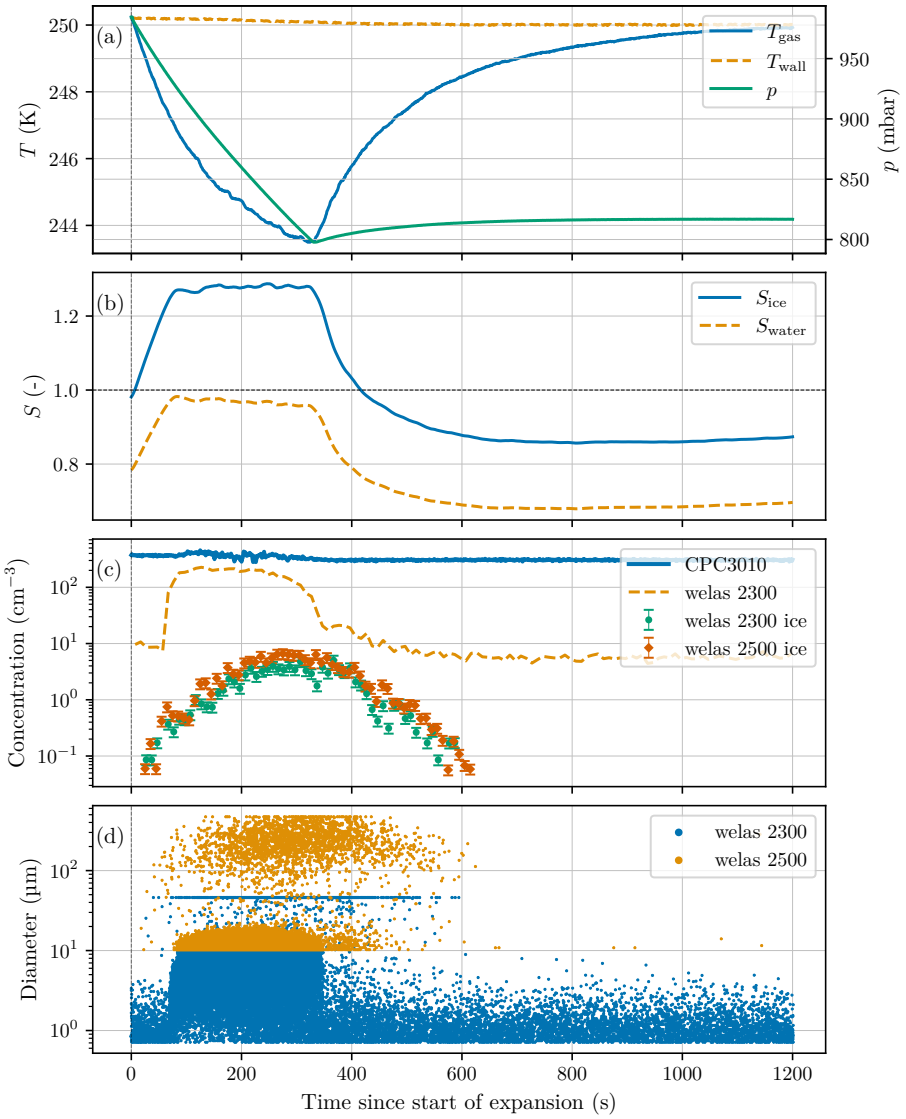

Figure 3.3.: Exemplary AIDA cloud expansion experiment at mixed-phase cloud conditions using Illite NX as an aerosol sample, which was injected into AIDA using the RBG. Panel (a) shows in green and yellow the gas temperature (T_{gas}) and the wall temperature (T_{wall}) of AIDA, respectively. The blue line represents the pressure (p) in the chamber. Panel (b) shows in yellow the saturation ratio with respect to water (S_{water}) and in blue the saturation ratio with respect to ice (S_{ice}). Panel (c) shows the aerosol concentration measured in AIDA (blue line), the total concentration measured with the welas 2300 (yellow line), which includes aerosol particles, cloud droplets and ice crystals, and the ice concentration measured with the welas 2300 (green symbols) and the welas 2500 (red symbols). The single particle data detected in the welas 2300 (blue dots) and the welas 2500 (yellow dots) are presented in panel (d). Particles at a diameter lower than about 4 µm are counted as aerosol particles, particles between 4 µm and 25 µm are cloud droplets and all particles larger than the ice threshold of 25 µm are detected as ice crystals.

conditions, the saturation with respect to water is 1 for a temperature of 0 °C and 1.45 for a temperature of −35 °C.

The first step of an aerosol-cloud experiment is the injection of the aerosol particles into the AIDA chamber in a predefined concentration and particle diameter range, using one of the methods described in section 3.1.2. Afterwards, the aerosol is characterized for its number concentration and size distribution by measurements with the CPC and the SMPS and APS, respectively.

The AIDA cloud expansion is then started by pumping the air out of AIDA and by that lowering the pressure (p) inside the chamber. The decrease in pressure induces a decrease in the gas temperature (T_{gas}) according to the adiabatic equation (equation 2.10; figure 3.3 (a)). The speed with which the air is pumped out of AIDA defines the cooling rate of the gas temperature, which is typically at about $3\,\mathrm{K\,min^{-1}}$ at the beginning of the expansion for the settings used in this work, and results in a simulated atmospheric updraft of maximum $5\,\mathrm{m\,s^{-1}}$. Because the wall temperature stays constant during and expansion experiment, the temperature gradient between the wall and the gas increases with an ongoing expansion time. This leads to an increased heat flux from the wall to the gas and slows down the cooling rate of the expansion. With a decreasing pressure and temperature, the humidity conditions with respect to ice (S_{ice}) and water (S_{water}) increase to supersaturated or saturated conditions, respectively (figure 3.3 (b)). Once the air in AIDA is saturated with respect to water, aerosol particles get activated as CCN and induce the formation of cloud droplets, which are detected in the single particle data of the OPC as a dense accumulation of data points in a diameter range between 4 µm and 25 µm (figure 3.3 (d)). Aerosol particles immersed in the droplets can act as INPs at the respective freezing temperature to induce the formation of ice crystals. Due to their asphericity, the ice particles are measured at larger optical diameters than the liquid droplets so that all particles larger than 25 µm are counted as ice crystals. The ice number concentration is calculated from the number of ice crystals in a certain time bin (figure 3.3 (c)), which steadily increases until 200 s after the start of the expansion where it reaches a maximum value. The saturation ratios with respect to water and ice reach their maximum values at about 80 s after the start of the expansion and stay constant thereafter.

In this experiment, the AIDA expansion ended at a pressure of 800 mbar, by stopping the pumping of air out of the chamber. After the end of an expansion, the temperature in the chamber slowly increases to the initial temperature, due to the heat flux from the wall. The increase in temperature induces a decrease in the saturation ratios with respect to ice and water until they reach subsaturated conditions. This causes an evaporation of the liquid cloud droplets and the ice crystals formed inside AIDA. Once the cloud is fully evaporated, the AIDA experiment is finished, and AIDA is set to an automated cleaning and preconditioning program in preparation of the next cloud expansion experiment.

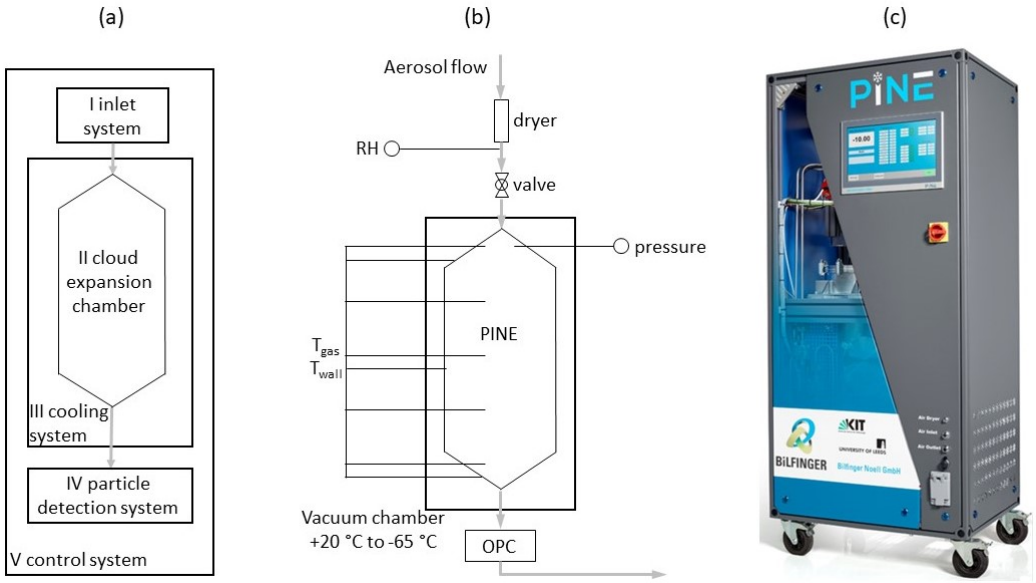

Figure 3.4.: Setup of the PINE chamber. (a) shows the five main parts of the PINE instrument (with minor changes from Möhler et al. (2021)), whereas (b) gives a more detailed overview of the single components of the several parts. Picture (c) shows the commercial version of the PINE chamber.

3.2. The Mobile Cloud Expansion Chamber PINE

AIDA is a cloud expansion chamber used for laboratory experiments on aerosol-cloud interactions. Due to the large volume of 84 m^3 and the long preparation time, its use is limited to two or three cloud expansion experiments per day. This is ideal for focused studies on specific research questions which require a comprehensive set of instruments for a full characterization of the ongoing processes. For ice nucleation or INP measurements in ambient air, however, where aerosol conditions undergo changes and short-term fluctuations, it is important to have an instrument for continuous measurements with a high time resolution. For this reason, the Portable Ice Nucleation Experiment (PINE) was developed, built and commercialized between 2016 and 2019 (development: Karlsruhe Institute of Technology in collaboration with the University of Leeds; commercialization: Bilfinger Noell GmbH). PINE is a mobile expansion chamber with a volume of 10 L, made for continuous measurements of INPs with a time resolution between 4 min and 6 min. Due to the automated operation with remote control option and the low maintenance, PINE is able to perform measurements also at remote places over long time periods of several months or years. PINE as a new INP instrument was first described in detail by Möhler et al. (2021), so the following part gives only a brief overview of the setup and working principle.

Setup of PINE The PINE instrument consists of 5 main parts (figure 3.4 left part, detailed in the right part): the inlet system (I), the cloud expansion chamber (II), the cooling system (III), the particle detection system (IV) and the control system (V).

The main part of the inlet system (part I) is a drying column (Perma Pure, MD-700-24S-1), which removes water vapor from the aerosol flow and by that lowers the dew point temperature to the required range for the measurements. A dew point sensor (DMT143, Vaisala) downstream of the dryer measures the dew point temperature of the aerosol flow entering PINE.
Part II of PINE is the cloud expansion chamber which is a vessel of 10 L volume. The wall temperature of the chamber is monitored with three thermocouples which are taped to the wall on the top, in the middle and at the bottom of the chamber. The gas temperature is recorded on five levels, three of them located close to the wall temperature sensors, and the other two are in between. The pressure in the chamber is measured with a pressure sensor. A valve upstream of the cloud expansion chamber opens and closes the connection to the aerosol sample flow depending on the operational mode of PINE.
Part III of PINE is the cooling system, which regulates the temperature in a range between 20 °C and −60 °C. The cloud expansion chamber is placed inside a vacuum chamber serving as an isolation, in which the pressure is lowered down to about 0.008 mbar, and the cooling power comes from a Stirling cooler (Thales, LPT9310, Johnson et al. (2014)).
All aerosol particles, cloud droplets and ice crystals leaving the cloud chamber during the flush and expansion mode (see following paragraph for details) are passing an OPC (part IV), which is a fidas-pine sensor from Palas GmbH. The basic working principle is similar to the welas sensors used at the AIDA chamber (3.1.4). While the welas analyzes only 10.5 % of the aerosol flow, the fidas-pine sensor was modified to analyze the whole aerosol flow and by that is more sensitive for low particle concentrations.
The whole operation of PINE is controlled with a LabView software running on an external computer (part V). It reads out and displays the time series of the pressure, all the temperature sensors, the dew point sensor and the single particle data from the OPC. It also sets the temperature of the cooler, the flow through the chamber and controls the valves for the automated operation of PINE.

Working Principle of PINE PINE is operated in a cycled mode in which sequences of runs are performed continuously. Each run consists of three modes, which are called flush, expansion and refill.
In the flush mode, the cloud expansion chamber is flushed with air containing the aerosol under investigation. During this mode, the temperature and the pressure in the chamber are constant and the OPC detects the larger aerosol particles. Smaller aerosol particles are not detected, because the OPC settings are optimized for counting cloud droplets and ice crystals, which are larger in diameter. Typical settings for the flow in the flush mode are between 1 L min^{-1} and 2 L min^{-1} for a duration between 5 min and 4 min, respectively, ensuring that the aerosol population under investigation is exchanged during the flush mode.
The flush mode is followed by the expansion mode, which is started by closing the valve on top of the chamber. The flow out of the chamber is maintained and by that the pressure and also the temperature is lowered. As in AIDA, the saturation with respect to ice and water increases with decreasing temperature. Once the aerosol in the chamber reaches liquid water saturated conditions, a liquid cloud forms and

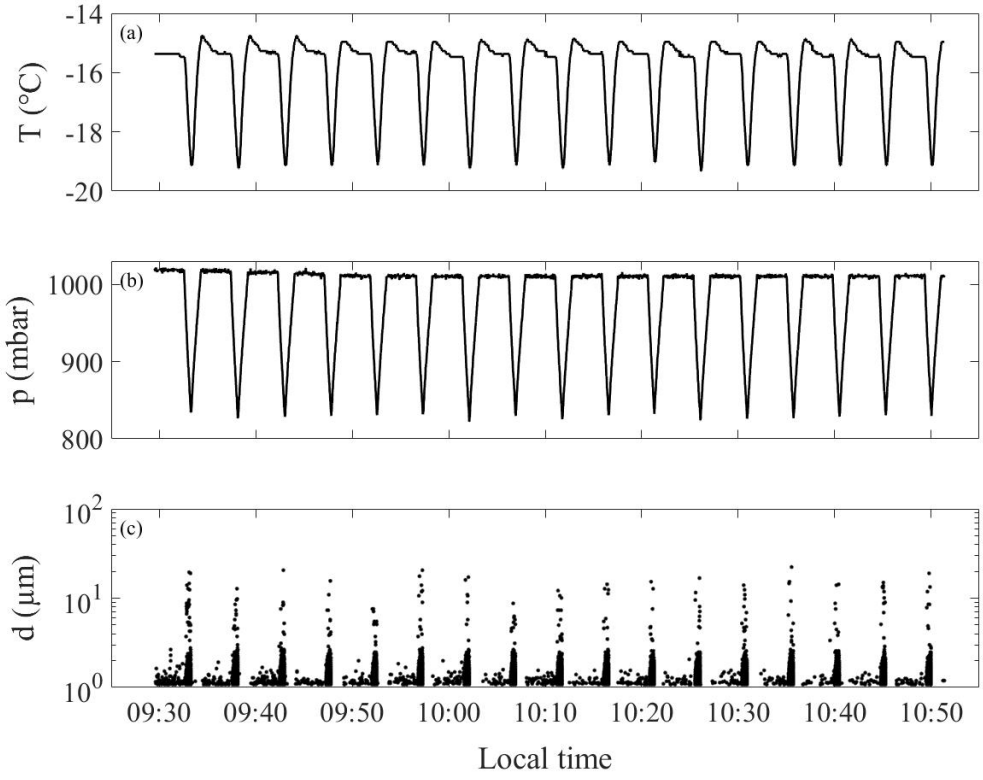

Figure 3.5.: Time series of 18 consecutive PINE runs. Panel (a) shows the gas temperature T measured with the lowest temperature sensor, panel (b) the pressure p measured inside the PINE chamber and panel (c) the diameter d of the single particle data detected with the OPC. In times of a constant temperature and pressure, the chamber is flushed and the OPC detects aerosol particles. During the expansion, the temperature and pressure decrease. In this time, the OPC detects liquid cloud droplets at diameters up to about 3 µm and ice crystals at particle diameters larger than that.

aerosol particles acting as INPs immersed in the droplets trigger the formation of ice crystals. The liquid cloud droplets and the ice crystals are detected in the OPC as described in 3.1.4. The threshold for the ice detection is individually set for each expansion by an automated software tool. To calculate the measured INP concentration following equation 3.3, the total number of ice crystals (ΔN_{ice}) counted during the expansion is divided by the analyzed air volume (ΔV_{exp}). ΔV_{exp} is derived from the volume flow during the expansion (Δf_{exp}) and the duration of the expansion (Δt_{exp}).

$$n_{\mathrm{INP,PINE}} = \frac{\Delta N_{\mathrm{ice}}}{\Delta V_{\mathrm{exp}}} = \frac{\Delta N_{\mathrm{ice}}}{\Delta f_{\mathrm{exp}} \cdot \Delta t_{\mathrm{exp}}} \tag{3.3}$$

Based on the calculation of the INP concentration, the detection limit of one experiment in PINE is approximately $0.5\,\mathrm{L}^{-1}$. The expansion mode ends when the pressure in the chamber reaches a predefined value. Typical settings for the expansion flow are $3\,\mathrm{L\,min}^{-1}$ and the set end pressure is usually 85 % of the initial pressure in the chamber.

The expansion mode is followed by the refill mode in which the chamber is refilled to the initial pressure with dry filtered air. The flow in the refill mode is set to the same value as the flow in the flush mode. After refilling, the chamber switches to the flush mode of the next run. Depending on the settings for the duration of the flush mode and the end pressure of the expansion, one run takes between 4 min and 6 min, which allows to perform 10 to 15 cloud expansion experiments per hour.
Depending on the aim of the measurements, PINE is operated either at constant temperature conditions or performs a temperature ramp in which the cooler changes the temperature in a given range and time. Measuring at a constant temperature has the advantage that the INP concentration is detected with the maximum time resolution of several minutes and hereby information about the short-term variation of INPs for a certain freezing temperature is given. When performing a temperature ramp, more information on the temperature dependent ice-nucleation ability of the aerosol is provided. Compared to the measurements at a constant temperature, the time resolution is reduced to the duration of the ramp, which is typically between 1 h and 2 h.
To ensure a proper performance of PINE, regular background tests are done, by performing several runs in which the chamber is flushed with particle free air. Hereby, all aerosol particles are removed from the chamber and each particle detected in the size range of the ice crystals would hint to potential internal frost formation or leaks in the chamber setup. For the background runs, the duration of the flush mode is increased to 10 min to allow a better exchange of the aerosol in the chamber and hereby limit the number of background runs. Typically, the chamber is aerosol free after 2 to 3 runs and no more ice crystals are detected in the expansion.

3.3. The Freezing Experiment INSEKT

[2] Another instrument used to quantify the ice nucleation behavior of aerosol particles, sampled either in the laboratory at AIDA or in field campaigns, is the INSEKT (Ice Nucleation Spectrometer of the Karlsruhe Institute of Technology) (Schneider et al., 2021b). For this method, aerosol particles from the AIDA chamber or ambient air are sampled on a nuclepore filter with a pore size of 0.4 µm and a diameter of 47 mm. The sampling duration varies between 30 min and 1 h for measurements at AIDA and about 4 h to several days for ambient INP measurements.
For the offline INP analysis with INSEKT, the sampled aerosol particles are washed off the filter with nanopure water. The resulting suspension is diluted twice (1:15 and 1:225) and 50 µL of the undiluted suspension and the two dilutions are pipetted into the wells of two PCR plates with a total number of 160 wells. 32 wells of the PCR plates are filled with nanopure water as a freezing reference. The so-prepared PCR plates are placed in the INSEKT instrument and are cooled at a rate of 0.33 $\mathrm{K\,min^{-1}}$ and the temperature dependent freezing of the water in the wells is observed with a camera. From the

[2] A slightly modified version of section 3.3 and 3.4 is part of a manuscript which is close to initial submission to the Journal *Review of Scientific Instruments*: Franziska Vogel, Lairssa Lacher, Jens Nadolny, Harald Saathoff, Ottmar Möhler, Thomas Leisner (2022): Development and first application of a new cloud simulation experiment for lab-based aerosol-cloud studies

temperature at which the single volumes froze an INP-temperature spectrum is calculated in 0.5 °C steps following the formulation from (Vali, 1971).

3.4. Investigated Aerosol Types

For the AIDA experiments done in the framework of this thesis, several aerosol samples were used. This section describes the aerosols probed in the experiments in section 7.4, 7.5, 4.2 and 6.3.

SDSA_01 – This soil dust sample originates from the Succulent Karoo biome near Soebatsfontein, a semi-arid desert region in South Africa. Sampling probes were directly collected from the soil surface, with some of them also containing biocrust (Maier et al., 2018). After collection, the material was sieved for particle diameters smaller than 20 µm.

ATD – Arizona Test Dust from Powder Technology Inc. (Minnesota, USA) contains natural dust particles that have a diameter between 0 µm and 3 µm. After collection, the sample is milled, dried in an oven and sieved for particles smaller than 3 µm in diameter. Analysis of the chemical composition showed a presence of 57.4 % of SiO_2, pointing to larger amounts of quartz (Möhler et al., 2006). ATD is often used as a reference material, since it is commercially available in larger amounts.

CFA_UK – This coal fly ash sample originates from one of the largest power plants in the United Kingdom and was collected from an electrostatic precipitator (Umo et al., 2019). Looking into the morphology, CFA_UK is a porous material with a specific pore volume of 0.053 $cm^3\,g^{-1}$, when assuming a maximum pore diameter of 100 nm (Umo et al., 2019). Before the experiments, the sample was sieved for particle diameters between 0 µm and 20 µm.

Illite NX - Illite NX is purchased as a dust surrogate, containing about 60 % pure Illite and about 15 % Illite-smectite. It was observed to have a similar chemical composition as natural dust samples and was therefore often used in laboratory studies (e.g. Broadley et al., 2012; Hiranuma et al., 2015)

USD01 - The USD01 (US Dust 01) dust sample is a surface soil sample collected in the Southern Great Planes in the US. It was provided as a powder sample sieved for diameter of < 63 µm. For the aerosol injection into AIDA, the sample was passed through a cyclone impactor to remove aerosol particles larger than about 5 µm in diameter.

USD02 - USD02 (US Dust 02) is a soil dust sample, that was collected in Big Spring, Texas. Before analysis it was sieved for diameters of < 53 µm. When injecting it into AIDA for ice-nucleation experiments, it was passed trough a cyclone impactor to remove particles larger than 5 µm in diameter.

USD03 - USD03 (US Dust 03) is an ambient deposit sample collected with a passive sampler in the Southern Great Plains. Because the sampled amount was small, it was used for ice-nucleation experiments in AIDA without any size segregation prior to the injection.

Snomax® - Snomax® is a commercially available, dried sample of dead bacteria, which is often used for the production of artificial snow. It is composed of fragments of P. syringae bacteria and some of them carry a protein on their surface, that triggers ice formation in a narrow temperature range around −7 °C

(e.g. Wood et al., 2002; Möhler et al., 2008b; Wex et al., 2015). For AIDA experiments, a certain amount of the dry sample is dissolved in water and then injected into the AIDA cloud chamber.

AS - Ammonium sulfate is used as a CCN when mixing it with low dust concentrations as an INP in the laboratory intercomparison studies in section 4.2.2 and to determine the homogeneous freezing onset temperature of pure water droplets in section 7.4.2. In both cases, it is injected into the AIDA chamber as described in section 3.1.2.

SOA – Secondary organic aerosol coatings can be obtained from various biological precursors in the gas phase. In the experiments presented here, the SOA coating material was generated through the dark reaction of ozone (O_3) with α-pinene. The reaction products then condensed on the pristine aerosol particles in the AIDA chamber.

H_2SO_4 – Sulfuric acid particles were used for comparing the homogeneous freezing onset temperature of different instruments, and as a coating material for the experiments described in section 7.5.2. For the first type of experiments, aqueous solution droplets were needed, which were generated as described in section 3.1.2. Using it as a coating material, gas-phase sulfuric acid molecules were formed by the reaction of SO_2 with OH radicals: $SO_2 + 2OH \longrightarrow H_2SO_4$. The OH radicals were formed by the dark reaction of tetramethylethylene (TME) with O_3.

4. Laboratory Intercomparison of INP Instruments

4.1. Introduction

First laboratory measurements of INPs at mixed-phase and cirrus cloud conditions were performed between the 1940s and 1970s by e.g. Cwilong (1945), Schaefer (1946), Vonnegut (1947) and Lindow et al. (1978) using different aerosol types such as bacteria, minerals and silver iodide. Also nowadays, laboratory ice-nucleation measurements are still important to quantify the contribution of pure aerosol systems to the overall atmospheric ice concentration. Based on these measurements, parameterizations to predict the INP concentration were developed to include this parameter in global models. Since the 1990s, INP measurements are also carried out in the field (e.g. Meyers et al., 1992). With the help of new instrument developments, more INP measurements have been and still are performed in the field to directly measure the INP concentration at their emission source and so obtain a better picture of the global distribution of the INP concentration from aerosol particles emitted from various sources (e.g. DeMott et al., 2010; Boose et al., 2016b; Lacher et al., 2017; Wex et al., 2019; Schrod et al., 2020b; Schneider et al., 2021b; Brunner et al., 2021). Figure 4.1 summarizes institutes worldwide performing field INP measurements with own instrumentation, including the three techniques of expansion chambers (green), CFDCs (yellow) and filter sampling (blue). Depending on the sampling location, ambient INP concentrations can range from about$1 \times 10^{-5}\,\mathrm{L}^{-1}$ at about $-5\,^{\circ}\mathrm{C}$ to several thousand L^{-1} at temperatures lower than $-25\,^{\circ}\mathrm{C}$ in the free troposphere or over regions with a high aerosol load such as deserts or highly polluted urban areas (Kanji et al., 2017). The summary of field INP measurements by Kanji et al. (2017) also shows the strong dependency of the INP concentration on the temperature in the mixed-phase cloud regime. This highlights that a full picture of the ambient INP concentration can only be obtained from INP measurements over a broad temperature range.

Several laboratory intercomaprison studies were conducted in the past by e.g. DeMott et al. (2011), Hiranuma et al. (2015), Wex et al. (2015), Burkert-Kohn et al. (2017) and DeMott et al. (2018) to compare the measured INP concentration or n_{s}, calculated from the INP concentration and the in parallel measured aerosol surface area concentration, from different instruments and techniques against each other. For comparison experiments of methods measuring immersion freezing INPs it is important to identify and use aerosol systems that include a well defined number fraction of INPs in the temperature range from about $-5\,^{\circ}\mathrm{C}$ to $-30\,^{\circ}\mathrm{C}$. One aerosol system that turned out to be appropriate was Snomax®, which shows a steep increase in the ice concentration in a narrow temperature range around $-7\,^{\circ}\mathrm{C}$. An exemplary study for that is presented by Wex et al. (2015), where 7 instruments were compared against each other (figure

4.2(a) and (b)). All instruments included in this study depicted the steep increase in n_s at -7±1 °C, which then transfers into a plateau value at about −10 °C. Similar measurements were later presented by DeMott et al. (2018) (figure 4.2(c)), for a different set of INP instruments. In this study, the steep increase agreed well with the one previously measured by Wex et al. (2015), but the subsequent plateau value was slightly lower. This could possibly be explained by different Snomax® stocks and the age of the stock. Due to the high freezing onset temperature of Snomax®, this aerosol can be well used when comparing freezing experiments and expansion chambers among each other. However, for CFDCs it not possible to measure at such high temperatures, since they reach the upper limit of their operational temperature.

To compare the freezing temperature of CFDCs and expansion chambers at colder conditions, the homogeneous freezing onset temperature of supercooled water droplets can be investigated, which is known to occur at around −35 °C (e.g. Benz et al., 2005).

For intercomparison studies on either the measured INP concentration in an aerosol or the calculated n_s, aerosol samples which are ice active in a broad temperature range are used. One comprehensive intercomaprison study by Hiranuma et al. (2015) compared 17 different INP instruments with each other, using Illite NX as an aerosol sample for experiments on immersion freezing (figure 4.3(a)). The results are presented as temperature dependent n_s values, which increased from 5×10^2 m^{-2} at −10 °C to 5×10^{12} m^{-2} at −35 °C. Different instruments and techniques showed an offset of 2 to 3 orders of magnitude among each other. In another intercomparison study from DeMott et al. (2018), the same aerosol sample was probed with partly different instruments and it was observed that the freezing occurred in the same temperature and n_s range (figure 4.3(b) and (c)). Nevertheless, the offset between the different instruments was 1 to 2 orders of magnitude lower compared to Hiranuma et al. (2015).

Several intercomparison studies with natural soil dust (e.g. DeMott et al., 2011; Burkert-Kohn et al., 2017; DeMott et al., 2018) showed the involved methods to be in agreement within 1 order of magnitude or less. The better agreement for the several instruments and techniques for natural soil dust than for Illite NX cannot be explained with the current knowledge.

In more recent years, intercomparison studies of INP instruments were also extended to field INP measurements, where INP concentrations are typically lower and the composition of the aerosol population is more complex. Nevertheless, DeMott et al. (2017) and Brasseur et al. (2022) found an offset between the different INP instruments and techniques in the same range as it was observed for the laboratory intercomparison studies.

Previous intercomparison studies showed partly high offsets between the different INP instruments and techniques of up to 3 orders of magnitude. Therefore, it is important to perform more studies to compare different methods and to develop new instruments to perform comparable INP measurements. In later field experiment, the instruments should then be operated at multiple locations and over long time periods. Also recent projects, such as the establishment of the ACTRIS (Aerosol, CLouds and Trace Gases Research Infrastructure) Topical Center for Cloud In Situ measurements, aim at including INP measurements as a variable for certain atmospheric monitoring stations.

Figure 4.1.: Locations of institutes currently operating instruments for field INP measurements. The different colors present the different measurement techniques.

The intercomparison studies presented in this thesis aimed at comparing some of the newly developed INP instruments with more established INP instruments, but also at searching for suitable aerosol samples for calibration experiments. The intercomparison experiments were only including instruments measuring the INP concentration in the mixed-phase cloud regime. Therefore experiments using Snomax®, supercooled liquid water droplets and different mineral dust aerosol were conducted to cover the full range of mixed-phase cloud temperatures from 0 °C to −35 °C. The intercomparison experiments with pure aerosol systems were conducted with high INP concentrations, to get an ice signal in all instruments well above their limit of detection. To conduct an intercomparison at atmospherically relevant INP concentrations, experiments with mixtures of solid ammonium sulfate particles and dust aerosol were conducted. Ammonium sulfate takes up water during an ice-nucleation experiment in the expansion chambers or the CFDCs and forms a liquid cloud. This additional amount of CCN leads to smaller cloud droplet sizes and thus the cloud droplets in AIDA settle down slower. Ice crystals are formed from the few available dust particles.

4.2. The Intercomparison Campaigns CAL01 and CAL02

4.2.1. Campaign Overview

As part of in the Eurochamp-2020 project as part of the ACcloud (AIDA Calibration Center for Cloud Physics) project, two AIDA campaigns were conducted to intercompare well established and newly developed INP instruments with each other, using various types of aerosol samples. The two campaigns, named CAL01 (CALibration01) and CAL02 (CALibration02), took place in May 2019 and February 2021, respectively, at the AIDA cloud chamber facility. They included instrumentation and contributions

Table 4.1.: Overview table of the instruments participating in the laboratory intercomparison studies CAL01 and CAL02, including the instruments name, the owning institute and the instrument type. The cross in the columns CAL01 and CAL02 indicates the instrument availability in the according campaign. Additional information for the instruments are given on the temperature range, the freezing mode they can detect, the lower limit of detection (LOD) and for the freezing experiments the liquid volume which is analyzed.

Instrument	Institute	CAL01	CAL02	Instrument type	Temp. Range (°C)	Freezing Mode	LOD (L^{-1})	Liquid volume (µL)
AIDA	KIT	x	x	Expansion chamber	0 to -90	Immersion, Deposition	0.5	
PINE-01-A	KIT	x	x		0 to -65	Immersion, Deposition	0.5	
PINE-04-02	KIT		x		0 to -65	Immersion, Deposition	0.5	
INKA	KIT	x	x	CFDC	-10 to -60	Immersion, Deposition	∼1	
mINKA	KIT		x		-10 to -60	Immersion, Deposition	∼1	
HINC	ETH Zurich	x			-10 to -60	Immersion, Deposition	3.1	
INSEKT	KIT	x	x	Filter sampling	0 to -25	Immersion	∼1e-2	50
μl-NIPI	Univ. Leeds	x			0 to -25	Immersion	∼1e-2	1
INDA	TROPOS	x			0 to -25	Immersion	∼1e-3	50
LINA	TROPOS	x			0 to -25	Immersion	∼1e-1	1
DFPC	ISAC-CNR	x			-10 to -22	Immersion, Deposition	∼1e-3	
DRINCZ	ETH Zurich		x		0 to -25	Immersion	∼1e-2	50

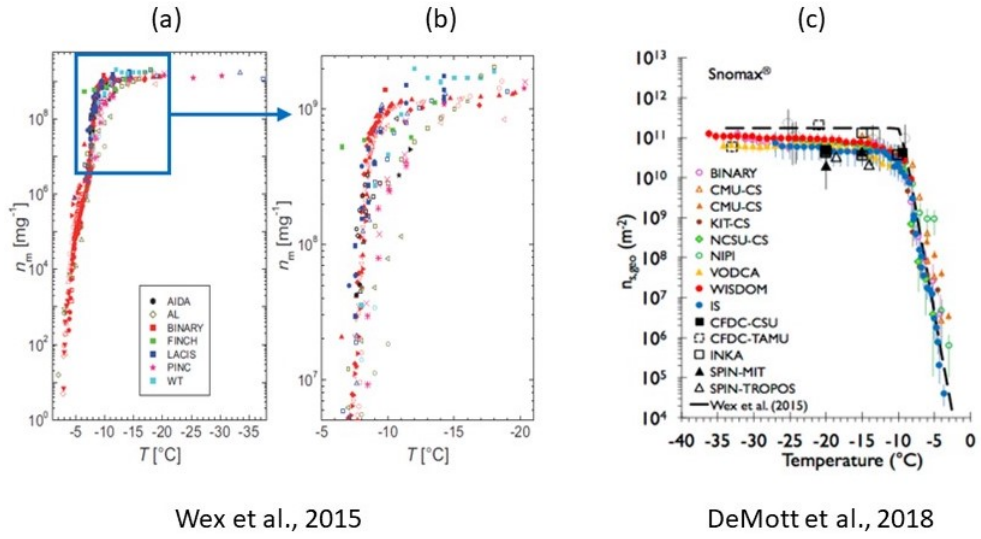

Figure 4.2.: Previous INP instrument intercomparison studies from Wex et al. (2015) (panel (a) and (b)) and DeMott et al. (2018) (panel(c)) using the Snomax® aerosol sample.

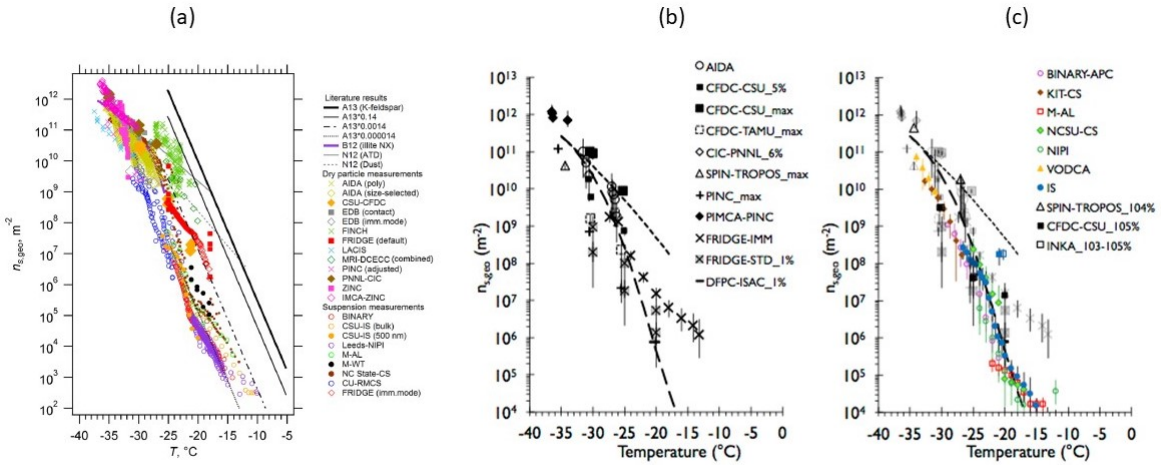

Figure 4.3.: Previous INP instrument intercomparison studies from Hiranuma et al. (2015) (panel (a)) and DeMott et al. (2018) (panel(b) and (c)) using the Illite NX aerosol sample.

from national and international partners from CNRS (France), ETH Zurich (Switzerland), ISAC-CNR Bologna (Italy), TROPOS Leipzig (Germany), University of Leeds (England) and ZAMG (Austria) [1]. In total, 12 instruments including several expansion-type cloud simulation chambers, CFDCs and offline freezing experiments, listed in detail in table 4.1, were compared against each other using 7 aerosol systems with different ice-nucleation properties in a temperature range between $-4\,°C$ and $-37\,°C$. A summary of the experiments is given in table 4.2.

[1] CNRS: French National Center for Scientific Research; ETH Zurich: Eidgenössische Technische Hochschule Zürich; ISAC-CNR: Institute of Atmospheric Sciences and Climate, National Research Council; TROPOS: Leibniz Institut für Troposphärenforschung; ZAMG: Zentralanstalt für Meteorologie und Geodynamik

Table 4.2.: Summary of the experiment from CAL01 and CAL02 giving the aerosol sample, the temperature inside AIDA (T_{AIDA}) prior to the expansion, the number concentration of aerosol particles inside AIDA $c_{n,ae}$ and the respective aerosol surface area concentration s_{ae} that was used to calculated n_s.

Aerosol	T_{AIDA} (°C)	$c_{n,ae}$ (cm^{-3})	s_{ae} ($\mu m^2\,cm^{-3}$)
Snomax®	-12	200	5
Snomax®	-4	150	5
Sulfuric acid droplets	-30	1000	-
ATD	-18	250	79
ATD	-22	100	50
ATD	-22	150	40
ATD	-26	100	55
ATD (before adding AS)	-22	40	8
ATD (before adding AS)	-26	20	5
Illite NX	-22	250	90
Illite NX	-26	300	46
SDSA_01	-22	150	38
SDSA_01	-26	250	56
SDSA_01 (before adding AS)	-18	20	5
ATD + AS	-22	10 + 300	4 (ATD only)
ATD + AS	-22	40 + 300	8 (ATD only)
ATD + AS	-26	20 + 300	5 (ATD only)
SDSA_01 + AS	-18	20 + 300	5 (SDSA_01 only)
SDSA_01 + AS	-22	10 + 300	3 (SDSA_01 only)
SDSA_01 + AS	-26	10 + 300	2 (SDSA_01 only)

Experiments using Snomax® were done to quantify the INP concentration for immersion freezing at already high temperatures of $-7\,°C$. To cover the lower end of immersion freezing temperatures, experiments with sulfuric acid solution droplets were conducted for the detection of homogeneous freezing.

For the intercomparison of the measured INP concentration and the related n_s values at temperatures in between, three mineral dust aerosols (ATD, Illite NX and SDSA_01) were probed, that were partly already used in previous studies. The probed dust samples show a steady increase in the INP concentration over several orders of magnitude in a broad temperature range between $-10\,°C$ and $-33\,°C$ and by that cover the measurement range of all instruments. INP concentrations of up to $5000\,L^{-1}$ at about $-27\,°C$ were probed, which is well above the limit of detection of the instruments. To perform experiments at lower INP concentrations of up to $500\,L^{-1}$ at about $-27\,°C$, which is closer to the range of atmospheric INP concentrations, mixtures of solid ammonium sulfate particles with dust aerosol were used.

All intercomparison experiments were conducted in the same way, to allow optimal and comparable sampling conditions for all instruments. An experiment started with the injection and the characterization of the aerosol sample as described in section 3.1.2 and 3.1.3. When creating internal mixtures of dust and solid ammonium sulfate particles in AIDA, the dust was injected and characterized first and afterwards the

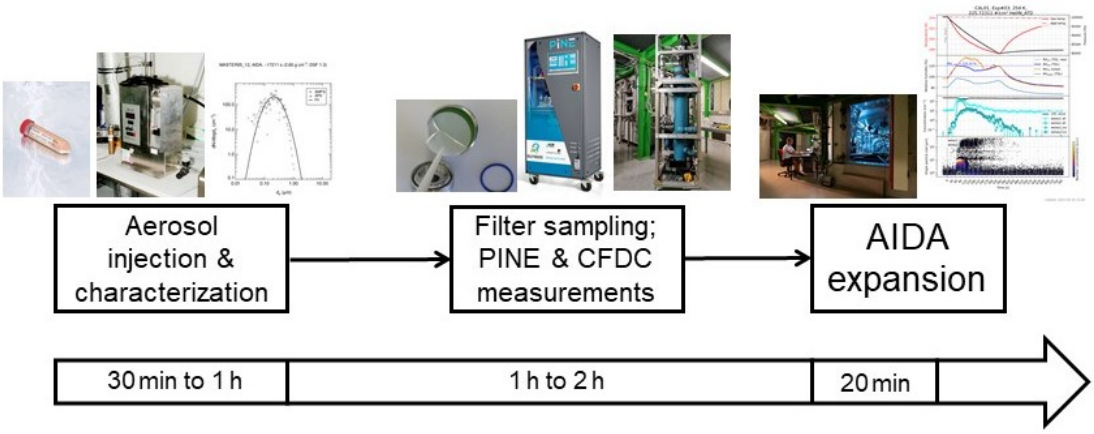

Figure 4.4.: Timeline of the experimental procedure of an intercomparison experiment including the three steps of aerosol injection and characterization, the filter sampling, PINE and CFDC measurements and the AIDA expansion with their respective duration.

ammonium sulfate was added in a particle number concentration ratio of about 1:19. This allowed for a better control and quantification of the low number concentration of the dust particles. The whole aerosol generation and characterization procedure took between 30 min and 60 min, depending on the aerosol type and the amount of injected aerosol. Thereafter, the PINE chamber and the CFDCs started their continuous online measurements and the filters for the several offline analysis techniques were sampled. Generally, this sampling period was limited to 1 h to 2 h, to provide enough time for PINE, the CFDCs and the filter sampling, but on the other hand to ensure that the aerosol population in AIDA did not change considerably due to settling losses inside the chamber. To finish an intercomparison experiment, an AIDA expansion was conducted as described in section 3.1.5.
The following sections discuss the results from the experiments with Snomax®, sulfuric acid solution droplets, pure mineral dust aerosol samples and mixtures of dust aerosol and ammonium sulfate.

4.2.2. Results and Discussion

Experiments with Snomax®

Experiments using Snomax® were conducted at temperatures between $-4\,^{\circ}\mathrm{C}$ and $-23\,^{\circ}\mathrm{C}$, and the results are presented as temperature dependent n_s values. The individual uncertainties for the instruments were calculated as about 40 % for the CFDCs and expansion chambers and about 70 % for the freezing experiments, but are not presented in the intercomparison plots. A steep freezing curve of Snomax® was detected by INSEKT and DRINCZ at a temperature of $-7\,^{\circ}\mathrm{C}$, as it was expected from previous measurements from Wex et al. (2015) (figure 4.5(a)). Both instruments mainly covered the steep increase in n_s and the freezing curves ended at $-12\,^{\circ}\mathrm{C}$, right after the transition to the plateau value. Also PINE detected the ice onset in the same temperature range as INSEKT and DRINCZ, but the increase was less pronounced than for the filter sampling methods. PINE was also able to measure the transition to the

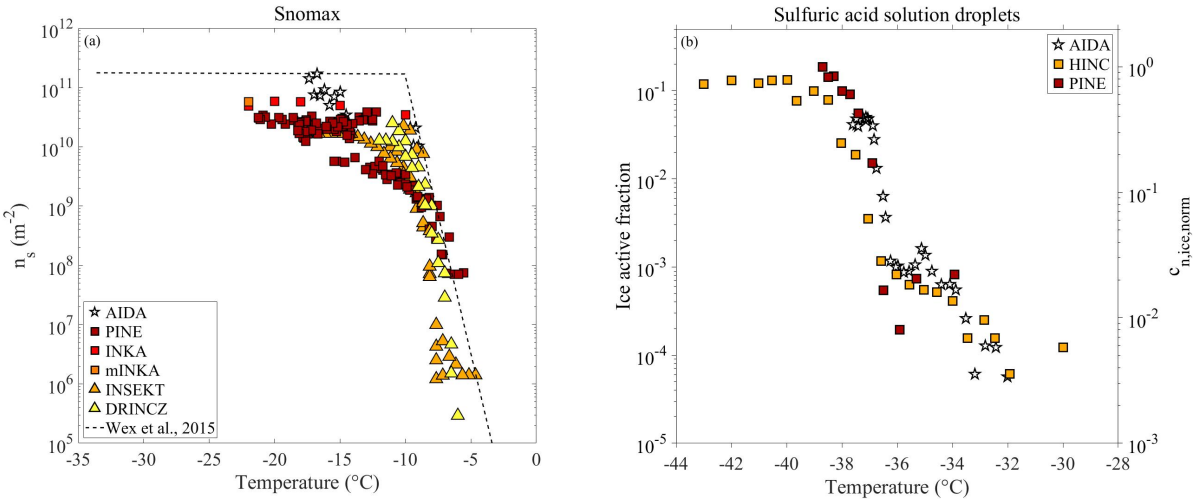

Figure 4.5.: Comparison of the different INP instruments and measurement techniques using Snomax® (panel (a)) and supercooled water droplets (panel (b)). The results of the Snomax® experiments are presented as temperature dependent INAS densities (n_s) and the dashed line represents the the measurement from Wex et al. (2015). The results of the comparison using supercooled liquid droplets are shown as an ice active fraction for HINC and AIDA and as a normalized ice concentration $c_{n,ice,norm}$ for PINE.

plateau value in the temperature range at about $-10\,°C$. The freezing onset of Snomax® occurs at a rather high temperature, where measurements with CFDCs are not possible, because the warm wall would reach temperatures above $0\,°C$ which would cause a melting of the ice layer on the wall. Thus they were not able to detect the steep increase in n_s, but measured, together with PINE, the plateau value over a wide temperature range between $-10\,°C$ and $-23\,°C$ with n_s values between $5 \times 10^9\,m^{-2}$ and $2 \times 10^{11}\,m^{-2}$. While the steep increase in n_s is well in agreement with Wex et al. (2015), the plateau value is about 1 to 2 orders of magnitude lower. This deviation can originate from different batches of Snomax® or already aged samples, which partly loose their ice-nucleating ability (Polen et al., 2016).

Experiments on Homogeneous Freezing of Supercooled Water Droplets

To compare the homogeneous freezing of supercooled water droplets in AIDA, PINE and HINC, the homogeneous freezing of sulfuric acid solution droplets was measured. The results for the comparison between AIDA, HINC and PINE are presented in figure 4.5(b), where the comparison of AIDA and HINC was part of CAL01 and the comparison data of PINE are taken from Möhler et al. (2021). AIDA and HINC measurements are presented as an ice active fraction, which equals the ratio of the ice concentration to the total aerosol number concentration. PINE results are presented as an ice concentration normalized to the maximum measured ice concentration $c_{n,ice,norm}$. The detection of homogeneous freezing of supercooled water droplets is characterized as a steep increase in the detected number of ice crystals, which is reflected in a steep increase in the ice active fraction for AIDA and HINC and $c_{n,ice,norm}$ for PINE. All three instruments measured this steep increase between $-36\,°C$ and $-37\,°C$, which is the temperature range expected from previous measurements.

The experiments using Snomax® and supercooled liquid water droplets were conducted to compare the measured INP concentration of different instruments for high and low temperatures in the mixed-phase cloud regime. Both experiments showed, that all instruments measured the INP concentration in the temperature range that was expected from literature (Wex et al. (2015) for Snomax® and Benz et al. (2005) for the homogeneous freezing).
However, it would be of great benefit to have an aerosol sample showing a similar behavior as Snomax® in the intermediate temperature range between $-15\,°C$ and $-20\,°C$, to allow a parallel comparison of all INP measurement techniques. As shown by Pummer et al. (2012), pollen washing water shows a steep temperature dependency in the required temperature range and thus future experiments probing this sample should be performed.

Experiments with Dust Aerosol

To compare the instruments with each other for the measured n_s over a broad temperature range, 4 experiments with ATD, 2 with Illite NX and 2 with SDSA_01 were performed during CAL01. While ATD and Illite NX were used in a number of previous studies, the natural soil dust sample SDSA_01 was used for the first time in an intercomparison study. Natural dust samples tend to show a better agreement between the instruments (DeMott et al., 2018) and therefore SDSA_01 was considered a potentially more natural calibration material. In contrast to Snomax®, where one protein on the surface triggers the freezing, dust shows a steady increase in the ice concentration over a wide temperature range due to multiple sites on the surface triggering the ice formation. All results in this section are presented as n_s as a function of the temperature.
The results from the ATD intercomparison (figure 4.6(a)) showed that all instruments measured the steady increase in n_s from $1 \times 10^5\,m^{-2}$ at about $-10\,°C$ to up to $1 \times 10^{12}\,m^{-2}$ at $-32\,°C$. However, the data from CAL01 show an offset between the different INP instruments and techniques of up to 4 orders of magnitude over the whole captured temperature range. Hereby, it tends that the freezing experiments INSEKT, INDA and μl-NIPI and the online methods PINE, INKA and HINC show a better agreement among each other, respectively. All instruments measured consistently lower n_s values than AIDA, which defined the upper end of the detected n_s range. This high offset between all the instruments pointed out that ATD is not an appropriate aerosol for comparison studies.
A similar offset as in the experiments with ATD was observed for those in which Illite NX was probed (figure 4.6(b)). Throughout the measured range of n_s between $1 \times 10^4\,m^{-2}$ and $8 \times 10^{11}\,m^{-2}$ at temperatures of $-7\,°C$ and $-32\,°C$, respectively, the instruments showed an offset of 2 to 3 orders of magnitude. In contrast to the ATD experiments, AIDA measured only slightly higher n_s values of 1 order of magnitude compared to the other instruments. The results are represented by the fit from Hiranuma et al. (2015) for wet suspended and dry dispersed Illite NX. Nevertheless, the data still show a high scatter, meaning that the new methods and instruments are in the same uncertainty range as the already existing methods. Therefore, no improvement was achieved.

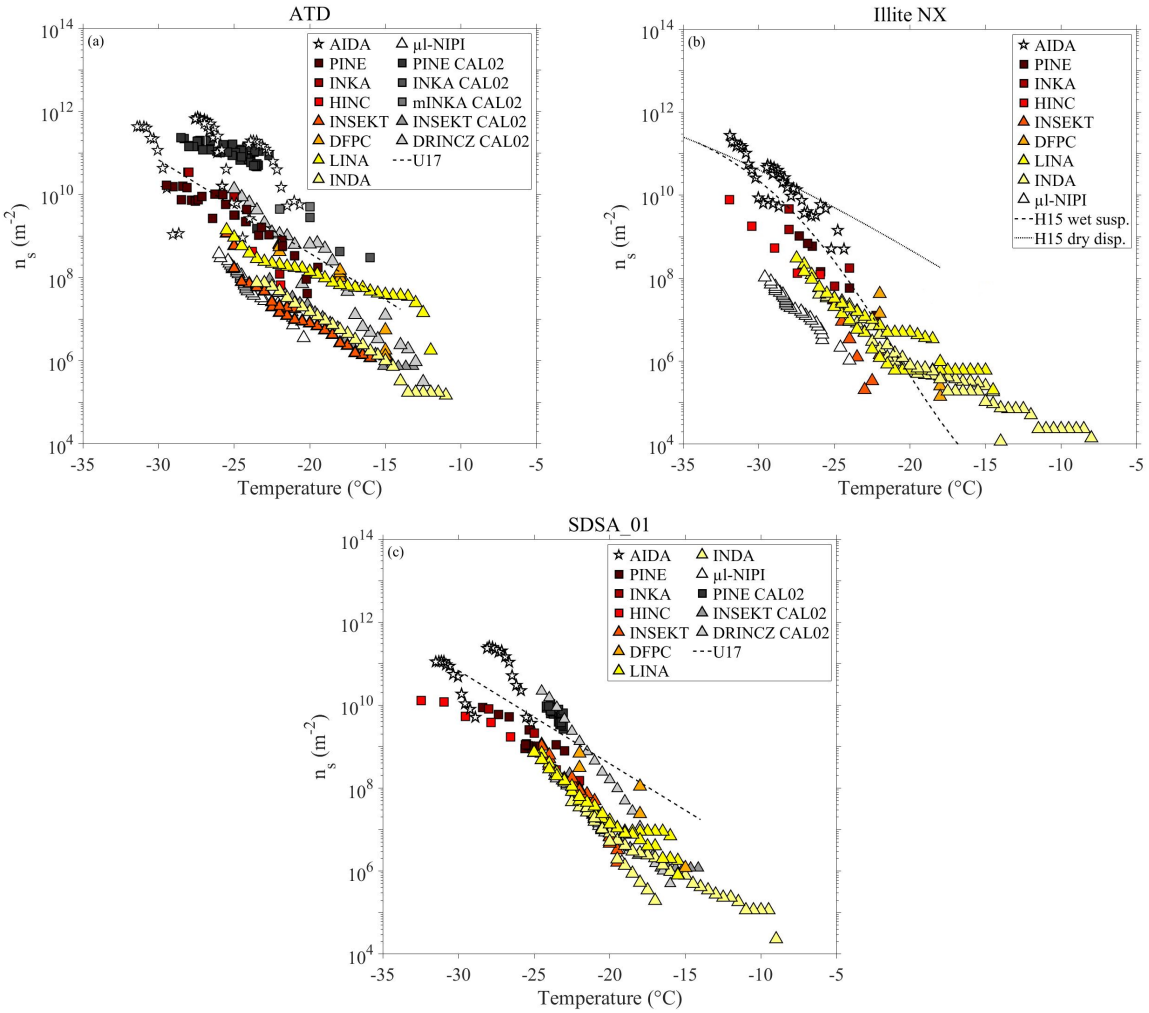

Figure 4.6.: Temperature dependent INAS densities (n_s) of all intercomparsion experiments with ATD (panel (a)), Illite NX (panel (b)) and SDSA_01 (panel (c)). The colored symbols are the data points from the CAL01 campaign, whereas the grey data points were obtained during the measurements of CAL02. The dashed line in panel (a) and (c) shows the dust parameterization from Ullrich et al. (2017) (U17). In panel (b), the dashed line represents the parameterization for wet suspended particles from Hiranuma et al. (2015) (H15) and the dotted line the one for dry dispersed Illite NX particles.

In contrast to the ATD and Illite NX results, the data gained during CAL01 using the natural soil dust sample SDSA_01 (figure 4.6(c)) showed an agreement within two orders of magnitude for the whole captured temperature range between $-8\,°C$ and $-28\,°C$. As for the other dust samples, all online and offline instruments measured up to 2 orders of magnitude lower n_s values than AIDA.

The up to 2 orders of magnitude better agreement of the different INP instruments and techniques for SDSA_01 compared to ATD and Illite NX showed that this material may be a more appropriate sample for intercomparison studies. Because it was used for the first time in this work, more experiments with different instruments should be preformed to extend this comparison.

In order to investigate the reproducibility of results using the same aerosol, experiments with ATD and SDSA_01 were repeated during CAL02 (gray data points in figure 4.6(a) and (c)) and a similar discrepancy

among the participating instruments as in CAL01 was observed. While INSKET showed the same results in CAL01 and CAL02, PINE and INKA showed between 1 to 2 orders of magnitude higher n_s values in CAL02 compared to CAL01. This may be related to slightly different sampling conditions or aerosol particles in the two campaigns. The pure dust samples during CAL02 were injected into AIDA in low concentrations, because after a short sampling period ammonium sulfate was added for the mixture experiments. These up to 1 order of magnitude different dust concentrations may lead to differences in the results.

An offset between different INP instruments and techniques can be related to their sensitivity for different freezing modes. INSEKT, LINA, INDA, μl-NIPI and DRINCZ are limited to immersion freezing only, because the INP concentration is obtained from the freezing of liquid suspension volumes. In contrast to that, the analysis with the DFPC is done by exposing the sampled filter to an environment in which water and ice sub- and supersaturated conditions at different temperatures can be reached. Thus this technique is also sensitive to detect ice crystals formed via deposition nucleation. Ice crystals that form at water subsaturated conditions are small in size at the beginning of their formation process and grow in size over time by deposition of water vapor on their surface. During an AIDA expansion, such ice crystals can be detected, because the way of the ice crystal to the detector can be a few minutes, which is enough time for them to grow to sizes that can be detected in the OPC. Also the cooling rate during an expansion of about $3\,\mathrm{K\,min^{-1}}$, at which AIDA is typically operated for expansions in the mixed-phase cloud regime, is slow enough that the ice crystals formed from the vapor phase have enough time to grow in size. The AIDA expansions for ATD and SDSA_01 at a temperature of $-26\,^{\circ}\mathrm{C}$ (figure 4.7) revealed that this could happen during an AIDA expansion at mixed-phase cloud conditions. Both experiments were done at the same start conditions of T_{gas} and S_{ice} and S_{water} (panel (a) and (b)). In the experiment using ATD (figure 4.7 left side), a steep increase in the ice concentration was observed at around 70 s after the start of the expansion. The welas single particle data showed a dense ice cloud, but no liquid cloud droplets in the size range covered by the two welas systems. This points to a potentially strong ice signal from deposition nucleation. In the expansion using SDSA_01 (figure 4.7 right side), a liquid cloud was detected in the welas at about 70 s after the start of the expansion. However, the welas 2500 already detected an ice signal before the occurrence of the liquid cloud, but less pronounced than for ATD. Therefore, also weaker ice signals of ice forming from the vapor phase can be detected in AIDA, which may lead to a higher total ice concentration measured in AIDA compared to the other INP instruments. An expansion in PINE is typically performed at a cooling rate of about $7\,\mathrm{K\,min^{-1}}$, which is more than double the one in AIDA. By that, the cooling process and the increase in the ice and water saturation is much faster. Also the time a particle needs to reach the detector is only a few seconds. Thus, ice crystals forming from the vapor phase may not grow to sizes that can be detected with the current sensitivity settings of the fidas-pine OPC. Such ice crystals a most likely not added to the total ice number concentration measured in PINE. CFDCs are sensitive for detecting ice that formed below water saturation. However, depending on the size of the aerosol particles it can become challenging to differentiate ice crystals from larger aerosol

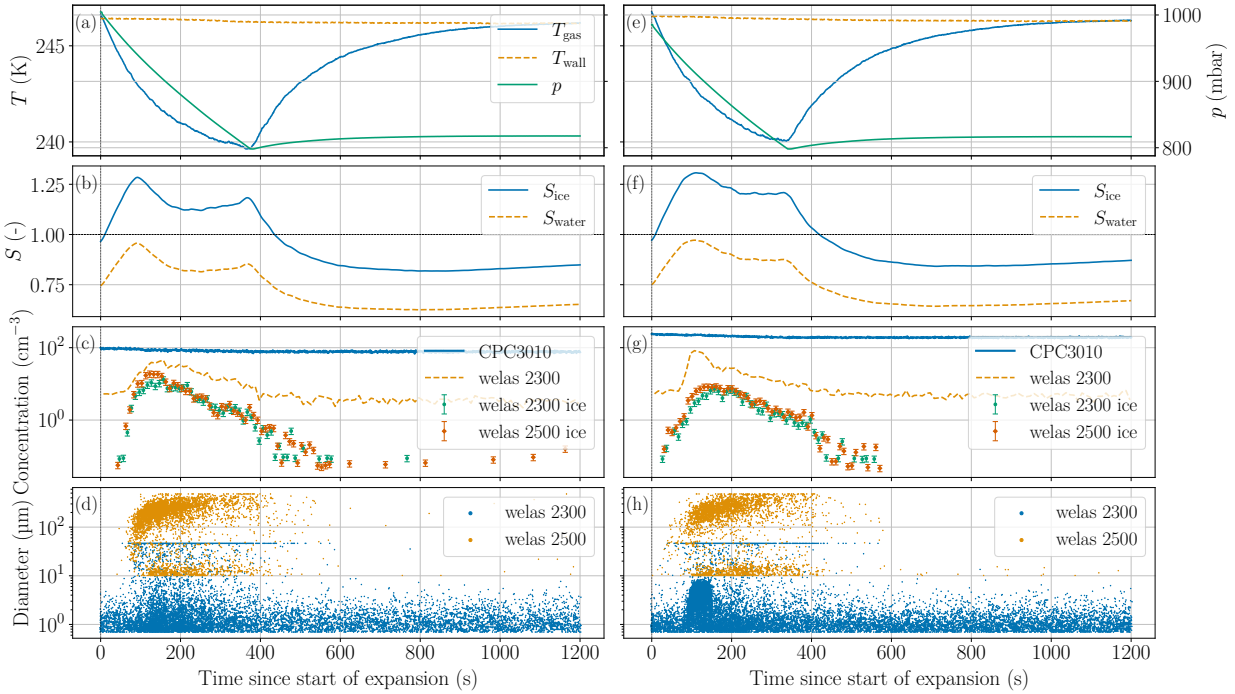

Figure 4.7.: AIDA expansion with ATD (left side) and SDSA_01 (right side) at mixed-phase cloud conditions, where panels (a) and (e) show the gas temperature in AIDA (T_{gas}) in blue, the wall temperature (T_{wall}) in orange and the pressure (p) in green. Panels (b) and (f) depict the saturation ratio with respect to ice (S_{ice}) and water (S_{water}) in blue and orange, respectively. In panel (c) and (g), the aerosol concentration measured with the CPC (blue), the total particle concentration detected with the welas 2300 (orange) and the ice number concentration measured with the welas 2300 and welas 2500 (green and red, respectively) is shown. The single particle data from the two welas systems welas 2300 (blue) and welas 2500 (orange) are shown in the panels (d) and (h).

particles. For the analysis of CFDC data one fixed water supersaturation value is used, at which the ice concentration is then calculated.

Aerosol particle inside AIDA can als get preactivated due to the PCF mechanism, which increases the ice activity of an aerosol. PINE and the CFDCs sampling though sampling lines at room temperature, where a potential preactivation gets lost again, because the water valor and ice in the pores melts and evaporates again. Also the offline methods are not sensitive for PCF.

The difference due to changing freezing pathways only applies for primary ice formation in the atmosphere, but another point that should be considered is the secondary ice production in clouds. Secondary ice formation leads to the production of multiple ice crystals from the freezing of a single droplet, which mainly occurs at temperatures between $-3\,°C$ and $-25\,°C$ (Korolev and Leisner, 2020). Dedicated studies whether this mechanism plays are role during AIDA expansions, PINE or CFDC measurements were not yet done.

Experiments with a Mixture of Dust and Ammonium Sulfate

Experiments with atmospherically relevant mixtures of low INP concentrations and high CCN concentrations were done with mixtures of ATD or SDSA_01 as INPs and ammonium sulfate particles as CCN. The

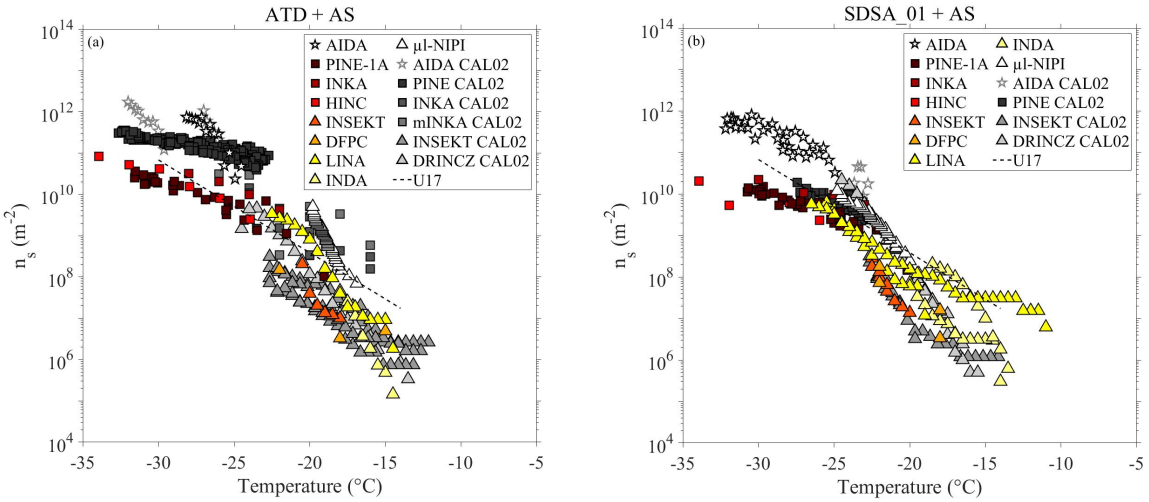

Figure 4.8.: Temperature dependent INAS densities (n_s) of all intercomparsion experiments with a mixture of ATD with AS (panel (a)) and a mixture of SDSA_01 with AS (panel (b)). The colored symbols are the data points from the CAL01 campaign, whereas the grey data points were obtained from the measurements during CAL02. The dashed line shows the dust parameterization from Ullrich et al. (2017).

results in figure 4.8 are presented in the same way as the experiments using dust only. A steady increase in n_s from about 1×10^6 m^{-2} at -12 °C to about 1×10^{12} m^{-2} at -34 °C is observed for both dust samples and was detected by all instruments. However, some methods depicted an offset of up to 2 orders of magnitude for both, the CAL01 and CLA02 campaign. The new methods PINE and HINC agree within a factor of 5 with each other over their whole covered temperature range between -20 °C and -32 °C, but measured consistently lower n_s values than AIDA. The results of the freezing experiments showed a good agreement among each other and with PINE, INKA, mINKA and HINC in the overlapping temperature range from -20 °C to -25 °C. LINA showed a higher offset to the other offline methods for SDSA_01 + AS, which may be related to the detection limit of the instrument. With low dust aerosol concentrations in AIDA and by that also low INP concentrations, the background correction for offline instruments becomes more uncertain which may lead to a higher scatter in the measured n_s.

In the experiments with pure dust aerosol and a mixture of dust as an INP and ammonium sulfate as a CCN, n_s values in the same range were measured for the same aerosol type. This showed that the instruments detected high and low INP concentrations with the same offset. The measured results with ATD and SDSA_01 in high and low concentrations were all represented by the dust parameterization from Ullrich et al. (2017).

As for the measurements with pure dust, the reproducibility of the results from CAL01 using the same aerosol was investigated during CAL02. It was shown that the results from AIDA, INKA and INSEKT are well overlapping with each other for both mixtures. The measurements from CAL02 using PINE showed n_s values in the same range for the mixture SDSA_01 + AS, but the PINE data from CAL02 using ATD + AS showed a higher n_s of about 1 order of magnitude.

Generally, the experiments using a mixture of CCN and INPs showed all instruments to agree within 2 orders of magnitude. As already observed and discussed for the intercomparison with pure dust aerosols, the additional online and offline INP instrument showed higher n_s values than AIDA.

4.3. Summary

The intercomparison studies presented in this work aimed at comparing new INP instruments and methods against instruments that are operated for already a longer time. Furthermore, INP instruments were compared for the first time for high and low INP concentrations using the same aerosol type.
Motivated by the work of e.g. Hiranuma et al. (2015), Wex et al. (2015), Burkert-Kohn et al. (2017) and DeMott et al. (2018), the 2 campaigns CAL01 and CAL02 were conducted at the AIDA facility, in which 12 different INP instruments were compared against each other using different aerosol systems. Snomax® was probed to compare the measured n_s for immersion freezing conditions at high temperatures and shows a steep increase in the ice concentration in a narrow temperature range at around $-7\,°C$. Sulfuric acid solution droplets were used to detect the homogeneous freezing of supercooled water droplets with AIDA, PINE and HINC, which is expected to occur at a temperature around $-35\,°C$. For the intercomparison of the instruments measuring n_s, the dust samples ATD, Illite NX and SDSA_01 were probed, which show a steady increase in n_s over a wide temperature range. The experiments with pure dust aerosol were performed at high INP concentrations, to obtain an ice signal in the different INP instruments well above their limit of detection. To probe also atmospherically relevant aerosol mixtures of low INP concentrations and high CCN concentrations, experiments with dust as an INP and ammonium sulfate as a CCN were conducted. These results are then important for INP instruments operated in field experiments.
The experiment using Snomax® showed that all instruments detected the freezing at temperatures around $-7\,°C$, which agreed with what was measured in Wex et al. (2015) and DeMott et al. (2018). PINE, INSEKT and DRINCZ also measured the transition to a plateau value at a temperature around $-10\,°C$. This plateau was captured by the CFDC and PINE measurements over a wide temperature range between $-10\,°C$ and $-23\,°C$.
The homogeneous freezing of supercooled water droplets was measured with AIDA and HINC as a steep increase in the detected ice active fraction and with PINE as a steep increase in the normalized ice number concentration in the expected temperature range around $-35\,°C$.
For the different pure dust samples, all instruments measured the steady increase in n_s in the covered temperature range. The range of measured n_s values for Illite NX was supported by the measurements from Hiranuma et al. (2015) and the measured n_s values for ATD and SDSA_01 were represented by the parameterization for dust in the immersion freezing mode from Ullrich et al. (2017). Nevertheless, the different INP instruments and methods showed a scatter of up to 4 orders of magnitude for ATD and Illite NX and up to 2 orders of magnitude for SDSA_01. Generally, all INP instruments tended to measure lower n_s values than AIDA, which may partly be explained by different freezing modes the

instruments are sensitive for. In some AIDA expansion experiments, it was observed that AIDA measured a strong ice crystals signal before the occurrence of liquid cloud droplets, giving indication for a different freezing mode. Other instruments, especially freezing experiments measure only ice crystal formation in the immersion freezing mode.

The results of the experiments with the mixtures of dust and ammonium sulfate showed a steady increase in the measured n_s for all instruments and in the same range as for the pure dust. Also the scatter of the measured n_s values was with around 2 orders of magnitude the same as for the pure dust sample. This showed that the INP instruments agree in the same way for high and low INP concentrations and for pure aerosol systems and atmospheric mixtures of aerosols types.

Some of the experiments from CAL01 with pure dust and the mixtures of dust with ammonium sulfate were repeated in CAL02. While for the SDSA_01 sample, n_s values in the same range and the same scatter of the INP instruments was observed, the results using ATD showed partly higher n_s values in CAL02 than in CAL01. This may be explained by slight changes in the aerosol injected into AIDA.

The two intercomparison studies CAL01 and CAL02 showed that for different probed aerosol types the measured n_s was within the range of what was already presented in the literature. New INP instruments, such as PINE, HINC, mINKA and DRINCZ showed the same offset as already existing instruments. A solid explanation and reason for the measured offset can not yet be given and further experiments are needed to understand this. A possible explanation may be that the various INP instruments and techniques are sensitive for different freezing processes. Future experiments should be conducted to identify the contribution of deposition nucleation in the mixed-phase cloud regime and with cooled sampling lines for PINE and the CFDCs to investigate a potential contribution of preactivated aerosol particles to the ice concentration.

5. Atmospheric INP Observations and Short-term Variation

5.1. Introduction

INPs originate from a large variety of aerosol emission sources around the globe and contribute to the primary ice formation in the atmosphere in the mixed-phase at temperatures between 0 °C and −35 °C and water saturated conditions and in the cirrus cloud regime at temperatures below −35 °C at water subsaturated conditions. Once formed in the atmosphere, the ice crystals can have a large impact on the cloud optical thickness and thus influence their radiative properties and the cloud phase feedback (e.g. Murray et al., 2021; Forster et al., 2021). Shortwave and longwave radiation is reflected on the cloud top surface back to space or on the bottom of the cloud back to the Earths' surface. Depending on the optical thickness of the cloud, one of these mechanisms dominates and therefore different clouds can have a positive or negative cloud phase feedback. A positive cloud phase feedback is referred to a warming of the atmosphere and a negative feedback to a cooling accordingly.
With an ongoing climate change and thus a warming of the atmosphere, the ambient air temperature will rise by up to 5 °C until the end of the century without taking any measures against it (IPCC, 2021). An increasing ambient air temperature leads to a thawing of iced regions, which can then release more aerosol particles acting as INPs and CCN. Also other vulnerable regions such as deserts or dry land may expand due to a shortage of water. Another factor is the anthropogenic influence, which was found to increase the INP concentration over the past centuries (Schrod et al., 2020a). An increase in the INP concentration in the atmosphere would lead to more ice formation in clouds. Such clouds are then optically thinner and have a positive cloud phase feedback. Therefore, one of the key parts is to understand the abundance of atmospheric INPs emitted from various aerosol sources. Some recent studies from e.g. Lacher et al. (2018), Wex et al. (2019), Schrod et al. (2020b) and Schneider et al. (2021b) investigated the INP variation at different locations around the globe regarding their seasonal change and by that the variation on a longer time scale. These studies are all based on CFDC or filter sampling measurements with a time resolution between 20 min to days. Filter measurements are valuable for investigating the temperature dependent freezing behavior of aerosols from different sources, but lack in providing information about the variation of the INP concentration on a shorter time scale of a few minutes to one hour. CFDCs measure with a time resolution of about 20 min, which captures the short-term variation, but require a lot of man power to operate them continuously. Therefore, CFDC measurements were limited to only short intensive measurement periods. A first full year record of INP measurements with a time resolution of 20 min is presented by Brunner et al. (2021), where continuous measurements with the newly developed

and automated CFDC HINC-Auto (automated Horizontal Ice Nucleation Chamber) were conducted with mainly free tropospheric aerosol at Jungfraujoch (3580 m a.s.l.). They found a seasonal change in the INP concentration and a diurnal variation in times of boundary layer intrusions. A major drawback of these measurements is the limit of detection of CFDCs, which only allows for measurements at temperatures of about −30 °C. To cover the INP variation caused by changing aerosol conditions, air masses and meteorological conditions at temperatures higher than −30 °C with a high time resolution, continuous long-term measurements with e.g. the PINE chamber are needed.

To represent the INP measurements and thus the ice formation in the atmosphere in regional and global weather prediction and climate models, paramterizations were developed (DeMott et al., 2010; Tobo et al., 2013; DeMott et al., 2015; Schneider et al., 2021b). While DeMott et al. (2010), Tobo et al. (2013) and DeMott et al. (2015) predicted the INP concentration as a function of the freezing temperature and the aerosol number concentration of particles larger than 0.5 µm in diameter, Schneider et al. (2021b) suggested to base the prediction on the freezing temperature and the ambient air temperature as well as to consider different sets of fit parameters depending on the season. Other parameterizations predict n_s and by that already include a normalization to the aerosol surface area concentration. Dust aerosol specific parameterizations were developed by Niemand et al. (2012) and Ullrich et al. (2017), one for soil dust by Steinke et al. (2016) and one for boreal environments including seasonality by Schneider et al. (2021b). Most of the INP and n_s parameterizations were developed on the basis of only a few measurements from field INP measurements or laboratory characterizations. Furthermore, some of them are limited to freezing temperatures below −15 °C, which excludes high temperature INPs from mainly biological origin. A further improvement of the parameterizations requires long-term INP measurements in a wide temperature range.

5.2. Campaign overview

INP measurements with PINE and INSEKT were conducted during 4 field campaigns performed at 3 rural locations in central Europe and one at a mountain station (figure 5.1) and the base dates of the campaigns are given in table 5.1. Based on the PINE data, which have a time resolution of about 6 min, the short-term variation in the measured INP concentration is discussed as well as potential influential factors. The comprehensive long-term data sets of both, PINE and INSEKT measurements were used to validate existing parameterizations for the INP concentration and n_s. As an outcome of these measurements, a new INP parameterization for rural aerosol was developed.

The following section briefly describes the goals and the sampling conditions of the four campaigns named Kosetice21, Swabian21, CALISHTO21 and CORONA.

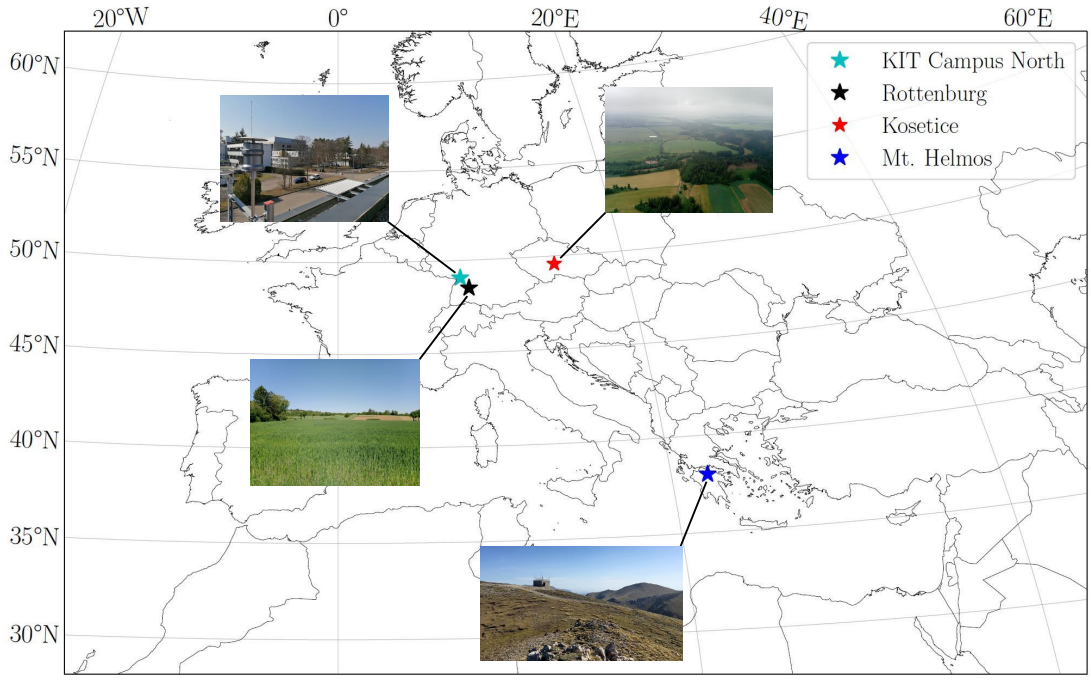

Figure 5.1.: Map of the 4 locations at which field INP measurements were performed. The Kosetice21 campaign took place in Kosetice (red star), Swabian21 in Rottenburg (black star), CALISHTO21 at Mt. Helmos (blue star) and CORONA at KIT Campus North (light blue star).

5.2.1. Kosetice21

The Kosetice21 campaign took place from April 28, 2021 until June 20, 2021 at the National Atmospheric Observatory in Kosetice (Czech Republic). Kosetice is situated in the central part of the Czech Republic at 15.1°E and 49.6°N at 534 m above sea level on a hill. The observatory is surrounded by farm land, grass land and smaller forest areas, away from any larger cities and by that represents a typical rural background site at which enhanced anthropogenic contributions to the aerosol population are rare.

The National Atmospheric Observatory in Kosetice is part of the ACTRIS network for aerosol measurements. During the Kosetice21 campaign, INP measurements were done for the first time at this station, where the first 6.5 weeks of the campaign, from April 28 until June 10, were meant to characterize the INP variation in late spring and summer. The last 10 days were then focused on comparing the total INP concentration against the PM1 INP concentration (discussed in detail in chapter 6) using highly time resolved measurements from PINE.

The whole campaign period was characterized by dry weather conditions, with a minimum temperature between 0 °C and 10 °C in May and June, respectively, and a maximum temperature of 15 °C to 30 °C (figure 5.2). The air masses came mostly from western directions, starting over the Atlantic ocean and then crossing France and Germany before reaching the measurement site (figure 5.3). Only towards the end of the campaign, the trajectories were more omnidirectional, with a partly longer residence time over

Table 5.1.: Overview of the four field INP measurement campaigns, giving the campaign name, the sampling location, time period of the measurements and the INP instruments in use. Note that for CORONA only the measurement period included in the presented analysis and discussion is given, but the campaign was started in March 2020 and was ongoing until March 2022.

Campaign	Location	Measurement period	INP instruments
Kosetice21	Kosetice, Czech Republic	Apr 28, 2021 to Jun 20, 2021	PINE-04-02, INSEKT
Swabian21	Rottenburg, Germany	Jun 02, 2021 to Sep 05, 2021	PINE-04-01, INSEKT
CALISHTO21	Mt. Helmos, Greece	Oct 12, 2021 to Nov 28, 2021	PINE-04-01, INSEKT
CORONA	KIT Campus North, Germany	Apr 01, 2021 to Sep 15, 2021	INSEKT

land. Therefore the air masses reaching the measurement site were not necessarily loaded with long range transported aerosol.

All instrumentation, including the PINE chamber, was mounted in measurement containers about 100 m off the station facility buildings. The main aerosol container is permanently equipped with a CPC, a SMPS and an APS to characterize the aerosol number concentration and size distribution. During the Kosetice21 campaign the container was additionally equipped with PINE and for the last 10 campaign days with an INSEKT filter sampling setup. All instruments sampled the ambient aerosol through a PM10 inlet, such that only aerosol particles smaller than 10 µm in diameter were transferred to the instruments. PINE and the INSEKT filter sampling setup shared one inlet, and by that were not influenced by other sampling instruments.

During the first 6.5 weeks of the campaign, in which the site was characterized for the INP variation, PINE measured most of the time at a constant temperature between $-21\,^{\circ}\mathrm{C}$ and $-24\,^{\circ}\mathrm{C}$. One day per week PINE was operated by running a temperature ramp between $-17\,^{\circ}\mathrm{C}$ and $-28\,^{\circ}\mathrm{C}$ to get a better picture of the temperature dependent freezing of the aerosol. For the size selective measurements in the last 10 days of the campaign, sampling through the PM10 inlet and through a PM1 cyclone impactor was switched every about 2 h. This allowed to get information on the total and PM1 INP concentration within a rather short time, without having larger changes in the ambient aerosol size distribution.

INSKET filters were sampled during the last 10 days of the campaign with a flow of $3\,\mathrm{L\,min^{-1}}$. In order to increase the time resolution of the INSEKT measurements, one filter in the morning hours, one in the afternoon hours and one during the night was sampled. All filters were analyzed following the description in section 3.3 and with a heat treatment, where the suspension is heated to $100\,^{\circ}\mathrm{C}$ to deactivate heat sensitive INPs.

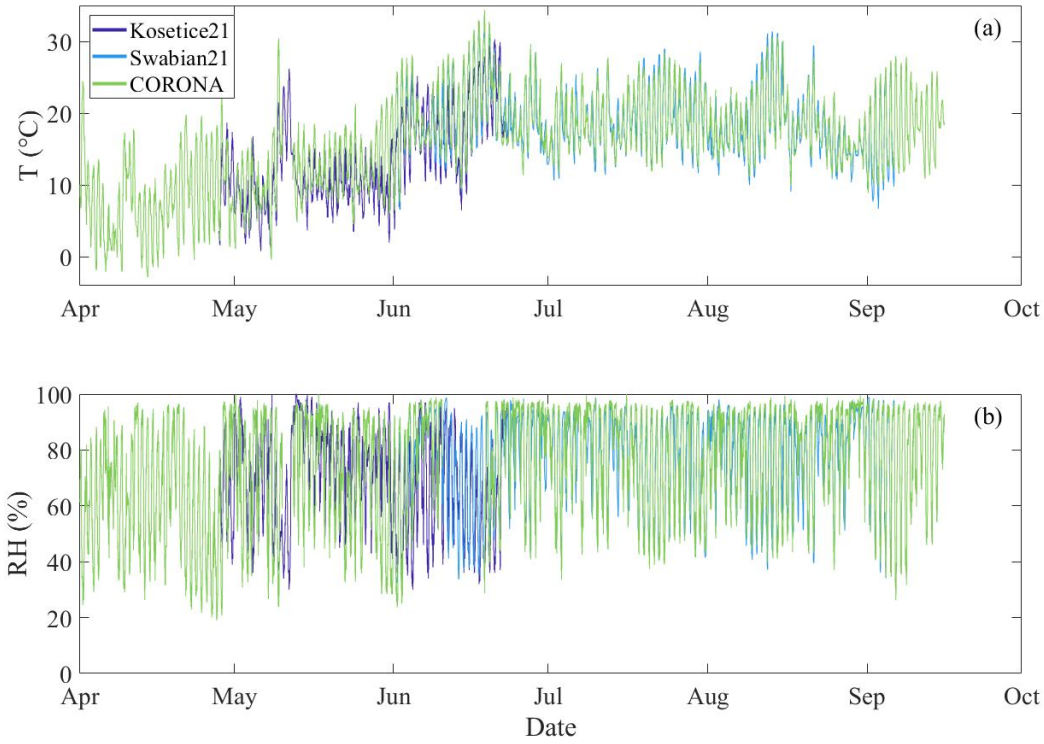

Figure 5.2.: Ambient air temperature (panel (a)) and the relative humidity (panel (b)) for three field campaigns Kosetice21 (dark blue), Swabian21 (light blue) and CORONA (green).

5.2.2. Swabian21

The Swabian21 campaign took place from June 02, 2021 until September 05, 2021, near Rottenburg, which is located in southwestern Germany at about 8.9°E and 48.5°N. Rottenburg is 349 m above sea level at the edge of the low mountain range Swabian Alb. The sampling site was on a grain field about 1 km northeast of Rottenburg, right in the updraft region of the Swabian Alb. South of the location is the Swabian Alb with only small cities and villages, and north of the location are larger cities such a Tübingen and Stuttgart and especially the latter one is known for high concentrations of anthropogenic aerosol. Thus, depending on the wind direction more rural or more urban and polluted aerosol particles are transported to the measurement site.

The measurements presented here were part of the MOSES (Modular Observation Solutions for Earth Systems) project. Generally, the campaign focused on hydro-meteorological extreme situations including deep convection with heavy rain fall and hail and heatwaves connected to droughts. For the first time, PINE was part of the sophisticated instrumentation of the KIT cube, including radar, lidar, radiation, precipitation and meteorological measurements and measured the short-term variation in the INP concentration throughout the whole campaign period including deep convective events.

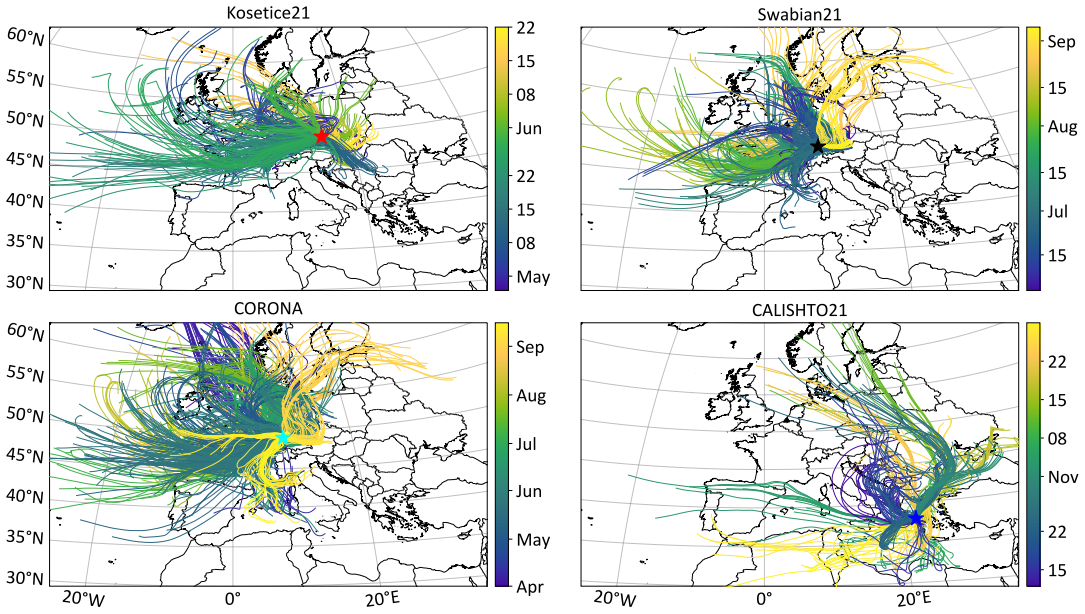

Figure 5.3.: Backwards trajectories calculated with the HYSPLIT (Hybrid Single-Particle Lagrangian Integrated Trajectory) model (Stein et al., 2015) for the whole campaign period for the four campaigns Kosetice21, Swabian21, CALISHTO21 and CORONA. Every 3 h one trajectory was calculated going 72 h back in time.

During the 14 weeks of INP measurements, the meteorological situation varied between hot and dry summer periods and colder and more humid periods. The ambient air temperature varied between 10 °C as a minimum and 32 °C as the maximum temperature (figure 5.2). The air masses came most of the time from western and northwestern directions and thus more polluted areas, with a few days in early June and early September where they came more from the east (figure 5.3).

The aerosol container had two PM10 inlets, one for the PINE and INSEKT filter sampling setup and a second one for the aerosol characterization instrumentation including two CPCs, an APS and a Fidas (Palas GmbH), which is an OPC to measure particles with a optical diameter larger than 0.18 µm. On top of the roof was a weather sensor for the measurement of the basic meteorological parameters such as temperature, pressure, humidity, precipitation, wind speed, wind direction and global radiation.

PINE measured the whole campaign period at a constant temperature of about −23 °C to capture the short-term variation in the INP concentration.

Since most of the time all instruments in the container were operated remotely, INSEKT filters were only sampled during periods of onsite operation. In these intensive operation periods the filter was changed every 4 h to 6 h to capture changes in the temperature dependent freezing on a shorter time scale. INSEKT filters were sampled with a flow of $10\,\mathrm{L\,min^{-1}}$ and analyzed with the regular analysis as described in section 3.3.

5.2.3. CALISHTO21

The CALISHTO21 campaign took place from October 12, 2021 until November 28, 2021 at the Helmos Atmospheric Aerosol & Climate Station in Greece, which is located on Mount Helmos at 22.2°E and 37.9°N at 2314 m above sea level. Mount Helmos and the according mountain range are situated on a peninsula in the southwestern part of Greece and are far away from sources of anthropogenic aerosol emissions. Due to the exposed location, the observatory can be inside the boundary layer, inside of clouds and in the free troposphere and depending on that different aerosols from both local emissions and long range transport can be present.

CALISHTO21 was conducted to get a better understanding of the formation and evolution of mixed-phase clouds. Therefore, the evolution of orographic clouds was investigated with several in-situ and remote sensing instruments regarding the microphysics and kinetics, thermodynamic and the impacts from boundary layer and free tropospheric aerosols. Within the given goals, PINE was operated to characterize the INP concentration in the mixed-phase cloud regime over the whole campaign period and the changing aerosol conditions.

Throughout the whole campaign period, the conditions mainly changed between in-cloud and free tropospheric conditions. The main sectors of air mass origin were northeast and southwest and only a few days at the beginning of the campaign were characterized with air masses from northwestern directions (figure 5.3). Air masses from northeastern directions transported aerosol particles from continental eastern Europe and air masses from the southwest were more loaded with aerosol particles of marine and coastal origin.

The station is part of the Global Atmospheric Watch Network and provides a comprehensive set of aerosol instrumentation, including measurements for the aerosol number concentration, size distribution and composition. Additionally to the already existing instrumentation, an APS was provided during CALISHTO21 to extend the measurements for the number concentration and size distribution of larger aerosol particles. The station provides several PM10 inlets for sampling and during the campaign, PINE and the INSEKT filter sampling setup shared one. On the roof of the station is some instrumentation to measure meteorological variables such as temperature, relative humidity, pressure, wind speed and wind direction.

Most of the time, PINE was operated at a constant temperature between $-23\,^{\circ}\mathrm{C}$ and $-26\,^{\circ}\mathrm{C}$. On selected days a temperature ramp between about $-17\,^{\circ}\mathrm{C}$ and $-28\,^{\circ}\mathrm{C}$ was performed.

In parallel to the PINE measurements, one INSEKT filter per day was sampled, to investigate the temperature dependent freezing of the ambient aerosol. The filters were sampled with a flow of $9\,\mathrm{L\,min^{-1}}$ and analyzed for the INP concentration as described in section 3.3.

5.2.4. CORONA

The CORONA campaign was started in March 2020 at KIT Campus North in Karlsruhe, which is situated at 8.4°E and 49.0°N and is about 120 m above sea level. KIT Campus North is located in a forest about 10 km north of the city of Karlsruhe and depending on the wind direction contributions from urban aerosol emissions to the aerosol population are possible. The measurement location on the Campus is close to a road and therefore the measurements can be influenced by car emissions.
CORONA was started during the first Covid-19 lockdown period to investigate possible changes due to less frequent traffic on the Campus. It was then extended to obtain a two year record of continuous filter sampling and aerosol characterization.
Because the CORONA measurements were performed for two years, the measurements cover two full annual cycles including all seasons. For the analysis in this thesis, only the period from April 01, 2021 until September 15, 2021 is considered. In this time period the temperature varied between 0 °C and 32 °C (figure 5.2). The air masses came mainly from western and northwestern directions and thus transported aerosol from the Atlantic ocean through France and Germany to the sampling site.
The CORONA campaign provided continuous measurements of the aerosol number concentration using several CPCs, and the aerosol size distribution using a SMPS, APS and a Fidas. Additionally to that, INSEKT filters were sampled for the analysis of the temperature dependent freezing of the sampled aerosol. All the sampling was done through a PM10 inlet from which the flow was split up to the several instruments.
The INSEKT filters were changed on a daily basis during weekdays and throughout the weekend one filter was sampled. The sampling flow was set to $8\,\mathrm{L\,min^{-1}}$ and the analysis for the INP concentration was done as described in section 3.3.

5.3. Results and Discussion

5.3.1. Short-term Variation in the Measured INP Concentration

Comparison to Existing Measurements

The results of previous field campaigns were summarized by Kanji et al. (2017), where INP measurements sampling aerosol from different sources are presented. While dust and biomass burning aerosol showed the highest INP concentrations of up to $1000\,\mathrm{L^{-1}}$ at temperatures of $-25\,°\mathrm{C}$ and lower, aerosol particles from marine, coastal, arctic and antarctic sources had the lowest INP concentrations between $1 \times 10^{-4}\,\mathrm{L^{-1}}$ and $100\,\mathrm{L^{-1}}$ at temperatures between $-6\,°\mathrm{C}$ and $-27\,°\mathrm{C}$. Compared to that, aerosol particles of biological origin showed high INP concentrations of up to $1\,\mathrm{L^{-1}}$ already at temperatures of about $-7\,°\mathrm{C}$. Most of the presented studies contributed only a few data points or data for only one temperature to the shaded areas in figure 5.4 and the sampling periods were restricted to short time periods of a few days or weeks.

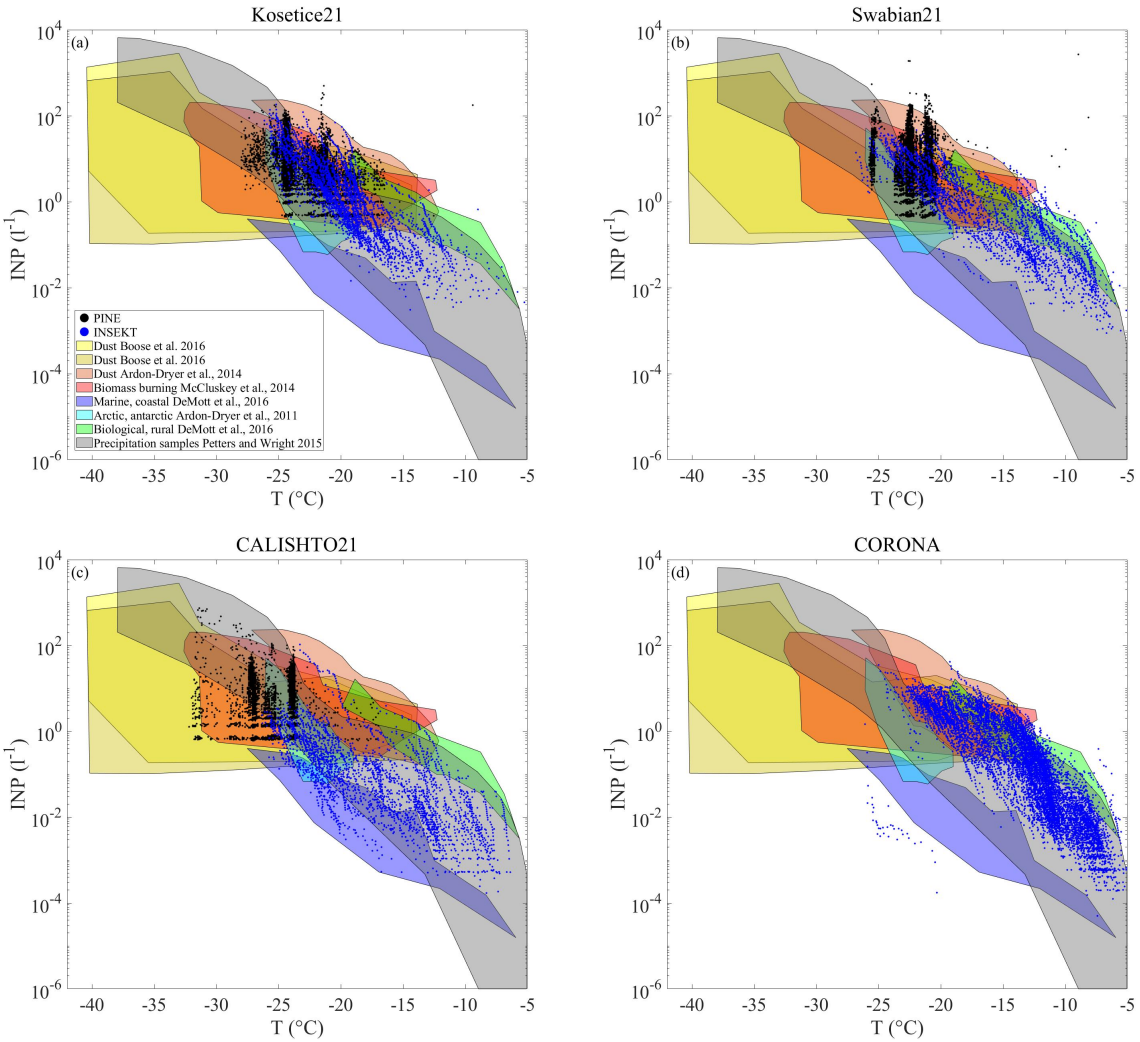

Figure 5.4.: INP-temperature spectra measured with PINE (black points) and INSEKT (blue points) during the four field campaigns Kosetice21 (panel (a)), Swabian21 (panel (b)), CALISHTO21 (panel (c)) and CORONA (panel (d)). The shaded areas are adapted from the overview plot presented in Kanji et al. (2017), where each colored area represents the measurements from one study. Yellow and orange areas are field measurements with dust (Ardon-Dryer and Levin, 2014; Boose et al., 2016b,a), the red area with biomass burning aerosol (McCluskey et al., 2014), purple with marine and coastal aerosol (DeMott et al., 2016), cyan with arctic and antarctic aerosol (Ardon-Dryer et al., 2011) and green with biological and rural aerosol particles (DeMott et al., 2016). The gray area represents experiments with precipitation samples.

Also the time resolution of the measurements was limited to some hours or days and by that the variation in the INP concentration was not pictured optimally.

The field campaigns presented in this work lasted between 8 weeks and 5 months including PINE measurements with a time resolution of about 6 min and INSEKT measurements with a time resolution between 4 h to 2 d. All data points from both, PINE and INSKET are presented within the summary plot from Kanji et al. (2017) in figure 5.4. The PINE measurements revealed a high variation of the measured INP concentration of almost 3 orders of magnitude at temperatures between $-22\,°C$ and $-30\,°C$, which can be referred not only to the air mass origin and by that to the type of aerosol, but also to a

short-term variation due to aerosol sampling close to the emission source. Also the INSEKT measurements showed variation in the INP concentration of up to 2 orders of magnitude for the Kosetice21, Swabian21 and CORONA campaign and up to 3 orders of magnitude for CALISHTO21 over a wide temperature range between about $-5\,°C$ and $-25\,°C$. Kosetice21, Swabian21 and CORONA show a similar trend and spread of the INP concentration, giving indication that the INP sources in these rural regions are similar. According to the measurements shown in Kanji et al. (2017), the PINE measurements from these campaigns can be more attributed to dust aerosol particles and the INSEKT measurements are within the biological, rural and dust origin shaded areas. Compared to Kosetice21, Swabian21 and CORONA, the CALISHTO21 campaign took place on a mountain station, which experiences a changing influence of free tropospheric and boundary layer aerosol. Also the air masses throughout the campaign period came from changing directions. This is reflected in a larger spread in the temperature dependent INP concentration, especially in the INSEKT measurements, where some filter analysis showed a freezing onset at about $-6\,°C$ and a comparably steep increase in the INP concentration thereafter, and other filters had a freezing onset at about $-15\,°C$ with a steady increase in the INP concentration.
This campaign overview showed that the variation in the INP concentration of aerosol particles from one source region can be up to 3 orders of magnitude for temperatures between about $-5\,°C$ and $-28\,°C$. Thus, future studies should include more measurements characterizing the short-term variation in the INP concentration.

Variation of the INP Concentration During Individual Campaigns

The time series of the individual campaigns were analyzed, to get a better idea of the time dependence of the short-term variation in the measured INP concentration.
The Kosetice21 campaign revealed a variation in the measured INP concentration between about $0.5\,L^{-1}$ and about $200\,L^{-1}$, with one peak concentration of up to $800\,L^{-1}$ detected on April 29 (figure 5.5). Generally, the campaign was characterized by periods with quite constant low INP concentrations from e.g. May 06 until May 14 and rather constant high INP concentrations between e.g. June 01 and June 10. In the time periods in between, the INP concentration varied frequently within 1 to 2 orders of magnitude. Two remarkable days are May 27 and June 01, where the INP concentration increased by about one order of magnitude within a few hours to the maximum value and decreased right after reaching the maximum to the initial value again. The temperature ramps performed every week underlined the freezing ability of the aerosol also for different temperatures and fit to the variation in the INP concentration in the respective time periods. A comparison of the trend in the measured INP concentration (black line in figure 5.5) with the trend in n_s (red line in figure 5.5) shows that they follow almost the same trend throughout the whole campaign period. One exception is the time between May 13 and May 18, where n_s stayed constant while the INP concentration increased or decreased. This might have been caused by opposing trends in the INP concentration and the aerosol surface area concentration.

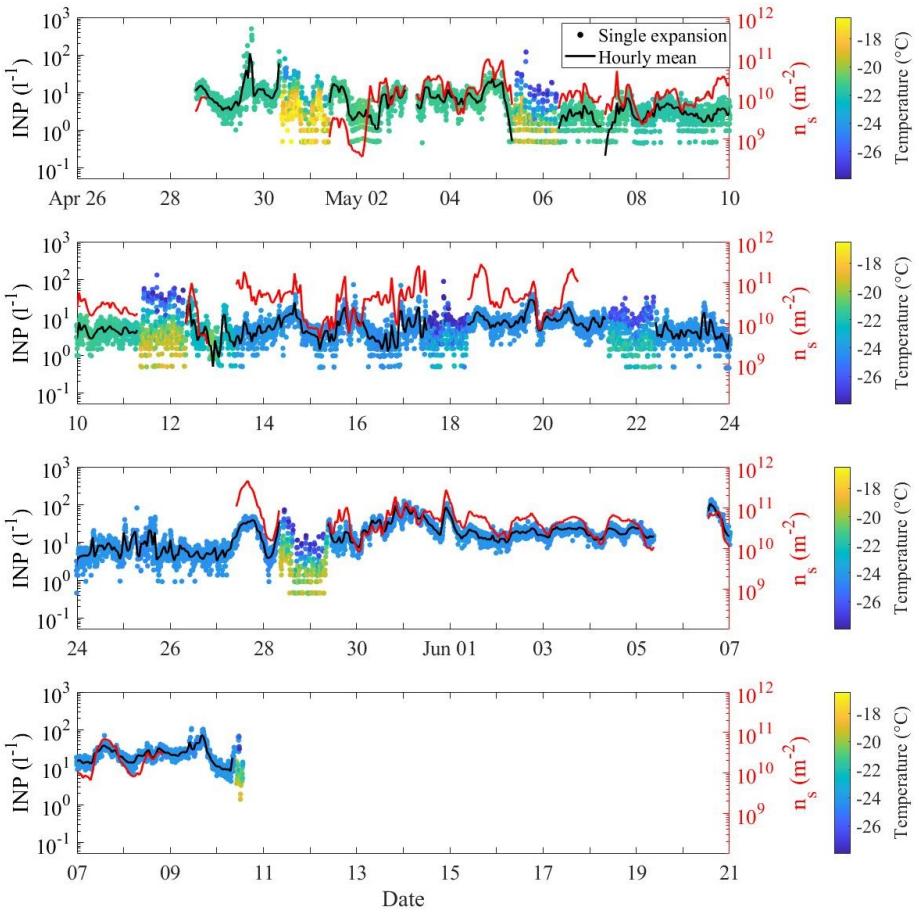

Figure 5.5.: Time series of the measured INP concentration of PINE during the Kosetice21 campaign. The color coded dots show the INP concentration from the single PINE expansions and the black line is the hourly average. When PINE performed a temperature ramp, shown as scans through a wider temperature range, no average is calculated. The red line presents the calculated n_s.

Throughout the 6.5 weeks of continuous INP measurements during Kosetice21 there is a strong variation in the INP concentration and n_s of 2 to 3 orders of magnitude. To search for potential driving factors for this variation, weekly correlations of the INP concentration with several meteorological and aerosol related variables were calculated using the Spearman correlation coefficient (figure 5.6). To identify an unambiguous variable that influences the short-term variation in the INP concentration, an enhanced positive or negative correlation coefficient would be needed for one or more variables and all weeks. In previous studies of e.g. DeMott et al. (2010) and Conen et al. (2015) a strong correlation of INPs measured at around $-30\,°C$ to the particle concentration of particles larger than 0.5 µm in diameter was found. Other studies such as Schneider et al. (2021b) found positive correlations between the INP concentration and the ambient air temperature. Similar to the findings in Brunner et al. (2021), no strong correlation between the INP concentration at a temperature of about $-22\,°C$ and the selected variables was observed. In week 1 and week 7 of the campaign it seems that there is a slightly enhanced positive (R = 0.49 and 0.66 respectively) correlation with the ambient air temperature and negative (R = -0.66 and -0.63 respectively)

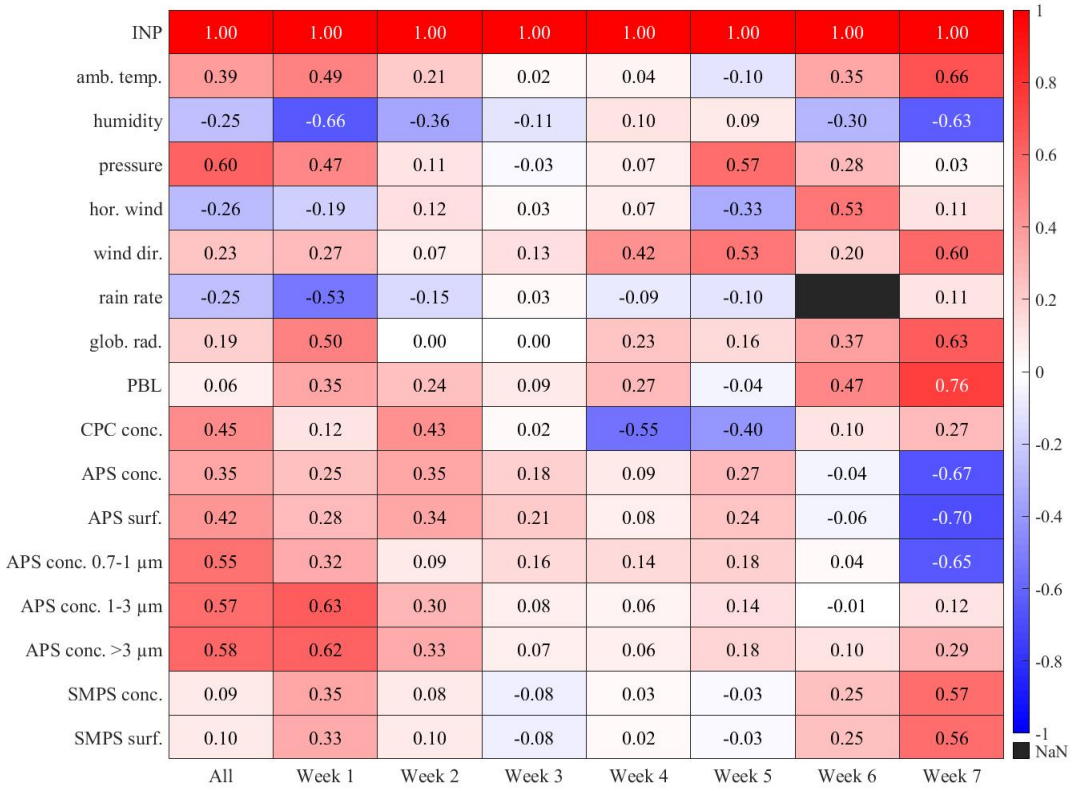

Figure 5.6.: Heatmap of the correlation between the INP concentration and several meteorological variables, the aerosol concentration measured with the CPC, SMPS and APS and the aerosol surface area concentration measured with the SMPS and APS. The correlation is given as the Spearman correlation coefficient and is calculated for the whole Kosetice21 campaign period and on a weekly basis.

correlation with the relative humidity. However, the data sets considered for these weeks are shorter, because the PINE measurements did not cover the full week. Therefore, only a few days in which the INP concentration follows the trend of e.g. the ambient air temperature are sufficient to increase the correlation coefficient. Of particular interest is week 3, in which non of the 16 chosen variables seemed to correlate with the measured INP concentration and all correlation coefficients are between -0.11 and 0.21. The correlation heatmap leads to the conclusion, that non of the considered meteorological variables and measured aerosol concentrations in different size ranges can explain the variation in the INP concentration, such that other factors like aerosol composition or an interplay of the investigated variables may play a more important role in this particular location and time.

A similar variation in the INP concentration as during Kosetice21 was observed in the Swabian21 campaign (black line in figure 5.7), where values between $0.5\,\mathrm{L}^{-1}$ and $300\,\mathrm{L}^{-1}$ were measured, with a few single PINE expansions also reaching values of up to $800\,\mathrm{L}^{-1}$. In contrast to Kosetice21, a diurnal variation is observed throughout extended parts of the campaign period, with higher INP concentrations during

daytime and lower INP concentrations during the night. This diurnal variation is especially pronounced from June 07 to June 12 and August 28 to September 05. The two time periods between June 12 and June 30 and August 06 and August 25 are more characterized by short-term fluctuations in the INP concentration. Additionally, these periods showed comparably low INP concentrations over a longer time with multiple PINE expansions showing no or only one ice crystal. The n_s time series (red line in figure 5.7), followed the trend in the INP concentration throughout the whole campaign and thus also showed a diurnal variation most of the time.

A diurnal variation gives the impression that the INP concentration is potentially correlated with diurnally changing variables such as the ambient air temperature, humidity, global radiation and the planetary boundary layer height (PBL). As for the Kosetice21 campaign, the Spearman correlation coefficient was calculated on a weekly basis (figure 5.8). It revealed that the ambient air temperature has in most of the weeks a positive correlation with a coefficient between 0.38 and 0.81 and the humidity a negative correlation with coefficients in a similar range. Only in weeks 4, 7 and 10 there was no clear correlation between the INP concentration and temperature and humidity, which is also reflected in the INP concentration where no diurnal variation was measured. Both, the global radiation and PBL, also show a positive correlation with the INP concentration in weeks with a more pronounced diurnal cycle with correlation coefficients in a range between about 0.3 and 0.74. All other meteorological variables and aerosol concentrations in different size ranges do not give a further hint on possible factors that influence the variation in the INP concentration. With the diurnal cycle in the ambient air temperature with higher temperatures during the day time, the biological activity of plants gets activated which may lead to an increase in aerosol emissions from such sources and thus also an increase in the measured INP concentration.

Both, the Kosetice21 and Swabian21 campaign were conducted during spring and summer in a rural environment. In contrast to that, CALISHTO21 took place in autumn at a mountain station with changing influence of aerosol from the boundary layer and the free troposphere. The difference in the sampling location is also reflected in the measured INP concentration which ranged from about $0.1\,\mathrm{L}^{-1}$ to about $500\,\mathrm{L}^{-1}$. On some days in mid and late November no or only one ice crystal was counted over long time periods, seen as a less dense signal of single expansion data (figure 5.9). The overall trend of the INP concentration is characterized by short-term changes within a few hours and periods of higher and lower INP concentrations. The first days of the campaign showed low INP concentrations with values of maximum $10\,\mathrm{L}^{-1}$, which was then followed by 5 days of INP concentrations between $5\,\mathrm{L}^{-1}$ and $100\,\mathrm{L}^{-1}$. Beginning of November, the highest INP concentrations over several days occurred, which was related to a potential dust event, where dust particles from the Sahara were transported to the station. On some days a temperature ramp was performed, which reflected the highly variable INP concentration in all measured temperatures.

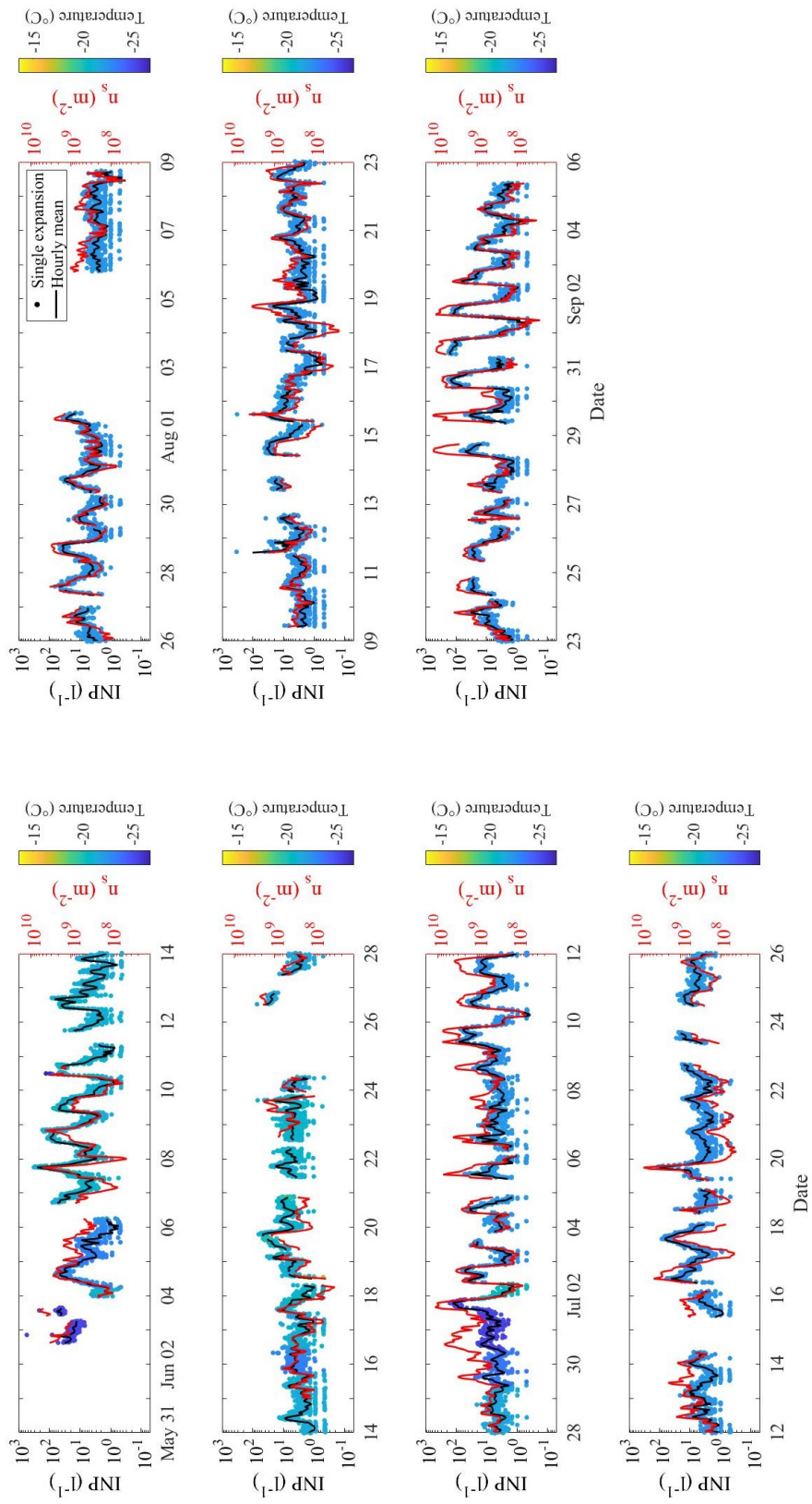

Figure 5.7.: Time series of the measured INP concentration of PINE during the Swabian21 campaign. The color coded dots show the INP concentration from the single PINE expansions and the black line is the hourly average. The red line presents the calculated n_s.

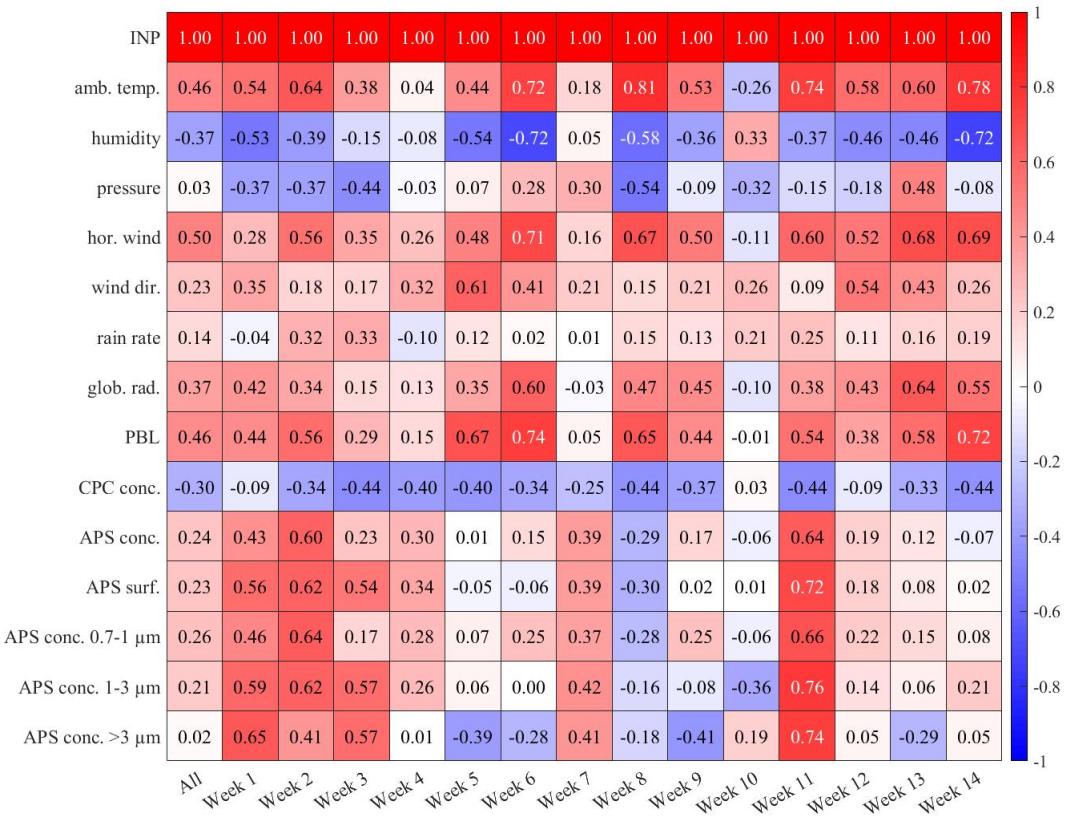

Figure 5.8.: Heatmap of the correlation between the INP concentration and several meteorological variables, the aerosol concentration measured with the CPC and APS and the aerosol surface area concentration measured with the APS. The correlation is given as the Spearman correlation coefficient and is calculated for the whole Swabian21 campaign period and on a weekly basis.

Due to the lack of available data, no correlations could be calculated for CALISHTO21, but since the location is quite sensitive to changes in the air mass origin and thus the origin of the aerosol, a stronger positive correlation to the wind direction would be expected.

All three campaigns showed the measured INP concentration with a time resolution of about 6 min over several weeks of continuous sampling and measured INP concentrations were between about $0.1\,\mathrm{L}^{-1}$ and $500\,\mathrm{L}^{-1}$, with some peaks with even higher INP concentrations. While the Swabian21 campaign revealed a diurnal variation of the INP concentration most of the time, the other campaigns showed more short-term changes in the INP concentration within several hours. For Kosetice21, non of the selected variables was identified to contribute to the INP variation, whereas in time periods during Swabian21 with a diurnal variation enhanced positive correlation coefficients for the ambient air temperature, global radiation and PBL and enhanced negative correlations for the humidity were observed. For the other time periods, with a more variable INP concentration, no unambiguous correlation with one or more variables was identified.

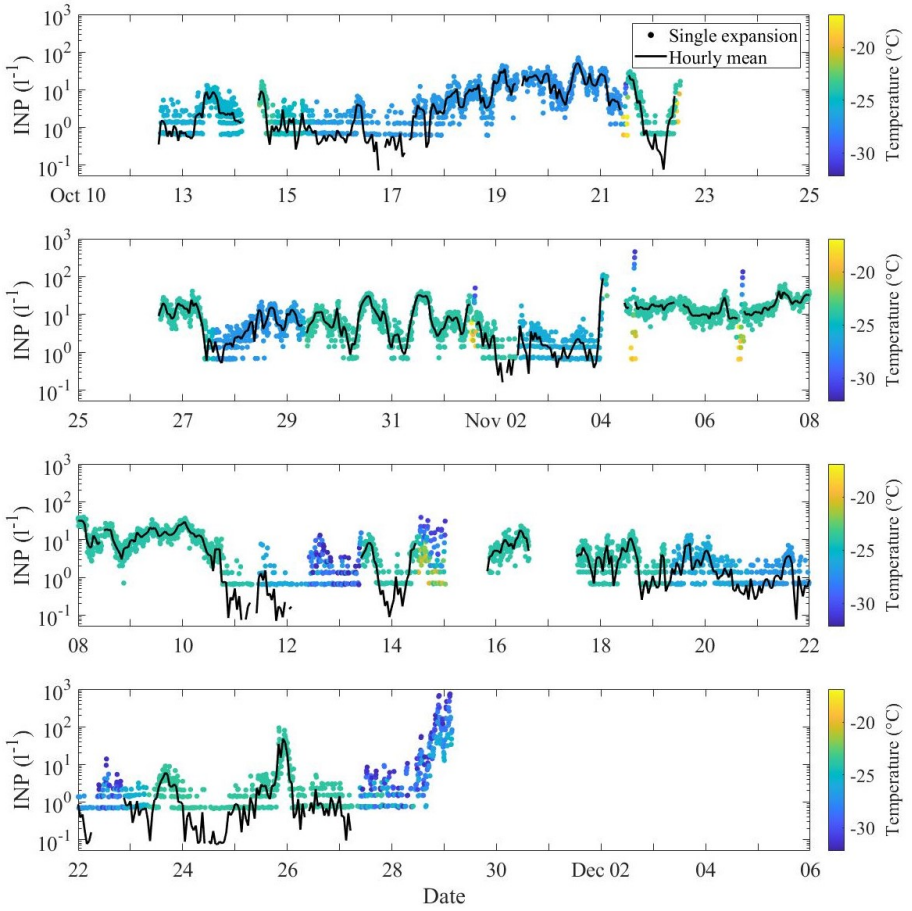

Figure 5.9.: Time series of the measured INP concentration of PINE during the CALISHTO21 campaign. The color coded dots show the INP concentration from the single PINE expansions and the black line is the hourly average. When PINE performed a temperature ramp, shown as scans through a wider temperature range, no average is calculated.

5.3.2. Prediction of the INP Concentration with Parameterizations

Relation to Existing Parameterizations

A key point in improving climate and weather prediction models is to better understand the ice formation in the atmosphere and the contribution of aerosol particles emitted from various sources. For this reason, several studies developed parameterizations to predict the INP concentration for different locations and aerosol types. In DeMott et al. (2010) (hereafter DeMott_10), an INP parameterization for for global aerosol at mixed-phase cloud conditions at temperatures lower than $-15\,^{\circ}\mathrm{C}$ was presented on the basis of 9 ground based and airborne field INP measurement campaigns. In Tobo et al. (2013) (hereafter Tobo_13) the DeMott_10 parameterization was modified considering measurements at temperatures higher than $-20\,^{\circ}\mathrm{C}$ and INP concentrations lower than $1\,\mathrm{L}^{-1}$ and of mainly biological origin. The parametrization of Tobo et al. (2013) was fitted by DeMott et al. (2015) (hereafter DeMott_15) using a comprehensive dataset of mainly laboratory measurements with dust aerosol. DeMott_10, Tobo _13 and DeMott_15 all assumed a dependence of the INP concentration on the freezing temperature and aerosol particles

Table 5.2.: Overview of the INP parameterizations from DeMott et al. (2010), Tobo et al. (2013), DeMott et al. (2015) and Schneider et al. (2021b), giving the name as it is referred to in the text, the equation, the fit parameters and the valid temperature range. In the equations, $n_{\text{aero},0.5}$ gives the aerosol number concentration of particles with a diameter larger than 0.5 µm, T_{f} the freezing temperature and T_{amb} the ambient air temperature.

Name	Equation	Fit parameters	Temp. range
DeMott_10	$c_{\text{INP,predicted}} = a(273.16 - T_{\text{f}})^{b}(n_{\text{aero},0.5})^{(c(273.16-T_{\text{f}})+d)}$	$a = 0.0000594$, $b = 3.33$, $c = 0.0264$, $d = 0.0033$	$-15\,^{\circ}\text{C}$ to $-35\,^{\circ}\text{C}$
Tobo_13	$c_{\text{INP,predicted}} = (n_{\text{aero},0.5})^{(a(273.16-T_{\text{f}})+b)} exp(c(273.16 - T_{\text{f}}) + d)$	$a = -0.074$, $b = 3.8$, $c = 0.414$, $d = -9.671$	$-5\,^{\circ}\text{C}$ to $-35\,^{\circ}\text{C}$
DeMott_15	$c_{\text{INP,predicted}} = (cf)(n_{\text{aero},0.5})^{(a(273.16-T_{\text{f}})+b)} exp(c(273.16 - T_{\text{f}}) + d)$	$a = 0$, $b = 1.25$, $c = 0.46$, $d = -11.6$, $cf = 1$	$-21\,^{\circ}\text{C}$ to $-35\,^{\circ}\text{C}$
Schneider_21	$c_{\text{INP,predicted}} = 0.1 \cdot exp(a1 \cdot T_{\text{amb}} + a2) \cdot exp(b1 \cdot T_{\text{f}} + b2)$	$a1 = 0.074$, $a2 = -18$, $b1 = -0.504$, $b2 = 127$	$-5\,^{\circ}\text{C}$ to $-25\,^{\circ}\text{C}$

with a diameter larger than 0.5 µm. Another approach is presented by Schneider et al. (2021b) (hereafter Schneider_21), where an INP parameterization for boreal environments was developed, which considered the INP concentration to be related to the freezing temperature and the ambient air temperature. All paramterizations including the fit parameters and the valid temperature range are given in table 5.2.

The four parameterizations (DeMott_10, Tobo_13, DeMott_15 and Schneider_21) were applied on the INP data of this work to compare the observed INP concentration ($c_{\text{INP,observed}}$) to the predicted INP concentration ($c_{\text{INP,predicted}}$). Hereby, the Kosetice21, Swabian21 and CORONA campaign are combined in one plot (figure 5.10), because the sampling sites were all in rural places in central Europe and thus the aerosol origin is assumed to be similar. Moreover, figure 5.4 showed a similar trend and range of the measured INP concentrations. Only the CALISHTO21 campaign (figure 5.12) is considered separately due to the different sampling location and thus likely a different influence of air masses. In order to give an estimate on how well the different parameterizations represent the measured INP concentration, 5 temperatures ($-8\,^{\circ}\text{C}$, $-12\,^{\circ}\text{C}$, $-16\,^{\circ}\text{C}$, $-20\,^{\circ}\text{C}$ and $-24\,^{\circ}\text{C}$) were picked and the percentage of represented data points within a factor x from the 1:1 line was calculated for $2 \leq$ factor x ≤ 20 (figure 5.11 and 5.13). The combination of all rural campaigns showed that 80 % or more of the measurements at $-20\,^{\circ}\text{C}$ and $-24\,^{\circ}\text{C}$ were represented within a factor of 10 or less by the DeMott_10, DeMott_15 and Schneider_21

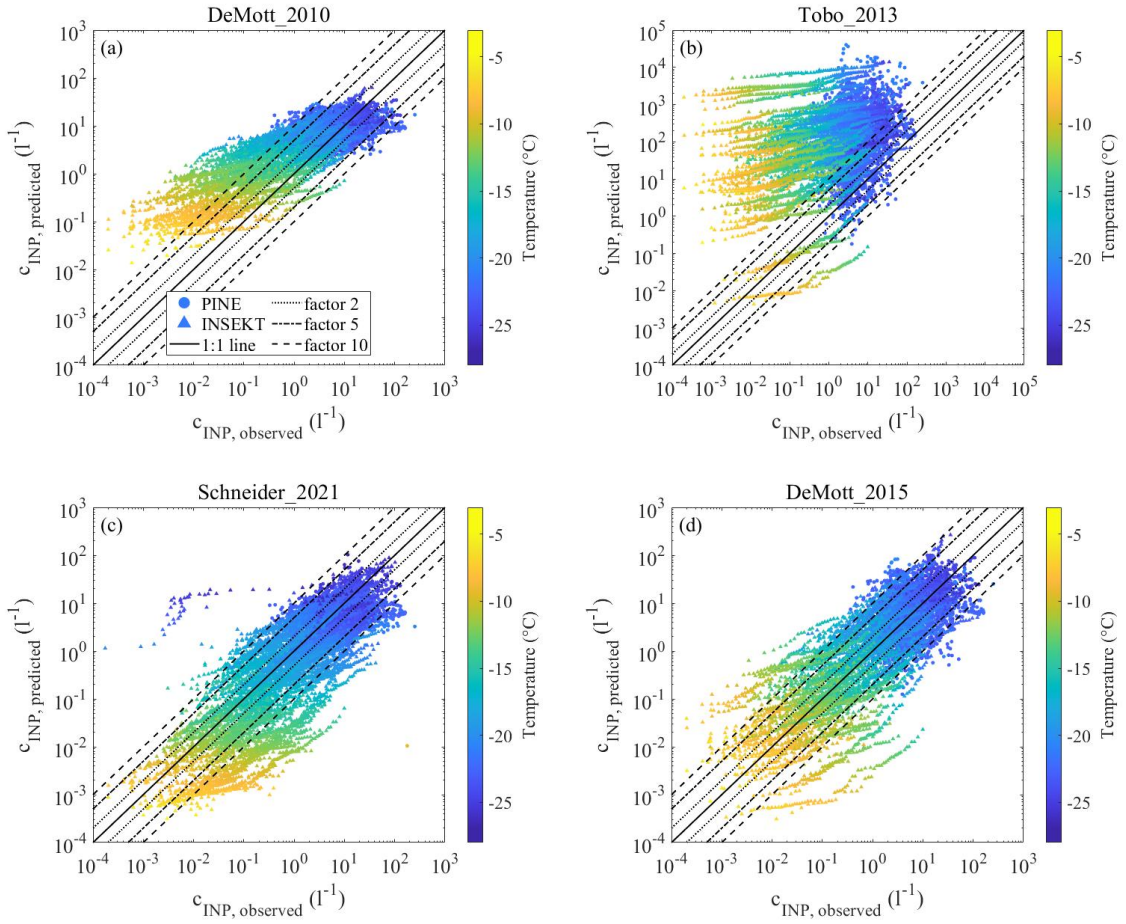

Figure 5.10.: The observed INP concentration ($c_{\mathrm{INP,observed}}$) of the Kosetice21, Swabian21 and CORONA campaign is compared against the predicted INP concentration ($c_{\mathrm{INP,predicted}}$) using four different parameterizations from DeMott et al. (2010), Tobo et al. (2013), Schneider et al. (2021b) and DeMott et al. (2015) (panel (a) to (d), respectively). The data points include both, PINE (dots) and INSEKT (triangles) measurements to cover a broad temperature range. The dotted, dashed-dotted and dashed line represent a deviation from the 1:1 line (solid line) of a factor of 2, 5 and 10, respectively.

parameterization. For the higher temperatures of −16 °C, −12 °C and −8 °C the representation of these parameterizations decreased, such that within a factor of 10 only 50 % of the data are represented with DeMott_10, and between 60 % and 80 % are represented with DeMott_15 and Schneider_21. The low representation for high nucleation temperatures with the DeMott_10 parameterization could be explained by the fact that it was developed using measurements below −15 °C, while DeMott_15 and Schneider_21 were extended for higher temperatures. DeMott_15 and Schneider_21 generally represent the trend in the measured INP concentration, but show a higher scatter around the 1:1 line. Schneider_21 tends to underestimate the INP concentration, giving a hint that the aerosol particles present in the rural environments were more active than the ones sampled in the boreal environment. The only parameterization that overestimated the measured INP concentration by up to 5 orders of magnitude was Tobo_13, which is

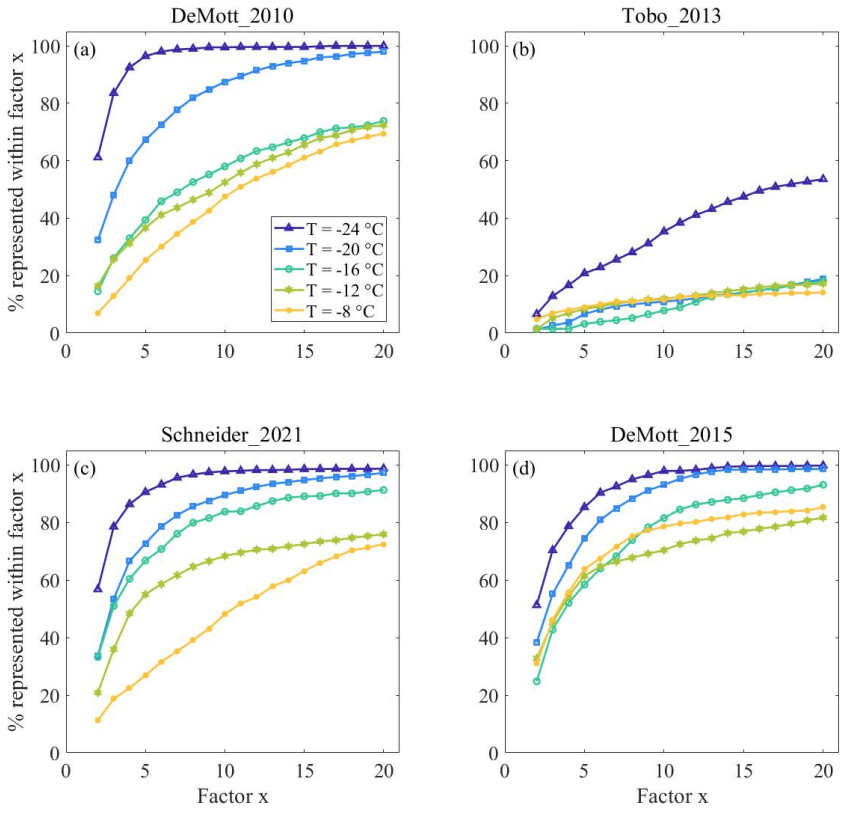

Figure 5.11.: Fraction in % of the INP concentration from Kosetice21, Swabian21 and CORONA, which is represented within a certain factor x by the predicted INP concentration of the parameterizations from DeMott et al. (2010), Tobo et al. (2013), Schneider et al. (2021b) and DeMott et al. (2015) (panel (a) to (d), respectively). These calculations are made for the temperatures −24 °C, −20 °C, −16 °C, −12 °C and −8 °C.

made for biological particles and clearly proofs that the measured aerosol particles were not primarily of biological origin.

The prediction of the INP concentration for CALISHTO21 showed for DeMott_10 a similar trend as for the rural INPs, where 90 % of the INPs measured at a temperature of −24 °C were represented within a factor of 10. The representation of the measured INP concentration decreased with an increasing nucleation temperature, such that only about 30 % or less of the measured INPs were represented within a factor of 10 for a nucleation temperature of −12 °C or higher. DeMott_15 generally represented the trend in the measured INP concentration, but the data is scattered around the 1:1 line, such that within a factor of 10 between 60 % and 90 % of the data are represented. Hereby, it does not tend that the representation decreased with an increasing nucleation temperature. The only parameterizaion with an increased representation of INP data for the mountain site compared to the rural sites is Tobo_13. It still overestimated the INP concentration, but compared to the rural aerosol by only 2 to 3 orders of magnitude.

The four field campaigns Kosetice21, Swabian21, CALISHTO21 and CORONA provide a very comprehensive data set of field INP measurements over long time periods of several weeks or months with a

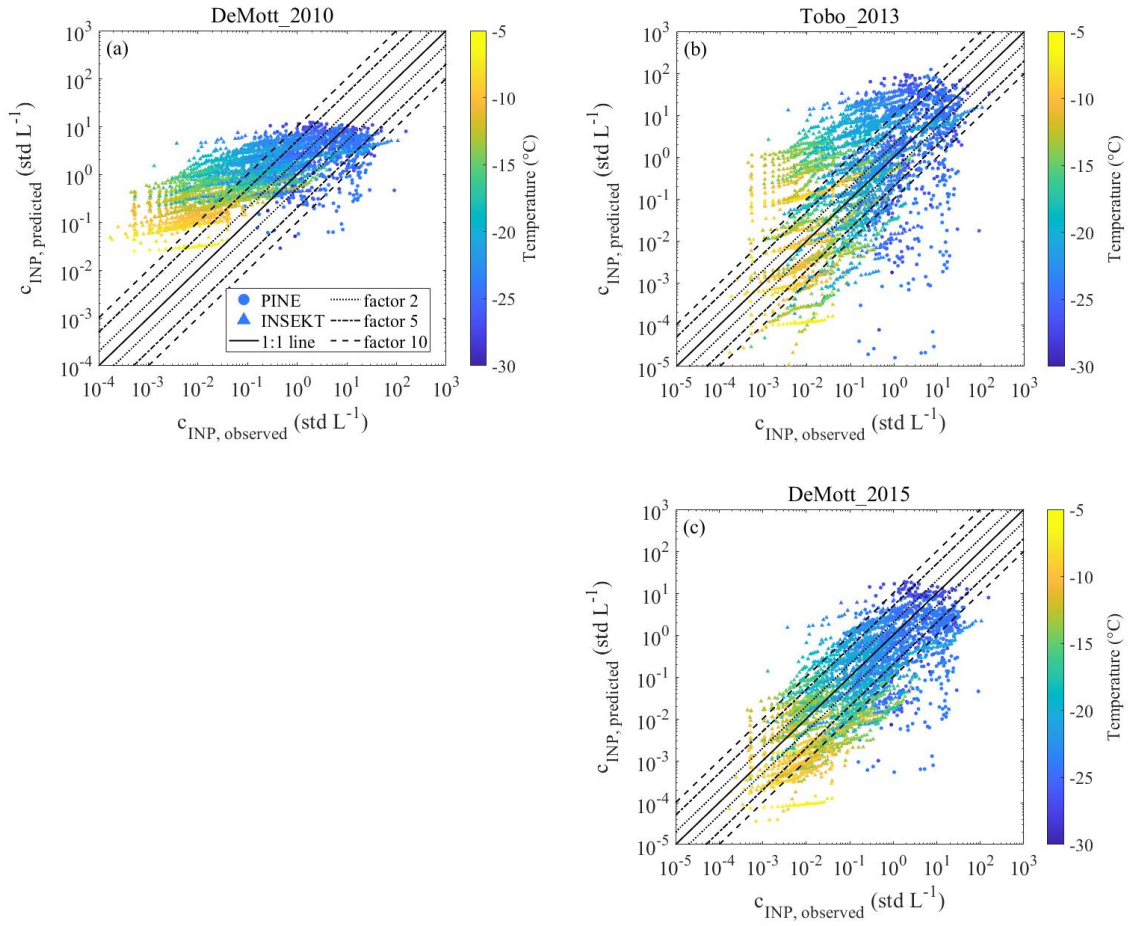

Figure 5.12.: The observed INP concentration ($c_{\mathrm{INP,observed}}$) of the CALISHTO21 campaign is compared against the predicted INP concentration ($c_{\mathrm{INP,predicted}}$) using three different parameterizations from DeMott et al. (2010), Tobo et al. (2013) and DeMott et al. (2015) (panel (a) to (c), respectively). The data points include both, PINE (dots) and INSEKT (triangles) measurements to cover a broad temperature range. The dotted, dashed-dotted and dashed line represent a deviation from the 1:1 line (solid line) of a factor of 2, 5 and 10, respectively.

time resolution between 6 min for PINE measurements and 4 h to 2 d for INSEKT measurements in a broad temperature range between −5 °C and −28 °C. Compared to the data sets that were used to develop the DeMott_10, Tobo_13 and DeMott_15 parameterization, the studies in this thesis are based on much more data points. Schneider_21 used a one year data record of INP measurements in the boreal forest with a time resolution of 1 to 3 days, but data at temperatures lower than −25 °C were not available due to the operation principle of INSEKT. Generally, the representation of the data sets from this work is still in a reasonable range, but in order to further improve the prediction of INPs in models, an improved parameterization is needed.

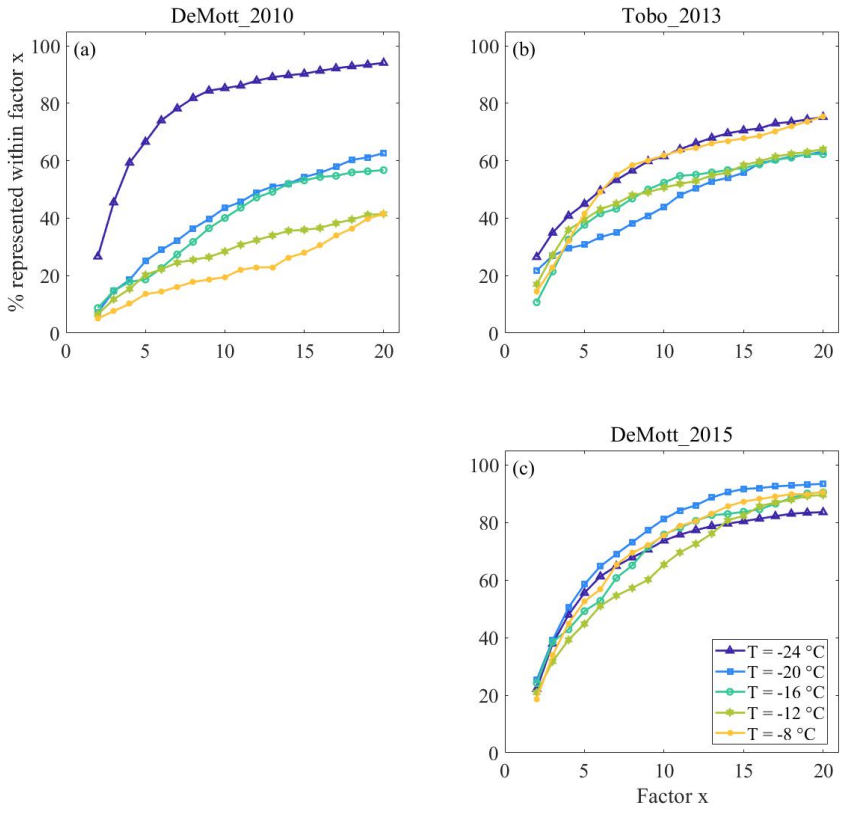

Figure 5.13.: Fraction in % of the INP concentration from CALISHTO21, which is represented within a certain factor x by the predicted INP concentration of the parameterizations from DeMott et al. (2010), Tobo et al. (2013) and DeMott et al. (2015) (panel (a) to (c), respectively). These calculations are made for the temperatures −24 °C, −20 °C, −16 °C, −12 °C and −8 °C.

Development of an Updated Parameterization for the INP Concentration

Even though DeMott_10 overestimated the INP concentration at temperatures higher than −16 °C by up to 3 orders of magnitude, it is the best approach because it was developed based on global INP measurements and thus considers aerosol particles from multiple sources. Regardless of the representation, DeMott_10 also showed the least scatter of the data. Therefore, the basic shape of the equation was used to fit new parameters for a parameterization for rural environments and higher temperatures. The new parameters are given as $a = 0.0000894$, $b = 2.8$, $c = 0.0894$ and $d = 0.9903$. Figure 5.14 presents the comparison of the DeMott_10 and DeMott_10 edit parameterization, where it can be seen that with the new fit parameters also the data points at nucleation temperatures higher than −16 °C are better represented. This is also reflected when calculating the representation for the selected temperatures of −24 °C, −20 °C, −16 °C, −12 °C and −8 °C, such that 80 % or more of data points are represented within a factor of 10. Also within a factor of 5, 60 % to 80 % of the data is still represented with the new parameterization.

The DeMott_10 parameterization was adapted for temperatures higher than −15 °C using a long-term record of INP measurements at three different rural sampling sites in central Europe during the spring

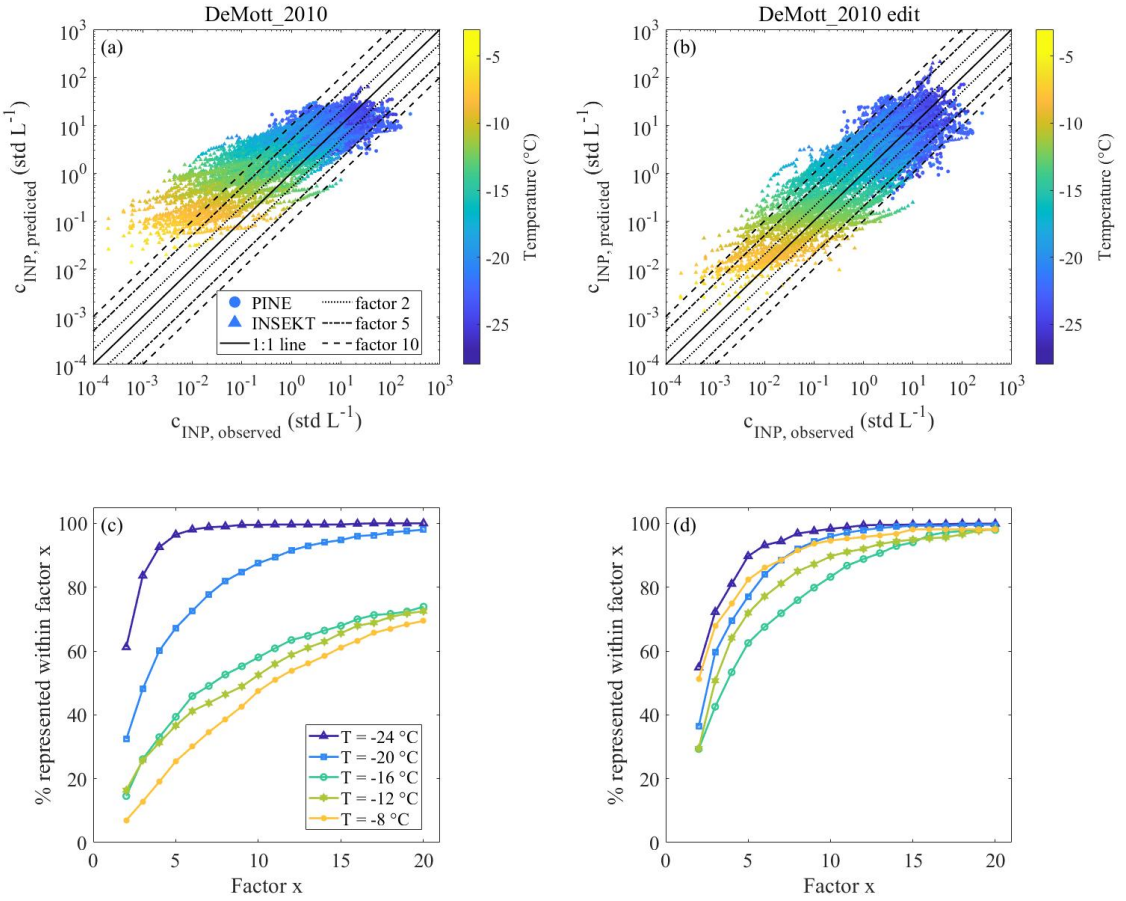

Figure 5.14.: Comparison of the DeMott_2010 edit against the original DeMott_2010 parameterization for the INP measurements from Kosetice21, Swabian21 and CORONA. Panel (a) and (b) compare the observed and the predicted INP concentration against each other and panel (c) and (d) show the fractional representation of the data within a certain factor x.

and summer season. Therefore, the edited DeMott_10 parameterization is potentially restricted for rural influenced environments and any seasonality cannot be excluded. The limitation of the new parameterization is shown when applying it on the data from CALISHTO21, where the representation of the INP concentration does not increase for all the selected temperatures (figure 5.15). To develop a solid parameterization for mountain sites that experience a changing influence of boundary layer and free tropospheric aerosol, a longer record of INP data is needed, which covers at least one whole annual cycle. Furthermore, variables like the humidity, accounting for free tropospheric and boundary layer conditions, may be more appropriate for predicting the INP concentration.

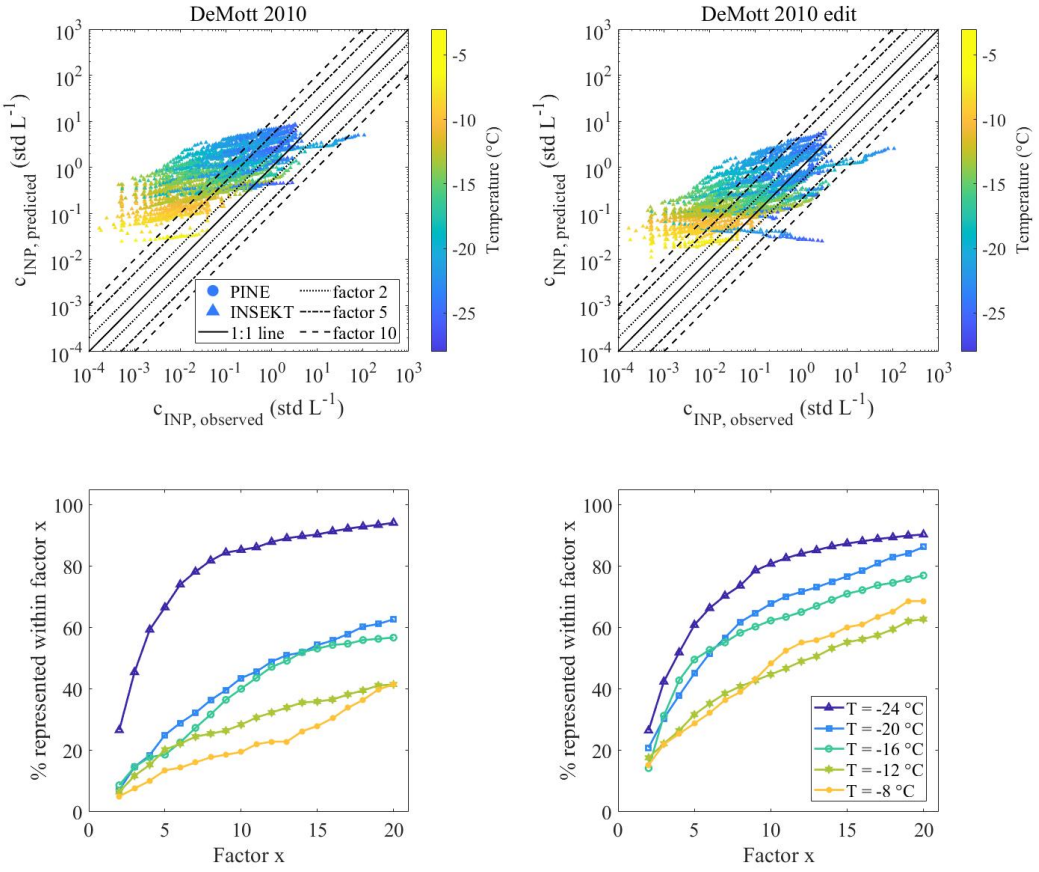

Figure 5.15.: Comparison of the DeMott_2010 edit against the original DeMott_2010 parameterization for the INP measurements from CALISHTO21. Panel (a) and (b) compare the observed and the predicted INP concentration against each other and panel (c) and (d) show the fractional representation of the data within a certain factor x.

5.3.3. Prediction of the INAS Density with Parameterizations

The INP concentration gives the number of ice crystals in an air volume, but is not related to any aerosol properties. For this reason, n_s can be calculated to normalize the ice number concentration to the aerosol surface area concentration, which is a common variable to describe the ice activity of an aerosol. Therefore, also n_s is predicted with parameterizations. Niemand et al. (2012) and Ullrich et al. (2017) (hereafter Niemand_12 and Ullrich_17) developed a parameterization for dust aerosol particles, where Niemand et al. (2012) used a cumulative approach and Ullrich et al. (2017) considered the largest particles to freeze first and thus only considered the aerosol surface area that was activated as ice in a certain time bin. Parameterizations of n_s for other aerosol sources were developed by Steinke et al. (2016) and Schneider et al. (2021b) (hereafter Steinke_16 and Schneider_21) for soil dust and boreal environments, respectively. Schneider et al. (2021b) also considered the seasonality of the aerosol such that a separate set of fit parameters is given for wintertime, summertime and the transition period. A summary of the n_s parameterizations is given in table 5.3 including the fit parameters and the valid temperature range.

Table 5.3.: Overview of the n_s parameterizations from Niemand et al. (2012), Steinke et al. (2016), Ullrich et al. (2017) and Schneider et al. (2021b), giving the name as it is referred to in the text, the equation, the fit parameters and the valid temperature range. In the equations, T_f is referred to the freezing temperature.

Name	Equation	Fit parameters	Temp. range
Niemand_2012	$n_{s,predicted} = exp(a \cdot (T_f - 273.15) + b)$	$a = -0.517$, $b = 8.934$	$-12\,°C$ to $-36\,°C$
Steinke_2016	$n_{s,predicted} = exp(a \cdot T_f + b)$	$a = -0.350$, $b = 110.266$	$-11\,°C$ to $-26\,°C$
Ullrich_2017	$n_{s,predicted} = exp(a \cdot T_f + b)$	$a = -0.517$, $b = 150.577$	$-14\,°C$ to $-30\,°C$
Schneider_2021	$n_{s,predicted} = exp(a \cdot T_f + b)$	$a = -0.543$, $b = 154$	$-5\,°C$ to $-25\,°C$

As for the INP parameterizations, the data sets of the Kosetice21, Swabian21 and CORONA campaign are presented and discussed together. Both, the Niemand et al. (2012) and Ullrich et al. (2017) parameterization, represent the trend of n_s throughout the investigated temperature range and 70 % or more of the data points are represented within a factor of 10 for the selected temperatures. When applying the Schneider_21 parameterization, the summertime parameter set was chosen, because the measurements are accounted to this season. Generally, this parameterization depicted the trend in n_s, but consistently underestimated the measured n_s by 2 to 3 orders of magnitude. This points to the fact that the INP population was not dominated by aerosol particles comparable the ones in a boreal forest environment and more ice active particles must have been present. Steinke_16 focused the parameterization on soil dust, which can have possible contributions to the rural aerosol sampled in the campaigns shown here. When applying the parameterization, it can be seen that it consistently overestimated the measured n_s by up to 3 order of magnitude for higher temperatures and up to 2 orders of magnitude for lower temperatures. This overestimation leads to the conclusion that the sampled aerosol had a lower ice activity as the soil dust probed in Steinke et al. (2016).

The n_s parameterizations were developed for certain aerosol types and point out that the aerosol present at the three sampling sites of Kosetice, Rottenburg and KIT Campus North had a similar ice activity as dust aerosol. In order to gain an insight into the present aerosol and INP population, measurements on the aerosol particle chemical composition with a similar time resolution as the INP measurements are required.

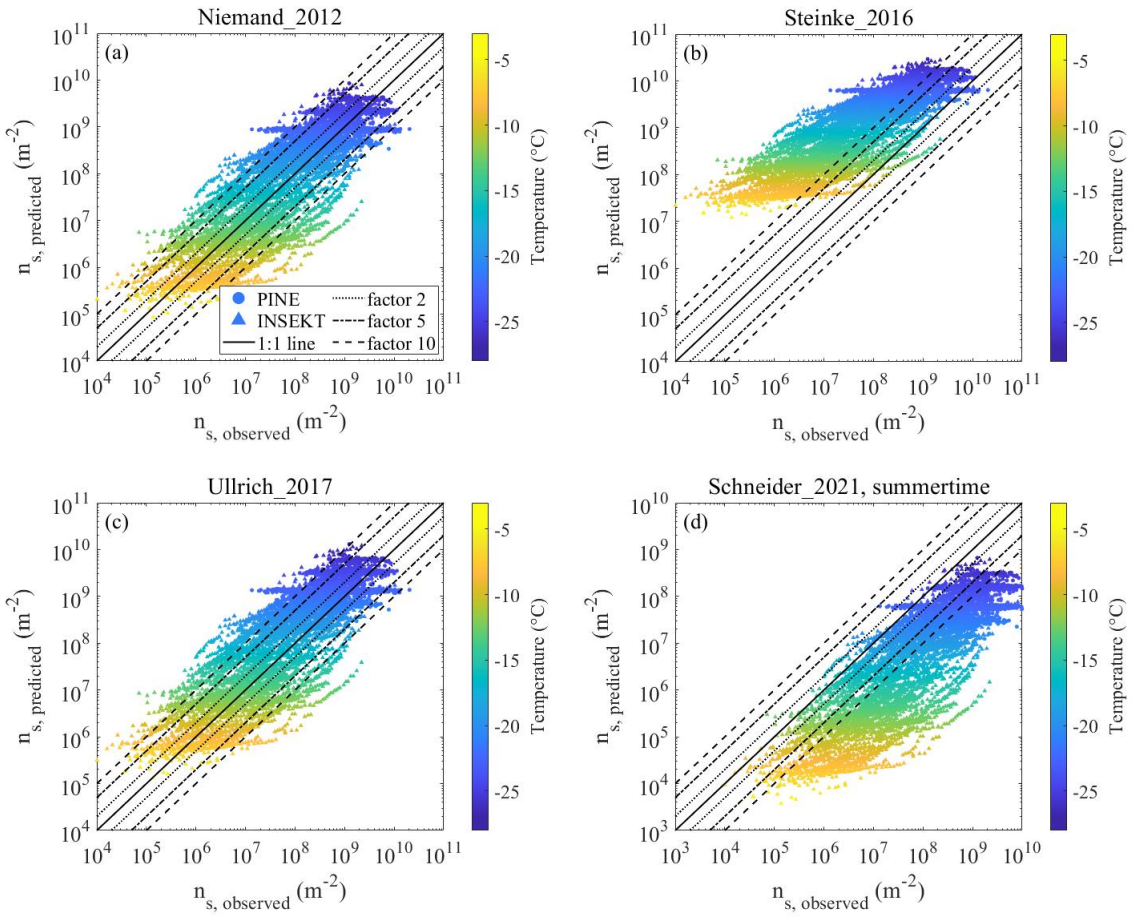

Figure 5.16.: The observed $n_{s,observed}$ of the Kosetice21, Swabian21 and CORONA campaign compared against the predicted $n_{s,predicted}$ using four different parameterizations from Niemand et al. (2012), Steinke et al. (2016), Ullrich et al. (2017) and Schneider et al. (2021b). The data points include both, PINE (dots) and INSEKT (triangles) measurements to cover a broad temperature range. The dotted, dashed-dotted and dashed line represent a deviation from the 1:1 line (solid line) of a factor of 2, 5 and 10, respectively.

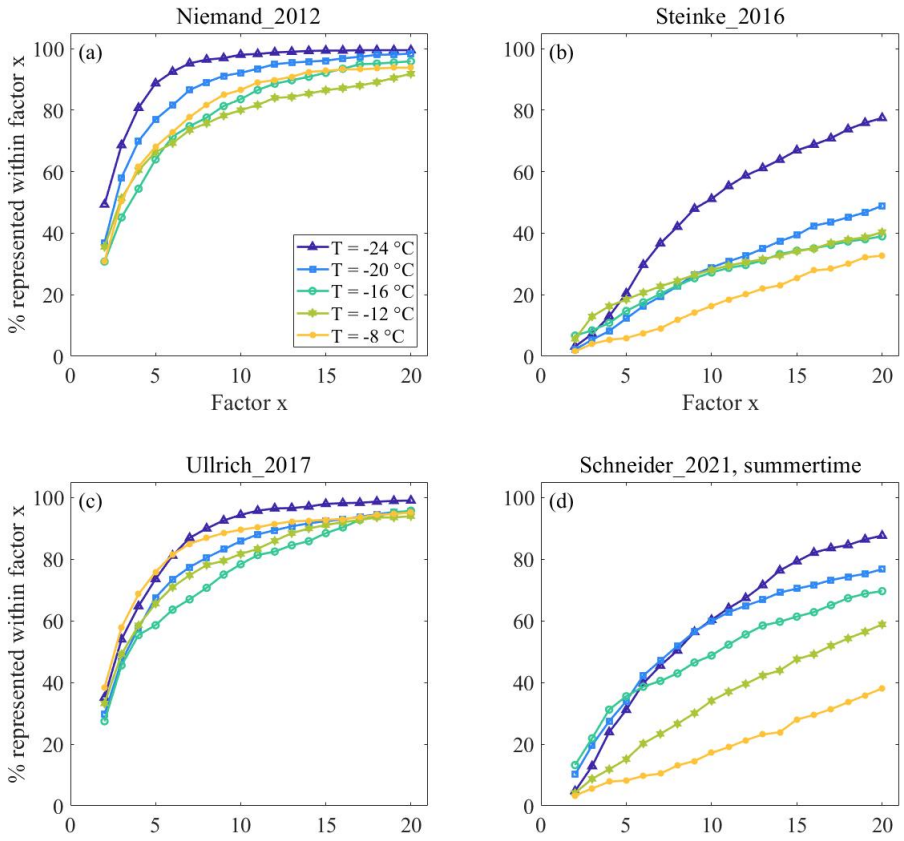

Figure 5.17.: Fraction in % of the measured n_s from Kosetice21, Swabian21 and CORONA, which is represented within a certain factor x by the predicted n_s of the parameterizations from Niemand et al. (2012), Steinke et al. (2016), Ullrich et al. (2017) and Schneider et al. (2021b). These calculations are made for the temperatures −24 °C, −20 °C, −16 °C, −12 °C and −8 °C.

5.4. Summary

In order to investigate the shot-term variation of atmospheric INP concentrations and by that further improve climate and weather models, it is of importance to provide long-term field measurements of INPs with a high time resolution at different locations. In this work, data of 3 field campaigns (Kosetice21, Swabian21 and CORONA) at rural sites in Kosetice (Czech Republic), Rottenburg (Germany) and KIT Campus North (Germany), respectively and one (CALISHTO21) at a mountain station on Mount Helmos (Greece) were conducted. Kosetice21, Swabian21 and CALISHTO21 provided continuous measurements with PINE with a time resolution of about 6 min over 7, 14 and 7 weeks, respectively. The time series of the INP concentrations showed that each campaign was characterized by changing periods of higher and lower INP concentrations. Only during the Swabian21 campaign a diurnal variation in the INP concentration was observed throughout most of the time. Kosetice21 and CALISHTO21 did not show a particular pattern, but changing INP concentrations with decreases or increases of 1 to 2 orders of magnitude within a few hours. The calculated times series of n_s for Kosetice21 and Swabian21 followed the trend of the INP concentration most of the time. For these two campaigns, correlations with meteorological variables and the aerosol concentration measured with different devices for different size ranges were calculated. In times of a diurnal cycle of the INP concentration, it correlated with the ambient air temperature, humidity, PBL and global radiation. For all other periods, which were characterized by short-term changes in the INP concentration, non of the selected variables were found to consistently correlate with the INP concentration, meaning that further investigations on the short-term variation need to be done. Such changes on a short time scale are likely triggered by local aerosol emissions, convection or ground level eddies.

To include INP measurements in models, parameterizations were developed to predict the INP concentration for different aerosol types and in different temperature regimes. An application of the most common paramterizations from DeMott et al. (2010); Tobo et al. (2013); DeMott et al. (2015) and Schneider et al. (2021b) to the data from this work showed that except Tobo_13, all parameterizations represented 80 % or more of the data within a factor of 10 for temperatures lower than $-20\,^{\circ}\mathrm{C}$. For higher temperatures, the representation generally decreased with the highest deviation for DeMott_10. However, DeMott_10 is seen as a representation of global INPs and represented the data from the rural environments in Kosetice, Rottenburg and KIT Campus North with the least scatter. Because of that, new parameters were fitted for an edited version of DeMott_10 to improve this parameterization especially for freezing temperatures higher than $-15\,^{\circ}\mathrm{C}$. With the new fit parameters, 80 % or more of the data points for all selected temperatures between $-8\,^{\circ}\mathrm{C}$ and $-24\,^{\circ}\mathrm{C}$ were represented within a factor 10. However, the new parameterization might be limited for rural areas and spring and summer season and extended measurements for a full annual cycle are suggested to proof this.

Another set of 4 parameterizations predicting n_s from Niemand et al. (2012), Steinke et al. (2016), Ullrich et al. (2017) and Schneider et al. (2021b) was applied to the combined data set of the Kosetice21,

Swabian21 and CORONA campaign. The paramterizations from Niemand et al. (2012) and Ullrich et al. (2017) were developed for dust aerosol and the ones from Steinke et al. (2016) and Schneider et al. (2021b) for soil dust and boreal environments, respectively. While the dust parameterizations predicted between 70 % and 90 % of the n_s values within a factor of 10, the one for boreal environments underestimated and the soil dust parameterization overestimated the measured n_s by 2 to 3 orders of magnitude. This gives a hint that the aerosol populations in Kosetice, Rottenburg and KIT Campus North were rather dust dominated or had a similar ice activity as dust aerosol.

The long-term measurements of INPs highlighted the need for field INP measurements with a high time resolution, because changes in the INP concentration of 1 to 2 orders of magnitude can occur within a few hours. Correlations of the INP concentration showed that there is not yet a solid explanation for such short-term changes and more measurements to quantify the origin are needed. When predicting the measured n_s values with existing paramterizations it was depicted that measurements of the chemical composition of the aerosol in combination with INP measurements are highly needed. This would give a better insight into the composition of ice active aerosol particles and therefore the aerosol origin. With the help of that our understanding of the strongest aerosol and INP sources can be improved, which then helps to better understand primary ice formation in mixed-phase clouds in the atmosphere and potentially changing conditions with ongoing climate change.

6. Size-Selective INP Measurements

6.1. Introduction

Atmospheric aerosol particles acting as INPs originate from various sources and the aerosol size can range from a few nanometer for newly formed particles up to several micrometer for e.g. dust aerosol (e.g. Lohmann et al., 2016). Over the past decades, laboratory and field studies were performed to quantify the ice activity of different aerosol species at mixed-phase cloud conditions at temperatures between 0 °C and −35 °C. Based on these measurements, parameterizations to predict the INP concentration were developed, where e.g. DeMott et al. (2010), Tobo et al. (2013) and DeMott et al. (2015) related the prediction on the number concentration of particles larger than 0.5 µm in diameter and the freezing temperature. A value for the ice nucleation ability of an aerosol is n_s, describing the amount of ice active sites per aerosol surface area. The n_s of a certain aerosol type strongly depends on the temperature, but is independent of the particle size, and therefore implies that the fraction of aerosols, which act as INPs at a certain temperature is increasing with the particle diameter or surface area.
Only a few laboratory and field studies investigated the difference in the total INP concentration and the INP concentration of selected size ranges. The field studies by Si et al. (2018) and Rinaldi et al. (2021) and the laboratory experiments by Mitts et al. (2021) were focused on coastal marine aerosol, arctic aerosol and supermicron and submicron sea spray aerosol, respectively, and generally found out that larger aerosol particles were more ice active than smaller aerosol particles. Especially the study by Mitts et al. (2021) on sea spray aerosol revealed a difference of 1 order of magnitude in the INP concentration and the calculated n_s and a shift of the freezing onset temperature by 3 °C to 4 °C towards lower temperatures for the submicron particles. Other laboratory studies by Welti et al. (2009), Lüönd et al. (2010), Welti et al. (2012) and Reicher et al. (2019) probed different mineral dust particles with diameters of 100 nm, 200 nm, 400 nm and 800 nm or dust aerosol particles of different sizes. As for the marine and sea spray aerosol, it was observed that with an increasing aerosol diameter also the ice activity of the aerosol increased. Three comprehensive field studies by Mason et al. (2016), Porter et al. (2020) and Córdoba et al. (2021) presented size selective filter measurements from different arctic, boreal and continental or rural sites in North America, Europe and tropical regions that are influenced by biomass burning aerosol, marine aerosol and African dust. This included a large variety of probed aerosol populations and the observed behavior was complex. Mason et al. (2016) and Córdoba et al. (2021) both observed that supermicron aerosol particles contributed with the highest fraction to the total measured INP concentration. But Porter

et al. (2020) also showed cases in which all aerosol particles were equally ice active or where smaller aerosol particles showed higher INP concentrations and n_s values than larger particles.
Because size selective INP measurements in both, the laboratory and the field are still rare, and the contribution of various aerosol species of different sizes is still not yet well understood, such measurements should be more included in future work. Therefore, it is not only of importance to study the temperature dependent freezing of aerosol of different sizes with filter measurements, but also the size dependent variation on a short time scale with instruments such as PINE.
Thus, size-selective INP measurements with PINE were performed for the first time in this work. This chapter presents the basic working principle and the characterization of the size-selective sampling methods together with the results from the laboratory and field measurements.

6.2. Methods

6.2.1. Aerosol Impaction

In order to select aerosol particles of a certain size, several principles based on the aerosol properties can be used. One commonly used method makes use of the particles' inertia, where the aerosol particles are selected depending on their aerodynamic diameter. Detailed descriptions on the theory and working principle can be found in e.g. Pruppacher and Klett (2010), Kulkarni (2011) and Hinds (2012), but a short introduction is given in the following part. In principle, an accelerated aerosol flow containing particles with diameters of the full size distribution is directed from its initial trajectory on a new trajectory. Particles with a too high inertia are not able to follow the streamlines and can escape the aerosol sample flow. Depending on the impactor type, the particles get impacted on a surface or leave the sample flow in a side flow. In case the particles' inertia is low enough, the particles are able to follow the streamlines and remain in the sample flow to be analyzed. The basic principle of aerosol impaction is described by the dimensionless Stokes number Stk, which encounters the stopping distance of a particle. In the calculation of Stk (equation 6.1) it is shown, that the particle diameter d and the velocity of the gas flow U are two important parameters. Depending on whether the aerosol is impacted on a body or accelerated in a nozzle, the third key parameter is the size of the impactor body or the impactor nozzle diameter D. Otherwise the Stokes number is described by the particle density ρ, the gas viscosity η and the Cunningham correction factor C_c, accounting for the velocity at the particle surface being larger than zero.

$$Stk = \frac{\rho C_c d^2 U}{9\eta D} \tag{6.1}$$

Impactors are characterized by a cutoff diameter d_{50}, describing the diameter at which at least 50 % of the particles with a diameter larger than d_{50} are removed from the size distribution. To give a first order estimate for d_{50}, the square root of the Stokes number at d_{50} can be taken. Since this is not known in most of the cases, an empirical approximation for d_{50} is given as

$$d_{50} = d_{50}\sqrt{C_c} - 0.078 = \frac{0.078}{-1+\sqrt{C_c}} \quad . \tag{6.2}$$

Note that this approximation is only valid for particles with a diameter larger than 0.2 µm and for a pressure in the nozzle that does not drop below 900 mbar.

There are four different impactor types making use of inertial impaction, namely body impactors, cascade or nozzle impactors, virtual impactors and cyclone impactors. To perform the size selected INP measurements in this work, one cascade impactor for filter sampling for INSEKT analysis and two cyclone impactors for PINE measurements were used and thus the specific impactors are described in detail in the following part.

6.2.2. Cyclone Impactor

Inside a cyclone impactor, the total aerosol flow is guided on a spiral trajectory by the asymmetric inlet geometry and by letting it impinge on the inner wall of the cyclone body. The spiral stream is guided downwards the cyclone body until it turns direction, flows up along the inner cyclone axis and exits the cyclone (figure 6.1 left hand side). Particles with a too high inertia are impacted on the wall of the cyclone body and only particles with a diameter of less or equal d_{50} follow the air flow to the exit. To use the same cyclone impactor for different d_{50} cutoffs, the aerosol flow needs to be increased or decreased to shift the cutoff size towards lower or higher values, respectively. An increase of the aerosol flow leads to an

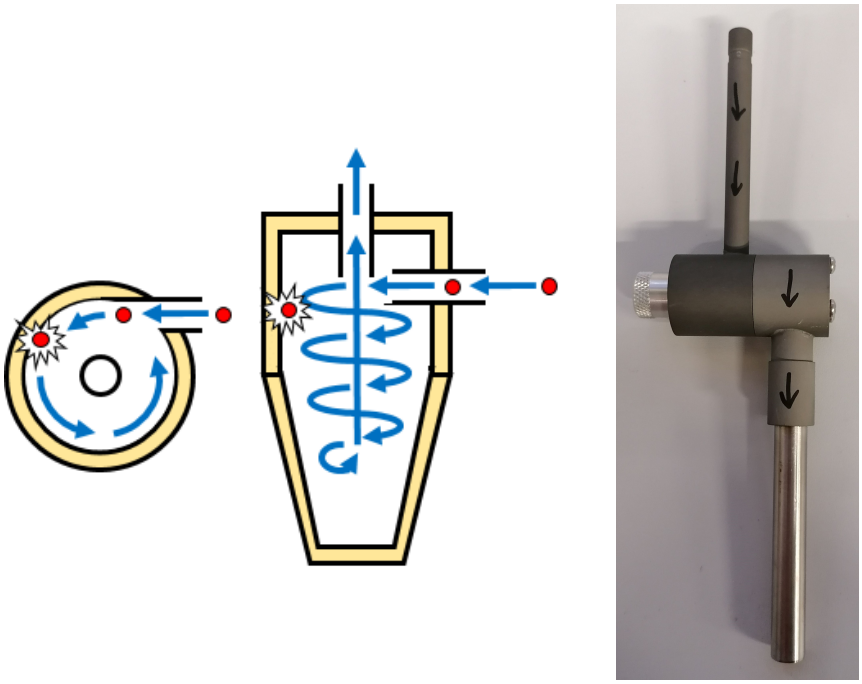

Figure 6.1.: The left hand figure shows a sketch of the general setup and working principle of a cyclone impactor; taken from Lindsley et al. (2017). The right hand side is a photo of the PM1 cyclone impactor that was used for the size-selective PINE measurements in this work.

increase in the centrifugal force and by that smaller particles deposit on the inner walls of the impactor. A decrease in the aerosol flow leads to the opposite behavior. Another way to change d_{50} would be to use a smaller or larger impactor body for a lower or higher d_{50}, respectively. A larger impactor body has a higher radius of curvature, leading to a decrease in the centrifugal force and thus also particles with a larger diameter can follow the aerosol flow out of the cyclone. A smaller impactor body induces the opposite effect.

To measure the difference in the total, PM2.5 and PM1 INP concentration with PINE, a PM2.5 (SCC 112, Met One Instruments^{TM}) and a PM1 cyclone impactor (SCC 111, Met One Instruments^{TM}) (figure 6.1 right hand side) were mounted upstream of the PINE chamber. Both impactors were manufactured to reach their d_{50} cutoff at a flow of $2\,\mathrm{L\,min^{-1}}$. Both impactors were verified regarding their d_{50} cutoff in the laboratory using the two different dust samples SDSA_01 and USD01. A dust concentration of about $200\,\mathrm{cm^{-3}}$ was injected into an aerosol vessel and the total aerosol size distribution and the aerosol size distribution behind the cyclone impactors were measured with a Frog OPC (Pallas GmbH). The OPC measures the optical diameter of the particles, but since the impaction of the cyclone is based on the aerodynamic diameter, it was transformed using equation 3.2 with a typical shape factor and particle density for dust of 1.2 and $2.6\,\mathrm{g\,cm^{-3}}$, respectively. The transmission efficiency curves for both dust samples in figure 6.2 proofed that the PM1 cyclone removed at least 50 % of the particles with a diameter larger than 1 µm. At a diameter of about 4 µm, the efficiency drops to 0 %, meaning that all particles larger than that got removed by the cyclone impactor. The measured d_{50} cutoff for the PM2.5 cyclone is between 3 µm and 3.5 µm, and by that slightly higher than what was given by the manufacturer. The efficiency of the PM2.5 cyclone drops to 0 % in the same diameter range as for the PM1 cyclone. However, it has to be noted that the uncertainty towards higher diameters increases, because the concentration of larger particles in the aerosol vessel was low.

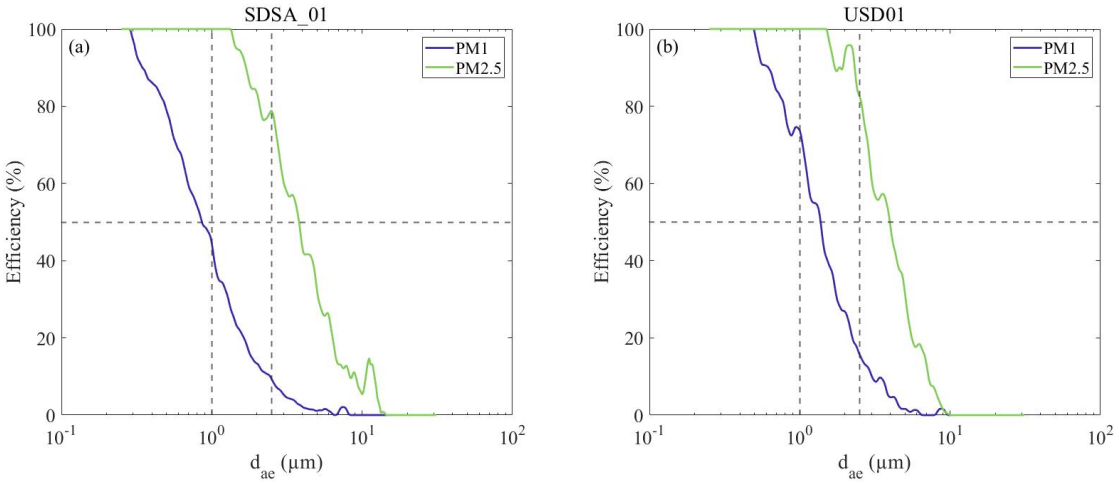

Figure 6.2.: Transmission efficiency for the PM1 (blue line) and PM2.5 (green line) cyclone impactor when sampling the dust aerosol SDSA_01 (panel (a)) and USD01 (panel (b)). The two dashed vertical lines indicate an aerodynamic diameter of 1 µm and 2.5 µm and the horizontal dashed line shows the 50 % transmission efficiency.

For the calculation of the aerosol surface area concentration needed for n_s in section 6.3 and 6.4, a perfect cutoff at 1 µm and 2.5 µm is assumed and all particles larger than these diameters are removed from the size distribution. For the PM1 cyclone impactor, it makes only a minor contribution to the uncertainty, which is dominated in general by the uncertainty in the size distribution measurement and the measurement of the INP concentration. However, for the PM2.5 cyclone impactor, where the d50 cutoff seems to be shifted by about 1 µm, the uncertainty can be increased by up to a factor of 2.

6.2.3. Cascade Impactor

Cyclone impactors were used for the PINE measurements, because they are operated at the same flow rate used for PINE. For the filter sampling for INSEKT analysis, a higher flow rate than for the PINE measurements is needed to collect a sufficient amount of aerosol particles and for this reason a cascade impactor optimized for a flow of $10\,\mathrm{L\,min^{-1}}$ with four different stages was used.
In general, a cascade impactor consists of one or more stages, where a nozzle with a certain diameter and below that an impaction plate makes one stage (figure 6.3, left side). With an increasing number of stages from top to bottom, the nozzle diameter decreases and thus the d_{50} cutoff decreases with each stage. Aerosol particles that are not able to follow the stream lines behind the nozzle settle down on the impaction plate. Depending on how the particles on the different impaction stages should be analyzed, a different collection method has to be used, which can a filter, aluminum foil or grease. A drawback of

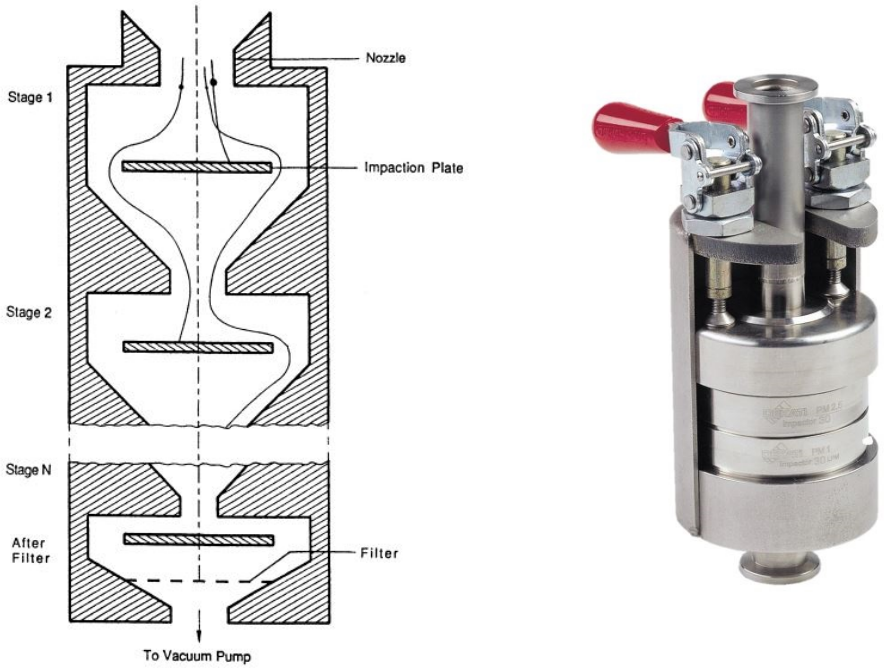

Figure 6.3.: The sketch on the left hand side shows the principle setup of a cascade impactor, taken from Kulkarni (2011). The right hand side is a photo of the cascade impactor (taken from Dekati (2019)) that was used in this work for the size selected filter sampling for INSEKT analysis.

collecting the particles on filters or aluminum foil is, that already collected particles can bounce off the plate and make it to the next stage.

The cascade impactor used in this work (PM10 Impactor, Dekati®) consists of four stages, where on the first stage particles larger than 10 µm in aerodynamic diameter, on the second stage particles between 2.5 µm and 10 µm, on the third stage particles between 1 µm and 2.5 µm and on the fourth stage all particles smaller than 1 µm are collected. Because the aerosol particles were analyzed regarding their ice-nucleation activity with INSEKT, they were collected on filters. Stage one, two and three carry filters of 25 mm in diameter and the fourth stage is made for a filters of 47 mm in diameter.

The collection efficiency of the cascade impactor was provided by the manufacturer in the manual (Dekati, 2019).

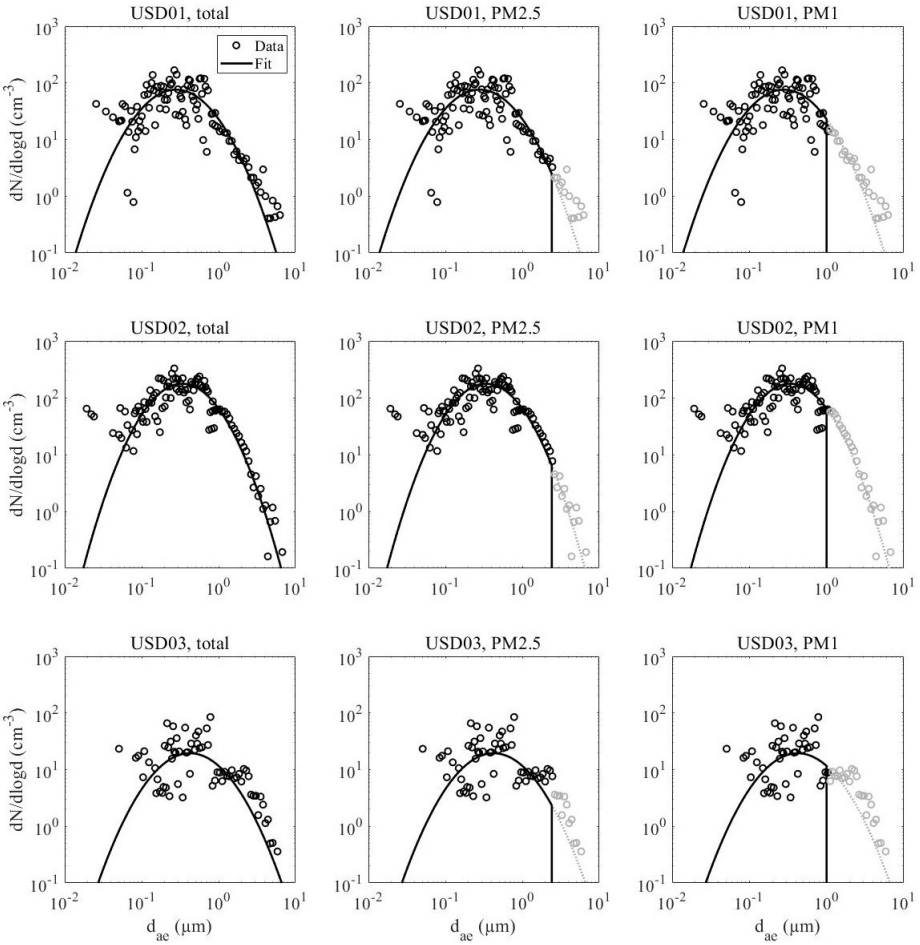

Figure 6.4.: Aerosol number size distribution of USD01, USD02 and USD03 before and behind the PM2.5 and PM1 cyclone impactor. The black data points and the black line indicate the part of the size distribution, that was used for the calculation of n_s. The gray points show the part of the size distribution, that was removed by the cyclone impactor.

6.3. Size Dependent Freezing of Dust Measured in the Laboratory

A first approach on measuring the change in the ice nucleation ability of aerosol when sampling INPs with PINE through a PM2.5 or PM1 cyclone impactor and for INSEKT analysis with the cascade impactor was done during the AIC02 campaign. AIC02 was conducted over three weeks in June and July 2021 at the AIDA cloud chamber facility using three dust samples from the US, namely USD01, USD02 and USD03. PINE was operated at temperatures between $-19\,°C$ and $-29\,°C$ and the INSEKT analysis provided INP data at temperatures between about $-8\,°C$ and $-25\,°C$ and thus extended to PINE measurements towards higher temperatures. The change in the aerosol size distribution considered for calculating n_s when using the cyclone impactors, is shown in the measurements in figure 6.4 and the change in the aerosol size distribution for the cascade impactor is shown in figure 6.5, where the black data points are those which remain in the aerosol flow after impaction and are analyzed. To obtain the size distribution for the different d_{50} cutoffs, the aerodynamic diameter was used. For the later calculation of the aerosol surface area concentration, both the SMPS and APS measurements were converted into the volume equivalent diameter following equation 3.1 and 3.2 with a dust typical density of $2.6\,g\,cm^{-3}$ and a shape factor of 1.2. Table 6.1 summarizes the aerosol surface area concentrations behind the cyclone impactors and on the several stages of the cascade impactor used to calculate n_s. The measurements shown in figure 6.6 are presented as temperature dependent n_s values.

All three dust samples show a steady increase in n_s over almost 5 orders of magnitude in the temperature range between about $-10\,°C$ and $-28\,°C$. A comparison of the PINE measurements of the total, the PM2.5 and the PM1 n_s using USD01 (figure 6.6 panel (b)) shows, that the total n_s has the highest values between $1 \times 10^8\,m^{-2}$ and $1 \times 10^{10}\,m^{-2}$ and the PM1 n_s has the lowest values between $5 \times 10^7\,m^{-2}$ and $6 \times 10^9\,m^{-2}$. The data of the PM2.5 n_s takes values in between. So aerosol particles with an aerodynamic diameter smaller than 1 µm had an about a factor of 2 lower ice activity than larger aerosol particles. The

Table 6.1.: Summary of the total aerosol concentration and the aerosol surface area concentration of the size-selective measurements performed during the AIC02 campaign. $c_{n,ae}$ and s_{ae} are the total aerosol number concentration and surface area concentration, respectively. $s_{ae,PM2.5}$ and $s_{ae,PM1}$ are the surface area concentrations of the aerosol measured behind the two cyclone impactors used for PINE. $s_{ae,PM1,PM2.5}$ and $s_{ae,PM2.5,PM10}$ are the aerosol surface area concentrations of the aerosol sampled on the cascade impactor stages for aerosol particles between 1 µm and 2.5 µm and between 2.5 µm and 10 µm in diameter. When a cell is empty it indicates that particles in this size range were not sampled.

Aerosol	$c_{n,ae}$ (cm^{-3})	s_{ae} ($\mu m^2\,cm^{-3}$)	$s_{ae,PM2.5}$ ($\mu m^2\,cm^{-3}$)	$s_{ae,PM1}$ ($\mu m^2\,cm^{-3}$)	$s_{ae,PM1,PM2.5}$ ($\mu m^2\,cm^{-3}$)	$s_{ae,PM2.5,PM10}$ ($\mu m^2\,cm^{-3}$)
USD01	200	81.4	-	22.3	-	-
USD01	100	31.6	21.9	9.7	9.8	15.5
USD02	250	60.6	-	50.6	-	-
USD02	200	64.5	52.7	23.4	33.9	13.6
USD03	17	24.3	15.9	2.6	10.6	12.4

data of the total n_s measured with INSEKT overlayed with the ones measured in PINE, but the PM1 n_s measured with INSEKT showed values in the same range as the total n_s. The two cascade impactor stages in between, sampling aerosol between 1 µm and 2.5 µm and between 2.5 µm and 10 µm in aerodynamic diameter, overlayed with each other and with the total and PM1 n_s (figure 6.6 panel (a)). When aerosol particles of all sizes carry the same concentration of ice active sites on their surface, they all have the same freezing probability. Because n_s is almost equal for all the selected size ranges for USD01, it can be concluded that particles in the whole diameter range are equally ice active and thus the size independent n_s approach is valid for this sample.

USD02 shows the same freezing behavior as USD01 for PINE and INSEKT measurements at temperatures lower than about −20 °C. For temperatures between −10 °C and −20 °C, USD02 aerosol particles with a diameter smaller than 1 µm and between 2.5 µm and 10 µm showed about a factor of 5 higher n_s values compared to the other size ranges (figure 6.6 panel (c) and (d)). Because this is the temperature range where aerosol particles of biological origin can be ice active, the filters sampled with the total aerosol population were analyzed with the heat treatment method to deactivate the heat sensitive aerosol particles.

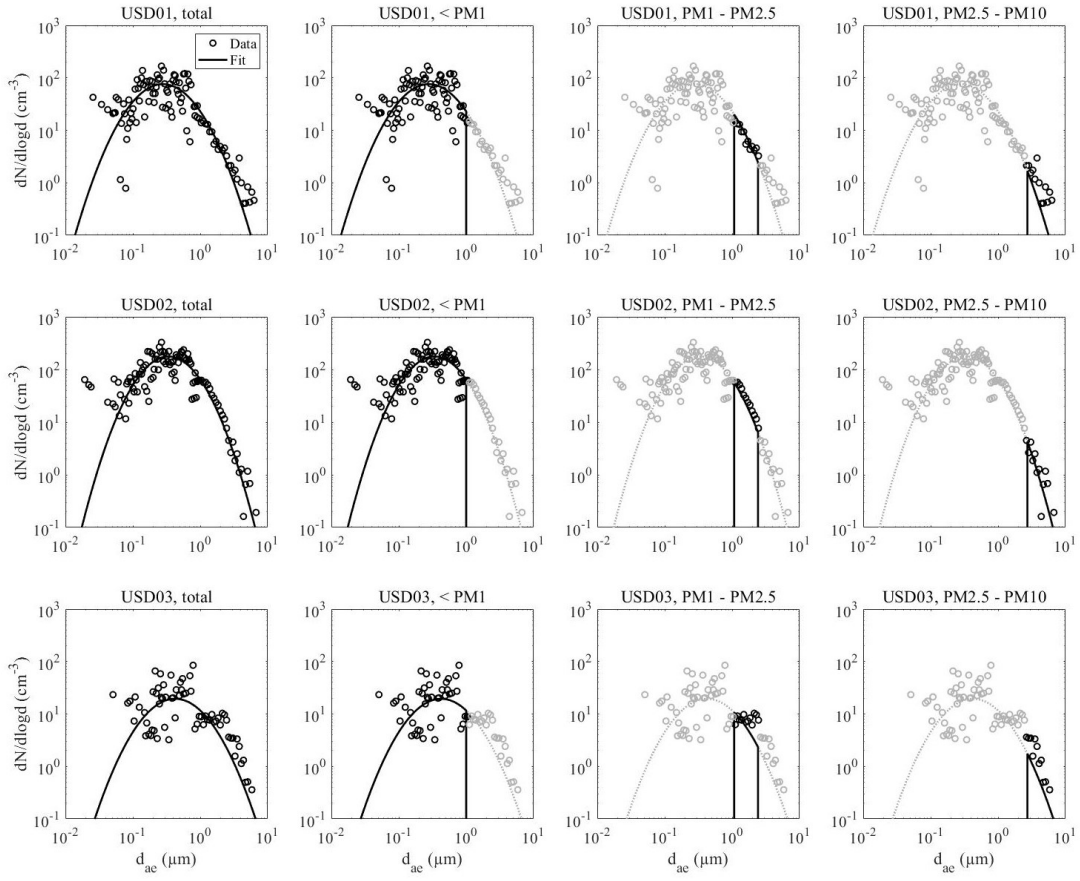

Figure 6.5.: Aerosol number size distribution of USD01, USD02 and USD03 before and behind the several stages of the cascade impactor. The black data points and the black line indicate the part of the size distribution, that was used for the calculation of n_s. The gray points show the part of the size distribution, that was removed at the several stages in the cascade impactor.

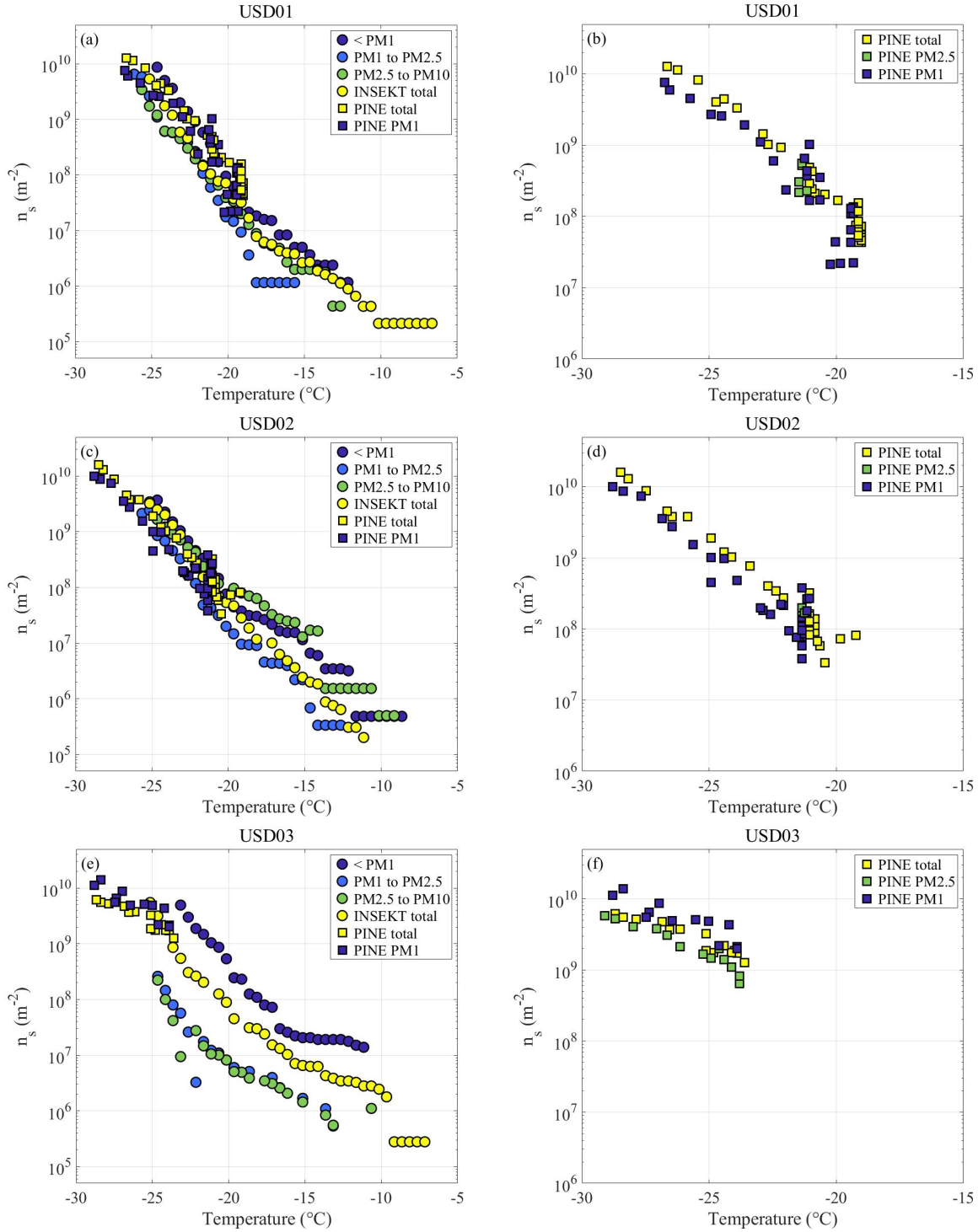

Figure 6.6.: n_s-temperature spectra of the size-selective PINE (squares) and INSEKT (circles) measurements. For the PINE measurements (panel (b), (d) and (f)), the total (yellow), PM2.5 (green) and PM1 (blue) n_s is shown. For the INSEKT measurements (panel (a), (c) and (e)), the total (yellow), PM2.5 to PM10 (green), PM1 to PM2.5 (light blue) and PM1 (blue) n_s is shown.

The heat treatment method (figure 6.7 panel (a) and (b)) revealed, that the temperature dependent freezing curves of USD01 remained the same with and without the heat treatment and so this sample does not

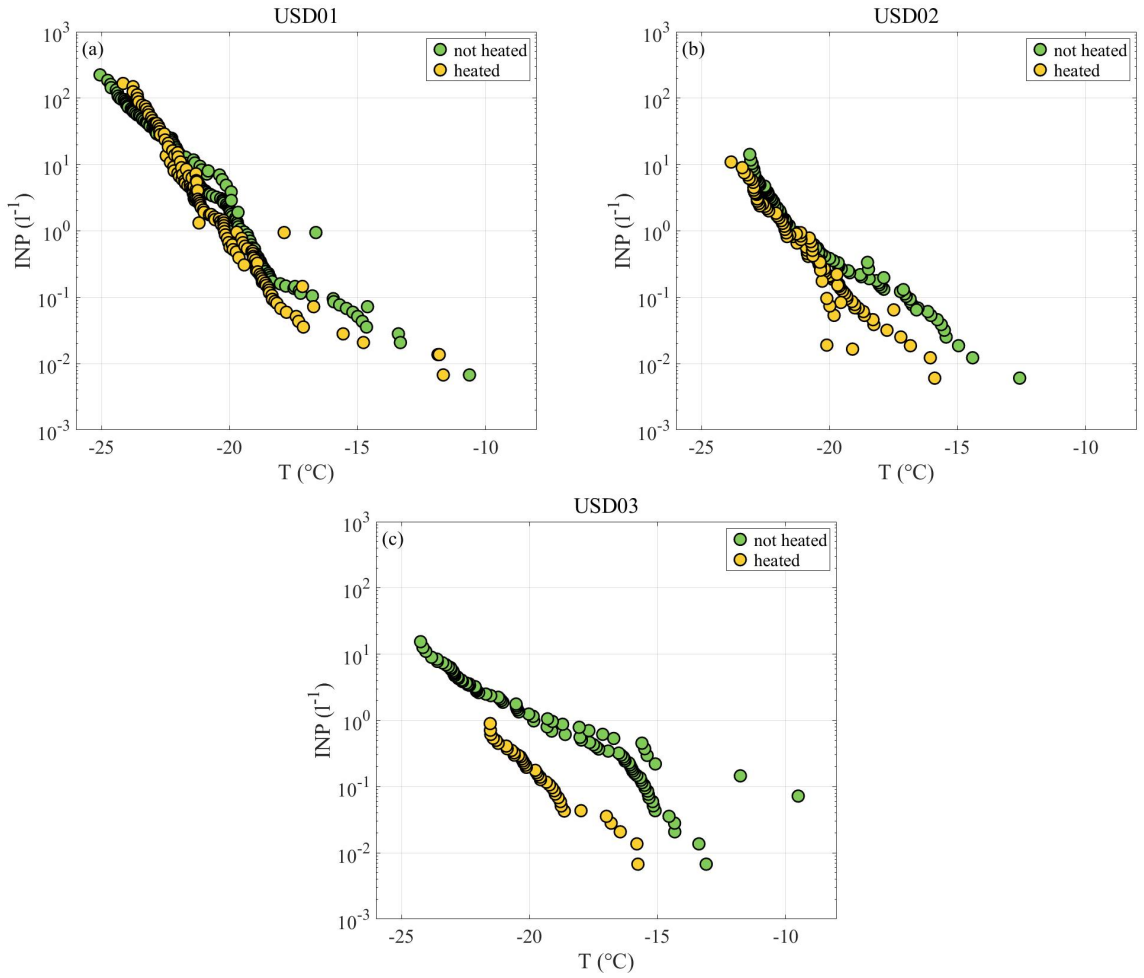

Figure 6.7.: INP-temperature spectra of the INSEKT analysis without (green) and with heat treatment (yellow) of the USD01 (panel (a)), USD02 (panel (b)) and USD03 (panel (c)) aerosol sample.

contain any heat sensitive materials. In comparison to USD01, the INP concentration of the heat treated USD02 was shifted about 1 order of magnitude towards lower INP concentrations in the temperature range between $-14\,°C$ and $-19\,°C$. This matched with the temperature range in which a difference in the size selected measurements was observed, meaning that the particles of USD02 with a higher ice nucleation activity could have been of biological origin. A size independent n_s approach for USD02 therefore is only valid at temperatures lower than $-20\,°C$.

In comparison to the USD01 and USD02 sample, USD03 showed a different behavior regarding the size dependent freezing. The analysis of the total n_s measured with PINE and INSEKT showed overlapping values and covered a range from about $1 \times 10^6\,m^{-2}$ at $-10\,°C$ to $5 \times 10^{10}\,m^{-2}$ at $-28\,°C$. The PM2.5 n_s measured with PINE had values of about a factor of 2 lower than the total n_s and the PM1 n_s was about a factor of 2 higher than the total n_s (figure 6.6 panel (f)). The same trend for the total and the PM1 n_s was observed for the INSEKT analysis, where the PM1 n_s reached values of up to a factor of 5 higher than the total n_s. The n_s for aerosol particles between 1 µm and 2.5 µm and 2.5 µm and 10 µm in aerodynamic

diameter took the same value and was overall 1 order of magnitude lower than the total n_s (figure 6.6 panel (e)). The somewhat different freezing behavior of USD03 was also reflected in the heat treated INSEKT analysis (figure 6.7 panel (c)), where the whole heat treated freezing spectrum was shifted by about 1 order of magnitude to lower INP concentrations. This means that the aerosol particles being active in the whole covered temperature range were heat sensitive and got deactivated. Thus potentially, the most active aerosol particles were the smaller ones, such as organic aerosols or microbes. Once all the large particles got removed from the aerosol size distribution, they did not dominate the surface area anymore and so the small particles were able to act as INPs without being suppressed by the big ones. For this aerosol sample the size independent n_s approach is not valid.
The main difference in the three probed aerosol samples is, that USD01 and USD02 are probes collected from the ground and USD03 is an ambient deposit sample (see section 3.4 for more information). Therefore, USD03 is more likely the dust population as it is also found in the atmosphere. Because of the different size dependent freezing behavior of USD03 compared to USD01 and USD02, more motivation for size dependent field measurements is given.

6.4. Total vs. PM1 INAS Density Measured in Kosetice

During the AIC02 campaign, the difference in the total, PM2.5 and PM1 n_s was studied with PINE and INSEKT in the laboratory using different dust samples. To extend these measurements also on ambient aerosol particles and thus a natural aerosol source, similar measurements were performed for 10 days during the Kosetice21 campaign (detailed description of the campaign is given in section 5.2.1). The inlet setup of PINE for field measurements has a d_{50} cutoff of 4 µm (Möhler et al., 2021) and so for the size-selective field measurements only the PM1 cyclone impactor was used. One analysis period was about 8 h to provide enough time for the filter sampling for INSEKT analysis. Within this time period, the inlet configuration for PINE measurements was switched between the PM1 cyclone impactor and no cyclone impactor every 1 h to 2 h. For the comparison with the INSEKT filter analysis, the sampling periods of PINE with and without the PM1 cyclone were averaged. As a first overview of the results, the temperature dependent freezing of the total and the PM1 INP concentration was viewed together with the regular and the heat treated INSEKT filter analysis in figure 6.8.
The 12 different measurements showed, that the PM1 INP concentration can either be the same as the total INP concentration or up to 1 order of magnitude lower. In case of a difference in the total and the PM1 INP concentration, it is represented throughout the whole temperature range between −20 °C and −28 °C covered by PINE. The INSEKT measurements covered the range of higher temperatures between −7 °C and −25 °C and in the overlapping temperature range with PINE they agreed in most of the cases within the given uncertainty. A comparison of the regular INSEKT analysis with the heat treated INSEKT analysis shows, that for almost all cases the freezing onset temperature of the heat treated INSEKT analysis was shifted by about 3 °C to 5 °C towards lower temperatures and the whole

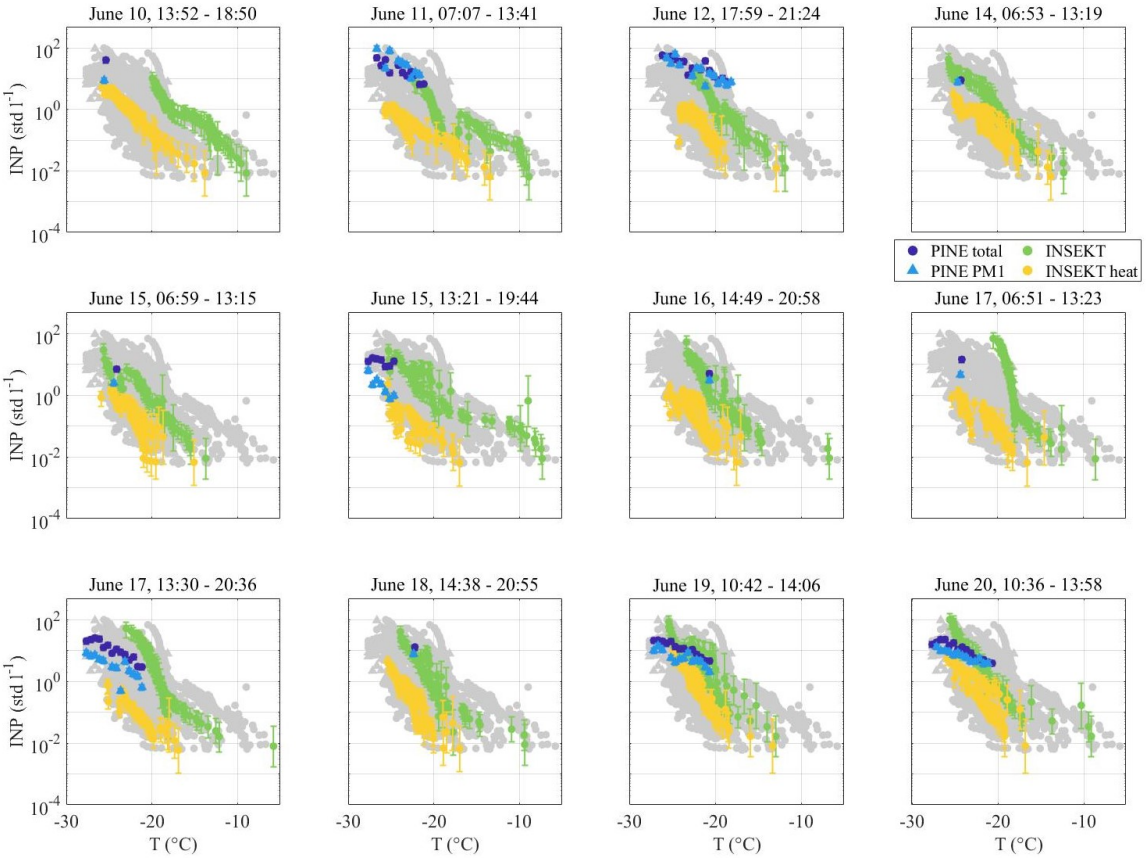

Figure 6.8.: Comparison of the total (dark blue) against the PM1 (light blue) INP concentration measured with PINE during the Kosetice21 campaign between June 10 and June 20. In parallel to the PINE measurements, one filter was sampled and analyzed with the regular INSEKT analysis (green points) and the heat treatment (yellow points). The gray data points in the background of each panel show the entity of data points.

INP spectrum was shifted to lower INP concentrations by up to 1 order of magnitude. This means that all aerosol particles being active at the several temperatures contained some heat sensitive components. Two remarkable cases are on June 10 and June 15, where the PM1 INP concentration lines up with the heat treated INSEKT analysis. These are also the days with the highest observed difference in the total and PM1 INP concentration. A possible explanation could be, that all particles larger than 1 µm in diameter and being removed by the PM1 cyclone impactor, were part of the heat sensitive aerosol population. However, it should be noted that in this first overview the INP concentration is shown, such that when aerosol particles are impacted and thus the number concentration of available INPs is reduced, it can be quite natural that the resulting INP concentration is reduced as a consequence.

One interesting case are the three measurement periods on June 14 and June 15, where the difference in the PM1 INP concentration to the total INP concentration increased from none to about 1 order of magnitude within about 36 h. Because the n_s provides a better insight in the size dependent freezing behavior due to the normalization to the surface area concentration, it was calculated using the combined SMPS and APS data for these three cases. The respective result in figure 6.9 revealed, that the calculated n_s showed the

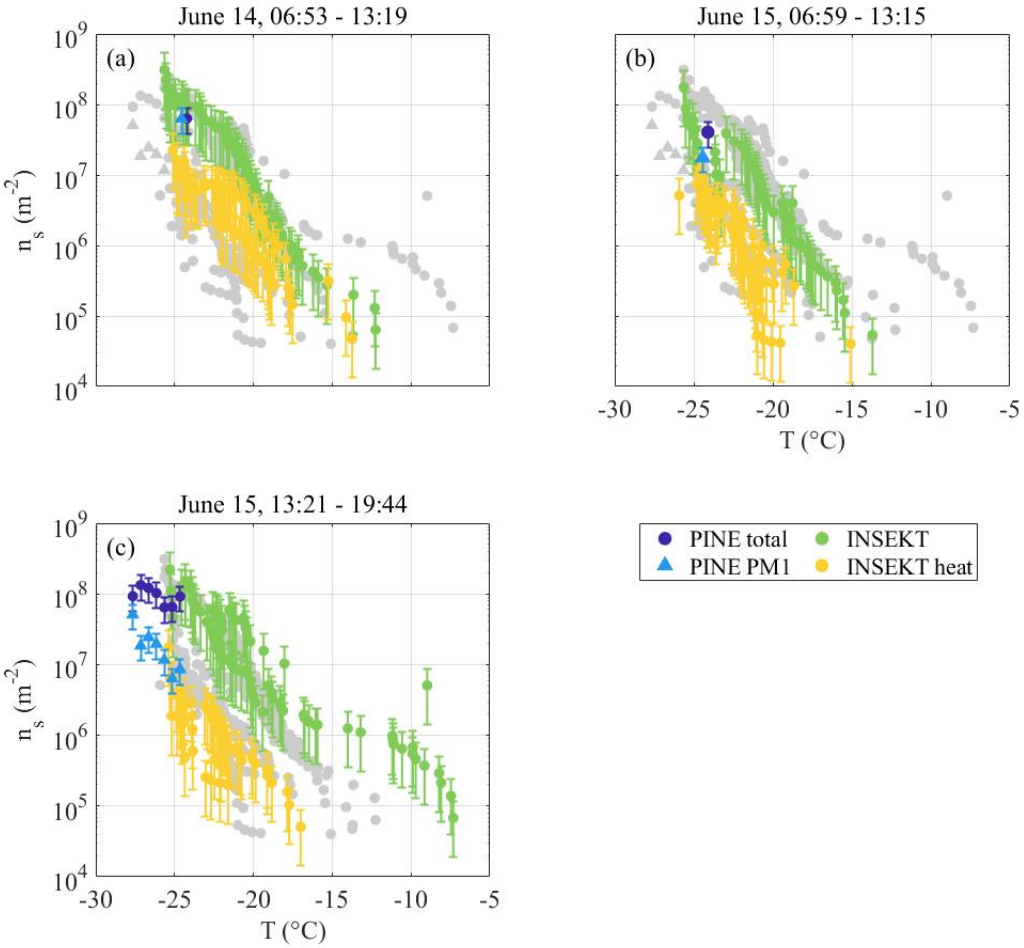

Figure 6.9.: Comparison of the total (dark blue) against the PM1 (light blue) n_s measured with PINE for three following sampling periods on June 14 and June 15 during the Kosetice21 campaign. In parallel to the PINE measurements, one filter was sampled and analyzed with the regular INSEKT analysis (green points) and the heat treatment (yellow points). The gray data points in the background of each panel show the entity of data points.

same trend for the total and the PM1 INP concentration. In order to investigate the origin of this change in the size dependent ice activity of the ambient aerosol population, one can search for possible explanations in the following three parameters: aerosol size distribution, meteorological conditions and air mass origin. A contribution from a changing aerosol size distribution was excluded since it did not change throughout the regarded time period, especially for the larger sizes (figure 6.10 panel (g)). The meteorological parameters of ambient air temperature, pressure, relative humidity, wind speed, wind direction and PBL (figure 6.10 panel (a) to (f)) show, that the average ambient air temperature increased during the three sampling periods, while the pressure and relative humidity decreased, giving some indication for a change in the meteorological situation.

To identify a possible explanation for the change in the difference between the total aerosol and PM1 n_s due to a change in the air mass origin, backwards trajectories were calculated using the HYSPLIT model.

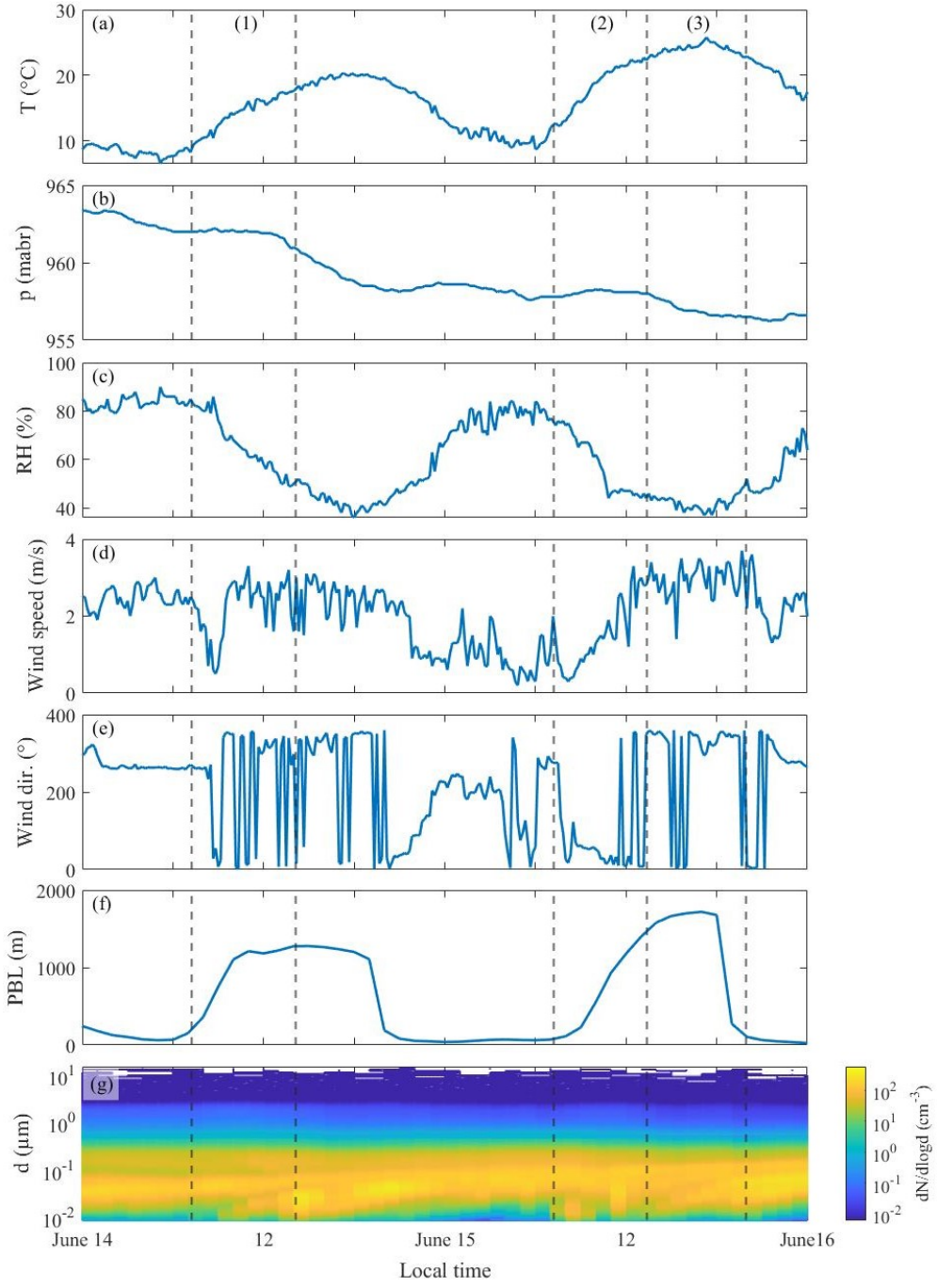

Figure 6.10.: Panel (a) to (g) show the ambient air temperature, pressure, relative humidity, wind speed, wind direction, planetary boundary layer height (PBL) and the aerosol size distribution, respectively. The vertical dashed line together with the numbers (1) to (3) indicate the sampling periods of PINE and INSEKT shown in figure 6.9.

For each sampling period two trajectory were calculated for 10 m above ground level and two for 500 m above ground level going 72 h back in time. A change in the air mass origin with height would imply a shear when going upwards in the atmosphere and thus more movement in the atmosphere. The color code of the trajectories gives the pressure level the air is coming from, which indicates if the air mass reaching the measurement site is more influenced by aerosol particles from lower or higher altitudes. Figure 6.11

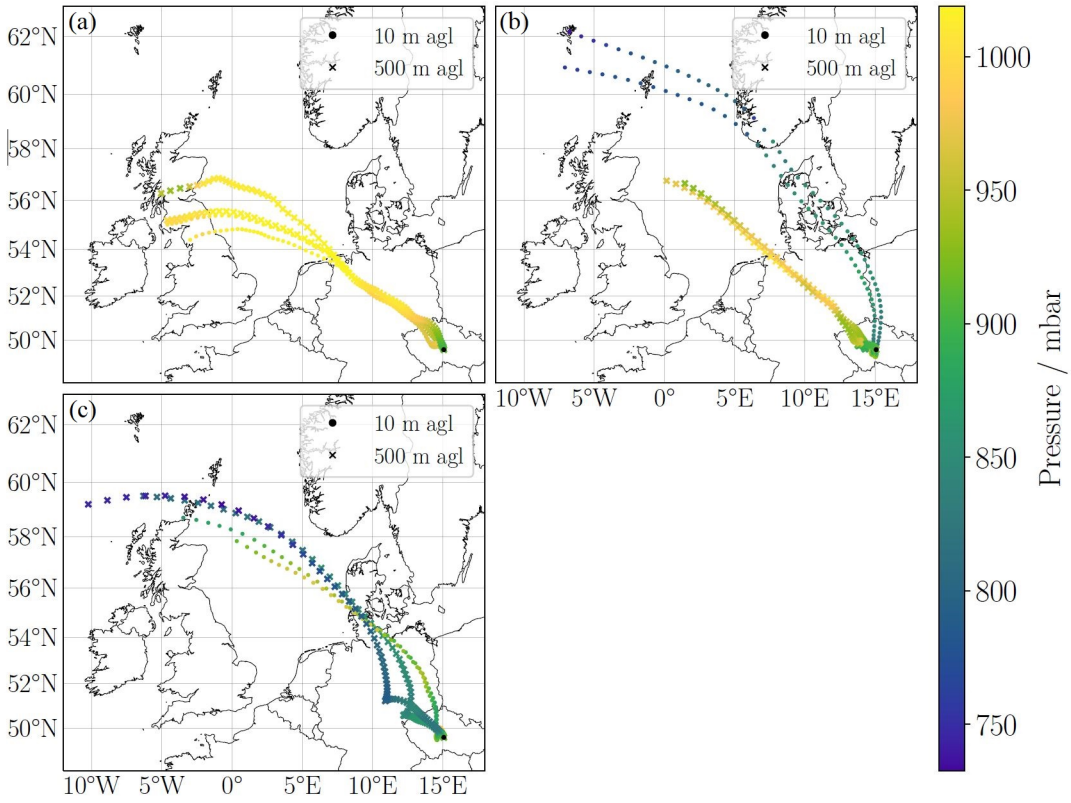

Figure 6.11.: Backwards trajectories calculated with HYSPLIT for 10 m above ground level (points) and 500 m above ground level (crosses) for the selected cases during Kosetice21. The colorbar on the right indicates the pressure level the air masses cam from. Panel (a) to (c) refer to the same sampling times as shown in figure 6.9.

shows in panel (a), that on June 14 the air masses on both pressure levels came from the northwest and by that crossed the North Sea and the northern and middle part of Germany. Both pressure levels were influenced by air masses that came from between 1000 mbar and 930 mbar. Panel (b) is about 24 h later on June 15, where the trajectory at 10 m above ground level still came from the same direction. Compared to that, the trajectory at 500 m above ground level changed its direction such that it came from more northern directions and from higher pressure levels of about 800 mbar. During the day of June 15, the 500 m above ground level trajectory stayed the same and the 10 m above ground level trajectory changed such that it came from the same direction and pressure level as the other one. The air masses originating from higher levels in the atmosphere can carry more long range transported aerosol particles. This potentially means, that in air masses reaching Kosetice containing long range transported aerosol, the larger particles are more ice active than the smaller particles. The air mass origin analysis gives only a hint to a possible explanation, but local effects such as enhanced pollen emissions or farming activities cannot be excluded. Both, changing air masses and local aerosol effects are related to a different aerosol composition, which highlights the need for parallel measurements of the chemical composition of the aerosol particles and the INP concentration with a similar time resolution as already discussed in chapter 5.

6.5. Summary

This study presented laboratory and field INP measurements where the resulting total n_s was compared against the PM2.5 and PM1 n_s for PINE measurements and against the PM1, PM1 to PM2.5 and PM2.5 to PM10 n_s for INSEKT analysis. While during the laboratory experiments, PINE and INSEKT probed the size effect of three dust samples from the US, during the field measurements in Kosetice PINE was used to characterize the size dependent freezing of the total against the PM1 ambient aerosol population. The size selection in the inlet of the PINE chamber was done by mounting a cyclone impactor upstream the chamber to remove aerosol particles larger than 2.5 µm or 1 µm in aerodynamic diameter. The INSEKT filter sampling was done with a cascade impactor, with in total four stages to sample aerosol particles in the diameter ranges of larger than 10 µm, between 2.5 µm and 10 µm, between 1 µm and 2.5 µm and smaller than 1 µm on separate filters. For the later analysis, only the last three stages were considered.
The laboratory measurements with three dust samples from the US, namely USD01, USD02 and USD03, showed for the USD01 and USD02 a similar freezing behavior, such that the total n_s was about a factor of 2 higher than the PM2.5 and PM1 n_s for the PINE measurements. The INSEKT analysis of USD01 of the several impactor stages revealed that they almost all showed the same n_s within the given uncertainty. For the USD02 sample, particles smaller than 1 µm and between 2.5 µm and 10 µm showed about a factor of 5 higher n_s than the other filter analysis for nucleation temperatures between $-10\,°C$ and $-20\,°C$. When analyzing these filters after heat treatment, it was shown that in the same temperature range heat labile aerosol particles were removed such that the INP concentration decreased. The USD03 sample showed a bit of a different freezing behavior for both the PINE and INSEKT analysis, in a way that the PM1 n_s was a factor of 2 higher than the total n_s, and the PM2.5 n_s was a factor of 5 lower than the total n_s. The same observation was made for the INSEKT filter analysis of the cascade impactor. A look into the heat treatment analysis of INSEKT showed that over the whole captured temperature range, the aerosol particles contained heat sensitive components and the freezing spectrum was shifted by about 1 order of magnitude to lower INP concentrations. The results of these measurements proofed a size-independent freezing of USD01 aerosol particles over the whole temperature range between $-8\,°C$ and $-28\,°C$ and for USD02 for temperatures lower than $-20\,°C$. A size dependent freezing was shown for USD02 at temperatures higher than $-20\,°C$ and for USD03 over the whole temperature range.
During the last 10 days of the Kosetice21 field campaign size dependent PINE measurements were done to compare the total and the PM1 n_s. One interesting case were 2 days of measurements in which the difference between the total and the PM1 n_s increased from no difference to a difference of 1 order of magnitude. Within the regarded time period, the aerosol size distribution remained constant and the meteorological conditions did not change considerably. However, an analysis of the air mass origin with the help of backwards trajectories showed that there was a shift from northwestern to northern directions and a change in the pressure level the air masses originated from, from between 1000 mbar and 930 mbar to 800 mbar.

Both the laboratory and field measurements highlighted that there are still many uncertainties in the freezing behavior of aerosol particles regarding their size. Because a change in the air mass origin and changes in heat sensitive aerosol particles lead to changes in the difference between the total n_s and the size selected n_s, it was shown that in the future a parallel analysis of the aerosol chemical composition with the same time resolution of the INP measurements is needed. Only by that, the understanding of the main sources of INPs and their dependency on the size can be improved.

7. Development and Application of the New Cloud Expansion Chamber AIDAm

7.1. Introduction

[1] Previous laboratory studies were conducted to investigate the freezing ability of different pure aerosol systems (e.g. Hiranuma et al., 2015; Wex et al., 2015; Ignatius et al., 2016; Ullrich et al., 2017), and dust particles turned out to be good INPs in both the mixed-phase and cirrus cloud regime (e.g. Chou et al., 2011; Atkinson et al., 2013; Kanji et al., 2017; Boose et al., 2019). Dust particles are emitted into the atmosphere from deserts or dry areas by wind dispersion and outgoing from their emission source, they are then lifted from ground level to upper tropospheric regions (e.g. Knippertz and Todd, 2012). Once the dust particles reach higher levels in the atmosphere, they can be transported over distances of up to a few thousand kilometers away from their emission source (e.g. Betzer et al., 1988; Weinzierl et al., 2017).
Compared to dust particles, aerosol particles such as SOA show a less pronounced heterogeneous ice nucleation ability (e.g. Ignatius et al., 2016; Wolf et al., 2020), and higher S_{ice} values, much closer to the homogeneous freezing are needed to induce heterogeneous ice formation. SOA in the atmosphere is formed by a gas-to-particle phase transition from e.g. the oxidation of alpha pinene, emitted as a biogenic precursor gas from forest areas (Hallquist et al., 2009). Materials such as sulfuric acid (H_2SO_4) freeze homogeneously at a temperature of $-35\,^{\circ}\mathrm{C}$ or lower (e.g. Koop et al., 2000; Schneider et al., 2021a). In the atmosphere, it is formed from sulfur dioxide (SO_2), emitted as a by-product from industrial combustion processes and volcanic eruptions, and OH radicals. Once SOA and H_2SO_4 have formed, they are transported through the atmosphere where they can then condense on the surface of aerosol particles (Seinfeld and Pandis, 2016). Hereby, a thin coating layer is applied on the particles' surface with the coating thickness being dependent on the amount of coating material present. The coating material is heterogeneously spread over the aerosol surface, but it is not fully understood which sites on the surface are the once the coating material goes to preferably (e.g. Sullivan et al., 2007, 2010).
Studies from the last 15 years (e.g. Knopf and Koop, 2006; Möhler et al., 2008a; Cziczo et al., 2009) investigated the influence of SOA and H_2SO_4 coatings on different aerosol particles at cirrus cloud conditions at temperatures between $-34\,^{\circ}\mathrm{C}$ and $-60\,^{\circ}\mathrm{C}$. Both coating types showed a suppression of the heterogeneous ice nucleation of the dust particles, represented as a difference in the relative humidity with

[1] A slightly modified version of this chapter is close to initial submission to the Journal *Review of Scientific Instruments*: Franziska Vogel, Larissa Lacher, Jens Nadolny, Harald Saathoff, Ottmar Möhler, Thomas Leisner (2022): Development and first application of a new cloud simulation experiment for lab-based aerosol-cloud studies

respect to ice where ice formation starts of up to 40 %. By that, the coatings applied on the aerosol surface shifted the freezing onset towards the homogeneous freezing line.
However, in most of the studies mentioned above the particles were coated at room temperature in an external vessel and were then transferred to the several instruments measuring the ice-nucleating properties. This does not represent atmospheric conditions, where the coating occurs at a similar temperature as the freezing processes at elevated altitudes in the atmosphere. Furthermore, the H_2SO_4 coating was often applied using hot sulfuric acid vapor with a temperature of about 150 °C. The high temperature may induce chemical reactions that could modify the properties of the dust particles and thus also influence their ice-nucleating properties. For further studies it is therefore important to coat the particles in a wide range of atmospherically relevant conditions and measure their ice-nucleating properties at the same conditions during the ongoing coating process.
The large cloud chamber volume of AIDA and the long preparation time for experiments limits the operation to a few cloud expansion experiments per day. Therefore, the much smaller and more flexible cloud expansion chamber AIDAm (AIDA mini), described in detail in the following section, was developed. It is located in the thermal housing of AIDA for repeated cloud expansion experiments with a turn-over time between the single cloud expansions of only 5 min to 7 min. AIDAm samples air from the AIDA chamber, which serves as a reservoir of aerosols with only slowly changing number concentrations and size distributions (see section 7.4). By that, AIDAm is able to monitor e.g. changes of the ice-nucleation ability of aerosol particles which are slowly modified by physical or chemical aging processes over longer time periods inside AIDA.

7.2. Setup of AIDAm

The construction of AIDAm was inspired by the Portable Ice Nucleation Experiment PINE (Möhler et al., 2021), which is a small and mobile cloud expansion chamber for ice nucleation studies and atmospheric INP measurements (see section 3.2). As PINE, AIDAm consists of a cloud chamber, a particle detector, and a control system for automated operation. However, it does not need a cooling system, because the cloud chamber is located inside the thermal housing of the AIDA chamber (figure 7.1). With a volume of 20 L, a height of 60 cm and a diameter of 25 cm, the AIDAm cloud chamber is about twice as large as the PINE cloud chamber. It is connected to the AIDA cloud chamber with two vertical stainless steel tubes (sample line and refill line) for sampling and investigating aerosols at temperature and humidity conditions which are controlled by the AIDA cloud chamber system as described in section 3.1.
The wall temperature (T_{wall}) of the AIDAm chamber is measured with three thermocouples attached to the outer wall at the top, the middle and on the bottom of the cloud chamber. The gas temperature (T_{gas}) inside the cloud chamber is measured with three additional thermocouples, located about 5 cm off the wall and at about 5 cm, 30 cm and 55 cm above the bottom of the chamber. Thus they are positioned close

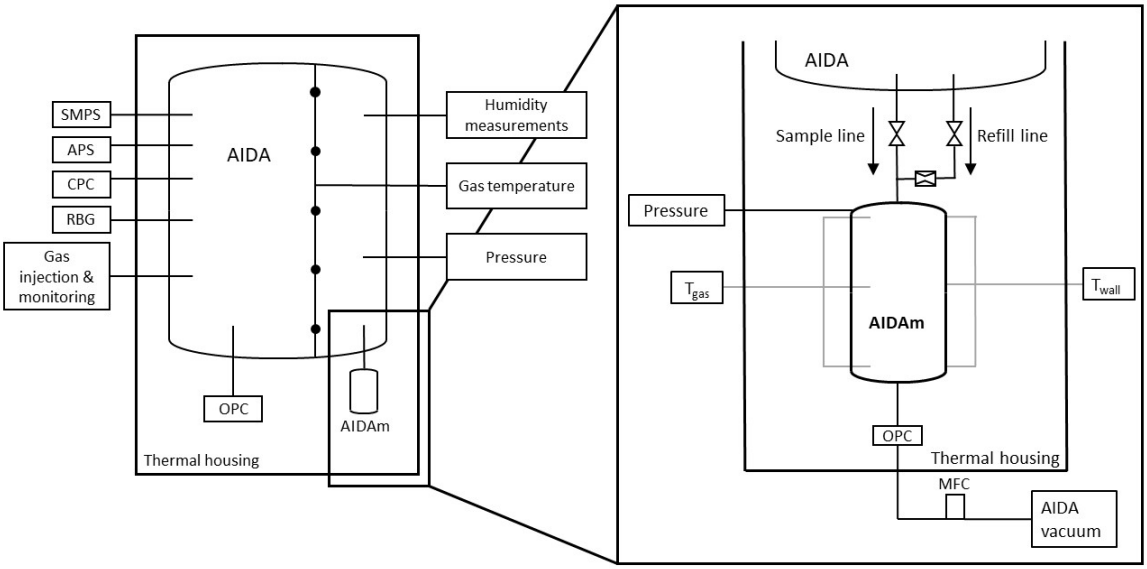

Figure 7.1.: Schematic (not to scale) of the AIDAm cloud expansion chamber (right part) located in the temperature-controlled housing of the AIDA cloud chamber (left part).

to the wall temperature sensors. The pressure in the AIDAm chamber is measured with a pressure sensor (VSC43MV, Thyracont).

The flow rate through AIDAm is controlled with a mass flow controller (MFC) that is connected to the AIDA vacuum system. The gas flow from the chamber passes an OPC, located below the chamber. It detects the different types of particles that can be present in the AIDAm chamber, namely non-activated aerosol particles, liquid cloud droplets and ice crystals. The OPC is a welas 2500 sensor connected to a Promo®2000 control unit (Palas GmbH), which is described in more detail in section 3.1.4.

7.3. Working Principle of AIDAm

AIDAm is operated in a similar way as PINE (Möhler et al., 2021), in which sequences of consecutive runs and operations are performed.

In the flush mode, the AIDAm chamber is flushed with air from the AIDA chamber, containing the aerosol particles under investigation. As shown in the upper panel of figure 7.2, the pressure (black line) and the

Table 7.1.: Typical values for the flow, the end pressure and the resulting duration for the three modes of a run.

Run mode	Flow ($L\,min^{-1}$)	End pressure (mbar)	Duration (s)
Flush	5 - 10	-	120 - 240
Expansion	5 - 10	900 - 750	20 - 90
Refill	orifice	-	40 - 90

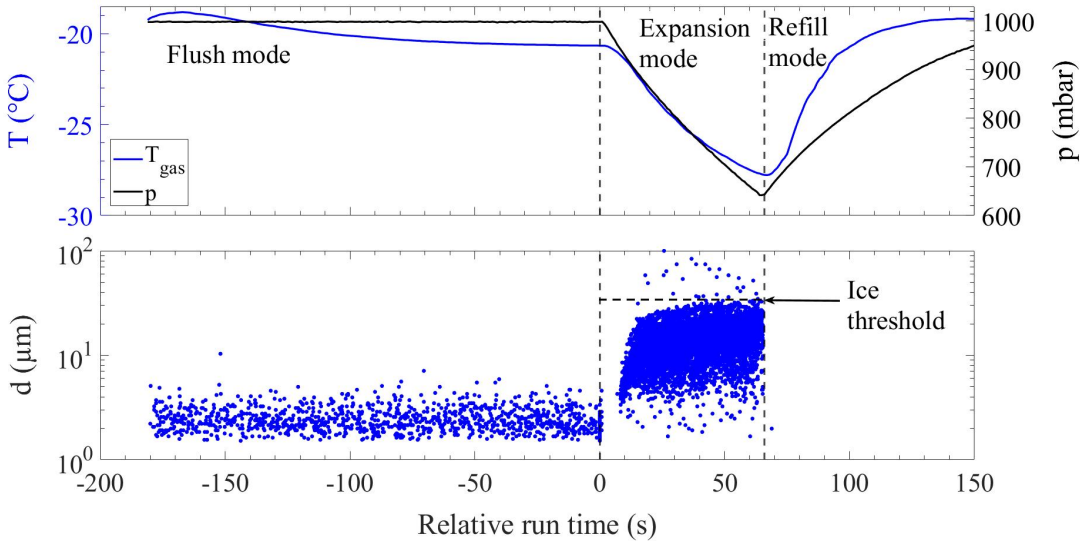

Figure 7.2.: Single run of an AIDAm expansion including the flush mode, the expansion mode and the refill mode. The upper panel shows in black the pressure and in blue the gas temperature measured in the AIDAm chamber. The lower panel shows the single particle data from the OPC, where each point represents the optical diameter of one detected particle. In the flush mode, only large aerosol particles are detected. During the expansion, a liquid cloud forms (seen as an accumulation of many data points) and ice crystals are detected as larger particles above the liquid cloud.

temperature (blue line) inside the chamber are constant. Only the larger aerosol particles are detected in the size range of the OPC (figure 7.2, lower panel). Each point represents one particle with its optical diameter d calculated from the detected size-dependent scattering intensity. Typical settings for the flush mode are a constant volume flow between 5 L min^{-1} and 10 L min^{-1} for a time between 2 min and 4 min (see table 7.1). By that, the AIDAm chamber is filled with fresh aerosol from AIDA.

The expansion mode is initiated by closing the valve in the sample line between AIDA and AIDAm. A constant expansion flow, with values between 5 L min^{-1} and 10 L min^{-1}, is applied to steadily reduce the chamber pressure from the start pressure, which is equal to the AIDA cloud chamber pressure, to the end pressure between 900 mbar and 750 mbar. The decrease of the pressure induces a decrease in temperature due to expansion cooling, which can be seen in the upper panel of figure 7.2, and an increase in the saturation with respect to ice and water to get supersaturated conditions. The expansion starts at a relative run time of 0 s and lasts for about 65 s in this case. The experiment presented in figure 7.2 shows the formation of a mixed-phase cloud, where both cloud droplets and ice crystals are visible in the OPC data. After about 6 s of the start of the expansion, a dense liquid cloud formed with particle diameters lower than about 35 µm, and only a few ice crystals were detected as larger particles with diameters above the ice threshold of 35 µm. As for PINE, the INP concentration is calculated from the ratio of the total number of ice crystals (ΔN_{ice}) detected during the expansion, and the volume of air that passed the OPC ($\Delta V_{exp} = \Delta t_{exp} \cdot \Delta f_{exp}$) during the presence of a cloud in AIDAm. The correction factor of 0.105 accounts for the fact that only 10.5 % of the total air volume passes the optical detection volume located in the center of the welas 2500 sampling tube.

$$n_{\mathrm{INP,AIDAm}} = \frac{\Delta N_{\mathrm{ice}}}{\Delta V_{\mathrm{exp}} \cdot\ 0.105} = \frac{\Delta N_{\mathrm{ice}}}{\Delta t_{\mathrm{exp}} \cdot\ \Delta f_{\mathrm{exp}} \cdot\ 0.105} \tag{7.1}$$

The final refill mode of an AIDAm run is started by opening the valve in the refill line (see figure 7.1). A small orifice in the refill line ensures a smooth refilling of the AIDAm chamber with aerosol from the AIDA chamber. Once the chamber is refilled to the AIDA pressure, the valve in the refill line is closed, the valve in the sample line is opened and the next run is started with the flush mode.

7.4. Validation of AIDAm

By comparison with AIDA and INSEKT results, the new AIDAm cloud expansion chamber was validated for measuring immersion freezing INPs, the correct freezing onset temperature of supercooled water droplets, and freezing processes at cirrus cloud temperatures. The immersion freezing experiments were conducted with a natural soil dust sample (SDSA_01). Dust aerosol is known to induce ice formation in the immersion freezing mode already at temperatures of about $-15\,^{\circ}\mathrm{C}$ to $-20\,^{\circ}\mathrm{C}$ (e.g. Hoose and Möhler, 2012; Murray et al., 2012; Ullrich et al., 2017; Kanji et al., 2017), and thus allows for comparisons in a temperature range, where all instruments are able to measure.

The experiments on homogeneous freezing of supercooled water droplets were conducted with AS particles. In the course of the expansion in AIDA or AIDAm, the AS aerosol particles acted as cloud condensation nuclei to form the supercooled liquid droplets, which then froze homogeneously according to further expansion cooling. The experiments at cirrus conditions where either conducted with aqueous sulfuric acid aerosol to investigate the response of AIDAm for homogeneous freezing of solute particles, or with mineral dust aerosols. The dust aerosol was used to investigate and document the transition from homogeneous freezing signals to heterogeneous ice nucleation. Start temperatures, aerosol types and aerosol number concentrations of the validation experiments are listed in table 7.2.

Table 7.2.: Summary of the AIDAm validation experiments, with the AIDA experiment temperature T_{AIDA}, the aerosol type, the aerosol number concentration $c_{n,ae}$ in the AIDA chamber, the number of AIDAm runs, and the respective ice nucleation mode.

T_{AIDA} (°C)	Aerosol	$c_{n,ae}$ (cm^{-3})	# AIDAm runs	Ice nucleation mode
-25	SDSA_01	175	41	Immersion freezing
-10 to -27	SDSA_01	180	63	Immersion freezing
-31	AS	195	53	Homogeneous freezing
-45	H_2SO_4	1000	10	Homogeneous freezing
-45	SDSA_01	160	18	Deposition nucleation

7.4.1. Immersion Freezing

Two immersion freezing experiments were conducted to compare AIDAm with AIDA and INSEKT. The first experiment was done at a constant temperature to also investigate the reproducibility of AIDAm measurements at the same settings. During the second experiment, the temperature in the thermal housing of AIDA was slowly reduced from $-10\,°C$ to $-27\,°C$ to obtain AIDAm results in a temperature range well overlapping with the INSEKT data. During both experiments, the aerosol particles in AIDA were also sampled on two filters for offline INP analysis with INSEKT. More than 100 AIDAm runs were conducted with various expansion flow settings between $7\,L\,min^{-1}$ and $10\,L\,min^{-1}$.

The results from the three instruments are presented in figure 7.3 as INAS (ice nucleation active surface site) densities (n_s) as a function of the nucleation temperature. The n_s approach gives the number of ice active sites on the surface of the aerosol particles and is calculated as the ratio of the measured INP number concentration to the total aerosol surface area concentration (Niemand et al., 2012; Ullrich et al., 2017; Schneider et al., 2021b). The n_s values also allow for comparing results from experiments with different aerosol concentrations. The calculation of the n_s uncertainties for AIDA and AIDAm are based on the individual uncertainties for the INP concentration and the total aerosol surface area concentration, and are about 40 %. The INSEKT measurements have an error of about 70 %.

The n_s values measured during the AIDA expansion increased from $1 \times 10^{10}\,m^{-2}$ at a temperature of $-28.5\,°C$ to $1 \times 10^{11}\,m^{-2}$ at $-31.5\,°C$ (black stars in figure 7.3). The results from AIDAm showed up to about one order of magnitude lower n_s values compared to AIDA (colored triangles in figure 7.3). Only for the expansions with a flow of $10\,L\,min^{-1}$, AIDAm data agreed well with AIDA data. The n_s measured with INSEKT (black circles in figure 7.3) ranged from $1 \times 10^{7}\,m^{-2}$ at a temperature of $-18\,°C$ to $5 \times 10^{9}\,m^{-2}$ at $-26\,°C$ and by that compared well with the AIDAm data within the given uncertainties.

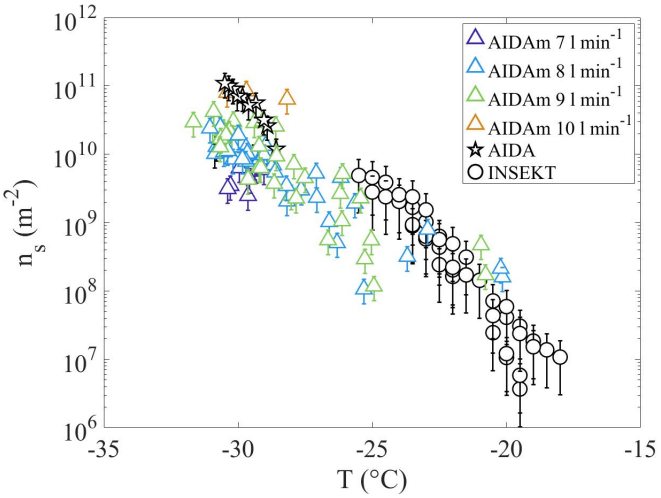

Figure 7.3.: Temperature dependent INAS densities n_s measured with AIDA (stars), AIDAm (triangles) and INSEKT (circles) for the natural soil dust sample SDSA_01. The AIDA temperature was set to $-25\,°C$. AIDAm was operated at expansion flow rates between $7\,L\,min^{-1}$ and $10\,L\,min^{-1}$, which are represented by different colors.

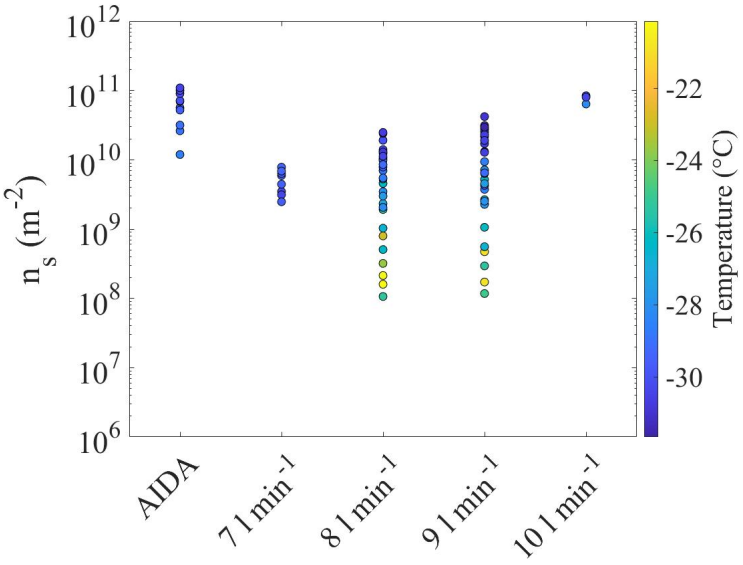

Figure 7.4.: Comparison of n_s values measured with AIDAm expansion flow rates of $7\,\mathrm{L\,min^{-1}}$, $8\,\mathrm{L\,min^{-1}}$, $9\,\mathrm{L\,min^{-1}}$, and $10\,\mathrm{L\,min^{-1}}$, and measured with AIDA. The color bar represents the respective ice nucleation temperature.

Figure 7.4 shows a comparison of the AIDA results with the AIDAm measurements for the different expansion flow settings between $7\,\mathrm{L\,min^{-1}}$ and $10\,\mathrm{L\,min^{-1}}$. The best agreement between AIDA and AIDAm measurements is observed for the highest AIDAm expansion flow of $10\,\mathrm{L\,min^{-1}}$. With a decreasing expansion flow, the deviation between AIDA and AIDAm increased to a factor of up to 5, 10 and 15 for the respective expansion flows of $9\,\mathrm{L\,min^{-1}}$, $8\,\mathrm{L\,min^{-1}}$ and $7\,\mathrm{L\,min^{-1}}$. This increasing deviation may be caused by a smaller fraction of aerosol particles to be activated as supercooled cloud droplets at lower expansion flow rates, and thus a smaller fraction of the aerosol surface that is available to induce immersion freezing. This leads to an underestimation of n_s. During an AIDA experiment, the number concentration of cloud droplets is measured revealing that almost all aerosol particles are activated as supercooled cloud droplets, which then contribute to immersion freezing.

The reproducibility of AIDAm measurements was investigated for an expansion flow of $9\,\mathrm{L\,min^{-1}}$ over a time period of several hours. The experiment was started with a concentration of $200\,\mathrm{cm^{-3}}$ of the SDSA_01 aerosol sample in AIDA, and over a time of 5 h AIDAm runs were performed with the same settings during three short time intervals. As shown in the lower panel of figure 7.5, the aerosol concentration in AIDA only slowly decreased from the initial concentration to about $175\,\mathrm{cm^{-3}}$, but showed no short-term fluctuations. These rather constant aerosol conditions can be kept in AIDA over a longer time, which allows to perform long-term aerosol sampling experiments with instruments like AIDAm. The upper panel in figure 7.5 shows three blocks of repeated AIDAm runs, which all showed n_s values between $2 \times 10^{10}\,\mathrm{m^{-2}}$ and $3 \times 10^{10}\,\mathrm{m^{-2}}$. By that, it is shown that AIDAm provides reproducible results for constant settings over a long measurement time.

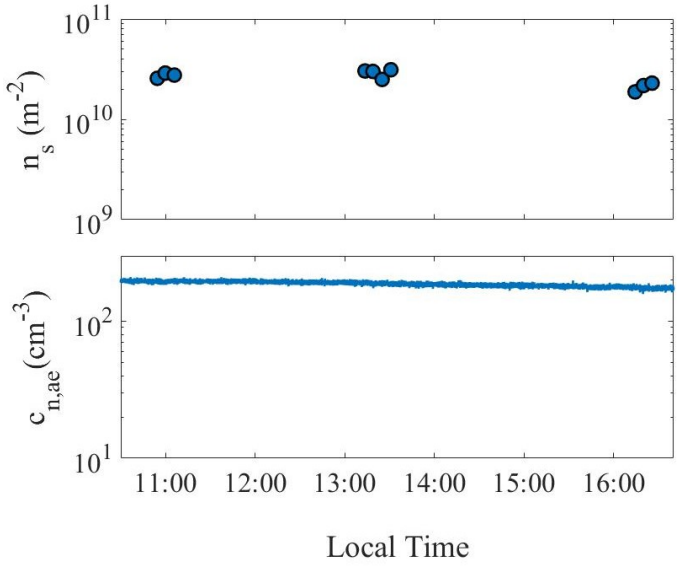

Figure 7.5.: INAS density (n_s) values measured in repeated AIDAm with an expansion flow of 9 L min^{-1} during three shorter time periods within the overall AIDA experiment duration of about 5 h (upper panel). The lower panel shows the aerosol number concentration $c_{n,ae}$ in AIDA during the same time period.

7.4.2. Homogeneous Freezing of Supercooled Water Droplets

To test and validate the onset temperature for homogeneous freezing of supercooled water droplets measured with AIDAm, an experiment with AS particles as seed aerosol for cloud droplet formation was performed. The freezing temperature of cloud droplets is well known from previous studies (e.g. Benz et al., 2005) and is also well formulated with classical nucleation theory (Pruppacher and Klett, 2010). AS was injected into AIDA as described in section 3.4. Due to the increasing relative humidity during AIDA or AIDAm expansion runs, AS takes up water, deliquesces and forms almost pure liquid cloud droplets which are then expected to freeze homogeneously at a temperature between −35 °C and −37 °C. AIDAm measured the homogeneous freezing onset temperature in a series of 53 runs, which were done with different expansion flow settings between 5 L min^{-1} and 10 L min^{-1}. In figure 7.6, one representative example is shown for each of the three run series with different expansion flow settings. The results are shown as normalized ice number concentrations $c_{n,ice,norm}$ plotted against T_{gas}. $c_{n,ice,norm}$ is calculated by dividing the measured ice number concentration $c_{n,ice}$ for each temperature step by the maximum ice number concentration $c_{n,ice,max}$ measured during the respective experiment:

$$c_{n,ice,norm} = \frac{c_{n,ice}}{c_{n,ice,max}} \quad . \tag{7.2}$$

The homogeneous freezing onset is indicated by a steep increase in $c_{n,ice,norm}$ (figure 7.6) which occurred in AIDAm runs at T_{gas} = −34.5 °C for all the probed expansion flows. This onset temperature is about 1.5 °C higher compared to the literature and to the result from the AIDA experiment (red line in figure 7.6). One explanation for this temperature offset may be related to the fact that the sensor measuring the

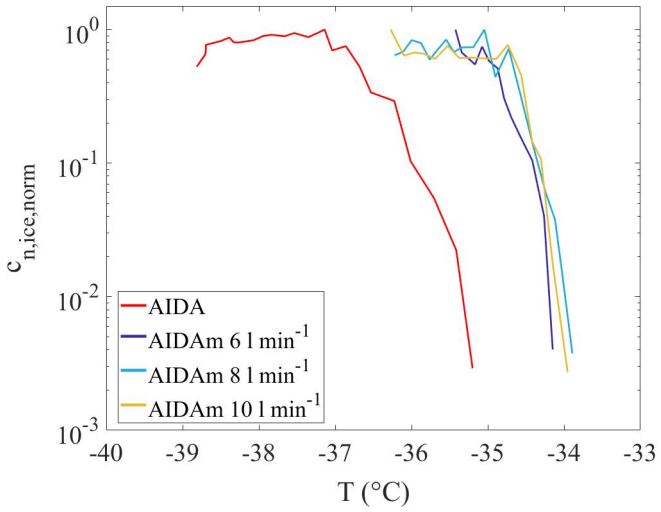

Figure 7.6.: Homogeneous freezing onset for supercooled water droplets measured with AIDA (red line) and AIDAm. The AIDAm expansions were done with different expansion flow rate settings of 6 L min^{-1}, 8 L min^{-1} and 10 L min^{-1}.

lowest temperature in AIDAm is still located about 5 cm above the bottom of the chamber. Therefore, the expanding gas can be further cooled on the way to the OPC below the chamber, and the minimum temperature of the aerosol can therefore be lower by about 1.5 °C. Any further results are not corrected for this temperature offset of 1.5 °C, but it will be considered for the uncertainties.

7.4.3. Homogeneous Freezing and Deposition Nucleation at Cirrus Cloud Temperatures

At temperatures below about −35 °C, any ice formation in the atmosphere occurs either by homogeneous freezing of aqueous aerosol components or by heterogeneous ice nucleation processes. For the latter case, aerosol particles are needed to trigger the formation of ice crystals. In the atmosphere, aerosol particles are often transported over longer distances and longer time periods to the upper troposphere. During transport, the aerosol particles can undergo surface coating processes, which then possibly change their ice nucleation ability and thereby their impact on cirrus cloud formation. Such coating processes can also influence the relative importance of homogeneous freezing and heterogeneous ice nucleation processes during cirrus cloud formation.

In this section, the capability of AIDAm to distinguish between homogeneous freezing and heterogeneous ice nucleation at cirrus formation conditions is demonstrated, which is key to understand and quantify the relative contribution of the two ice nucleation modes during the coating experiments that will be discussed in section 7.5. The homogeneous freezing experiments were conducted with aerosol particles composed of an aqueous H_2SO_4 solution and the deposition ice nucleation experiments were performed with SDSA_01 soil dust aerosol particles. All AIDA experiments and AIDAm runs discussed in this section were conducted at a start temperature of −45 °C and AIDAm used the same expansion flow

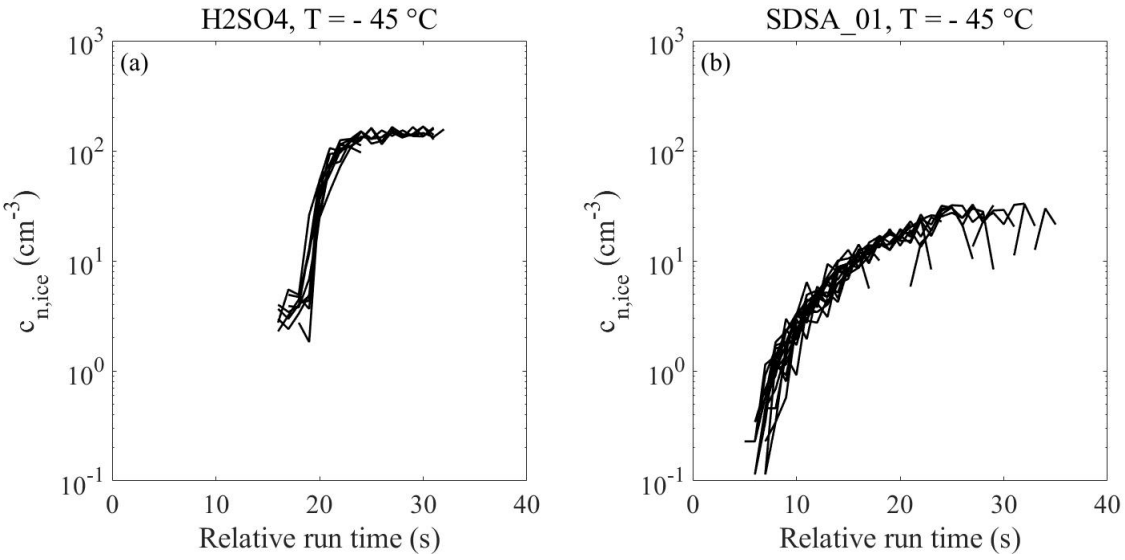

Figure 7.7.: Freezing behavior of aqueous H_2SO_4 particles (panel (a)) and the natural soil dust aerosol SDSA_01 (panel (b)), measured with AIDAm during 10 and 18 runs, respectively. The temperature in AIDAm at the start of the expansions was −45 °C in both cases.

rates of 5 L min^{-1}. The AIDAm runs were then analyzed for the temporal change of the ice number concentration $c_{n,ice}$ at a one-second time resolution.

During the AIDAm homogeneous freezing runs (figure 7.7(a)), the measured $c_{\mathrm{n,ice}}$ showed a steep increase in a short time interval around a relative run time of about 20 s. This is due to the steep increase of homogeneous freezing rates with decreasing temperature (Koop et al., 2000) and is also observed in AIDA homogeneous freezing experiments (e.g. Schneider et al., 2021a). Such a step-wise increase during the AIDA and AIDAm cloud expansion runs clearly indicates the occurrence of homogeneous freezing.

A different freezing behavior is observed during the AIDAm runs with the SDSA_01 aerosol (figure 7.7(b)). Ice started to form already at a relative run time of about 6 s, when the ice saturation ratio S_{ice} was still low. The ice crystal number concentration then steadily increased for a run time of about 15 s, caused by the heterogeneous ice nucleation on the dust particle surfaces to occur over a wide range of S_{ice}, which increased during the expansion run. This behavior is characteristic for heterogeneous ice nucleation like deposition nucleation or pore condensation and freezing, and was also observed in previous AIDA experiments with different mineral dust aerosol types at cirrus cloud formation conditions (e.g. Möhler et al., 2006).

The freezing curves from series of 10 and 18 runs shown in figures 7.7(a) and 7.7(b), respectively, also document the high reproducibility of AIDAm experiments conducted at the same start temperature and expansion flow rate. The variability from run to run is rather low. This demonstrates that different freezing modes like homogeneous freezing or deposition ice nucleation, or a gradual shift from one to the other mode e.g. during ongoing surface coating procedures, can well be identified and measured with AIDAm. The optimum expansion flow rate for AIDAm runs at cirrus formation temperatures was found

to be 5 L min^{-1}. At this expansion flow rate, the steady increase of the ice number concentration with increasing S_{ice} was well detected for a long time period after the start of the expansion (figure 7.7(a)), and the homogeneous freezing conditions were still reached well before the end of the expansion run (figure 7.7(a)). A higher expansion flow rate would result in a higher increase rate of S_{ice} and a shorter run time to reach homogeneous freezing conditions, which would result in a reduced sensitivity and time resolution to detect heterogeneous ice formation. With a too low expansion flow rate, the homogeneous freezing conditions may not be reached anymore in an AIDAm run.

7.5. Effect of Coating on Deposition Ice Nucleation

Previous laboratory ice nucleation experiments have shown that surface coating can significantly change the ice nucleation behavior of mineral dust particles at cirrus cloud temperatures (e.g. Knopf and Koop, 2006; Möhler et al., 2008a; Cziczo et al., 2009). Most of these experiments have been conducted for a limited number of specific coating amounts or with coating layers generated at conditions far from those during the atmospheric coating process. Here we present new results from experiments in which three different dust aerosol types were steadily coated with either H_2SO_4 or SOA inside the AIDA chamber over a time period of about 5 h.

The coating process was induced and controlled by the chemical reaction of the precursor gases SO_2 and α-pinene at a temperature of -45 °C or -55 °C, and by that simulating typical tropospheric formation processes of the coating materials H_2SO_4 or SOA, respectively. A summary of the experimental parameters including the type of pristine aerosol and the coating material is given in table 7.3. During the ongoing coating process, AIDAm continuously measured the ice-nucleation ability of the aerosols sampled from the AIDA chamber. Therefore, the combination of AIDA and AIDAm provided a unique opportunity for investigating the modification of the ice-nucleation behavior of aerosols during ongoing coating processes typical for atmospheric aerosol transport conditions and for time scales of hours to days.

Table 7.3.: Summary of the coating experiment parameters.

T_{AIDA} (°C)	Aerosol	Coating	$c_{n,ae}$ (cm^{-3})	# AIDAm runs
-45	ATD	H_2SO_4	220	118
-45	CFA_UK	H_2SO_4	170	117
-45	CFA_UK	SOA	160	125
-45	SDSA_01	SOA	165	119
-45	SDSA_01	H_2SO_4	160	120
-55	SDSA_01	H_2SO_4	195	115

7.5.1. Coating Experiment Procedure

Figure 7.8 shows the timeline of a typical experiment of coating of aerosols inside the AIDA chamber. At the beginning of an experiment, AIDAm is operated with particle-free air from AIDA for 15 min to 30 min in order to measure the background conditions for ice crystal detection. Thereafter, a certain amount of the dust aerosol is injected into the AIDA chamber. During the whole experimental procedure, the number concentration and the size distribution of the aerosol in the AIDA chamber are measured every second and every 30 min to 60 min, respectively. Right after the dust injection, AIDAm started to measure the aerosol ice-nucleation behavior as described in section 7.5.1 in a series of runs with the same settings to obtain a consistent data set throughout the whole experiment.

The ice nucleation behavior of the non-coated aerosol is measured during the first 1.5 h to 2 h. The first step of the coating procedure was the addition of O_3 following a similar procedure as described by Saathoff et al. (2009) to mainly check any background contamination in the AIDA chamber reacting with O_3. The initial maximum O_3 concentrations were about 70 ppb and 700 ppb for the SOA and the H_2SO_4 coating experiments, respectively. After O_3 addition, the ice-nucleation activity was measured for about 30 min to 60 min, before the volatile precursors SO_2 or α-pinene were added to initiate the chemical formation of the coating compounds H_2SO_4 and SOA, respectively.

The upper pathway in figure 7.8 represents the SOA coating with α-pinene being added several times in amounts ranging between 80 ppt and 1.3 ppb over a total time period of up to 5 h. By that, SOA compounds of low volatility were formed at a low rate and continuously condensed on the aerosol particles already present in the AIDA chamber.

The lower pathway in figure 7.8 represents the H_2SO_4 coating, which was started by adding SO_2. Then, tetramethylethylene (TME) was added in amounts of 7 ppb to 15 ppb to the AIDA chamber to generate, by reaction with O_3, OH radicals, which then reacted with SO_2 to initiate the gas-phase formation of H_2SO_4 molecules. TME was added in small amounts about three or four times per hour, in order to slowly

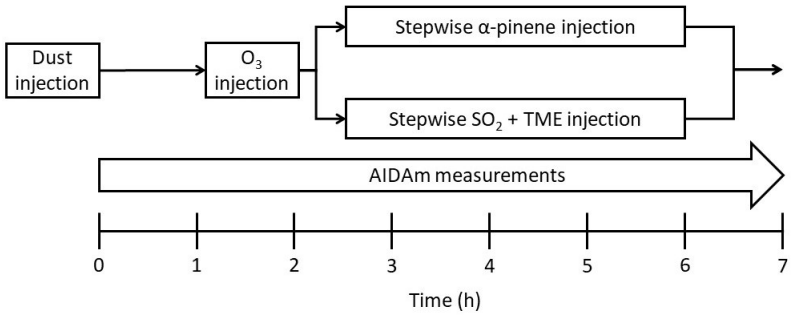

Figure 7.8.: Flow chart showing the typical experimental procedure of a coating experiment. The upper and lower pathways represent the SOA and H_2SO_4 coating, respectively. The precursor gases were added several times in small amounts to slowly increase the coating amount for a time period of about 5 h. Tetramethylethylene (TME) was also added several times per hour to form OH radicals by reaction with O_3. The OH radicals then reacted with SO_2 to initiate the gas-phase formation of H_2SO_4 molecules.

increase the coating amount over a longer time period. Because SO_2 is also lost to the chamber walls with a time constant of about 1 h, new portions of SO_2 were added to the AIDA chamber every hour. This caused a step-wise increase of the SO_2 concentration, and thereby also a step-wise increase of the H_2SO_4 coating. The change of the ice-nucleation activity was measured with AIDAm during the coating process which lasted for about 5 h.

7.5.2. H_2SO_4 Coating Experiments

The effect of H_2SO_4 coating on the heterogeneous ice nucleation activity was investigated for the three aerosol types ATD, SDSA_01 and CFA_UK at a temperature of −45 °C, and for SDSA_01 also at a temperature of −55 °C. All experiments were analyzed in the same way as the measurements discussed in section 7.4.3. The time series of ice number concentrations measured in individual runs are depicted in figure 7.9 as solid lines with the color code for the time (in hours) relative to the start of the AIDAm runs. The ice onset for all three experiments at −45 °C (figures 7.9 (a) to (c)) occurs at about 5 s relative

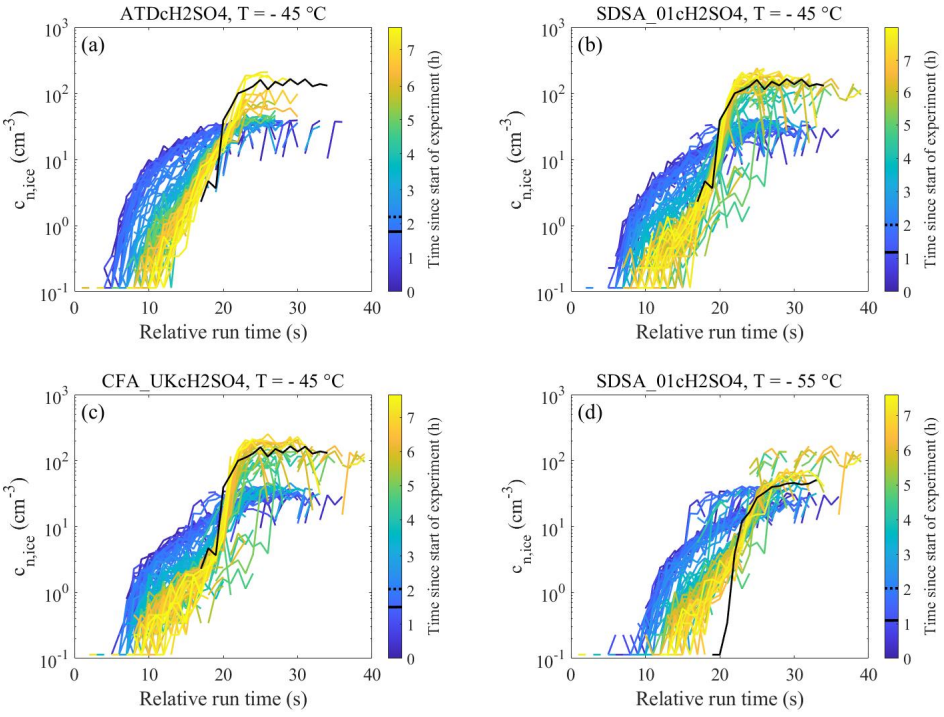

Figure 7.9.: Time series of ice number concentrations plotted as a function of relative run time for all AIDAm runs during AIDA experiments with H_2SO_4 coating to ATD (panel (a)), SDSA_01 (panels (b) and (d)), and CFA_UK (panel (c)) aerosols. The color code shows the experiment time in hours from when the AIDAm runs were started. The AIDA temperature was −45 °C during the experiments shown in panels (a) to (c), and −55 °C during the experiment shown in panel (d). The blueish lines represent the AIDAm runs with the non-coated dust aerosols sampled from AIDA, the greenish and yellowish lines the AIDAm runs with the coated aerosol. The solid black line shows one representative AIDAm run for homogeneous freezing of aqueous H_2SO_4 aerosols (figure 7.7(a)). The solid black line in the color bar indicates the O_3 injection, and the dashed line the start of the coating procedure.

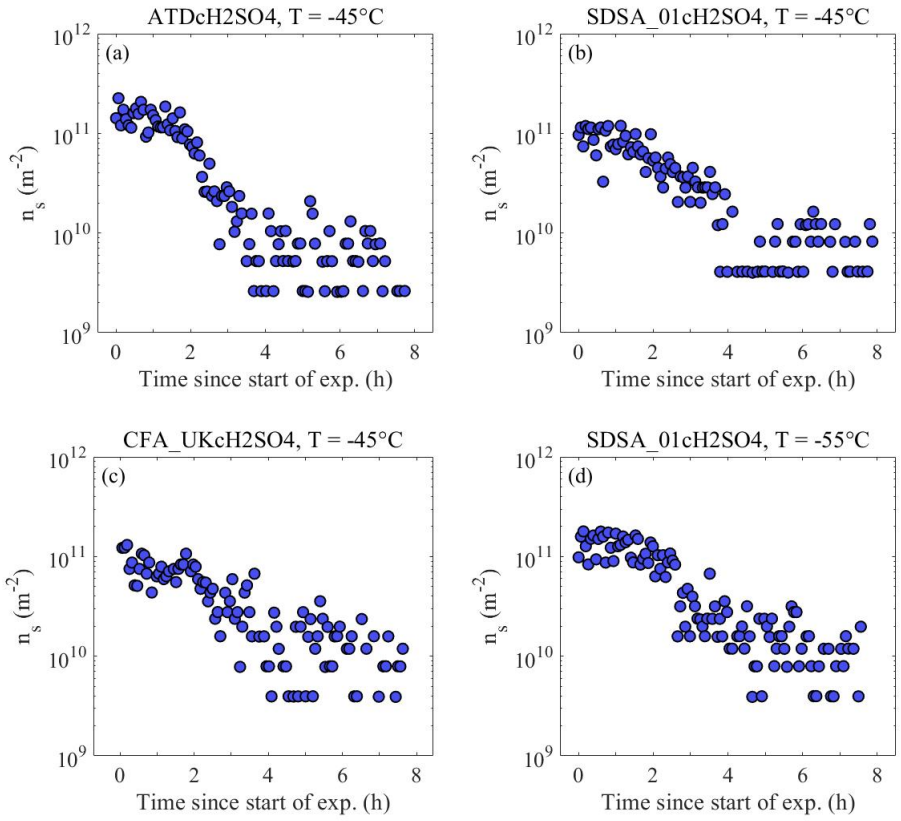

Figure 7.10.: Time series of INAS densities measured with AIDAm during the AIDA experiments with H_2SO_4 coating. The INAS densities were calculated for each AIDAm run at a relative run time of 15 s. The INAS density is a measure for the ice nucleation activity of the aerosol particles which is decreasing in the course of the experiments due to the increasing coating amount on the aerosol particle surfaces. The experiments in panels (a) to (d) are the same as in figure 7.9, panels (a) to (d).

run time for the non-coated aerosol (blue colors). From this we can conclude that the heterogeneous ice nucleation activity before coating is very similar for all three aerosol types investigated here, with a steady increase of the ice nucleation activity after the ice formation onset. Only for ATD, the $c_{\mathrm{n,ice}}$ curves are somewhat steeper right after the ice onset, indicating a slightly higher ice nucleation activity at low ice supersaturations.

The ice saturation ratio S_{ice} is increasing in the course of an AIDAm expansion run as explained in section 7.4.3 and also shown in figure A.3 in the appendix and discussed in the according section (section A). With a linear fit between ice saturated conditions ($S_{\mathrm{ice}} = 1.0$) at the start of the expansion and $S_{\mathrm{ice}} = 1.38$ at a run time of 20 s, the homogeneous freezing onset during AIDAm runs, that started at a temperature of -45 °C (see section 7.4.3), the ice saturation ratio is about 1.1 after 5 s run time when heterogeneous ice nucleation was observed to start for the non-coated aerosols.

Ozone was added to the aerosol in AIDA at an experiment time of 1.8 h, 1.3 h and 1.3 h for ATD, SDSA_01 and CFA_UK, respectively, indicated by the solid black lines in the color bars of figure 7.9. The $c_{\mathrm{n,ice}}$

curves did not change after ozone addition, which means that the ozone alone did not affect the aerosol ice-nucleation activity. The coating procedure started at an experiment time of 2.2 h, 2.0 h and 2.0 h for ATD, SDSA_01 and CFA_UK, respectively, indicated by the dashed black lines in the color bars of figure 7.9. During the coating with H_2SO_4 (transition to green and yellow colors), the ice formation onset was shifted towards later run times for all three aerosol types, but the shape of the curves remained almost the same (greenish colors and experiment times up to 5 h). From this we can conclude that thin coating layers suppress the deposition ice-nucleation activity of these aerosols at low S_{ice}, and shifted the onset of heterogeneous ice formation to higher S_{ice} values.

The coating induced reduction of the ice-nucleation activity is also presented in figure 7.10 which shows time series of n_s calculated for each AIDAm run at a relative run time of 15 s. The n_s is a measure for the ice nucleation activity of the aerosol particles per particle surface area. For the experiments at -45 °C (panels (a), (b) and (c)), the n_s decreased by about one order of magnitude during the first 3 h of coating time, from about 1×10^{11} m^{-2} for the non-coated aerosols to about 1×10^{10} m^{-2} for the coated aerosols. For the experiment at -55 °C (panel (d)), the n_s decreased slightly slower than during the experiment with the same aerosol at -45 °C (panel (b)).

The precursors were added at the same rates and amounts in both experiments at different temperatures, but the chemical conversion rates and molecular condensation rates to the particle surface may be reduced at the lower temperature. No instrument was available to directly measure the type and amount of coating on the aerosol particles. However, the median particle diameters were derived from log-normal fits to the aerosol size distributions measured every 30 min to 60 min during the coating experiments. Figure A.4 in the appendix shows the median diameters measured during the experiments with SDSA_01 at -45 °C and coating with H_2SO_4 (panel (c)) and SOA (panel (d)). The n_s measured during the same experiments are also shown in panels (a) and (b). For all coating experiments, the increase of the particle diameter was within the uncertainty range of about ± 20 nm for the median diameter, which means that the coating thickness at the end of the coating period was less than 20 nm.

After about 5 h experiment time, the shape of the $c_{n,ice}$ curves were clearly changing during all four experiments shown in figure 7.9. A second steep increase of the ice number concentration occurred at a run time of about 20 s, which is the time when homogeneous freezing was observed with AIDAm in experiments with pure aqueous H_2SO_4 aerosol particles (figure 7.7(a)). One representative $c_{n,ice}$ curve measured with AIDAm during the homogeneous freezing experiments is shown as a solid black line in figure 7.9. This surface coating induced change in the ice-nucleation behavior is caused by an increasing contribution of homogeneous freezing of the coating layer to the overall ice-nucleation activity of the aerosol, while the contribution from heterogeneous ice-nucleation at the surface of the solid dust aerosol particles is reduced by the coating layer.

For the experiment with SDSA_01 at -55 °C (figure 7.9 (d)), the shape of the $c_{n,ice}$ curves for the non-coated aerosol was similar to the experiments at -45 °C, but the ice onset occurred at a run time of about 8 s compared to about 5 s for the experiment with the same aerosol at the higher temperature (figure

7.9(b)). This shows that the heterogeneous ice nucleation activity of non-coated dust aerosols decreases with decreasing temperature when the ice saturation ratio is kept constant. This was also observed by (Ullrich et al., 2017) for different desert dust aerosol samples.

7.5.3. SOA Coating Experiments

The suppression of the heterogeneous ice-nucleation activity by surface coatings was also investigated for the coating of CFA_UK and SDSA_01 aerosols with SOA material. With about 160 cm^{-3} to 170 cm^{-3}, the aerosol number concentrations were similar for all coating experiments with CFA_UK and SDSA_01 (see table 7.3). The aerosol coating was performed in the AIDA cloud chamber at a temperature of −45 °C, similar to the experiments with H_2SO_4 coating, but with ozone and α-pinene as gaseous precursors for the organic coating material (see section 3.4 and 7.5.1).

Figure 7.11 shows the time series of ice number concentrations $c_{n,ice}$ from all AIDAm runs conducted during the SOA coating experiments. The data is presented in the same way as for the experiments with H_2SO_4 coating (see Fig. 7.9), with the color code for the time (in hours) relative to the start of the AIDAm runs. The ice formation onset times and the $c_{n,ice}$ curves for the non-coated aerosols (blue colors) agree well for the two experiment series with CFA_UK (figures 7.10(c) and 7.12(a)) and SDSA_01 (figures 7.10(b) and 7.12(b)) aerosols from the H_2SO_4 coating experiments. This underlines the high precision and accuracy of ice-nucleation measurements with AIDAm.

As a first step of the coating procedure, O_3 was added to the AIDA chamber at an experiment time of 1.4 h and 1.1 h for the experiments with CFA_UK and SDSA_01, respectively, indicated by the solid black

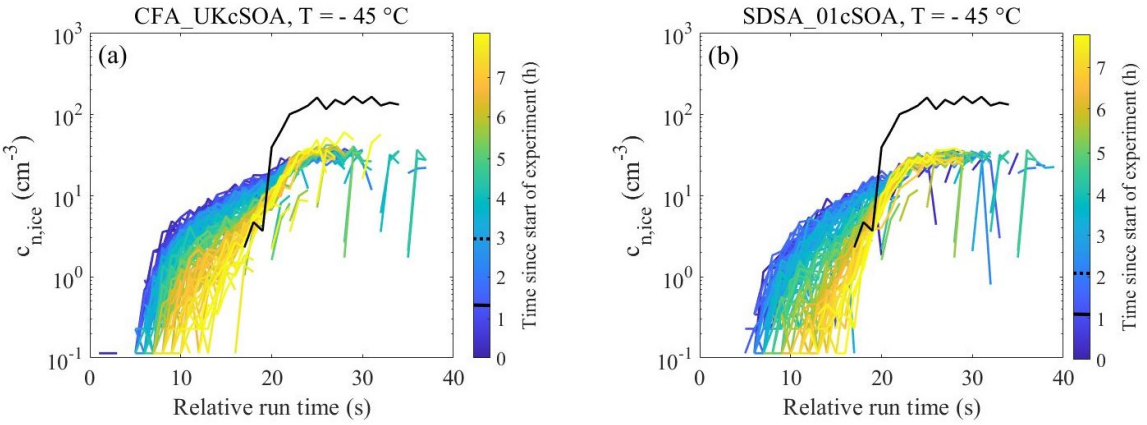

Figure 7.11.: Time series of ice number concentrations plotted as a function of relative run time for all AIDAm runs during AIDA experiments with SOA coating on CFA_UK (panel (a)) and SDSA_01 (panel (b)) aerosols. The color code shows the AIDA experiment time in hours the AIDAm runs were started. The AIDA temperature was −45 °C during both experiments. The blue colored lines represent the AIDAm runs with the non-coated dust aerosols sampled from AIDA, the greenish to yellowish lines the AIDAm runs with the coated aerosol. The solid black line shows the average curve of one representative AIDAm run with aqueous H_2SO_4 aerosols (figure 7.7(a)). The solid black line in the color bar indicates the start of the O_3 injection, and the dashed line the start of the coating procedure.

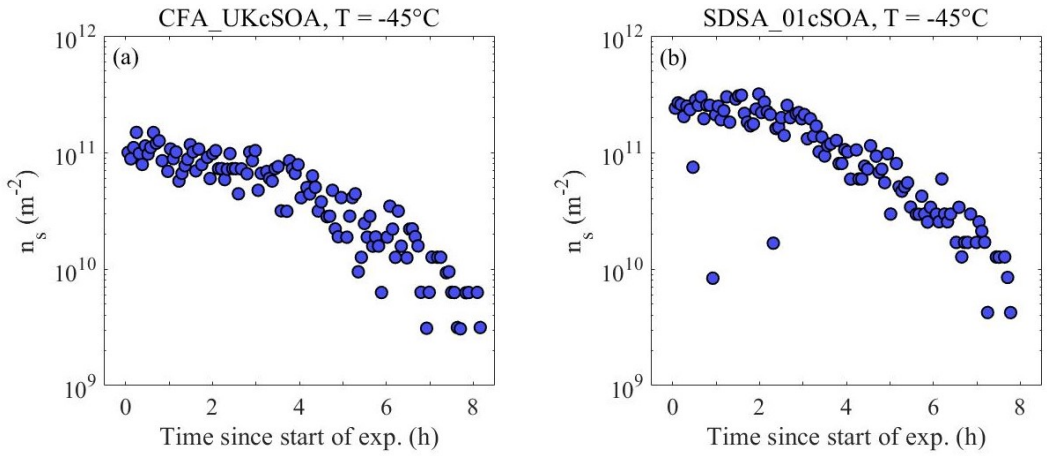

Figure 7.12.: Time series of INAS densities measured with AIDAm during the AIDA coating experiments with SOA. The INAS densities were calculated for each AIDAm run at a relative run time of 15 s. The INAS density is a measure for the ice nucleation activity of the aerosol particles which is decreasing in the course of the experiments due to the increasing coating amount on the aerosol particle surfaces. The experiments in panels (a) and (b) are the same as in figure 7.11, panels (a) and (b).

lines in the color bars of figure 7.11. As during the H_2SO_4 coating experiments, the $c_{n,ice}$ curves did not change after O_3 addition. The coating procedure started at an experiment time of 3.0 h and 2.2 h for the experiments with CFA_UK and SDSA_01 aerosols, respectively, indicated by the dashed black lines in the color bars of figure 7.11.

During the coating with SOA (transition to green and yellow colors and experiment times up to 5 h), the ice formation onset was shifted towards later run times for both aerosol types, but the shape of the curves remained almost the same. This coating induced reduction of the ice-nucleation activity is also shown in figure 7.12, with time series of n_s calculated for each AIDAm run at a relative run time of 15 s. As for the H_2SO_4 coating, the n_s also decreased during the SOA coating experiments by about one order of magnitude, but at a lower rate and over a longer experiment time of about 6 h.

The slower deactivation of the heterogeneous ice-nucleation activity can be caused by a lower rate of coating during the experiments with SOA coating compared to the experiments with H_2SO_4 coating. As mentioned in section 7.5.2, we were not able to directly quantify the type and amount of coating, but concluded from measurements of the median diameter of the aerosol size distributions (Fig. A.4) that the thickness of the coating layer was less than 20 nm for all coating experiments. From the n_s results shown in figures 7.10 and 7.12 we can therefore conclude that thin coating layers of both H_2SO_4 and SOA can suppress the heterogeneous ice-nucleation activity of dust aerosols at cirrus formation temperatures by more than one order of magnitude. This is supported by the results of previous studies (Kanji et al., 2019), where a similar decrease in n_s was observed for desert dust with similar coating thicknesses as in the experiments here.

In contrast to the H_2SO_4 coating experiments, the shape of the $c_{n,ice}$ curves was only slightly changed throughout the coating procedure. The steep increase that occurred in the H_2SO_4 coating experiments

at a relative run time of about 20 s due to homogeneous freezing of the H_2SO_4 coating layer is less pronounced in the AIDAm runs at the end of the SOA coating period. Also the ice number concentrations measured during these runs is much lower compared to the homogeneous freezing runs with pure aqueous H_2SO_4 aerosols (solid black lines in figures 7.11(a) and 7.11(b)). This lower relative contribution of homogeneous freezing to the overall ice formation at the end of the SOA coating experiments is probably caused by a lower amount of SOA coating. A lower coating thickness during the SOA experiments was also indicated by the slower decrease of the heterogeneous ice-nucleation activity (see figures 7.10 and 7.12), as discussed above.

7.6. Summary

AIDAm is a new cloud expansion chamber of 20 L volume which was developed for lab-based aerosol-cloud process studies with a high time resolution of minutes and for automated long-term measurement series of INPs over hours or days. It is mounted inside the thermal housing of the AIDA cloud expansion chamber (e.g. Möhler et al., 2003; Möhler et al., 2006) and is directly connected to it with a straight vertical sampling tube. Therefore, it can sample aerosol particles in a wide size range directly from the AIDA chamber, which serves not only as a long-term reservoir of atmospherically relevant aerosol particles, but also as a place for dedicated physical and chemical modification of the aerosol particles at well controlled temperature, pressure and humidity conditions. Aerosol processing and ice-nucleation experiments in AIDAm are restricted to the same temperature range as AIDA, between $-5\,^{\circ}C$ and $-90\,^{\circ}C$. The operation principle of AIDAm is similar to the recently developed Portable Ice Nucleation Experiment PINE (Möhler et al., 2021) and is based on a series of runs which are composed of three modes called flush mode, expansion mode and refill mode. During the flush mode, the cloud chamber is flushed with air from AIDA containing the aerosol under investigation. During the expansion mode, the aerosol in the AIDAm cloud chamber is expanded in order to activate the sampled aerosol particles as cloud condensation nuclei and ice-nucleating particles. During the refill mode, the cloud chamber is refilled until the initial pressure conditions are reached. A single run takes about 6 min and can be repeated with automated control over long time periods of hours or days.

The new AIDAm instrument was tested and validated for experiments on immersion freezing of soil dust aerosol particles at mixed-phase cloud temperatures, homogeneous freezing of cloud water droplets, as well as heterogeneous and homogeneous ice formation processes relevant for cirrus clouds. The experiments on immersion freezing were analyzed for the temperature-dependent INAS density (n_s), which is a parameter for the ice-nucleation activity per aerosol surface area (e.g. Niemand et al., 2012; Ullrich et al., 2017). The n_s measured with AIDAm showed good agreement with results from the AIDA cloud chamber experiments and the INSEKT method only for expansion flow rates close to $10\,L\,min^{-1}$. At lower expansion flow rates the AIDAm results showed an increasing low bias compared to the other methods, with a difference of up to one order of magnitude at an expansion flow rate of $7\,L\,min^{-1}$. The

reason for this discrepancy could be incomplete activation of aerosol particles to supercooled cloud droplets at lower expansion rates inside the AIDAm chamber. At higher expansion flow rates, n_s for immersion freezing of dust aerosols was measured with low variability in repeated runs over several hours. This showed that AIDAm ice-nucleation measurements are well reproducible in repeated runs with identical run parameters, and slight changes of the ice-nucleation activity e.g. due to surface coating can well be detected with AIDAm. The onset temperature for homogeneous freezing of solution droplets was measured with AIDAm at temperatures between $-34\,°C$ and $-35\,°C$, independent of the expansion flow rate. The observed freezing temperature is about $1.5\,°C$ higher compared to AIDA, which may be caused by a somewhat larger temperature non-homogeneity in the much smaller AIDAm chamber during the expansion. The AIDAm measurements at cirrus cloud temperatures revealed that heterogeneous ice formation on mineral dust aerosols can clearly be distinguished from homogeneous freezing of sulfuric acid solution particles, when looking into the rate of ice crystal detection with expansion time and the onset time of ice formation after the start time of the expansion. The time of ice onset is closely related to the ice supersaturation of ice formation.

After setup and validation, the new combination of AIDAm and AIDA cloud simulation chambers was used for investigating the impact of surface coating with sulfuric acid on the ice-nucleating activity of coal fly ash and two dust aerosols in the deposition ice-nucleation mode. The surface coating was performed inside the AIDA chamber over a time period of several hours, while AIDAm was continuously sampling the aerosol for ice-nucleation measurements. The experiments were carried out at a temperature of $-45\,°C$ for all three aerosol types, and additionally at $-55\,°C$ for one of the dust aerosols.

In all four experiment series with sulfuric acid coating, a clear transition was observed from deposition nucleation behavior to homogeneous freezing. The deposition nucleation behavior is characterized by an early ice formation onset at low ice supersaturations in the AIDAm chamber, followed by a steady increase of ice crystal formation over a longer time period of the expansion run. The homogeneous freezing behavior is characterized by a later ice formation onset followed by a steep increase of the ice crystal formation. Towards the end of the coating period, the ice formation curves agreed well to those measured for pure sulfuric acid solution aerosols. From this we conclude that already thin sulfuric acid coating layers of about 20 nm on coal fly ash and dust aerosols can completely suppress the deposition nucleation of ice at low ice supersaturations, and that the freezing behavior of coated aerosols is dominated by the homogeneous freezing behavior of the soluble coating material.

Similar experiments were conducted for SOA coating on coal fly ash and dust aerosols. During these experiments, the suppression of deposition nucleation was also observed, but the transition to homogeneous freezing behavior was less pronounced, probably caused by a lower coating thickness at the end of the SOA coating period. The amount of coating was not directly measured, but an upper limit of 20 nm for the average coating thickness from aerosol size distribution measurements was inferred.

8. Summary and Outlook

Primary ice formation in clouds is induced by so called ice-nucleating particles (INPs), which stem from a small fraction of the total atmospheric aerosol population originating from a large variety of sources. By triggering the ice formation, INPs have a major impact on the microphysical properties of clouds, which are vital for maintaining the natural water cycle and markedly influence the radiation budget of the Earth. Changes in the INP source emissions and abundance in the atmosphere due to changing environmental conditions and atmospheric transport patterns cause variations in the measured INP concentration on long and short time scales from between weeks to years and minutes to hours, respectively. The long-term variation measured at a mountain site and in the boreal forest was found to be connected to the annual seasonal cycle (e.g. Conen et al., 2015; Brunner et al., 2021; Schneider et al., 2021b). Some studies by e.g. Welti et al. (2018), Bi et al. (2019), Paramonov et al. (2020), Brunner et al. (2021) and Lacher et al. (2021) investigated the short-term variation of the INP concentration during intensive field campaigns in different locations by performing INP measurements with a time resolution of 20 min, and observed a range of INP concentrations over 3 orders of magnitude at a single temperature and up to 7 orders of magnitude for the temperature range in the mixed-phase cloud regime. While Paramonov et al. (2020) and Brunner et al. (2021) did not find a clear correlation of the observed variation with the analyzed meteorological variables and aerosol composition, Lacher et al. (2021) found enhanced correlations to chemical tracers of dust and marine aerosol. To improve on this, automated and continuous INP sampling with a high time resolution is required and only recently three of such instruments were developed (Bi et al., 2019; Brunner and Kanji, 2020; Möhler et al., 2021). These instruments can be used to quantify both the short-term and long-term variation of INPs and by that, possible driving factors which may need more attention in future INP monitoring can be identified. The data from long-term and highly time-resolved INP monitoring may also contribute to improve the representation of ice in clouds in global climate change projections, which is currently highly uncertain. This thesis focuses on laboratory and field measurements to investigate the short-term variation in the measured INP concentration at different thermodynamic conditions induced by atmospheric coating processes and changing ambient aerosol populations.

The laboratory and field experiments were conducted using two cloud expansion chambers and a filter sampling and subsequent freezing technique. For laboratory ice nucleation experiments under well-controlled conditions with a careful characterization of the aerosol size distribution, particle number concentration and cloud formation conditions, the AIDA (Aerosol Interaction and Dynamics in the Atmosphere) cloud expansion chamber was operated (e.g. Möhler et al., 2006; Wagner et al., 2006). For the AIDA experiments presented and discussed in chapter 4, 6 and 7, mixed-phase cloud conditions in the

temperature range between −10 °C and −26 °C were investigated. Chapter 7 also includes measurements at cirrus cloud conditions, which were performed in the temperature range from −45 °C to −55 °C.
To perform INP measurements, especially in the field, with a time resolution of a few minutes, the mobile cloud expansion chamber PINE (Portable Ice Nucleation Experiment) was operated for automated and continuous sampling (Möhler et al., 2021). Because of the high time resolution, PINE is capable of monitoring changes in the INP concentration on a short time scale of a few minutes and thus can capture fast changes in the atmospheric INP concentration. PINE was part of the measurements discussed in chapter 4, 5 and 6. In addition to the cloud expansion chamber experiments, the aerosol particles under investigation were sampled on filters and later analyzed in the laboratory using the freezing experiment INSEKT (Ice Nucleation Spectrometer of the Karlsruhe Institute of Technology) (Schneider et al., 2021b). This instrument complemented the INP measurements in chapters 4 to 7.

The following sections will summarize the activities, results and conclusions related to the key questions addressed in this thesis.

How do various INP instruments compare for high and low INP concentrations and different aerosol samples and what can we learn for future intercomparison studies?

Intercomparison studies of INP instruments have already been subject of laboratory campaigns in the past, and offsets in the measured INP concentration or the related n_s of up to 4 orders of magnitude were observed for different dust samples (e.g. Hiranuma et al., 2015; DeMott et al., 2018) for immersion freezing over a wide temperature range between −5 °C and −35 °C. Wex et al. (2015) and DeMott et al. (2018) performed measurements using Snomax®, which shows a steep increase in the measured n_s at a high temperature of about −7 °C. As recently new INP instruments were developed to advance the field INP measurements, this thesis aimed on intercomparing 12 instruments of different types (expansion chambers, continuous flow diffusion chambers and freezing experiments) with each other, including new and already existing instruments. The experiments with Snomax® from Wex et al. (2015) and DeMott et al. (2018) were repeated to quantify the measured n_s at high temperatures. PINE, INSEKT and DRINCZ detected the characteristic steep increase in n_s of this aerosol in the same range as previous studies. The subsequent plateau value, which is reached at around −10 °C, was detected by all instruments over a wide temperature range. The homogeneous freezing of supercooled water droplets was measured to compare AIDA, PINE and HINC at the lower end of the temperature range of mixed-phase cloud conditions. All three instruments detected the homogeneous freezing at around −36 °C, which was expected from the well-known freezing behavior of supercooled water droplets (e.g. Benz et al., 2005).
As a second part, the INP instruments were compared with each other for the measured n_s over a wide temperature range with different dust aerosol samples. In particular a number of experiments at low concentrations were performed, because atmospheric INP concentrations are often detected at very low values close to the limit of detection of the instruments. The results showed an offset between the different instruments of up to 4 orders of magnitude for ATD (Arizona Test Dust) and up to 2 orders of

magnitude for the natural soil dust sample SDSA_01 (South African Soil Dust 01) in the temperature range between −7 °C and −32 °C. This offset was similar for the experiments with high and low INP concentrations. Because the different INP instruments may be sensitive for different freezing pathways, future studies should aim at investigating the contribution of different ice formation processes to the total INP concentration measured with the different instruments.

Which variables influence the short-term variation in atmospheric INP concentrations and how can the prediction of INPs in models be improved based on the conducted long-term measurements of ambient INP concentrations?

The short-term variation of the INP concentration in ambient air at mixed-phase cloud conditions at temperatures between −15 °C and −30 °C was measured with the PINE chamber during continuous sampling between 8 and 14 weeks in three different field campaigns. Two of them were conducted in rural locations in the central Czech Republic and Southern Germany, and the third one took place on a mountain site in Greece. The continuously measured INP concentration with a time resolution of about 6 min revealed that the ambient INP concentration varied between about 0.1 L^{-1} and 300 L^{-1} for an INP activation temperature of about −23 °C at all three sampling sites. While the INP time series from the campaigns in the Czech Republic and in Greece did not show a regular, but more a random pattern, the INP data from the measurements in Southern Germany showed a clear diurnal variation throughout most of the campaign period. For the observed variation in the INP concentration in the Czech Republic, no clear correlation to any of the measured meteorological or aerosol attributed variables was identified, which lead to the conclusion that the variation may have been more driven by local aerosol emissions, e.g. due to biological or farming activities, which was not reported for this work. During times of a diurnal variation of the INP concentration measured in Southern Germany, enhanced correlations with the ambient air temperature, global radiation and the planetary boundary layer height and anti-correlations with the relative humidity were observed, which also undergo a pronounced diurnal cycle.

On the basis of the two field campaigns in the rural locations and additional offline INP analysis of filters collected at the institute facility of IMK-AAF, a new parameterization was developed to predict the INP concentration. This new parameterization was adapted from DeMott et al. (2010), who suggested a prediction of the INP concentration based on the number concentration of aerosol particles larger than 0.5 µm in diameter, measured during several field campaigns at different locations around the world. The modified parameterization is valid for the rural environments of this work and for a wide temperature range from −3 °C to −28 °C. Within a factor of 10, the previous parameterization by DeMott et al. (2010) represented 90 % or more of the data at temperatures lower than −20 °C, but only about 60 % of the data for higher temperatures. The new parameterization represents at least 80 % of the data within a factor of 10 from the 1:1 line throughout the whole temperature range.

Are larger aerosol particles better INPs and what can we learn from size-selective INP measurements?

Some parameterizations for predicting the INP concentration consider the ice activity of an aerosol as a value normalized to the aerosol surface area concentration (e.g. Niemand et al., 2012; Steinke et al., 2016; Ullrich et al., 2017; Schneider et al., 2021b). These parameterizations assume that the normalized ice nucleation activity, called INAS density (n_s), of a certain aerosol type strongly depends on the temperature, but is independent of the particle size, and therefore implies that the fraction of aerosols, which act as INPs at a certain temperature is increasing with the particle diameter or surface area. To confirm or validate this assumption, size selective INP measurements were performed in the laboratory with three different dust aerosols from the US and in the field with ambient aerosol particles, in parallel to size distribution measurements of the aerosol particles under investigation. Two of the probed US dust samples showed a size-independent n_s of the aerosol and the third dust sample showed an about 1 order of magnitude higher n_s for aerosol particles with a diameter smaller than 1 µm. A possible explanation for this change in the size-dependent freezing behavior of the dust samples was given by the filter-based offline INP analysis in the standard way and after performing a heat treatment. The heat treatment is supposed to deactivate heat sensitive material on the aerosol surface. For the dust samples which showed the same n_s for all analyzed size ranges, the heat treatment did not change the ice-nucleation ability, but for the dust sample in which smaller aerosol particles seemed to be more effective INPs, the heat treatment reduced the ice-nucleation activity by about 1 order of magnitude. This indicates that heat sensitive components, such as organic material and proteinaceous structures on the aerosol surface of particles in the submicron range caused an enhanced freezing ability.

Size-selective INP measurements sampling ambient air were conducted during 10 consecutive days in a rural environment using PINE, where during the day time the sampling was switched between the total and the PM1 sampled aerosol every 1 to 2 h. A more detailed analysis was done for a selected case, in which the difference in n_s between the total and the PM1 sampled aerosol increased from close to zero to 1 order of magnitude within 36 h. This was found to be potentially related to a change in the air mass origin and thus a different aerosol and INP population transported to the sampling site.

What is the temporal change of the ice-nucleation ability of aerosol particles during atmospheric coating procedures at cirrus cloud conditions and how can this be measured in the laboratory?

Aerosol particles that are emitted into the atmosphere can be transported over larger distances and so have an extended residence time of several days or weeks before they get removed by scavenging processes (e.g. Rohde and Grandell, 1972; Radke et al., 1980). The longer an aerosol particle remains in the atmosphere and the more potential coating material is present in the gas-phase, the more likely the aerosol particles collect sufficient coating amounts on their surface to modify their ice nucleation ability. Previous studies investigated the effect of different atmospheric coatings on the freezing ability of various dust aerosols in the temperature range between $-20\,^{\circ}\mathrm{C}$ and $-60\,^{\circ}\mathrm{C}$. For mixed-phase cloud conditions, it was observed

that secondary organic aerosol (SOA) coatings with a coating thickness of up to 60 nm did not change the freezing ability of the pristine aerosol (Kanji et al., 2019), because the coating may be dissolved in the water droplets before they freeze. In the cirrus cloud regime, both sulfuric acid and SOA coatings were found to at least partly suppress the freezing ability of the aerosol (e.g. Knopf and Koop, 2006; Möhler et al., 2008a; Cziczo et al., 2009). At these temperature conditions, the liquid water phase is not present and the coating remains on the aerosol surface. However, all these studies were limited to selected stages of the aerosol coating procedure due to a lack of available instrumentation to continuously monitor the change in the ice nucleation activity of the aerosol with a high time resolution of a few minutes. Therefore, a new small cloud expansion chamber named AIDAm (AIDAmini), which is placed inside the thermal housing of AIDA, and is thus operated at the same thermodynamic conditions as AIDA, was setup and validated successfully in this work. To investigate the temporal change in the ice nucleation ability of dust aerosol and coal fly ash, these aerosol particles were injected into AIDA at temperatures of $-45\,^{\circ}\mathrm{C}$ and $-55\,^{\circ}\mathrm{C}$ in the cirrus cloud regime and slowly coated with sulfuric acid or SOA over a time period of about 5 h. The ice activity of the aerosol was monitored over the whole experiment time with AIDAm, which sampled the aerosol from the AIDA chamber and performed repeated cloud expansions with a time resolution of about 5 min. When coating the pristine aerosol with sulfuric acid, it was observed that a coating with a thickness of about 20 nm fully suppressed the ice activity of the dust or coal fly ash and the homogeneous freezing of the pure sulfuric acid became the dominant ice formation process. The freezing suppression by the SOA coating was also visible in a change in the ice nucleation ability, but did not completely suppress the ice activity of the pristine aerosol. Previous studies investigating the coating effect of sulfuric acid and SOA in the cirrus cloud regime did not report the applied coating thickness, and reported the total amount of used coating material instead. The experiments with AIDAm in this thesis showed for the first time the slow decrease in the ice activity of aerosol particles that are coated during continuous laboratory measurements. Furthermore, the complete or almost complete freezing suppression due to sulfuric acid and SOA coating, respectively, by already thin coating layers, highlighted the importance of considering coating processes in the atmosphere, which clearly change the freezing conditions of aerosol particles and by that have a major impact on cirrus cloud formation.

This thesis showed the high value of automated INP measurements with a high time resolution for laboratory experiments, in which a temporal change in the ice nucleation activity of the probed aerosol is expected, and for field INP measurements, where short-term variations can occur. At the same time, new results pointed out that there are still many open questions that need to be addressed in future work to improve our understanding of INP sources and their potential spatial and temporal variation at different scales.

For future intercomparison studies it is suggested to carefully investigate the different heterogeneous freezing mechanisms that can be detected with the individual instruments. One selected aerosol sample

may systematically be investigated at different conditions in the mixed-phase cloud regime to identify the amount of ice that forms below and above water saturation.

Some of the variations in the INP concentration measured in the field were related to diurnal changes in meteorological variables, but more randomly occurring variations could not be explained with the currently available measurements. Also, the INP measurements sampling size-selected aerosol particles showed transitions from a size-independent freezing to a size-dependent freezing for different aerosol samples and air masses. To get a better idea whether the measured variation in the ambient INP concentration, or the changes in the size-selective INP measurements is related to the aerosol composition, it is suggested to perform parallel measurements of INPs and the chemical composition of the aerosol particles. Ideally, such measurements would be performed at multiple different locations to cover many aerosol source regions and over at least one full annual cycle.

Because INP measurements based on aerosol filter samples are limited in the time resolution, it would be benefitial to equip the PINE chamber with an additional heated inlet for heated and non-heat INP analysis with a high time resolution.

To better understand the dependency of the aerosol size on their freezing ability, more systematic size-selective INP measurements should be conducted. The size of the INPs, especially close to their source locations, is crucial to understand their potential to be transported through the atmosphere. For a further automation of the size-selective INP measurements, the PINE inlet may be modified in a way such that it can be switched between sampling of the total and size-selected aerosol, e.g. by using cyclone or other impactors. In combination with the heated inlet, one could scan through a broad parameter range within a short time period. For intensive field campaigns one may consider to take filter samples of total and size-selected aerosols in parallel for offline INP analysis.

The laboratory measurements using AIDAm showed a freezing suppression of the heterogeneous ice nucleation of dust aerosol and coal fly ash during slow coating processes with sulfuric acid or SOA at cirrus cloud conditions. Future studies may repeat these measurements with the additional quantification of the coating thickness or the coating amount on the aerosol particles. The experiments should also be extended towards lower temperatures to cover the whole cirrus cloud regime and be performed with different aerosol samples.

Even though INPs are rare in the atmosphere, they are crucial for processes in weather and climate systems. More than seven decades of atmospheric ice nucleation research in the laboratory and INP measurements in the field addressed and answered a number of questions and problems, but we are still far from a complete understanding of the sources and types of INPs, nor do we understand their temporal and spatial variation as e.g. observed in this thesis. The new methods and instruments developed and the laboratory and field measurements conducted as part of this thesis may provide an important basis for gaining a more detailed understanding of atmospheric INPs and their role in weather and climate systems.

A. Appendix for Chapter 7

A slightly modified version of this chapter is part of a manuscript, which is close to initial submission to the Journal *Review of Scientific Instruments*: Franziska Vogel, Lairssa Lacher, Jens Nadolny, Harald Saathoff, Ottmar Möhler, Thomas Leisner (2022): Development and first application of a new cloud simulation experiment for lab-based aerosol-cloud studies

Temperature Calibration for AIDAm

AIDAm is located in the AIDA cold box with a very homogeneous temperature control (ref). The temperature in this box is measured with thermocouples which are calibrated against a reference sensor which has an accuracy of $\pm 0.1\,°C$. Figure A.1 shows the uncorrected reading of the AIDAm temperature (T_{gas}, red symbols) compared to the AIDA cold box temperature in the temperature range from $-21\,°C$ to $-60\,°C$. From this data, a calibration function (polynomial fit of third order)

$$T_{gas,corr} = T_{gas} + (0.0001227 \cdot T_{gas}^3 + 0.01376 \cdot T_{gas}^2 + 0.5308 \cdot T_{gas} + 4.067) \tag{A.1}$$

was derived for the AIDAm temperature sensors. The calibrated temperatures ($T_{gas,corr}$) are shown as yellow symbols in Fig. A.1.

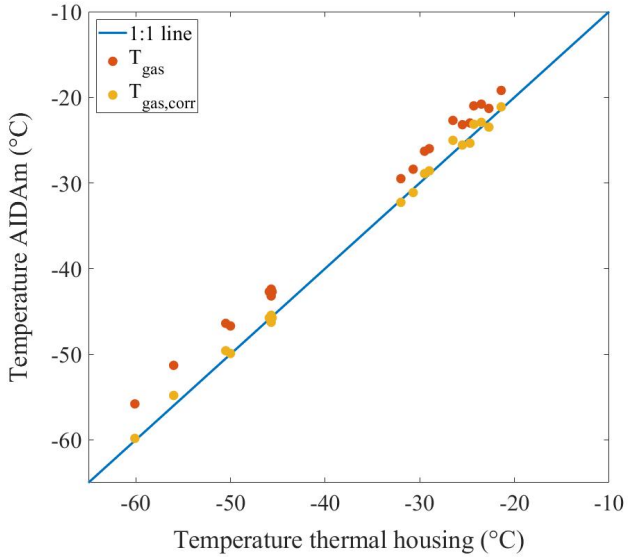

Figure A.1.: Raw (red symbols) and calibrated (yellow symbols) temperatures in AIDAm, compared to the AIDA cold box temperature.

Single AIDAm Runs with SDSA_01, SDSA_01cH_2SO_4 and SDSA_01cSOA

In the main paper, we showed the $c_{n,ice}$ curves for the pure SDSA_01 sample, the pure H_2SO_4 solution droplets and the transition from the pure dust sample to the H_2SO_4 and SOA coated dust particles. Additionally to that, figure A.2 shows single AIDAm runs on how the cloud formation in AIDAm changes from the non-coated SDSA_01 to the H_2SO_4 or the SOA coated sample, respectively at a temperature of $-45\,°C$. In both AIDAm runs with the non-coated dust, the first ice crystals in the single particle data show up at about 7 s after the start of the expansion and with ongoing time in the expansion, the amount of ice crystals increases. In the coating experiments presented in section 7.5.2 and 7.5.3, both coating types showed a different effect on the SDSA_01 such that for the H_2SO_4 coating homogeneous freezing was observed towards the end of the experiment. Compared to that, the SOA coating did not deactivate the SDAS_01 in such a extend and the deposition nucleation was still visible. This is also observed in the single run experiments, where for the H_2SO_4 coating only a few ice crystals appear at about 12 s of relative run time and after 20 s, where the homogeneous freezing sets in, a dense signal of ice crystals is observed. For the single run with the SOA coated SDSA_01, ice formation starts at about 15 s of relative run time. Afterwards, the number of ice crystal counts increases gradually, similar to the non-coated dust.

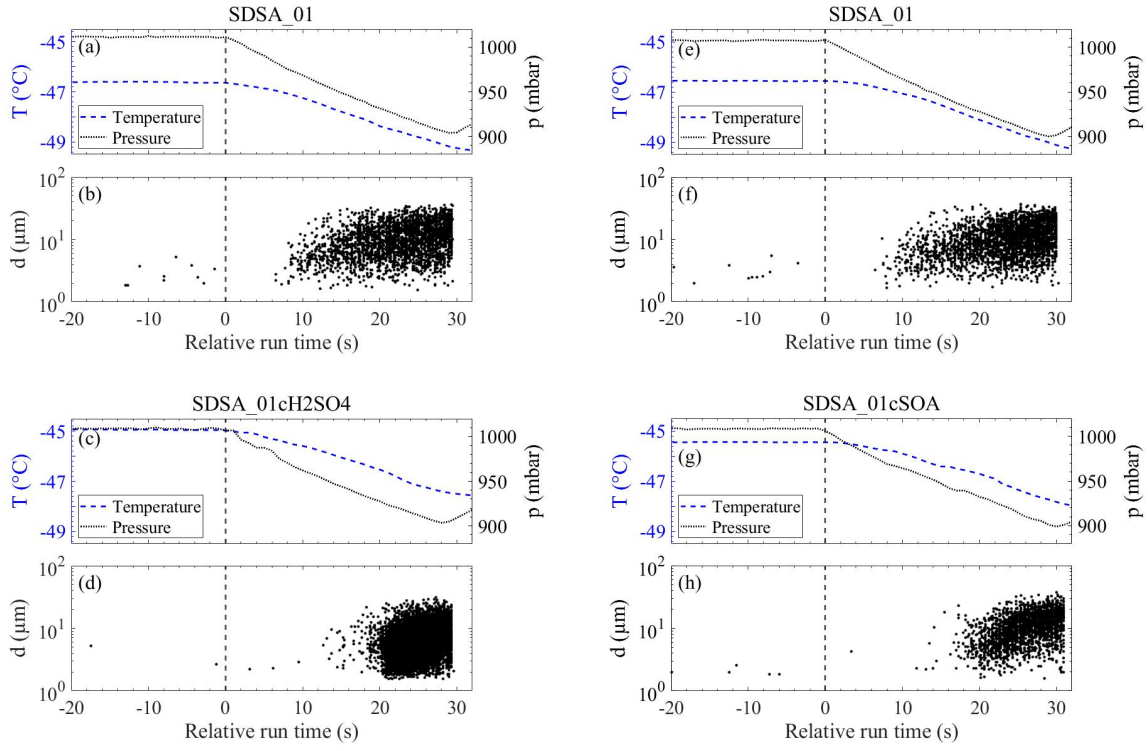

Figure A.2.: Panels (a), (b), (e) and (f) show the single run of the SDSA_01 sample at $-45\,°C$. Panels (c) and (d) are a single run with SDSA_01 coated with H_2SO_4 and panels (g) and (h) a single run of SDSA_01 coated with SOA at the same temperature. The temperature and pressure curve during the AIDAm expansion are shown in panels (a), (c), (e) and (g), and the according single particle data from the OPC are shown in panel (b), (d), (f) and (h).

Calculation of S_{ice}

The setup of AIDAm has no instrument included to directly measure the humidity in the chamber, but an estimate for the saturation with respect to ice (S_{ice}) during an expansion is given here. At the beginning of an expansion it is assumed that S_{ice} is at saturated conditions and therefore has a value of 1. During the course of an experiment, S_{ice} increases linearly and without the presence of ice nucleating particles reaches the values for homogeneous freezing. From the experiment with the pure H_2SO_4 solutes it is known that the homogeneous freezing is observed after 20 s and 23 s of relative run time for $-45\,^{\circ}\mathrm{C}$ and $-55\,^{\circ}\mathrm{C}$, respectively. The according S_{ice} values are calculated following the latest parameterization for homogeneous freezing (Schneider et al., 2021a). The calculation presented in figure A.3 are only valid for the experiments at cirrus cloud conditions made with a flow of $5\,\mathrm{L\,min^{-1}}$.

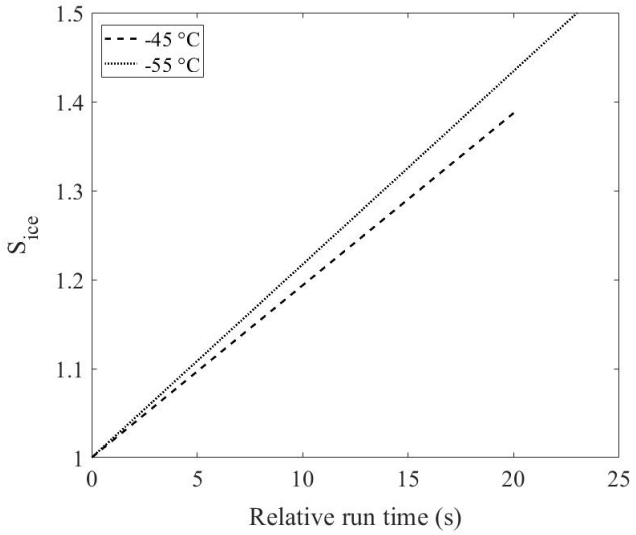

Figure A.3.: Linear fit of the saturation with respect to ice (S_{ice}) for the experiments done at $-45\,^{\circ}\mathrm{C}$ (dashed line) and $-55\,^{\circ}\mathrm{C}$ (solid line).

Change in Median Aerosol Diameter during Coating Procedures

During the coating procedure, the coating materials condense on the surface of the dust aerosol particles and build up a coating layer with a certain thickness. The size distribution of the aerosol in AIDA was measured with the SMPS and APS every 30 min to 60 min throughout the whole coating experiment and from the log-normal fits of the aerosol size distribution the mean diameter of the aerosol can be determined. figure A.4(c) and (d) show the change in the mean diameter of the SDSA_01 sample during the H_2SO_4 and the SOA coating at $-45\,^{\circ}\mathrm{C}$, respectively. A linear fit to the data points shows that in both cases the gradient in only slightly positive, showing that there is no significantly measurable change in the mean diameter during the coating procedure. Nevertheless, an estimate for the maximum coating thickness is given by the 1-sigma range of the fit and is about 20 nm for both the H_2SO_4 and the SOA coating.

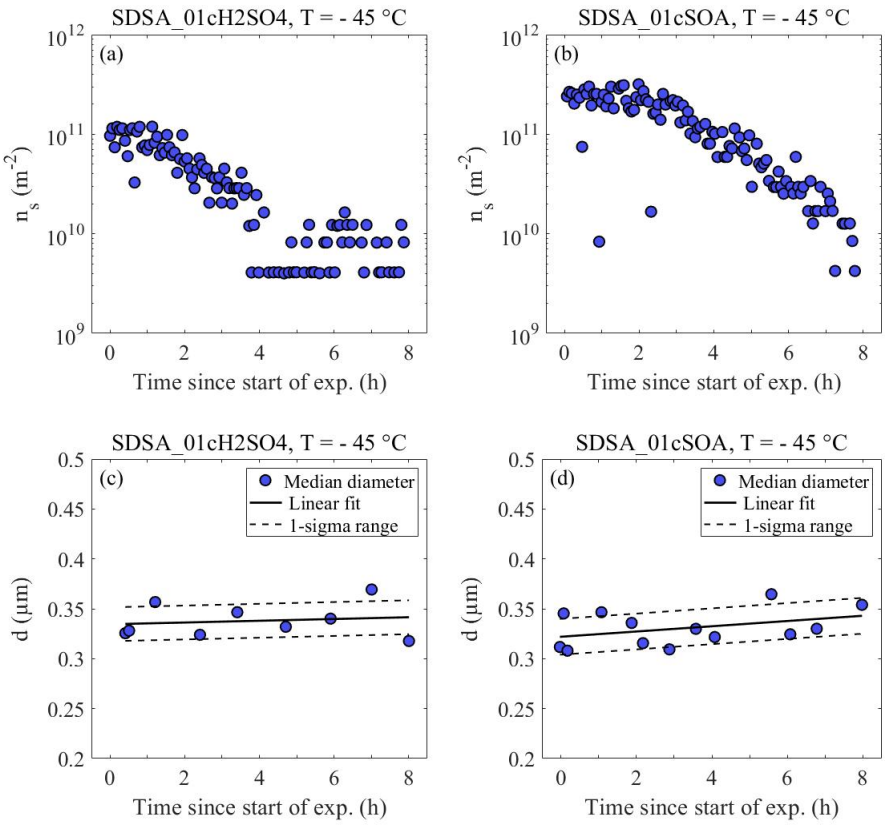

Figure A.4.: Change in the INAS density ((a) and (b)) for the coating experiments of SDSA_01 with H_2SO_4 and SOA. (c) and (d) show the median diameter from the combined size distribution measurements of the SMPS and the APS. Size distributions were measured every 30 min to 60 min. A linear fit and the according 1-sigma range show the change in the median diameter during the coating procedure and the estimated maximum thickness of the coating material condensed on the dust sample, respectively.

List of Abbreviations and Symbols

Abbreviation	Description
ACTRIS	Aerosol, CLouds and Trace Gases Research Infrastructure)
AIDA	Aerosol Interaction and Dynamics in the Atmosphere
AIDAm	Aerosol Interaction and Dynamics in the Atmosphere mini
APS	Aerodynamic Particle Sizer
AS	Ammonium Sulfate
ATD	Arizona Test Dust
CCN	Cloud Condensation Nuclei
CFA_UK	Coal Fly Ash from the United Kingdom
CFDC	Continuous Flow Diffusion Chamber
CPC	Condensation Particle Counter
DFPC	Dynamic Processing Filter Chamber
DMS	Dimethyl Sulfite
DRINCZ	DRoplet Ice Nuclei Counter Zurich
FINCH	Fast Ice Nucleus CHamber
FRIDGE	Frankfurt Ice Nuclei Deposition Freezing Experiment
H_2SO_4	Molecular formula of sulfuric acid
INAS density	Ice Nucleation Site density
INDA	Ice Nucleation Droplet Array
INKA	Ice Nucleation Instrument of the KArlsruhe Institute of Technology
INP	Ice-Nucleating Particle
INSEKT	Ice Nucleation Spectrometer of the Karlsruhe Institute of Technology
HINC	Horizontal Ice Nucleation Chamber
HYSPLIT	Hybrid Single-Particle Lagrangian Integrated Trajectory
LINA	Leipzig Ice Nucleation Array
mINKA	mobile Ice Nucleation Instrument of the KArlsruhe Institute of Technology
MOSES	Modular Observation Solutions for Earth Systems
MSA	Methanesulfonic acid
OH	Molecular formula of Hydroxide
OPC	Optical Particle Counter

O_3	Molecular formula of ozone
PBL	Planetary Boundary Layer
PCF	Pore Condensation and Freezing
PINE	Portable Ice Nucleation Experiment
RBG	Rotating Brush Generator
SDSA_01	Soil Dust South Africa 01
SMPS	Scanning Mobility Particle Sizer
SOA	Secondary Organic Aerosol
SO_2	Molecular formula of sulfur dioxide
(Sp-)APicT	(Single Path) AIDA PCI in-cloud Tunable Diode Laser)
TME	TetraMethylEthylene
USD01	US Dust 01
USD02	US Dust 02
USD03	US Dust 03
welas	WEißLichtAerosolSpektrometer
μl-NIPI	μl Nucleation by Immersed Particles Instrument

Symbol	**Description**
C_c	Cunningham correction factor
$c_{INP,observed}$	Observed INP concentration
$c_{INP,predicted}$	Predicted INP concentration
$c_{n,ae}$	Aerosol number concentration
$c_{n,ice}$	Ice number concentration
$c_{n,ice,max}$	Maximum ice number concentration
$c_{n,ice,norm}$	Normalized ice number concentration
c_p	Specific heat capacity of dry air at constant pressure
D	Nozzle diameter
d	Particle diameter
d_{ae}	Aerodynamic diameter
d_{me}	Volume equivalent diameter
d_{ve}	Mobility diameter
d_{50}	50 % cutoff diameter
e	Water vapor pressure
$e_{sat,ice}$	Saturation pressure with respect to ice
$e_{sat,water}$	Saturation pressure with respect to water

η	Gas viscosity
Δf_{exp}	Flow during an expansion
$f_{\mathrm{m}}(d_{\mathrm{p}})$	Particle mass per size bin
$f_{\mathrm{n}}(d_{\mathrm{p}})$	Particle number per size bin
$f_{\mathrm{s}}(d_{\mathrm{p}})$	Particle surface per size bin
ΔG	Gibbs free energy
k	Boltzmann constant
n_{ae}	Number of aerosol particles
ΔN_{ice}	Number of ice crystals per expansion
N_{ice}	Number of ice crystals
$n_{\mathrm{INP,AIDAm}}$	INP concentration measured with AIDAm
$n_{\mathrm{INP,PINE}}$	INP concentration measured with PINE
n_{p}	Particle number
n_{s}	INAS density
$n_{\mathrm{s,observed}}$	Observed INAS density
$n_{\mathrm{s,predicted}}$	Predicted INAS density
R	Specific gas constant for air
r	Radius
RH	Relative humidity
ρ	Particle density
S_{ae}	Aerosol surface area
s_{ae}	Aerosol surface area concentration
S_{ice}	Saturation with respect to ice
Stk	Stokes number
S_{water}	Saturation with respect to water
σ	Surface tension
T	Temperature
T_{AIDA}	AIDA temperature
Δt_{exp}	Duration of an expansion
T_{f}	Freezing temperature
T_{gas}	Gas temperature
T_{wall}	Wall temperature
U	Gas flow
V	Volume
ΔV_{exp}	Analyzed air volume per expansion
χ	Dynamic shape factor

B. Bibliography

Abdalmogith, S. S., and R. M. Harrison, 2005: The use of trajectory cluster analysis to examine the long-range transport of secondary inorganic aerosol in the UK. *Atmospheric Environment*, **39 (35)**, 6686–6695, doi:https://doi.org/10.1016/j.atmosenv.2005.07.059.

Amino, T., Y. Iizuka, S. Matoba, R. Shimada, N. Oshima, T. Suzuki, T. Ando, T. Aoki, and K. Fujita, 2021: Increasing dust emission from ice free terrain in southeastern Greenland since 2000. *Polar Science*, **27**, 100 599, doi:https://doi.org/10.1016/j.polar.2020.100599.

Ardon-Dryer, K., and Z. Levin, 2014: Ground-based measurements of immersion freezing in the eastern Mediterranean. *Atmospheric Chemistry and Physics*, **14 (10)**, 5217–5231, doi:10.5194/acp-14-5217-2014.

Ardon-Dryer, K., Z. Levin, and R. P. Lawson, 2011: Characteristics of immersion freezing nuclei at the South Pole station in Antarctica. *Atmospheric Chemistry and Physics*, **11 (8)**, 4015–4024, doi:10.5194/acp-11-4015-2011.

Atkinson, J. D., B. J. Murray, M. T. Woodhouse, T. F. Whale, K. J. Baustian, K. S. Carslaw, S. Dobbie, D. O'Sullivan, and T. L. Malkin, 2013: The importance of feldspar for ice nucleation by mineral dust in mixed-phase clouds. *Nature*, **498**, 355–358, doi:10.1038/nature12278.

Benz, S., K. Megahed, O. Möhler, H. Saathoff, R. Wagner, and U. Schurath, 2005: T-dependent rate measurements of homogeneous ice nucleation in cloud droplets using a large atmospheric simulation chamber. *Journal of Photochemistry and Photobiology A: Chemistry*, **176 (1)**, 208–217, doi:https://doi.org/10.1016/j.jphotochem.2005.08.026.

Betzer, P. R., et al., 1988: Long–range transport of giant mineral aerosol particles. *Nature*, **336**, 568–571, doi:10.1038/336568a0.

Bi, K., et al., 2019: Measurements of Ice Nucleating Particles in Beijing, China. *Journal of Geophysical Research: Atmospheres*, **124 (14)**, 8065–8075, doi:https://doi.org/10.1029/2019JD030609.

Boose, Y., P. Baloh, M. Plötze, J. Ofner, H. Grothe, B. Sierau, U. Lohmann, and Z. A. Kanji, 2019: Heterogeneous ice nucleation on dust particles sourced from nine deserts worldwide – Part 2: Deposition nucleation and condensation freezing. *Atmospheric Chemistry and Physics*, **19 (2)**, 1059–1076, doi:10.5194/acp-19-1059-2019.

Boose, Y., A. Welti, J. Atkinson, F. Ramelli, A. Danielczok, H. G. Bingemer, M. Plötze, B. Sierau, Z. A. Kanji, and U. Lohmann, 2016a: Heterogeneous ice nucleation on dust particles sourced from nine deserts worldwide – Part 1: Immersion freezing. *Atmospheric Chemistry and Physics*, **16 (23)**, 15 075–15 095, doi:10.5194/acp-16-15075-2016.

Boose, Y., B. Sierau, M. I. García, S. Rodríguez, A. Alastuey, C. Linke, M. Schnaiter, P. Kupiszewski, Z. A. Kanji, and U. Lohmann, 2016b: Ice nucleating particles in the Saharan Air Layer. *Atmospheric Chemistry and Physics*, **16 (14)**, 9067–9087, doi:10.5194/acp-16-9067-2016.

Boucher, O., et al., 2013: *Clouds and Aerosols*, book section 7, 571–658. Cambridge University Press, Cambridge, United Kingdom and New York, NY, USA, doi:10.1017/CBO9781107415324.016.

Brasseur, Z., et al., 2022: Measurement report: Introduction to the HyICE-2018 campaign for measurements of ice-nucleating particles and instrument inter-comparison in the Hyytiälä boreal forest. *Atmospheric Chemistry and Physics*, **22 (8)**, 5117–5145, doi:10.5194/acp-22-5117-2022.

Broadley, S. L., B. J. Murray, R. J. Herbert, J. D. Atkinson, S. Dobbie, T. L. Malkin, E. Condliffe, and L. Neve, 2012: Immersion mode heterogeneous ice nucleation by an illite rich powder representative of atmospheric mineral dust. *Atmospheric Chemistry and Physics*, **12 (1)**, 287–307, doi:10.5194/acp-12-287-2012.

Brunner, C., B. T. Brem, M. Collaud Coen, F. Conen, M. Steinbacher, M. Gysel-Beer, and Z. A. Kanji, 2021: The diurnal and seasonal variability of ice nucleating particles at the High Altitude Station Jungfraujoch (3580 m a.s.l.), Switzerland. *Atmospheric Chemistry and Physics Discussions*, **2021**, 1–26, doi:10.5194/acp-2021-710.

Brunner, C., and Z. A. Kanji, 2020: Continuous online-monitoring of Ice Nucleating Particles: development of the automated Horizontal Ice Nucleation Chamber (HINC-Auto). *Atmospheric Measurement Techniques Discussions*, **2020**, 1–33, doi:10.5194/amt-2020-306.

Budke, C., and T. Koop, 2015: BINARY: an optical freezing array for assessing temperature and time dependence of heterogeneous ice nucleation. *Atmospheric Measurement Techniques*, **8 (2)**, 689–703, doi:10.5194/amt-8-689-2015.

Burkert-Kohn, M., H. Wex, A. Welti, S. Hartmann, S. Grawe, L. Hellner, P. Herenz, J. D. Atkinson, F. Stratmann, and Z. A. Kanji, 2017: Leipzig Ice Nucleation chamber Comparison (LINC): intercomparison of four online ice nucleation counters. *Atmospheric Chemistry and Physics*, **17 (18)**, 11 683–11 705, doi:10.5194/acp-17-11683-2017.

Chahine, M. T., 1992: The hydrological cycle and its influence on climate. *Nature*, **359**, 373–380, doi:10.1038/359373a0.

Chang, K., J. Bench, M. Brege, W. Cantrell, K. Chandrakar, D. Ciochetto, C. Mazzoleni, L. R. Mazzoleni, D. Niedermeier, and R. A. Shaw, 2016: A Laboratory Facility to Study Gas–Aerosol–Cloud Interactions in a Turbulent Environment: The π Chamber. *Bulletin of the American Meteorological Society*, **97 (12)**, 2343 – 2358, doi:10.1175/BAMS-D-15-00203.1.

Chou, C., O. Stetzer, E. Weingartner, Z. Jurányi, Z. A. Kanji, and U. Lohmann, 2011: Ice nuclei properties within a Saharan dust event at the Jungfraujoch in the Swiss Alps. *Atmospheric Chemistry and Physics*, **11 (10)**, 4725–4738, doi:10.5194/acp-11-4725-2011.

Conen, F., S. Henne, C. E. Morris, and C. Alewell, 2012: Atmospheric ice nucleators active $\geq$-12 °C can be quantified on PM_{10} filters. *Atmospheric Measurement Techniques*, **5 (2)**, 321–327, doi:10.5194/amt-5-321-2012.

Conen, F., S. Rodriguez, C. Hüglin, S. Henne, E. Herrmann, N. Bukowiecki, and C. Alewell, 2015: Atmospheric ice nuclei at the high-altitude observatory Jungfraujoch, Switzerland. *Tellus B*, **67**, doi:10.3402/tellusb.v67.25014.

Córdoba, F., et al., 2021: Measurement report: Ice nucleating abilities of biomass burning, African dust, and sea spray aerosol particles over the Yucatán Peninsula. *Atmospheric Chemistry and Physics*, **21 (6)**, 4453–4470, doi:10.5194/acp-21-4453-2021.

Creamean, J. M., et al., 2019: Ice Nucleating Particles Carried From Below a Phytoplankton Bloom to the Arctic Atmosphere. *Geophysical Research Letters*, **46 (14)**, 8572–8581, doi:https://doi.org/10.1029/2019GL083039.

Cwilong, B. M., 1945: Sublimation in a Wilson Chamber. *Nature*, **155**, 361–362, doi:10.1038/155361b0.

Cziczo, D. J., K. D. Froyd, S. J. Gallavardin, O. Moehler, S. Benz, H. Saathoff, and D. M. Murphy, 2009: Deactivation of ice nuclei due to atmospherically relevant surface coatings. *Environmental Research Letters*, **4 (4)**, 044 013, doi:10.1088/1748-9326/4/4/044013.

Cziczo, D. J., K. D. Froyd, C. Hoose, E. J. Jensen, M. Diao, M. A. Zondlo, J. B. Smith, C. H. Twohy, and D. M. Murphy, 2013: Clarifying the Dominant Sources and Mechanisms of Cirrus Cloud Formation. *Science*, **340 (6138)**, 1320–1324, doi:10.1126/science.1234145.

David, R. O., et al., 2019a: Development of the DRoplet Ice Nuclei Counter Zurich (DRINCZ): validation and application to field-collected snow samples. *Atmospheric Measurement Techniques*, **12 (12)**, 6865–6888, doi:10.5194/amt-12-6865-2019.

David, R. O., C. Marcolli, J. Fahrni, Y. Qiu, Y. A. P. Sirkin, V. Molinero, F. Mahrt, D. Brühwiler, U. Lohmann, and Z. A. Kanji, 2019b: Pore condensation and freezing is responsible for ice formation below water saturation for porous particles. *Proceedings of the National Academy of Sciences*, **116 (17)**, 8184–8189, doi:10.1073/pnas.1813647116.

Dekati, 2019: *Dekati® PM10 Impactor User Manual ver. 3.4*. Dekati.

DeMott, P. J., Y. Chen, S. M. Kreidenweis, D. C. Rogers, and D. E. Sherman, 1999: Ice formation by black carbon particles. *Geophysical Research Letters*, **26 (16)**, 2429–2432, doi:https://doi.org/10.1029/1999GL900580.

DeMott, P. J., A. J. Prenni, X. Liu, S. M. Kreidenweis, M. D. Petters, C. H. Twohy, M. S. Richardson, T. Eidhammer, and D. C. Rogers, 2010: Predicting global atmospheric ice nuclei distributions and their impacts on climate. *Proceedings of the National Academy of Sciences*, **107 (25)**, 11 217–11 222, doi:10.1073/pnas.0910818107.

DeMott, P. J., et al., 2011: Resurgence in Ice Nuclei Measurement Research. *Bulletin of the American Meteorological Society*, **92 (12)**, 1623 – 1635, doi:10.1175/2011BAMS3119.1.

DeMott, P. J., et al., 2015: Integrating laboratory and field data to quantify the immersion freezing ice nucleation activity of mineral dust particles. *Atmospheric Chemistry and Physics*, **15 (1)**, 393–409, doi:10.5194/acp-15-393-2015.

DeMott, P. J., et al., 2016: Sea spray aerosol as a unique source of ice nucleating particles. *Proceedings of the National Academy of Sciences*, **113 (21)**, 5797–5803, doi:10.1073/pnas.1514034112.

DeMott, P. J., et al., 2017: Comparative measurements of ambient atmospheric concentrations of ice nucleating particles using multiple immersion freezing methods and a continuous flow diffusion chamber. *Atmospheric Chemistry and Physics*, **17 (18)**, 11 227–11 245, doi:10.5194/acp-17-11227-2017.

DeMott, P. J., et al., 2018: The Fifth International Workshop on Ice Nucleation phase 2 (FIN-02): laboratory intercomparison of ice nucleation measurements. *Atmospheric Measurement Techniques*, **11 (11)**, 6231–6257, doi:10.5194/amt-11-6231-2018.

Després, V., et al., 2012: Primary biological aerosol particles in the atmosphere: a review. *Tellus B: Chemical and Physical Meteorology*, **64 (1)**, 15 598, doi:10.3402/tellusb.v64i0.15598.

Eichler, A., S. Brütsch, S. Olivier, T. Papina, and M. Schwikowski, 2009: A 750 year ice core record of past biogenic emissions from Siberian boreal forests. *Geophysical Research Letters*, **36 (18)**, doi:https://doi.org/10.1029/2009GL038807.

Fahey, D. W., et al., 2014: The AquaVIT-1 intercomparison of atmospheric water vapor measurement techniques. *Atmospheric Measurement Techniques*, **7 (9)**, 3177–3213, doi:10.5194/amt-7-3177-2014.

Flagan, R. C., 1999: On Differential Mobility Analyzer Resolution. *Aerosol Science and Technology*, **30 (6)**, 556–570, doi:10.1080/027868299304417.

Forster, P., et al., 2021: *The Earth's Energy Budget, Climate Feedbacks, and Climate Sensitivity.*, chap. 7. Cambridge University Press, in Press.

Froyd, K. D., et al., 2022: Dominant role of mineral dust in cirrus cloud formation revealed by global-scale measurements. *Nature Geoscience*, **15**, 177–183, doi:10.1038/s41561-022-00901-w.

Hallquist, M., et al., 2009: The formation, properties and impact of secondary organic aerosol: current and emerging issues. *Atmospheric Chemistry and Physics*, **9 (14)**, 5155–5236, doi:10.5194/acp-9-5155-2009.

Hill, T. C. J., B. F. Moffett, P. J. DeMott, D. G. Georgakopoulos, W. L. Stump, and G. D. Franc, 2014: Measurement of Ice Nucleation-Active Bacteria on Plants and in Precipitation by Quantitative PCR. *Applied and Environmental Microbiology*, **80 (4)**, 1256–1267, doi:10.1128/AEM.02967-13.

Hinds, W. C., 2012: *Aerosol technology: properties, behavior, and measurement of airborne particles*. John Wiley & Sons.

Hiranuma, N., et al., 2015: A comprehensive laboratory study on the immersion freezing behavior of illite NX particles: a comparison of 17 ice nucleation measurement techniques. *Atmospheric Chemistry and Physics*, **15 (5)**, 2489–2518, doi:10.5194/acp-15-2489-2015.

Hoose, C., and O. Möhler, 2012: Heterogeneous ice nucleation on atmospheric aerosols: a review of results from laboratory experiments. *Atmospheric Chemistry and Physics*, **12 (20)**, 9817–9854, doi:10.5194/acp-12-9817-2012.

Huang, S., W. Hu, J. Chen, Z. Wu, D. Zhang, and P. Fu, 2021: Overview of biological ice nucleating particles in the atmosphere. *Environment International*, **146**, 106 197, doi:https://doi.org/10.1016/j.envint.2020.106197.

Huffman, J. A., et al., 2013: High concentrations of biological aerosol particles and ice nuclei during and after rain. *Atmospheric Chemistry and Physics*, **13 (13)**, 6151–6164, doi:10.5194/acp-13-6151-2013.

Ignatius, K., et al., 2016: Heterogeneous ice nucleation of viscous secondary organic aerosol produced from ozonolysis of α-pinene. *Atmospheric Chemistry and Physics*, **16 (10)**, 6495–6509, doi:10.5194/acp-16-6495-2016.

IPCC, 2021: *Summary for Policymakers*. Cambridge University Press.

Jaenicke, R., 1982: Physical Aspects of the Atmospheric Aerosol. *Chemistry of the Unpolluted and Polluted Troposphere*, H. W. Georgii, and W. Jaeschke, Eds., Springer Netherlands, Dordrecht, 341–373, NATO Advanced Study Institutes Series, doi:10.1007/978-94-009-7918-5_14.

Järvinen, E., P. Vochezer, O. Möhler, and M. Schnaiter, 2014: Laboratory study of microphysical and scattering properties of corona-producing cirrus clouds. *Appl. Opt.*, **53 (31)**, 7566–7575, doi:10.1364/AO.53.007566.

Johnson, D. L., I. M. Mckinley, J. I. Rodriguez, H. Tseng, and B. A. Carroll, 2014: Characterization Testing of the Thales LPT 9310 Pulse Tube Cooler.

Kanji, Z. A., L. A. Ladino, H. Wex, Y. Boose, M. Burkert-Kohn, D. J. Cziczo, and M. Krämer, 2017: Overview of Ice Nucleating Particles. *Meteorological Monographs*, **58**, 1.1–1.33, doi: 10.1175/AMSMONOGRAPHS-D-16-0006.1.

Kanji, Z. A., R. C. Sullivan, M. Niemand, P. J. DeMott, A. J. Prenni, C. Chou, H. Saathoff, and O. Möhler, 2019: Heterogeneous ice nucleation properties of natural desert dust particles coated with a surrogate of secondary organic aerosol. *Atmospheric Chemistry and Physics*, **19 (7)**, 5091–5110, doi:10.5194/acp-19-5091-2019.

Kanji, Z. A., A. Welti, J. C. Corbin, and A. A. Mensah, 2020: Black Carbon Particles Do Not Matter for Immersion Mode Ice Nucleation. *Geophysical Research Letters*, **47 (11)**, e2019GL086 764, doi: https://doi.org/10.1029/2019GL086764.

Knippertz, P., and M. C. Todd, 2012: Mineral dust aerosols over the Sahara: Meteorological controls on emission and transport and implications for modeling. *Reviews of Geophysics*, **50 (1)**, doi:https: //doi.org/10.1029/2011RG000362.

Knopf, D. A., and T. Koop, 2006: Heterogeneous nucleation of ice on surrogates of mineral dust. *Journal of Geophysical Research: Atmospheres*, **111 (D12)**, doi:https://doi.org/10.1029/2005JD006894.

Köhler, H., 1936: The nucleus in and the growth of hygroscopic droplets. *Transactions of the Faraday Society*, **32**, 1152–1161.

Koop, T., B. Luo, A. Tsias, and T. Peter, 2000: Water activity as the determinant for homogeneous ice nucleation in aqueous solutions. *Nature*, **406**, 611–614, doi:10.1038/35020537.

Korolev, A., and T. Leisner, 2020: Review of experimental studies of secondary ice production. *Atmospheric Chemistry and Physics*, **20 (20)**, 11 767–11 797, doi:10.5194/acp-20-11767-2020.

Kulkarni, P., 2011: *Aerosol measurement : principles, techniques, and applications*. Wiley, Hoboken, N.J.

Lacher, L., U. Lohmann, Y. Boose, A. Zipori, E. Herrmann, N. Bukowiecki, M. Steinbacher, and Z. A. Kanji, 2017: The Horizontal Ice Nucleation Chamber (HINC): INP measurements at conditions relevant for mixed-phase clouds at the High Altitude Research Station Jungfraujoch. *Atmospheric Chemistry and Physics*, **17 (24)**, 15 199–15 224, doi:10.5194/acp-17-15199-2017.

Lacher, L., M. Steinbacher, N. Bukowiecki, E. Herrmann, A. Zipori, and Z. A. Kanji, 2018: Impact of Air Mass Conditions and Aerosol Properties on Ice Nucleating Particle Concentrations at the High Altitude Research Station Jungfraujoch. *Atmosphere*, **9 (9)**, doi:10.3390/atmos9090363.

Lacher, L., et al., 2021: Sources and nature of ice-nucleating particles in the free troposphere at Jungfraujoch in winter 2017. *Atmospheric Chemistry and Physics*, **21 (22)**, 16 925–16 953, doi: 10.5194/acp-21-16925-2021.

Ladino Moreno, L. A., O. Stetzer, and U. Lohmann, 2013: Contact freezing: a review of experimental studies. *Atmospheric Chemistry and Physics*, **13 (19)**, 9745–9769, doi:10.5194/acp-13-9745-2013.

Langer, G., and J. Rodgers, 1975: An Experimental Study of the Detection of Ice Nuclei on Membrane Filters and Other Substrata. *Journal of Applied Meteorology and Climatology*, **14 (4)**, 560 – 570, doi:10.1175/1520-0450(1975)014<0560:AESOTD>2.0.CO;2.

Lighty, J. S., J. M. Veranth, and A. F. Sarofim, 2000: Combustion Aerosols: Factors Governing Their Size and Composition and Implications to Human Health. *Journal of the Air & Waste Management Association*, **50 (9)**, 1565–1618, doi:10.1080/10473289.2000.10464197.

Lindow, S. E., D. C. Arny, and C. D. Upper, 1978: Distribution of ice nucleation-active bacteria on plants in nature. *Applied and Environmental Microbiology*, **36 (6)**, 831–838, doi:10.1128/aem.36.6.831-838. 1978.

Lindsley, W., B. Green, F. Blachere, S. Martin, B. Law, P. Jensen, and M. Schafer, 2017: *Sampling and characterization of bioaerosols*, BA1–115.

Lohmann, U., F. Lüönd, and F. Mahrt, 2016: *An Introduction to Clouds: From the Microscale to Climate*. Cambridge University Press, Cambridge.

Lund, M. T., G. Myhre, and B. H. Samset, 2019: Anthropogenic aerosol forcing under the Shared Socioeconomic Pathways. *Atmospheric Chemistry and Physics*, **19 (22)**, 13 827–13 839, doi:10.5194/ acp-19-13827-2019.

Lüönd, F., O. Stetzer, A. Welti, and U. Lohmann, 2010: Experimental study on the ice nucleation ability of size-selected kaolinite particles in the immersion mode. *Journal of Geophysical Research: Atmospheres*, **115 (D14)**, doi:https://doi.org/10.1029/2009JD012959.

Mahrt, F., C. Marcolli, R. O. David, P. Grönquist, E. J. Barthazy Meier, U. Lohmann, and Z. A. Kanji, 2018: Ice nucleation abilities of soot particles determined with the Horizontal Ice Nucleation Chamber. *Atmospheric Chemistry and Physics*, **18 (18)**, 13 363–13 392, doi:10.5194/acp-18-13363-2018.

Maier, S., A. Tamm, D. Wu, J. Caesar, M. Grube, and B. Weber, 2018: Photoautotrophic organisms control microbial abundance, diversity, and physiology in different types of biological soil crusts. *The ISME Journal*, **12**, 1032–1046, doi:10.1038/s41396-018-0062-8.

Marcolli, C., 2014: Deposition nucleation viewed as homogeneous or immersion freezing in pores and cavities. *Atmospheric Chemistry and Physics*, **14 (4)**, 2071–2104, doi:10.5194/acp-14-2071-2014.

Marcolli, C., 2020: Technical note: Fundamental aspects of ice nucleation via pore condensation and freezing including Laplace pressure and growth into macroscopic ice. *Atmospheric Chemistry and Physics*, **20 (5)**, 3209–3230, doi:10.5194/acp-20-3209-2020.

Mason, R. H., et al., 2016: Size-resolved measurements of ice-nucleating particles at six locations in North America and one in Europe. *Atmospheric Chemistry and Physics*, **16 (3)**, 1637–1651, doi:10.5194/acp-16-1637-2016.

McCluskey, C. S., P. J. DeMott, A. J. Prenni, E. J. T. Levin, G. R. McMeeking, A. P. Sullivan, T. C. J. Hill, S. Nakao, C. M. Carrico, and S. M. Kreidenweis, 2014: Characteristics of atmospheric ice nucleating particles associated with biomass burning in the US: Prescribed burns and wildfires. *Journal of Geophysical Research: Atmospheres*, **119 (17)**, 10 458–10 470, doi:https://doi.org/10.1002/2014JD021980.

McFiggans, G., et al., 2006: The effect of physical and chemical aerosol properties on warm cloud droplet activation. *Atmospheric Chemistry and Physics*, **6 (9)**, 2593–2649, doi:10.5194/acp-6-2593-2006.

Meyers, M. P., P. J. DeMott, and W. R. Cotton, 1992: New Primary Ice-Nucleation Parameterizations in an Explicit Cloud Model. *Journal of Applied Meteorology and Climatology*, **31 (7)**, 708 – 721, doi:10.1175/1520-0450(1992)031<0708:NPINPI>2.0.CO;2.

Mitts, B. A., X. Wang, D. D. Lucero, C. M. Beall, G. B. Deane, P. J. DeMott, and K. A. Prather, 2021: Importance of Supermicron Ice Nucleating Particles in Nascent Sea Spray. *Geophysical Research Letters*, **48 (3)**, e2020GL089 633, doi:https://doi.org/10.1029/2020GL089633.

Möhler, O., et al., 2003: Experimental investigation of homogeneous freezing of sulphuric acid particles in the aerosol chamber AIDA. *Atmospheric Chemistry and Physics*, **3 (1)**, 211–223, URL https://hal.archives-ouvertes.fr/hal-00295233.

Möhler, O., et al., 2006: Efficiency of the deposition mode ice nucleation on mineral dust particles. *Atmospheric Chemistry and Physics*, **6 (10)**, 3007–3021, doi:10.5194/acp-6-3007-2006.

Möhler, O., S. Benz, H. Saathoff, M. Schnaiter, R. Wagner, J. Schneider, S. Walter, V. Ebert, and S. Wagner, 2008a: The effect of organic coating on the heterogeneous ice nucleation efficiency of mineral dust aerosols. *Environmental Research Letters*, **3 (2)**, 025 007, doi:10.1088/1748-9326/3/2/025007.

Möhler, O., D. G. Georgakopoulos, C. E. Morris, S. Benz, V. Ebert, S. Hunsmann, H. Saathoff, M. Schnaiter, and R. Wagner, 2008b: Heterogeneous ice nucleation activity of bacteria: new laboratory experiments at simulated cloud conditions. *Biogeosciences*, **5 (5)**, 1425–1435, doi:10.5194/bg-5-1425-2008.

Möhler, O., et al., 2021: The Portable Ice Nucleation Experiment (PINE): a new online instrument for laboratory studies and automated long-term field observations of ice-nucleating particles. *Atmospheric Measurement Techniques*, **14 (2)**, 1143–1166, doi:10.5194/amt-14-1143-2021.

Murphy, D. M., and T. Koop, 2005: Review of the vapour pressures of ice and supercooled water for atmospheric applications. *Quarterly Journal of the Royal Meteorological Society*, **131 (608)**, 1539–1565, doi:https://doi.org/10.1256/qj.04.94.

Murray, B. J., K. S. Carslaw, and P. R. Field, 2021: Opinion: Cloud-phase climate feedback and the importance of ice-nucleating particles. *Atmospheric Chemistry and Physics*, **21 (2)**, 665–679, doi:10.5194/acp-21-665-2021.

Murray, B. J., D. O'Sullivan, J. D. Atkinson, and M. E. Webb, 2012: Ice nucleation by particles immersed in supercooled cloud droplets. *Chem. Soc. Rev.*, **41**, 6519–6554, doi:10.1039/C2CS35200A.

Nagare, B., C. Marcolli, A. Welti, O. Stetzer, and U. Lohmann, 2016: Comparing contact and immersion freezing from continuous flow diffusion chambers. *Atmospheric Chemistry and Physics*, **16 (14)**, 8899–8914, doi:10.5194/acp-16-8899-2016.

Niemand, M., et al., 2012: A Particle-Surface-Area-Based Parameterization of Immersion Freezing on Desert Dust Particles. *Journal of the Atmospheric Sciences*, **69 (10)**, 3077–3092, doi:10.1175/JAS-D-11-0249.1.

O'Sullivan, D., B. J. Murray, T. L. Malkin, T. F. Whale, N. S. Umo, J. D. Atkinson, H. C. Price, K. J. Baustian, J. Browse, and M. E. Webb, 2014: Ice nucleation by fertile soil dusts: relative importance of mineral and biogenic components. *Atmospheric Chemistry and Physics*, **14 (4)**, 1853–1867, doi:10.5194/acp-14-1853-2014.

Paramonov, M., R. O. David, R. Kretzschmar, and Z. A. Kanji, 2018: A laboratory investigation of the ice nucleation efficiency of three types of mineral and soil dust. *Atmospheric Chemistry and Physics*, **18 (22)**, 16 515–16 536, doi:10.5194/acp-18-16515-2018.

Paramonov, M., et al., 2020: Condensation/immersion mode ice-nucleating particles in a boreal environment. *Atmospheric Chemistry and Physics*, **20 (11)**, 6687–6706, doi:10.5194/acp-20-6687-2020.

Polen, M., E. Lawlis, and R. C. Sullivan, 2016: The unstable ice nucleation properties of Snomax® bacterial particles. *Journal of Geophysical Research: Atmospheres*, **121 (19)**, 11,666–11,678, doi:https://doi.org/10.1002/2016JD025251.

Porter, G. C. E., S. N. F. Sikora, M. P. Adams, U. Proske, A. D. Harrison, M. D. Tarn, I. M. Brooks, and B. J. Murray, 2020: Resolving the size of ice-nucleating particles with a balloon deployable aerosol sampler: the SHARK. *Atmospheric Measurement Techniques*, **13 (6)**, 2905–2921, doi:10.5194/amt-13-2905-2020.

Pratt, K. A., P. J. DeMott, J. R. French, Z. Wang, D. L. Westphal, A. J. Heymsfield, C. H. Twohy, A. J. Prenni, and K. A. Prather, 2009: In situ detection of biological particles in cloud ice-crystals. *Nature Geoscience*, **2**, 398–401, doi:10.1038/ngeo521.

Pruppacher, H., and J. Klett, 2010: *Microphysics of Clouds and Precipitation*. Atmospheric and Oceanographic Sciences Library, Springer Netherlands.

Pummer, B. G., H. Bauer, J. Bernardi, S. Bleicher, and H. Grothe, 2012: Suspendable macromolecules are responsible for ice nucleation activity of birch and conifer pollen. *Atmospheric Chemistry and Physics*, **12 (5)**, 2541–2550, doi:10.5194/acp-12-2541-2012.

Radke, L. F., P. V. Hobbs, and M. W. Eltgroth, 1980: Scavenging of Aerosol Particles by Precipitation. *Journal of Applied Meteorology and Climatology*, **19 (6)**, 715 – 722, doi:10.1175/1520-0450(1980)019<0715:SOAPBP>2.0.CO;2.

Reicher, N., C. Budke, L. Eickhoff, S. Raveh-Rubin, I. Kaplan-Ashiri, T. Koop, and Y. Rudich, 2019: Size-dependent ice nucleation by airborne particles during dust events in the eastern Mediterranean. *Atmospheric Chemistry and Physics*, **19 (17)**, 11 143–11 158, doi:10.5194/acp-19-11143-2019.

Rinaldi, M., et al., 2021: Ice-nucleating particle concentration measurements from Ny-Ålesund during the Arctic spring–summer in 2018. *Atmospheric Chemistry and Physics*, **21 (19)**, 14 725–14 748, doi:10.5194/acp-21-14725-2021.

Rogers, D. C., 1988: Development of a continuous flow thermal gradient diffusion chamber for ice nucleation studies. *Atmospheric Research*, **22 (2)**, 149–181, doi:https://doi.org/10.1016/0169-8095(88)90005-1.

Rohde, H., and J. Grandell, 1972: On the removal time of aerosol particles from the atmosphere by precipitation scavenging. *Tellus*, **24 (5)**, 442–454, doi:https://doi.org/10.1111/j.2153-3490.1972.tb01571.x.

Rubino, M., A. D'Onofrio, O. Seki, and J. A. Bendle, 2016: Ice-core records of biomass burning. *The Anthropocene Review*, **3 (2)**, 140–162, doi:10.1177/2053019615605117.

Saathoff, H., K.-H. Naumann, O. Möhler, Å. M. Jonsson, M. Hallquist, A. Kiendler-Scharr, T. F. Mentel, R. Tillmann, and U. Schurath, 2009: Temperature dependence of yields of secondary organic aerosols from the ozonolysis of α-pinene and limonene. *Atmospheric Chemistry and Physics*, **9 (5)**, 1551–1577, doi:10.5194/acp-9-1551-2009.

Salby, M. L., 2012: *Physics of the Atmosphere and Climate*. Cambridge University Press.

Schaefer, V. J., 1946: The Production of Ice Crystals in a Cloud of Supercooled Water Droplets. *Science*, **104 (2707)**, 457–459, doi:10.1126/science.104.2707.457.

Schiebel, T., 2017: Ice Nucleation Activity of Soil Dust Aerosols. Ph.D. thesis, Karlsruher Institut für Technologie (KIT), doi:10.5445/IR/1000076327, 12.04.02; LK 01.

Schill, G. P., et al., 2020: The contribution of black carbon to global ice nucleating particle concentrations relevant to mixed-phase clouds. *Proceedings of the National Academy of Sciences*, **117 (37)**, 22 705–22 711, doi:10.1073/pnas.2001674117.

Schmale, J., et al., 2018: Long-term cloud condensation nuclei number concentration, particle number size distribution and chemical composition measurements at regionally representative observatories. *Atmospheric Chemistry and Physics*, **18 (4)**, 2853–2881, doi:10.5194/acp-18-2853-2018.

Schneider, J., et al., 2021a: High Homogeneous Freezing Onsets of Sulfuric Acid Aerosol at Cirrus Temperatures. *Atmospheric Chemistry and Physics Discussions*, **2021**, 1–30, doi:10.5194/acp-2021-319.

Schneider, J., et al., 2021b: The seasonal cycle of ice-nucleating particles linked to the abundance of biogenic aerosol in boreal forests. *Atmospheric Chemistry and Physics*, **21 (5)**, 3899–3918, doi:10.5194/acp-21-3899-2021.

Schrod, J., et al., 2020a: Ice-nucleating particle concentrations of the past: insights from a 600-year-old Greenland ice core. *Atmospheric Chemistry and Physics*, **20 (21)**, 12 459–12 482, doi:10.5194/acp-20-12459-2020.

Schrod, J., et al., 2020b: Long-term deposition and condensation ice-nucleating particle measurements from four stations across the globe. *Atmospheric Chemistry and Physics*, **20 (24)**, 15 983–16 006, doi:10.5194/acp-20-15983-2020.

Schulz, M., G. d. Leeuw, and Y. Balkanski, 2004: Sea-salt aerosol source functions and emissions. *Emissions of Atmospheric Trace Compounds*, Springer, 333–359.

Seinfeld, J. H., and S. N. Pandis, 2016: *Atmospheric chemistry and physics: from air pollution to climate change*. John Wiley & Sons.

Si, M., et al., 2018: Ice-nucleating ability of aerosol particles and possible sources at three coastal marine sites. *Atmospheric Chemistry and Physics*, **18 (21)**, 15 669–15 685, doi:10.5194/acp-18-15669-2018.

Sipilä, M., et al., 2010: The Role of Sulfuric Acid in Atmospheric Nucleation. *Science*, **327 (5970)**, 1243–1246, doi:10.1126/science.1180315.

Solomon, A., G. de Boer, J. M. Creamean, A. McComiskey, M. D. Shupe, M. Maahn, and C. Cox, 2018: The relative impact of cloud condensation nuclei and ice nucleating particle concentrations on phase partitioning in Arctic mixed-phase stratocumulus clouds. *Atmospheric Chemistry and Physics*, **18 (23)**, 17 047–17 059, doi:10.5194/acp-18-17047-2018.

Stein, A. F., R. R. Draxler, G. D. Rolph, B. J. B. Stunder, M. D. Cohen, and F. Ngan, 2015: NOAA's HYSPLIT Atmospheric Transport and Dispersion Modeling System. *Bulletin of the American Meteorological Society*, **96 (12)**, 2059 – 2077, doi:10.1175/BAMS-D-14-00110.1.

Steinke, I., et al., 2016: Ice nucleation activity of agricultural soil dust aerosols from Mongolia, Argentina and Germany. *Journal of Geophysical Research: Atmospheres*, **121**, doi:10.1002/2016JD025160.

Stier, P., et al., 2005: The aerosol-climate model ECHAM5-HAM. *Atmospheric Chemistry and Physics*, **5 (4)**, 1125–1156, doi:10.5194/acp-5-1125-2005.

Storelvmo, T., 2017: Aerosol Effects on Climate via Mixed-Phase and Ice Clouds. *Annual Review of Earth and Planetary Sciences*, **45 (1)**, 199–222, doi:10.1146/annurev-earth-060115-012240.

Storelvmo, T., I. Tan, and A. V. Korolev, 2015: Cloud Phase Changes Induced by CO2 Warming—a Powerful yet Poorly Constrained Cloud-Climate Feedback. *Current Climate Change Reports*, **1**, 288–295, doi:10.1007/s40641-015-0026-2.

Sullivan, R. C., S. A. Guazzotti, D. A. Sodeman, and K. A. Prather, 2007: Direct observations of the atmospheric processing of asian mineral dust. *Atmospheric Chemistry and Physics*, **7 (5)**, 1213–1236, doi:10.5194/acp-7-1213-2007.

Sullivan, R. C., et al., 2010: Irreversible loss of ice nucleation active sites in mineral dust particles caused by sulphuric acid condensation. *Atmospheric Chemistry and Physics*, **10 (23)**, 11 471–11 487, doi:10.5194/acp-10-11471-2010.

Tegen, I., and K. Schepanski, 2009: The global distribution of mineral dust. *IOP Conference Series: Earth and Environmental Science*, **7**, 012 001, doi:10.1088/1755-1307/7/1/012001.

Tobo, Y., A. J. Prenni, P. J. DeMott, J. A. Huffman, C. S. McCluskey, G. Tian, C. Pöhlker, U. Pöschl, and S. M. Kreidenweis, 2013: Biological aerosol particles as a key determinant of ice nuclei populations in a forest ecosystem. *Journal of Geophysical Research: Atmospheres*, **118 (17)**, 10,100–10,110, doi:https://doi.org/10.1002/jgrd.50801.

TSI, 2002: *Model 3010 Condensation Particle Counter Instruction Manual*. TSI.

TSI, 2013: *Aerodynamic Particle Sizer® Spectrometer Model 3321 User's Manual*. TSI.

TSI, 2021: *Scanning Mobility Particle Sizer™ Spectrometer (SMPS™) Model 3938*. TSI.

Ullrich, R., C. Hoose, O. Möhler, M. Niemand, R. Wagner, K. Höhler, N. Hiranuma, H. Saathoff, and T. Leisner, 2017: A New Ice Nucleation Active Site Parameterization for Desert Dust and Soot. *Journal of the Atmospheric Sciences*, **74 (3)**, 699 – 717, doi:10.1175/JAS-D-16-0074.1.

Umo, N. S., R. Wagner, R. Ullrich, A. Kiselev, H. Saathoff, P. G. Weidler, D. J. Cziczo, T. Leisner, and O. Möhler, 2019: Enhanced ice nucleation activity of coal fly ash aerosol particles initiated by ice-filled pores. *Atmospheric Chemistry and Physics*, **19 (13)**, 8783–8800, doi:10.5194/acp-19-8783-2019.

Vali, G., 1971: Quantitative Evaluation of Experimental Results an the Heterogeneous Freezing Nucleation of Supercooled Liquids. *Journal of the Atmospheric Sciences*, **28 (3)**, 402–409, doi: 10.1175/1520-0469(1971)028<0402:QEOERA>2.0.CO;2.

Vali, G., P. J. DeMott, O. Möhler, and T. F. Whale, 2015: Technical Note: A proposal for ice nucleation terminology. *Atmospheric Chemistry and Physics*, **15 (18)**, 10 263–10 270, doi:10.5194/acp-15-10263-2015.

Vergara-Temprado, J., et al., 2017: Contribution of feldspar and marine organic aerosols to global ice nucleating particle concentrations. *Atmospheric Chemistry and Physics*, **17 (5)**, 3637–3658, doi: 10.5194/acp-17-3637-2017, URL https://acp.copernicus.org/articles/17/3637/2017/.

Vergara-Temprado, J., A. K. Miltenberger, K. Furtado, D. P. Grosvenor, B. J. Shipway, A. A. Hill, J. M. Wilkinson, P. R. Field, B. J. Murray, and K. S. Carslaw, 2018: Strong control of Southern Ocean cloud reflectivity by ice-nucleating particles. *Proceedings of the National Academy of Sciences*, **115 (11)**, 2687–2692, doi:10.1073/pnas.1721627115.

Vonnegut, B., 1947: The Nucleation of Ice Formation by Silver Iodide. *Journal of Applied Physics*, **18 (7)**, 593–595, doi:10.1063/1.1697813.

Wagner, R., S. Benz, O. Möhler, H. Saathoff, and U. Schurath, 2006: Probing ice clouds by broadband mid-infrared extinction spectroscopy: case studies from ice nucleation experiments in the AIDA aerosol and cloud chamber. *Atmospheric Chemistry and Physics*, **6 (12)**, 4775–4800.

Wagner, R., J. Kaufmann, O. Möhler, H. Saathoff, M. Schnaiter, R. Ullrich, and T. Leisner, 2018: Heterogeneous Ice Nucleation Ability of NaCl and Sea Salt Aerosol Particles at Cirrus Temperatures. *Journal of Geophysical Research: Atmospheres*, **123 (5)**, 2841–2860, doi:https://doi.org/10.1002/2017JD027864.

Wagner, R., A. Kiselev, O. Möhler, H. Saathoff, and I. Steinke, 2016: Pre-activation of ice-nucleating particles by the pore condensation and freezing mechanism. *Atmospheric Chemistry and Physics*, **16 (4)**, 2025–2042, doi:10.5194/acp-16-2025-2016.

Weinzierl, B., et al., 2017: The Saharan Aerosol Long-Range Transport and Aerosol–Cloud-Interaction Experiment: Overview and Selected Highlights. *Bulletin of the American Meteorological Society*, **98 (7)**, 1427–1451, doi:10.1175/BAMS-D-15-00142.1.

Welker, R. W., 2012: Chapter 4 - Size Analysis and Identification of Particles. *Developments in Surface Contamination and Cleaning*, R. Kohli, and K. Mittal, Eds., William Andrew Publishing, Oxford, 179–213, doi:https://doi.org/10.1016/B978-1-4377-7883-0.00004-3.

Welti, A., F. Lüönd, Z. A. Kanji, O. Stetzer, and U. Lohmann, 2012: Time dependence of immersion freezing: an experimental study on size selected kaolinite particles. *Atmospheric Chemistry and Physics*, **12 (20)**, 9893–9907, doi:10.5194/acp-12-9893-2012.

Welti, A., F. Lüönd, O. Stetzer, and U. Lohmann, 2009: Influence of particle size on the ice nucleating ability of mineral dusts. *Atmospheric Chemistry and Physics*, **9 (18)**, 6705–6715, doi:10.5194/acp-9-6705-2009.

Welti, A., K. Müller, Z. L. Fleming, and F. Stratmann, 2018: Concentration and variability of ice nuclei in the subtropical maritime boundary layer. *Atmospheric Chemistry and Physics*, **18 (8)**, 5307–5320, doi:10.5194/acp-18-5307-2018.

Wex, H., et al., 2015: Intercomparing different devices for the investigation of ice nucleating particles using Snomax as test substance. *Atmospheric Chemistry and Physics*, **15 (3)**, 1463–1485, doi:10.5194/acp-15-1463-2015.

Wex, H., et al., 2019: Annual variability of ice-nucleating particle concentrations at different arctic locations. *Atmospheric Chemistry and Physics*, **19 (7)**, 5293–5311, doi:10.5194/acp-19-5293-2019.

Whitby, K. T., 1978: The physical characteristics of sulfur aerosols. *Sulfur in the Atmosphere*, R. HUSAR, J. LODGE, and D. MOORE, Eds., Pergamon, 135–159, doi:https://doi.org/10.1016/B978-0-08-022932-4.50018-5.

Wilbourn, E. K., D. C. O. Thornton, C. Ott, J. Graff, P. K. Quinn, T. S. Bates, R. Betha, L. M. Russell, M. J. Behrenfeld, and S. D. Brooks, 2020: Ice Nucleation by Marine Aerosols Over the North Atlantic Ocean in Late Spring. *Journal of Geophysical Research: Atmospheres*, **125 (4)**, e2019JD030 913, doi:https://doi.org/10.1029/2019JD030913.

Wilson, J. C., and B. Y. Liu, 1980: Aerodynamic particle size measurement by laser-doppler velocimetry. *Journal of Aerosol Science*, **11 (2)**, 139–150, doi:https://doi.org/10.1016/0021-8502(80)90030-0.

Wolf, M. J., et al., 2020: A biogenic secondary organic aerosol source of cirrus ice nucleating particles. *Nature Communications*, **11**, 4834, doi:10.1038/s41467-020-18424-6.

Wood, S. E., M. B. Baker, and B. D. Swanson, 2002: Instrument for studies of homogeneous and heterogeneous ice nucleation in free-falling supercooled water droplets. *Review of Scientific Instruments*, **73 (11)**, 3988–3996, doi:10.1063/1.1511796.

Yau, M. K., and R. R. Rogers, 1996: *A short course in cloud physics*. Elsevier.

Zelinka, M. D., D. A. Randall, M. J. Webb, and S. A. Klein, 2017: Clearing clouds of uncertainty. *Nature Climate Change*, **7**, 674–678, doi:10.1038/nclimate3402.

C. List of Figures

D. List of Tables

Acknowledgments

At the end of my PhD, it is the time to thank all the people who supported me in different ways and contributed to the success of this work.

At first, I would like to thank Prof. Dr. Thomas Leisner and Prof. Dr. Benjamin J. Murray for being my referee and co-referee and for all the helpful discussions we had around instrument developments and field INP measurements.

I am especially thankful to Dr. Ottmar Möhler, who gave me the opportunity to do my PhD in his working group and to Dr. Larissa Lacher, for her support during my laboratory and field campaigns. You both gave me all the help and encouragement I needed to work on my own ideas and gave me the chance to be part of multiple international collaborations. Without all our discussions about PINE measurements and the results of my work, this thesis would have never been what it turned out to be.

The CAL01 and CAL02 campaigns were a big effort shared among many people. I am very thankful to everyone who contributed with their own INP measurements and for the discussions we had about the experiments. All your input and ideas helped a lot to interpret the results of these measurements.

I am thankful to Dr. Vladimír Ždímal and Dr. Naděžda Zíková from the ICPF CAS for their help in the organization and conduction of the Kosetice21 campaign. Many thanks also to the facility members of the National Atmospheric Observatory in Kosetice for hosting me during my 2 weeks stay and for providing the meteorological data of the campaign period.

A great thanks to the whole Swabian MOSES team, who warmly welcomed me during the Swabian21 campaign and gave me the opportunity to perform INP measurements with PINE and INSEKT. I really enjoyed the time we spent together at the container area in Rottenburg.

Thanks to Martin Kohler from IMK-TRO for providing the meteorological data from the measuring mast at KIT Campus North, which I needed for the analysis of the CORONA data set.

I want to thank Dr. Konstantinos Eleftheriadis from NCSR Demokritos and Prof. Dr. Athanasios Nenes from EPFL for inviting us to join the CALISHTO21 campaign with one of our PINE chambers. Many

thanks also to all the technicians and scientists I met onsite for the joyful stay in Kalavryta and for their continuous support whenever my instrument needed some maintenance.

I thank Prof. Dr. Daniel Knopf and Dr. Naruki Hiranuma for initiating the AIC02 campaign at the AIDA facility and for giving me the opportunity to be part of this great collaboration. My work profited a lot from the size-selective INP measurements I was able to perform within this campaign.

During my PhD work I received a lot of support during the AIDA campaigns and in preparation and conduction of the field campaigns. Therefore, I would like to thank Rainer Buschbacher, Tomasz Chudy, Olga Dombrowski, Jens Nadolny, Georg Scheurig and Steffen Vogt for all their assistance. Especially Jens Nadolny contributed a lot to the success of the AIDAm and PINE measurements by writing all the LabView control software and fixing each bug and special wish that came up. Olga Dombrowski and the INSEKT student assistants, I would warmly thank for analyzing the majority of the INSEKT filters I sampled for my work. Without your efforts I would have never managed to get all the analysis ready in time. Many thanks to Susanne Bolz who helped me with each organizational and bureaucracy issue and to Frank Schwarz for the continuous IT support. Thanks to the whole IMK-AAF for creating such a nice working atmosphere and to the whole AG-Möhler for all the great offline and online discussions.

In the end I want to address my deepest thanks to my friends for all the evenings and weekend trips we had together. You always managed to reset my mind from work. Without you, the last years would have never been as great as they were.

Very special thanks to my parents and my two sisters. You always believed in what I did, and encouraged me to keep on going through this PhD journey, no matter how difficult it was.